High Temperature Transport Properties of Lead Chalcogenides and Their Alloys

Thesis by
Heng Wang

In Partial Fulfillment of the Requirements for the Degree
of
Doctor of Philosophy

CALIFORNIA INSTITUTE OF TECHNOLOGY
Pasadena, California

2014
(Defended May 14, 2014)

ACKNOWLEDGEMENTS

This is probably the most difficult part when writing this thesis because the feelings I want to express will be beyond my language in English.

I am most grateful to my wife Jie Zhang for her tremendous support physically and mentally. I haven't been responsible financially to the family while pursuing the best for my PhD. Despite of the poor lives we have lived for the past six years I have only received endless encouragement from her -- not a single complaint. Should this research be of any meaning to anyone, it is made possible because she believed in me.

I am so blessed to have Dr. Jeff Snyder as my advisor. He is absolutely all one can ask for as a mentor, not only because of his borderless knowledge that enlightens me all the time, but also the way he treats us with kindness, respect, and trust. I would call myself a wonderful advisor if I could be half like him in the future.

The former and current members of the thermoelectric group at Caltech all deserve my special thank. I cherish the experience I had with each of them. Discussions with former postdoc Yanzhong Pei, now a professor at Tongji University in China have led to quite a few collaborations. I need also to thank Yoshiki Takagiwa for wonderful collaboration in band structure calculation. Part of experiments in this research was performed by visiting scholars Eugen Schechtel, Xianlong Cao, Jianli Wang, and Cheng-Lung Chen and I would like to acknowledge them for their contribution.

I also would like to thank the families, both my parents and in-laws for understanding and supporting the life path I have chosen. Without them it would be impossible for me to have all this done.

The single most joyful moment in the past six years is the birth of Ruibin, our first child. I am thankful that he has been a great baby boy who brought us endless happiness. His happy face dismisses all the tiredness and mishaps along the way.

ABSTRACT

This thesis describes a series of experimental studies of lead chalcogenide thermoelectric semiconductors, mainly PbSe. Focusing on a well-studied semiconductor and reporting good but not extraordinary *zT*, this thesis distinguishes itself by answering the following questions that haven't been answered: What represents the thermoelectric performance of PbSe? Where does the high *zT* come from? How (and how much) can we make it better? For the first question, samples were made with highest quality. Each transport property was carefully measured, cross-verified and compared with both historical and contemporary report to overturn commonly believed underestimation of *zT*. For n- and p-type PbSe *zT* at 850 K can be 1.1 and 1.0, respectively. For the second question, a systematic approach of quality factor *B* was used. In n-type PbSe *zT* is benefited from its high-quality conduction band that combines good degeneracy, low band mass and low deformation potential, whereas *zT* of p-type is boosted when two mediocre valence bands converge (in band edge energy). In both cases the thermal conductivity from PbSe lattice is inherently low. For the third question, the use of solid solution lead chalcogenide alloys was first evaluated. Simple criteria were proposed to help quickly evaluate the potential of improving *zT* by introducing atomic disorder. For both $PbTe_{1-x}Se_x$ and $PbSe_{1-x}S_x$, the impacts in electron and phonon transport compensate each other. Thus, *zT* in each case was roughly the average of two binary compounds. In p-type $Pb_{1-x}Sr_xSe$ alloys an improvement of *zT* from 1.1 to 1.5 at 900 K was achieved, due to the band engineering effect that moves the two valence bands closer in energy. To date, making n-type PbSe better hasn't been accomplished, but possible strategy is discussed.

TABLE OF CONTENTS

LIST OF FIGURES

LIST OF TABLES

Chapter 1

Introduction

Thermoelectric effects are processes that make conversion of energy directly between heat and electricity. Unlike the conventional approach that uses different types of engines, the thermoelectric conversion is made possible entirely by solid-state devices, through charge transport inside solids. Among the merits of a thermoelectric generator or cooler are no moving parts, no maintenance needed, compact and quite. With all these desirable features, will thermoelectric generation provide the society lots of energy and be part of the new energy solution in the near future? Not very likely due to cost and efficiency. However, thermoelectrics see no competitor as the technology for applications that requires for example, precise, on-spot temperature control; quite and vibration free cooling; maintenance-free on location power for embedded sensors and other low energy consuming devices; and continuous power supply in remote places with ambient heat source. There is then a good reason to expect interests on thermoelectric technology would continue to increase. This thesis research is aimed at developing better performing thermoelectric materials and providing the community useful knowledge that can be used to develop better materials.

This thesis is organized in the following way: the first chapter will give a general introduction of thermoelectric effects and general background of this research as well as a summary. Chapter 2 will talk about experimental details. From Chapter 3, major results from different studies will be presented. The detailed semiconductor physics theories that are pertinent to this research are separated into topics and placed in each chapter of most relevance. Such discussions comes after the presentation of results of each study, in such a way interested readers will get more details that they need while others looking for general results or data will not be distracted from unnecessary information intended to help a deeper understanding of the results. Summaries of each study will be included in the introduction section at the beginning of each chapter.

1.1 Thermoelectric Effects

Thermoelectric phenomena consist of three correlated effects, namely the Seebeck effect, the Peltier effect and the Thomson effect. These are illustrated below in Figure 1.1. When a pair of two different conductors is exposed to a temperature gradient a voltage is generated between two ends, this is the Seebeck effect. Reversibly if a voltage is applied to such a pair of conductors there is heat absorbed or released at the junction depending on specific setup, this is called the Peltier effect. There is a third effect, the Thomson effect: while a single type of conductor is exposed to both a temperature gradient and a voltage, heat will be absorbed on one side and released on the other. In practice, the Seebeck effect is more convenient for measurements and the voltage generated per degree of temperature difference, namely the Seebeck coefficient $S = V/\Delta T$, is often discussed when characterizing thermoelectric performances.

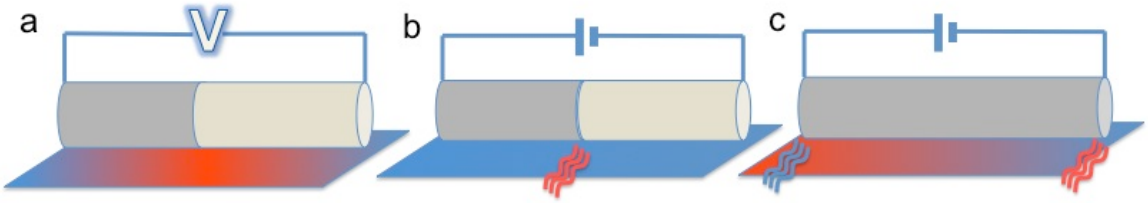

Figure 1.1. Thermoelectric effects a) Seebeck effect, b) Peltier effect, c) Thomson effect

Seebeck effect is not an interface effect, but measuring it does require contact of two different conductors. The Seebeck coefficient of a specific material can be determined relative to a standard conductor (usually metal) whose absolute Seebeck coefficient has been determined. This enabled us to obtain and compare Seebeck coefficient of each specific material directly. The temperature driven flux of carriers in any material is from the hot side to the cold side. Thus when the charge carriers are electrons the counteracting electric field will be against temperature gradient as well, resulting in a negative Seebeck coefficient. Oppositely if the charge carriers are holes, the Seebeck coefficient will be positive.

Rigorous discussion about the thermodynamic nature of Seebeck voltage can be found in classic articles by early explorers in thermoelectric research[1-4]. In a short way, the temperature driven carrier flux can be seen as a flow of entropy, so the Seebeck coefficient is equivalent to the entropy transferred by carriers with one coulomb of charge. In a very intuitive way, Seebeck voltage can be regarded as the compensating electric field in response to the charge flow as a result of temperature

gradient when the system is at steady state (not equilibrium). Two common analogies of this are 1) the bias to stabilize the uneven distribution of carriers with more on the hot side and less on the cold side, or 2) the bias to balance the net diffusion of carriers as particles in an ideal gas that move towards the cold end due to higher kinetic energy. Neither of these simplified images is completely correct. The flux of carriers is the result of 1) the charge density difference: one would expect this in intrinsic semiconductors, but not much in metals or heavily doped semiconductors, 2) the energy distribution difference: more high energy/velocity carriers at higher temperatures, and 3) the temperature dependent scattering of carriers that favors the diffusion towards the low temperature side. The latter two explained why Seebeck coefficient as an open circuit voltage, would be affected by carrier scattering processes.

1.2 Devices and Thermoelectric Materials

A typical thermoelectric module is illustrated in Figure 1.2. Columns of thermoelectric materials are bonded thermally in parallel and electrically in series. The basic unit consists of a pair of n-type and p-type thermoelectrics in order to produce larger voltage.

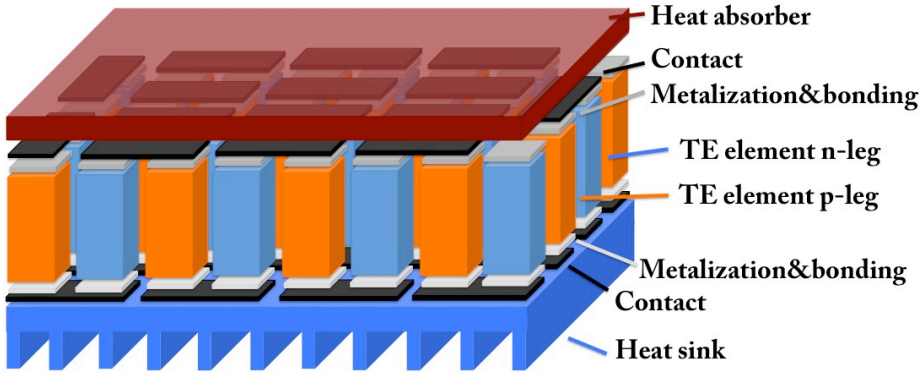

Figure 1.2. Schematic of a thermoelectric module

The power generation with thermoelectric devices is a thermodynamic process whose efficiency is subject to the limit of Carnot efficiency. In theory, to maximize efficiency one wants to use high quality, high temperature heat sources on one side and sufficient active cooling on the other. In reality, conventional heat engines make more sense economically when high quality heat sources are available, except for few niche applications when their reliability or vibration becomes a concern. Using heat sources with higher temperature also raises considerable challenges to materials as well as construction. On the other hand to decrease the temperature on the cold side requires

active cooling, which adds extra weight and complexity to the device, and consumes power itself. So there is always a trade off in device design between weight, cost, and efficiency.

For a basic unit of n- and p-legs between hot side temperature T_1 and cold side temperature T_2, accounting for the power generated due to Seebeck effect, and heat released on the cold side via heat conduction, Peltier effect and Joule heating, through rather straightforward derivation. One comes to the expression of conversion efficiency:

$$\eta = \frac{T_1 - T_2}{T_1} \frac{\frac{m}{m+1}}{1 + \frac{Kr}{S^2}\frac{m+1}{T_1} - \frac{1}{2}\frac{T_1 - T_2}{m+1}} \qquad \text{Equation 1.1}$$

m stands for the ratio in electrical resistance of the load and device. Given the temperatures on both side, and the optimized m value, the efficiency increases with the increase of S^2/Kr, *S*, *K* and *r* are the sum of absolute Seebeck coefficient, heat conductance and electrical resistance of both legs, respectively. Their combination is called the thermoelectric figure of merit *Z*, and on the material level, this correspond to $z = S^2/\kappa\rho$, κ and ρ being the thermal conductivity and electrical resistivity, respectively. In the material research, the dimensionless figure of merit *zT* is the most used quantity to describe the performance of a material. From Equation 1.1 it is obvious that the maximum conversion efficiency is determined by the figure of merit *zT* of the material.

The power factor, namely S^2/ρ, is also often used in describing the performance of a thermoelectric material, partly because the thermal conductivity κ especially at high temperature is not as easily measured as electrical properties. Intuitively, it might appear that materials with higher power factor output more power thus the power factor becomes the metric for thermoelectric generators when efficiency is not the concern. This notion is wrong, and a system level consideration would show actually the maximum power one can get from a device is also related to its figure of merit *zT*. Power factor should not be a metric of performance for thermoelectrics in almost any circumstances.

To date, the best thermoelectric materials in real application has *zT* around 1 within some temperature range.[5, 6] Advanced thermoelectrics developed in labs have claimed[7, 8] *zT* of 1.5 to 2.2 peaking at different temperatures. Improving *zT* beyond this is extraordinarily difficult, because all the parameters in the expression of *zT* can't be modified without affecting others. Start with Seebeck coefficient, following its thermodynamic nature, it can be readily seen that for conductors

with fewer carriers, adding one electron brings large configuration entropy because there are many available empty states, so Seebeck coefficient is large in these conductors. On the other hand, for metals the configuration entropy is small because there are not as many empty states for the added electron, which means Seebeck coefficient is small. The electrical resistivity, however, decreases monotonously as one add more and more carriers to the system. As a result of compromise, the best thermoelectric materials are always heavily doped semiconductors with carrier density on the order of 10^{18} to 10^{21} cm^{-3}, as shown in Figure 1.3:

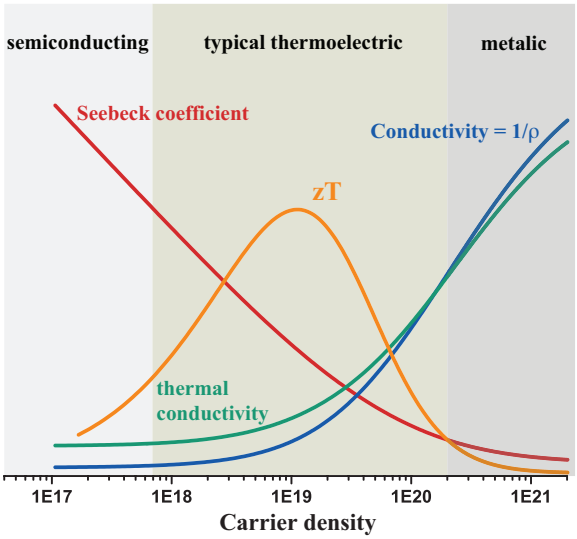

Figure 1.3. Schematic trend of transport properties versus carrier density, zT is usually optimized in the heavily doped semiconductor regime.

The domain of thermoelectric materials sits in between conventional semiconductors and metals. Doping is essential to thermoelectrics, same as for their applications in integrated circuits, optical sensors/detectors or photovoltaic. High mobility is also important, same as for these other applications. On the other hand thermoelectric semiconductors are so heavily doped that their transport properties are more like metals than semiconductors. The doping levels are orders of magnitude higher than in other semiconductors, intrinsic impurities or self-doping is less important than foreign impurities. The mobility is mostly governed by the electron-phonon interaction and other scattering centers like ionized impurities or interfaces are often effectively screened or overwhelmed.

Good thermoelectrics have a few common characteristics: 1) a decent band gap that is large enough to inhibit excitation of minority carriers. The band gap should also be narrow and the bonding

should be covalent so the carriers will be more delocalized. Less electronegativity difference between atoms is favorable. 2) For lower thermal conductivity, compounds formed between heavier elements are likely better thermoelectrics compared to their analogs with light elements. 3) Complex structures with large number of atoms in the unit cell, so the heat carrying phonon is damped. 4) Those with more symmetrical crystal structure tend to have better electronic properties than others with lower symmetry. 5) The crystal absorbs good amount of non-compensated defects so the compound could be heavily doped. After putting these together it is not surprising that good thermoelectric performance was first found in semiconductors like Bi_2Te_3,[9-11] PbTe,[12, 13] $Si_{1-x}Ge_x$.[14-16] For decades they held the record of *zT* for low temperature, mid-to-high temperature and high temperature applications. A few breakthroughs were made in the 90s with the concept of PGEC (phonon glass electron crystal) proposed by Slack[17]. Compounds like skutterudites[18-20], clatherates[21, 22], and Zintl phases[23, 24] were identified as promising thermoelectrics, where the structure features a covalent bonded backbone and loose bonded ions called "rattlers". Progresses in these systems have lead to compounds that outperform traditional PbTe or $Si_{1-x}Ge_x$. More examples of emerging thermoelectric compound include[25,26] Bi or $Bi_{1-x}Sb_x$ (for cryogenic applications), Mg_2Si,[27-30] Half-Heusler compounds,[31-33] layered oxyselenide BiCuSeO,[34-36] superionic[37, 38] Cu_xSe or Zn_4Sb_3, and tetrahedrite (or stannite)[39, 40] Cu_xMX_y (M: Sn, Sb; X: Se, S), all combining decent *zT* with merits in other aspects (and also challenging obstacles as well). There has been also very active research on oxides and organic polymers/metal-organic complexes as thermoelectrics. These systems are in their infancy in term of thermoelectric properties, and the physical pictures of transport are quite different compared with band conducting semiconductors listed above.

1.3 IV-VI compounds

Among all the binary compounds (AB type) formed between group IV and group VI elements, the lead chalcogenides PbS, PbSe and PbTe, as well as GeTe (at high temperatures, rhombohedral structure near room temperature) and SnTe (at room temperature and above) crystalize in cubic rock salt structure. The other compounds, namely SnS, SnSe, GeS, GeSe in contrary form layered, orthorhombic crystals with different symmetry between room temperature and high temperatures. This has led to entirely different electronic band structures of these two groups of compounds. The ones in the first group are narrow gap semiconductors with fairly high carrier mobilities, making them good thermoelectrics. The ones in the latter group are also semiconductors, but with larger gap of around 1 eV so they found more applications in optoelectronics and possibly solar cells.

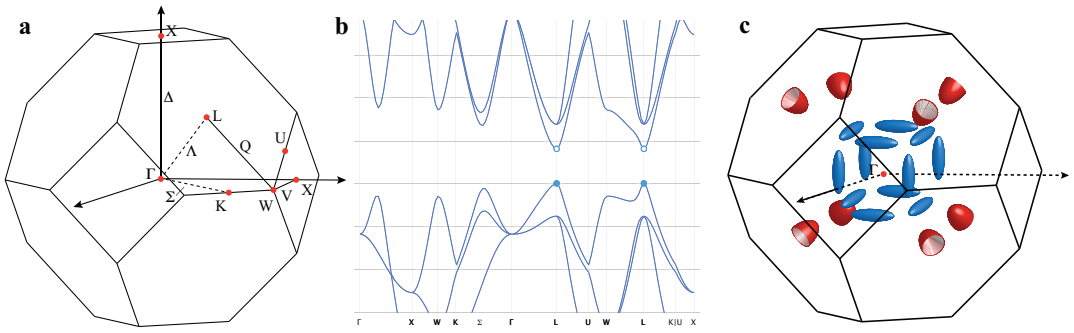

Figure 1.4. a) Brillouin zone of the rock salt lead chalcogenides, b) a sketch of the band structure, and c) the schematic *L* (red) and *Σ* (blue) carrier pockets, transport properties are determined by the *L* pockets for electrons and both *L* and *Σ* pockets for holes. Band structure taken from the Materials Project https://materialsproject.org calculated for PbSe.

Among the rock salt IV-VI compounds, PbS was the first one found to have "good" thermoelectric properties[1] (compared with other available candidates then). This is probably due to its natural occurrence as a mineral. It is difficult to tell that between Soviet Union and the United States, who demonstrated its potential as a thermoelectric material first. Early Soviet Union literature[41] mentioned a "photocell" based on PbS developed in 1940 at Leningrad Physical and Technical Institute that converts energy from light into electricity with an efficiency of 3.7 % (This result is quite likely overestimated since the module simply used PbS and metallic n-leg). Around the same time in the United States, in her 1947 review[42] Telkes proposed PbS (doped by extra Pb or S) for possible thermoelectric power generation application and had experimentally built a device with 7 % efficiency made of PbS and ZnSb. This result, was considered overestimated by the Soviet Union scientists[41] although they thought the device is made of p- and n- type PbTe. In both countries it was soon realized that the PbTe based compound would be more efficient. The Soviets studied PbTe based compounds as early as later 1940s, surprisingly for cooling purpose[1]. In mid 1950s, they built prototypes of thermoelectric refrigerators 40-50 liter in capacity using PbTe-PbSe alloys as the n-leg, and (probably) $Sb_{2-x}Bi_xTe_3$ for p-leg, these were able to get -5 °C cabinet temperature while ambient temperature is around 20 °C (I have to provide this ambient temperature since this was in St. Petersburg). The power consumption was around 70 W, which is probably more efficient than compressor based fridges at that time. Similar work must have been done in the United States as well. By the year of 1960, very systematic experimental data on transport properties of doped PbTe have been described[13] by Fritts from 3M company, USA and by[43] Stil'ban from Leningrad Physical and Technical Institute, Soviet Union. The mid 60s saw the advent of thermoelectric generators (RTGs) using PbTe, for both spacecrafts/satellites (the SNAP series RTGs in the US) and domestic

applications. The PbTe component is still used in the most advanced MMRTG (MM stands for multi-mission, Figure 1.5) that is loaded on the Mars Rover "Curiosity" landed in 2012.

Lead chalcogenides are among the most well-studied semiconductors. They are line compounds crystalizing in simple high symmetry structures, with relatively low level of defects. They are narrow gap semiconductor with fast moving electrons and holes, and their carrier densities are easily tunable from high 10^{16} cm^{-3} to low-to-mid 10^{20} cm^{-3} both n- and p-type: ideal for optoelectronic and thermoelectric applications.

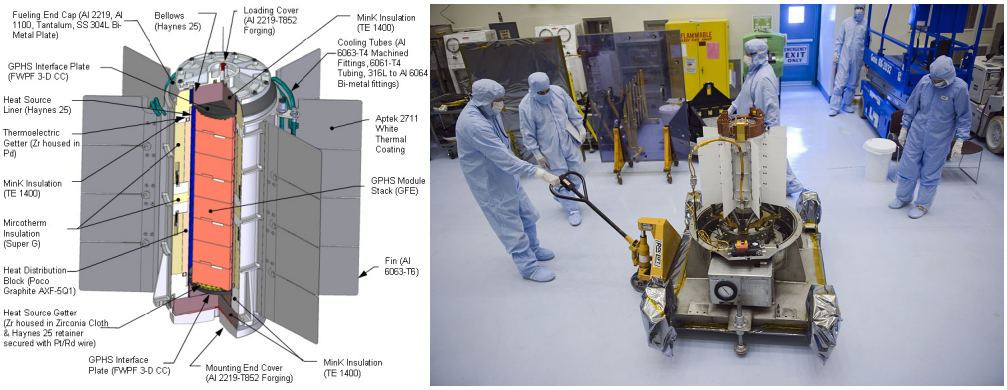

Figure 1.5. Schematic diagram of a MMRTG and a picture of it being tested at a NASA facility. Images from Google.

Lots of early fundamental studies on Pb chalcogenides (more on PbTe than the other two) were published between mid 1960s and late 1980s. Both Soviet Union scientists and those in other countries (mainly United States) contributed extensively making it hard to tell who was the first to report anything. Gibson measured[44] the band gaps of Pb chalcogenides using optical absorption spectrum and showed that in contrary with most semiconductors, the band gaps in this class of compound increases with temperature. This feature is actually very important for their good thermoelectric performance found at high temperatures. Low temperature cyclotron resonance[45] and Nernst effect[46] was carried out to determine the effective masses of charge carriers. It was also found that the carrier mobility decreases with temperature much faster than expected from electron-phonon interaction and this was later found by Smirnov[47] the result of a increasing carrier effective mass with temperature. The particularity in transport properties of p-type PbTe was also noticed and a two-valence-band structure was proposed (by Allgaier[48] and Airapetyants[49] et al.) to explain the experimental result, which was later confirmed by band structure calculations[50, 51] of Pb chalcogenides. The nonparabolicity of conduction and valence bands was also found[52-54] and Ravich

et al. derived[12] a simplified analytical description of effective masses and transport coefficients for the non-parabolic case, based on Kane's original model[55] for InSb. These were all summarized in the monograph[12] on lead chalcogenide semiconductors written by Ravich and Smirnov in 1970. They form the framework of knowledge on these compounds today.

The PbTe materials used in the early RTGs have peak *zT* around 0.8 for both n-type and p-type.[5] These are since regarded as a symbolic performance of PbTe. Two breakthroughs during the first few years of the 21st century brought back a major research interest (as well as funding and R&D effort) in PbTe based thermoelectrics: the first is the $PbSe_{0.98}Te_{0.02}$/PbTe quantum dot superlattice (a thin-film structure with alternating layers of different composition each with fixed thickness between 5 to 50 nm) prepared by Harman et al., who reported *zT* of 1.6 at[56] 300 K and later 3 at[57] 550 K; the second is the $AgPb_{18}SbTe_{20}$ bulk material with *zT* 2.1 at 800 K reported[58] by Hsu et al. The ideas described in these works have deeply influenced a lot of research in PbTe and even other thermoelectric materials for more than a decade. However, the lack of successful report on repeating these works ever since has pointed to an inconvenience fact that these *zT* are hugely overestimated.

Following the similar "nanostructuring" idea, the thermoelectric group at Michigan State University and Northwestern University performed a series of studies on PbTe based compounds leading to several dozens of reports on high *zT* (around 1.5) Pb chalcogenides[59-61]. These are strong evidence of the compounds' great potential of achieving state-of-the-art performance. While it is still an open question here whether "nanostructuring" is the key to it. Despite of creative approach and elegant nano-scale microstructure characterization, there was always too weak an argument to pinpoint them as the primary reason of high *zT*. In 2008 Heremans et al. reported[62] *zT* enhancement (1.5) in PbTe through resonant thallium doping. This is an inspiring idea to focus on the increase of power factor rather than the prevailing idea of reducing thermal conductivity for higher *zT*. It is later realized however, that the high *zT* achieved by thallium doping, is not particularly better than what a regular dopant such as Na or K are capable of.[63] The idea of resonant effect[64, 65] in Pb chalcogenides is likely to manifest only at low temperatures before overwhelmed by the lattice phonon scattering, even then it requires simultaneous tuning of the density of resonant impurity and free carriers to a level that is not always achievable. A much more successful example of resonant effect on *zT* can be found[66] in In doped SnTe, where the presence of In dramatically increased the power factor of SnTe (more significant than Tl for PbTe). Compared to SnTe doped properly with regular impurities the *zT* of In doped SnTe has increased from 0.6 to 0.8 at 773 K (30% increase). In 2011,

our group demonstrated[7] the improvement of zT in PbTe through tuning the electronic band structure so that the secondary band extreme aligns with the primary at a designed temperature. This picture rationally explained zT enhancement observed in many systems and has successfully guided experiments to discover new compounds with better zT. These progresses mentioned above are summarized in Figure 1.6 and Figure 1.7.

Many believe that the practical use of any of the Pb-containing IV-VI compounds is very unlikely. For domestic applications the growing environmental concern, no matter valid or just emotional, is against the use of Pb; for space applications (RTGs) the long term degradation of PbTe brings about great difficulty in device design that favors more and more other candidates such as skutterudites that are much better in the same metric. Nonetheless, the lead chalcogenides are one of the most well studied groups of semiconductors. Also they have highly symmetric structure and simple defect chemistry, and are simple for synthesis without competing phases. These makes them perfect platforms for developing science and ideas that can be transferred to other thermoelectric systems or solid-state materials in general.

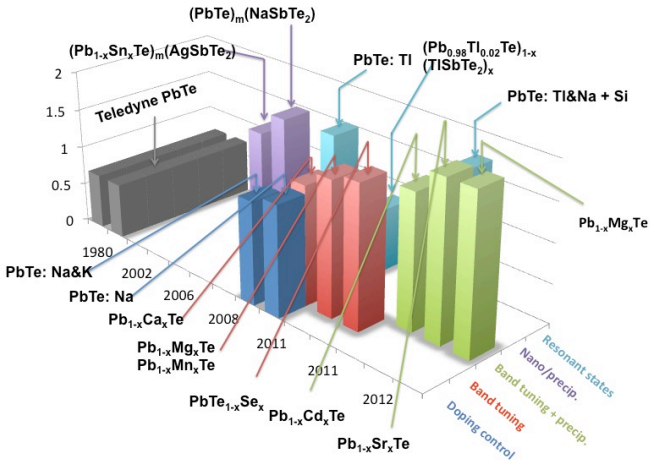

Figure 1.6. Progress made in p-type PbTe, using different strategies (as claimed).

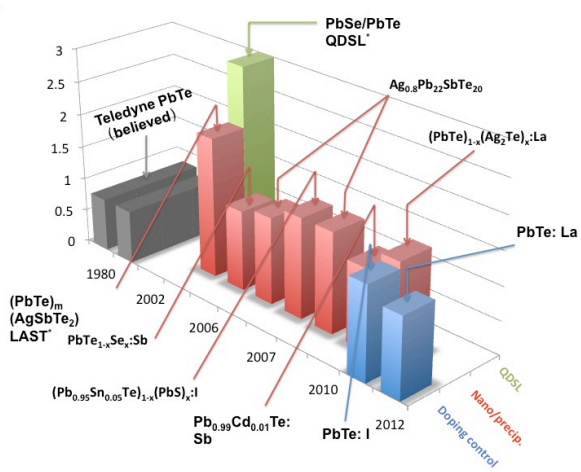

Figure 1.7. Progress made in n-type PbTe, using different strategies (as claimed).

1.4 Summary of Research

Within such general background, this thesis research is primarily focused on bulk PbSe, the less studied analog of PbTe, synthesized by conventional melting and reacting technique. My research contains two major parts: the first involves characterizing and understanding of the properties of binary PbSe when doped either p type or n type. Historically the transport properties of PbTe have been widely studied and advanced theories were proposed to explain these results. These could be adopted for PbSe. So the main challenge comes from obtaining samples with best quality and accurately evaluating their properties. As for the theoretical part, with modern computation capability I modeled electrical transport of any doping level at any temperature, which determined key parameters for thermoelectric performance that haven't been done accurately. I also tried to answer the question why PbSe (and PbTe as well) is good in both n-type and p-type from the aspect of the merit of its energy bands. I compared the effect of different donor atoms on cation and anion site, revealing the effect of short-range potential scattering from dopant impurities, which has not been experimentally demonstrated and is often overlooked when the effect of ionized impurity on transport is discussed. I also demonstrated the key parameters that determine the overall zT of a system composed of multiple bands and provided guidelines for optimizing zT in a multi-band system.

The second part of my research involves the attempt to improve zT via alloying or, forming solid solutions, as well as understanding the transport behavior of solid solutions in general. Forming

solid solutions has long been employed in thermoelectric research because of the lattice thermal conductivity reduction it brought. There are other influences on transport properties that need to be taken into account when designing better thermoelectric materials. For instance, the mobility of carriers will also be reduced due to the scattering of carriers from atomic disorder. I found the most direct example of this in n-type $PbTe_{1-x}Se_x$, where no other physical parameters changes with alloy composition. This allowed me to propose a simple criteria that gives an estimate of whether a certain system of solid solution would be thermoelectrically beneficial or not. I further moved on to the other complete solid solution system between lead chalcogenides: the n-type $(PbSe)_{1-x}(PbS)_x$. The conduction band effective mass in this case also changes with composition. When this is taken into account the transport behaviors of the alloys can again be well predicted. In these two systems, simply using solid solution to reduce thermal conductivity have failed to increase zT overall due to the similar degree of reduction in mobility.

I then continued to study p-type $(PbSe)_{1-x}(SrSe)_x$. In this system remarkable increase of zT was observed due to the tuning of band structures. The influence of disorder and the changing of band structure on thermoelectric performance are separately evaluated. The result suggests the solid solution strategy, though long been proposed, still has its new facet that needs more careful exploration.

Chapter 2

Experimental Methods

2.1 Synthesis

All three lead chalcogenides are line compounds with very limited solubility of extra Pb or chalcogen ~ 0.5% near melting temperature. There are no other phases that exist in the phase diagram. Synthesis of these compounds by melting the elements is relatively easy and repeatable. Forming of the binaries from elements are exothermal reactions. The reaction in the case of Pb and Se starts slightly above the melting point of Pb (about 320 °C) and is self-sustained. The local temperature could be well above 600 °C (so it's glowing red). This leads to serious safety concern while making batches over 50 g in lab conditions because the sudden release of heat might bring chalcogen vapor pressure inside quartz ampoules (16mm inner diameter, about 18mm in length) to a dangerous point. On the other hand, even for Pb and S, the reaction will start at sufficiently low temperature so that the sulfur vapor pressure (which reaches 1 atm at 440 °C) inside will not be too high for the tubes, which are not very durable under positive pressure from inside. The PbS formed at interface will not block further reaction so making PbS is actually quite safe, given proper precaution. In contrast, the synthesis of SnS requires special setup and careful temperature control to avoid tube explosion. One possible reason is that the melting of Sn happens well before its reaction with sulfur starts so the elements are separated even when they were well mixed in solid form. As the reaction happens the formed SnS (melting temperature around 880 °C) in solid form blocked further reaction thus the sulfur will eventually build up enough vapor pressure to break the ampoule.

The most careful procedure of making compound semiconductors from elements in this thesis study involves:

1. Cleaning the inside of quartz tube with water or compressed air.

2. Heat-treating the wall of tube by heat a region with torch until it's glowing white (goggle on) but not softened, and gradually move that region upward. This helps to annihilate the micro-cracks on the wall. It also removes any possible organic residue on the inside of the wall and reduces the dangling/absorbed oxygen on the surface of SiO_2. A more standard way of doing this would be to bake the tubes in a furnace with inert atmosphere at 1000 °C.

3. Coating the wall with carbon if reactive elements are involved, by heating the tube rinsed with acetone (tilted, almost horizontal). Tube is rotated while the torch is moving upward. Rinsing the inside with acetone, to remove the organic residue not fully carbonized or not deposited on the wall.

4. Baking tubes in a furnace at 350 °C for a couple of hours. This ensures all organic residues being burned; other than the carbon coating on the wall (which will get oxidized above 400 °C).

5. Loading tubes with elements. Use metals in big chunk form instead of small pieces/powder. Remove surface oxide layers then cut small, load elements with high vapor pressure first, then reactive element or doping agents, Pb metal is usually on top. For large batch sizes elements should be pre-mixed after sealing.

6. Melting, quenching and annealing. In most cases the heating is at a speed of 100 °C per hour. The maximum temperature is around 50-100 degrees above the compounds melting point to ensure fast enough solidification everywhere across the ingot during quenching. Even so, when the ampoule diameter is large (~16mm), the delay of solidification at the center of the ampoule is considerable, so that the red glow is still seen for about 10 seconds after quenching, and the ingot appears hollow as the solidification progress towards the center. A good post-annealing process is very necessary in this case to ensure homogeneity and annihilate defects.

P-type Pb chalcogenides seem to have rather complicated defect chemistry that even though the greatest caution was paid during synthesis there is no guarantee to obtain high quality samples. Adding extra anion in starting materials to compensate defects helps, but a general guideline to eliminate the uncertainty can't be given so far. The melting temperature of PbSe is 1080 °C, about 150 °C higher than PbTe. This has exponentially increased the uncertainty from influences of either defects or grain boundary layers, which makes the mobility of samples abnormally low at room temperature (while Seebeck coefficient and carrier density are normal). Such defects or grain boundary layers might also come from impurities released by the quartz itself regardless of the

presence of Na. However, it has to selectively affect hole transport not the electrons as n-type samples prepared this way almost never have such problem. Trying to avoid either of these two possibilities, the soaking time at maximum temperature is limited to 1-2 hours for Na doped PbSe, whereas for n type samples they are usually kept for 12 or 24 hours to ensure best mixing of dopant. Near the end of this thesis research I tried to synthesis Na doped PbSe by melting the elements and hold at 977 °C: not enough to form a liquid phase but enough for Na to distribute throughout the ingot (5 g size) via either vapor transfer or solid-state diffusion. Result of this experiment is very comparable with the high quality samples made previously by forming a liquid phase. Complete melting of the ingot is not a necessary step for good PbSe doped with Na because the Na diffusion is fast enough.

When making Na doped $Pb_{1-x}Sr_xSe$ samples, there is additional concern due to reactive Sr element. The melt temperature should be further increased above 1080 °C to ensure complete liquid formation, while the high Sr content makes it too reactive even with carbon coating. As a result, a two-step method is used so that liquid phase was formed for a short period followed by solid state mixing and consolidation, then prolonged annealing in solid state. Details will be given in the specific chapter.

It would be worthy to note for those are going to work on these compounds that after PbSe were synthesized and the ampoule were opened, a very strong smell of rotten eggs is very often released, suggesting the forming of H_2Se (or less likely H_2S with S impurity from Se) during the process. However the source of element H is unknown: possibly they came from the quartz tubes, which contains hydrated SiO_2 (surface bonded water). H_2Se when released into an inert environment would react with Na making its fresh surface black in seconds, while when this surface is exposed in air it will be oxidized quickly again into white sodium oxides in a second as well. This is a very annoying and disturbing reaction, but eventually doesn't affect the role of Na as fully activated dopant, either because the mole fraction of affected surface is very small, or Na in the surface product is not as stable as in PbSe lattice. The forming of H_2Se during synthesis is also suspected to be associated with the formation of defects/impurities that caused low mobilities in p-type PbSe around room temperature. Possible mechanisms are: 1) deficient of Se in PbSe produces donor like defects unwanted in p-type samples, 2) the oxygen once bonded with hydrogen could be released and form insulating grain boundary layers. For the first hypothesis, note that altering Pb and Se ratio to 1: 1.008 in the start material has failed to prevent low mobilities at room temperature from happening in all p-type $PbSe_{1-x}Te_x$ samples.

PbS has the highest melting point of 1120 °C among the Pb chalcogenides, interestingly the ingots after reacting Pb and S were found at around 1080 °C (actual temperature). This could be an indication of the vapor pressure of PbS being less than that of PbSe so the melting point is decreased quite significantly, or result of recrystallization with fast vapor transfer.

The ingots (weighing 3 to 30 g) after annealing where crushed and sintered into 12.7 mm disks weighing about 1.2 grams using an induction heating rapid hot press[67]. The instrument was home built based on an Instron mechanical testing system with a vacuum chamber and a 25 kW RF power supply passing large current through a copper coil that is water cooled. The system operates under inert atmosphere (pumped down to 10^{-5} torr than back filled with Ar 0.1 atm to slightly above 1 atm as needed). The system is built with a maximum heating rate of 620 K/min: faster even than a commercial SPS (spark plasma sintering) machine. The highest operating temperature is 1450 K (It uses type C thermocouple inserted into the die for temperature monitoring. Above 1000K frequent thermocouple failure occur. At 1473 K even Inconel-sheathed thermocouples quartz-insulated from the die have a good chance of failure, probably due to elemental vapor corrosion). The axial load is set at 510 kg (about 40 MPa for a disk of 12.7 mm diameter). The uncontrolled cooling speed is also fast since the chamber is not heated while water-cooled copper shields are attached to each sides of the chamber wall. High strength graphite die 70 mm in diameter are used as susceptors, the majority of heat is generated from the surface less than 8 mm deep. On the other hand the magnetic field at the center of the coil (where the samples are) is very weak (no more than 200 Gausses estimated with coil diameter 100 mm and current 250 A). So unlike the SPS process where large DC current flows through the conductive sample causing ions to migrate and chemistry variation, samples in the rapid hot press are heated passively with no external field. Since the size of the die is much larger than that for SPS it allows multiple disks (as much as 12) to be sintered in a single run compared with the one by one process for SPS. That being said, the stacking of multiple samples should however be conducted with caution. As the maximum number of samples that can be loaded in one run is often not limited by the dimension of the die, for some system such as n-type PbSe, this number could be 10 or even larger. P-type PbSe has inferior mechanical strength than the n-type, so most practically this number should be around 6. For p-type PbSe doped with Na and Tl (≤ 2%), most runs with more than 3 samples at a time would result in breakage of nearly all samples. In extreme cases cracks form along multiple radial directions. Co-doping PbSe with Na and Tl significantly degraded its mechanical strength.

Most thermoelectric materials are fairly easy to sinter, that is, their melting points are not high as some ceramics, and they tend to be soft for the thermal conductivity to be low so the grains are easier to deform at high temperature. Relative densities of above 98% are easy to achieve for samples without phase transition. Small adjustments in hot press parameters (temperature, hold time, or pressure) will not change the transport properties of samples. There are published study that claims by optimizing the processing parameter the *zT* of p-type PbTe can be increased to 1.8, this result, should be instead an error in the thermoelectric property measurement. For the synthesis of PbSe, good densities can be obtained by pressing as low as 550 °C for less than 5 minutes. In most cases, in order to provide enough time for grains to rearrange and strains to relax, the hot pressing is usually performed higher at 600 °C for 20 minutes to 1 hour.

2.2 Seebeck Coefficient Measurement

The detail of the high temperature Seebeck measurement system was described by my former colleague Shiho Iwanaga in *Review of Scientific Instruments 82,* 063905 (2011). There is another review on thermoelectric measurements in general by Kasper Borup et al. that is under preparation at the time this paragraph is being composed. It suggests lots of good practices and precautions to avoid error in property measurements and should be of good reference for those reading this section of this thesis.

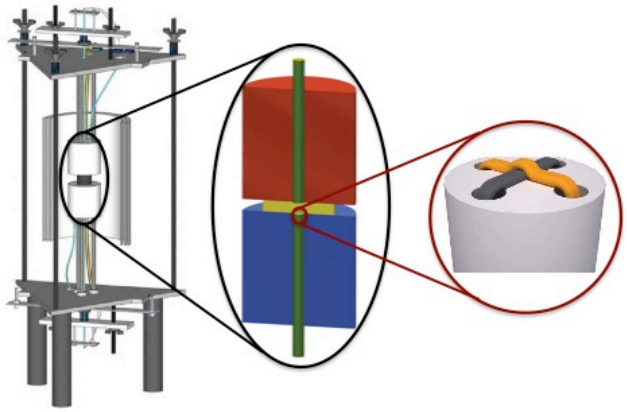

Figure 2.1. Schematic of the sample stage of Seebeck coefficient measurement setup.

The setup[68] shown in Figure 2.1 was used to measure Seebeck coefficient along the thickness direction of a sheet (usually disk) sample in a dynamic vacuum environment. It uses uniaxial 4-point geometry. This assures that temperature and voltage are acquired at exactly the same point

closest to the sample. Two chromel-Nb thermocouples are used for temperature and voltage measurements, they are made by crossing and tapping two 0.005-inch metal wires through a 4-bore 1/16-inch mullite tube. Thin wires further ensure the signals are taken at the same point without own size effect, and mullite tube are used because their thermal conductivity are lower than alumina so there will be less cold finger effect. Both the measurement temperature and the temperature gradient are established by two heater blocks made of BN, each with 6 cartridge heaters embedded and connected in 3 parallel groups. The cold finger effect is further reduced by having probes pass through the heater blocks. Voltages are measured using Nb wires (yellow one in Figure 2.1).

Each measurement is carried out in the following pattern: The two groups of heaters are controlled by PID control to ramp (and cool) and stabilize at user-defined temperatures. Then while keeping the average temperature constant one of them further ramp to a higher temperature and the other correspondingly cool to a lower one, thus producing an oscillation of about 10 K that takes about 50 minutes (also user-defined). Voltage and temperature are continuously recorded during the oscillations and the final Seebeck coefficient is obtained by a linear fit of $\Delta V/\Delta T$ from all recorded points during this period (about 30 in total, the averaging is weighed for each point by its deviation). This way of data processing gives more accurate results compared with a single point $\Delta V/\Delta T$ method because there is often a "dark voltage" meaning a nonzero ΔV when $\Delta T = 0$.

The maximum temperature (limited by the heater rating) for this system is about 700 °C. Chromel-Nb is not a good thermocouple near room temperature and it is also hard for the PID control to establish enough temperature gradient while maintaining the average temperature, thus result under 100 °C from this system is always used with caution. A similar room temperature setup uses type T thermocouples (copper-constantan) provides more reliable room temperature Seebeck values (S is calculated by single point $\Delta V/\Delta T$).

Good thermal and electrical contact is essential for accurate measurements. The heater blocks and thermocouple probes are thus pressed against sample surface under constant spring force. Graphite foils are also placed between both sides of the sample and the blocks. They provide protection for thermocouple from contamination by reaction with samples, and also help to improve thermal contact. Ideally both the heater blocks and probes should be pressed against the sample as firm as possible, however, Pb chalcogenides are soft especially at high temperatures and their linear coefficient of thermal expansion is large thus excessive pressure often causes deformation and embedment of probes into the sample. So in practice both pressures are kept small. This could

potentially lead to an underestimate of Seebeck coefficient at high temperatures as the temperature difference measured by thermocouples becomes larger than the real difference across the sample.

The contamination of probes by elements from samples is a very serious concern even with the presence of graphite foils. Its effect is not always easy to notice. A series of measurements on n-type $PbSe_{1-x}S_x$ were once affected by this, the Seebeck results were good at room temperatures but systematically overestimated as temperature increases, up to a 20% overestimate at 850 K. This was realized because the large values are unexpected from good knowledge about these compounds, otherwise this is very difficult to identify because for each measurement the *S* values are perfectly linear with temperature with little scatter seen. In principle, all the probes should be replaced regularly every a few months.

2.3 Hall and Resistivity Measurements

These properties are measured along the in-plane direction of a sheet sample in dynamic vacuum. The homebuilt setup has a boron nitride (BN) ceramic sample holder placed in a slit vacuum chamber set in between two poles of a 2T iron-core electromagnet.

The BN sample holder (Figure 2.2) has four rectangular holes on its two sides. Each holds a rectangular cartridge heater that is special designed with heating zone only in the front half. About one third of each heater is exposed to keep the temperature at the leads cool enough (overheating this part leads to insulation failure and corrosion of exposed heater wire that leads to frequent heater failure way below its power rating). Each heater is rated 120V 200W (60 Ω), but are connected in parallel to a DC current source of 60V, 10A maximum output. The sample temperature is measured by two type C thermocouples that are placed within the sample holder underneath each sample. When operating the holder is placed in a 0.8 inch (2 cm) wide stainless-steel slit with its wall attached to the water-cooled magnetic pole, therefore a significant heat loss through radiation can be expected. This would cause excessive power consumption, which means shorter heater life. Besides, it would make the real temperature of the sample surface (or the average across its thickness) much lower than the value recorded by the thermocouple. To reduce the radiation loss, the sample holder is wrapped with two layers of woven glass fiber as radiation shield (the part on top of samples are removable). With radiation shield the temperature of samples are very close to (<10 °C at 600 °C) that around the thermocouples. The system works at only about 90 W to get to 600 °C (the maximum power output is around 250 W). At higher temperature (>700 °C) the screws

and poles used to press leads against the sample begin to fuse together and thermal expansion causes lost of the pressure for good electric contact. 700 °C should be regarded as the maximum operating temperature.

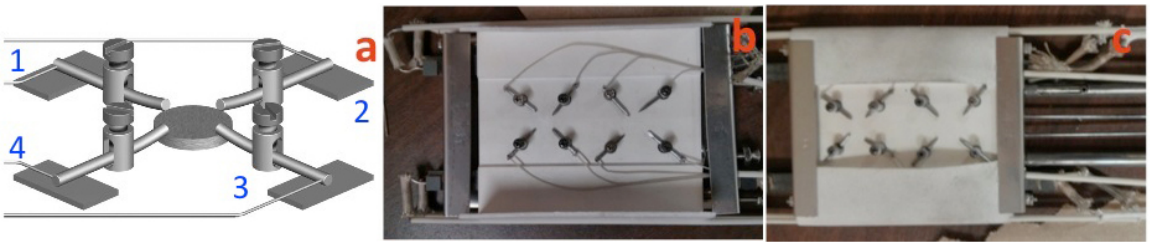

Figure 2.2. Sample holder of the Hall effect and resistivity measurement setup, a) schematic of sample and measurement geometry, b) c) picture of sample holder without and with insulation.

Measurements are based on (DC) Van der Pauw method, and each measurement is carried out in a quasi-steady-state manner: The temperature continue to ramp with a set rate once measurement is started till the set maximum then cool with the same rate, meanwhile the resistivity and Hall effect test are carried out repeatedly. Before performing each test, the contact resistance is checked, by grounding 1 probe and applying same positive voltage to the other three and measure the resistance. This is done for all 8 probes (when there are two samples). Next, the temperature is measured, then a DC current (set by user, 100 mA by default) is passed through probe 1 and 2, while voltage is measured between 3 and 4, the resistance $R_{12\text{-}34}$ is the average of 8 measurements. Similarly $R_{23\text{-}41}$ is also obtained then the sheet resistance R is determined by solving numerically the equation:

$$e^{-\pi R_{12-34}/R} + e^{-\pi R_{23-41}/R} = 1 \qquad \text{Equation 2.1}$$

The resistivity ρ is obtained by $\rho = Rd$, d being the thickness of the sample. After ρ is determined for both samples, the temperature is measured again and the average is recorded as the temperature for resistivity. Measuring ρ for two samples takes about 2 minutes. For the Hall effect test, the DC current is pass through probe 1 and 3 with the presence of magnetic field of 2T and measures the voltage between 2 and 4, then analogously for 2-4 and 1-3, after 8 measurements for each the magnetic field flips its direction and the same measurement is repeated. Two averaged resistance are calculated with:

$$R_{H,1} = (V_{24}(B) - V_{24}(-B))d / I_{13}2B \qquad \text{Equation 2.2}$$

$$R_{H,2} = (V_{13}(B) - V_{13}(-B))d / I_{24}2B \qquad \text{Equation 2.3}$$

The Hall coefficient is the average $R_H = (R_{H,1} + R_{H,2})/2$. Measuring R_H for two samples takes about 16 minutes. The current program will not record temperature for the Hall effect test; but instead uses the temperature for the just finished resistivity measurements. Within the 16 minute span the temperature would have increased 25 °C. Nonetheless, for normal semiconductors R_H has only weak temperature dependence so the error due to temperature drift would well be within uncertainty of measurement itself.

Good Van der Pauw measurement requires the sample being regular shaped (not necessarily round or squre). Each probe should be placed on the edge (not anywhere inside) of the sample with contact area as small as possible, and be equally separated from its neighbors. Preferably the 4 probes should form a perfect cross. If the sample is not a full-disk, the probes should be placed on the (sharp) corners rather than edges. Good Ohmic contact (linear I-V curve) marked by low contact resistance is essential for reliable results. This value depends on the specific material system (how their chemical potential align with that of molybdenum) and varies from 1 to 2 for heavily doped samples to high tens for undoped samples. Readings from 4 probes should be comparable and an abnormally large contact resistance usually means loss contact, inhomogeneity or cracked sample.

The following should also be kept in mind to minimize error: first, the sample should be as thin as possible, given it is mechanically robust. Thinner samples produce larger Hall voltage, which means better signal-to-noise ratio. Second, the thickness should be as uniform as possible, otherwise taking a good average for thickness is helpful. Even for a sample with unparalleled surfaces (~ 10% difference) as long as the right averaged thickness is used, could give very close result compared with the same sample when well polished (< 2% difference). Third, the size of the sheet should be much larger than its thickness. Also the ratio of contact area over sample thickness should also be small. Last, avoid using alumina spacer underneath thin samples for better pressure from the leads as it increases the interfacial thermal resistance that in turn lead to a big temperature difference between sample and thermocouple.

A BN spray is available for high temperature measurements, which suppresses the evaporation of elements under dynamic vacuum from the free surface. A BN coated sample after measurement would have both surfaces remaining gray and metallic look, whereas a free surface after the same run becomes dusty black.

2.4 Thermal Conductivity Measurement

Thermal conductivity is determined using laser flash technique from a Netzsch LFA 457 (Figure 2.3) apparatus along the thickness direction of a disk sample. Laser flash method was developed by[69] Parker et al. in 1961 and is the most used technique nowadays in determining thermal conductivity at high temperatures.

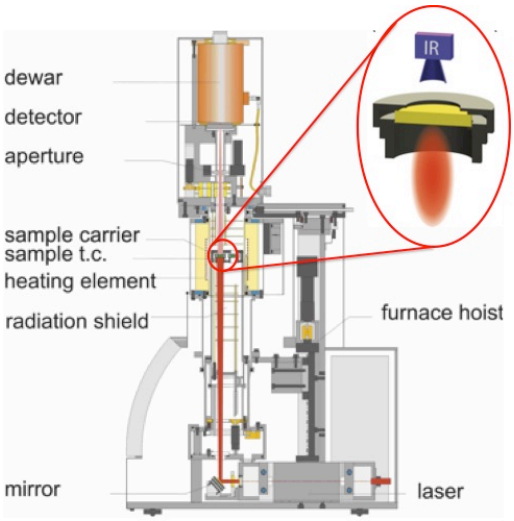

Figure 2.3. The LFA 457 system for high temperature thermal conductivity measurement.

In the LFA 457 up to 3 samples are placed in a small furnace. The furnace once closed is evacuated and then purged with Ar so the measurements are performed under dynamic Ar flow. The temperature of samples is measured by a thermocouple placed close to the sample holders. Each SiC sample holder (inset of Figure 2.3) has two windows, the one underneath the sample being bigger. Samples are coated with graphite to ensure better light absorption. A short pulse of laser (~ 50 μS) is shined on the bottom surface of the sample and the temperature response on the other surface is monitored by an InSb infrared detector. The thermal diffusivity ideally assuming 1-D heat transfer and delta function shaped laser pulse, is determined by the thickness of sample l, and the time for the temperature response to reach half of its maximum $t_{1/2}$:

$$D_T = 0.1388\frac{l^2}{t_{1/2}} \qquad \text{Equation 2.4}$$

The thermal conductivity κ is then calculated with $\kappa = D_T C_p d$, C_p is the heat capacity under constant pressure and d is the density.

In real cases, corrections need to be made to take into account the heat loss on the surface and heat transfer along the radial directions to the sides, as well as finite pulse wide of the laser. This can be done by choosing a proper correction model for each sample before measurement, and the detailed calculation is automated using the LFA. Different models are offered by LFA 457 including the Cowan model[70] from the 1960s which considered heat loss on surface due to radiation and convection, together with square shaped laser pulse correction and the Cape-Lehman model[71] from around the same time which further included heat transfer along the radial directions, both with "+" or "-" pulse correction where "+/-" really meant "with/without". In general, when the sample is thin, such as films and $t_{1/2}$ is small, the finite width of the laser pulse should be considered while the heat transfer can be regarded one dimensional; On the other side when the sample is thick and $t_{1/2}$ is large, the laser can be regarded instant; but heat transfer to the sides need to be taken into account. For bulk thermoelectric materials, the samples are usually thick, and $t_{1/2}$ on the order of hundreds of millisecond, the correction for heat loss and heat transfer sideways is more important. Also experimentally, it is better to use sample holders with bigger aperture given it is fully covered by the sample, and perform the measurements on relatively thin (~ 1 mm) samples.

The heat capacity C_p is another property needed to determine κ. This quantity can be measured using drop Calorimetry, differential scanning Calorimetry, and even relative methods comparing to a "standard" in commercial thermal diffusivity system like LFA 457. It turns out accurate C_p measurement is rather challenging and the result can be easily affected by operator errors. In fact, it is necessary to compare measured values with that from theory, i.e., the Dulong-Petit C_v value, $3k_B$/atom, when above Debye temperature (otherwise from the Debye integral) plus the volume expansion correction term[72] $9\alpha^2 T/\beta d$, α is the linear coefficient of thermal expansion, β is the isothermal compressibility, and d is the density. In normal cases, any experimental value, if noticeably different from the theory, likely contains certain error during measurement and it is indeed more accurate to use the theoretical values instead. Consider α and β is not readily available to many systems, using Dulong-Petit heat capacity at lower temperatures (roughly Debye temperature) and values ~10% above that at higher temperatures should be a reasonable estimate. For this thesis study on Pb chalcogenides, the fitting equation C_p/k_B atom^{-1} = 3.07 + 4.7 × 10^{-4} (T/K-300) is used. This is from Blachnik's drop calorimetry measurement[73], which is consistant with theoretical calculated values within 2% error (Figure 2.4).

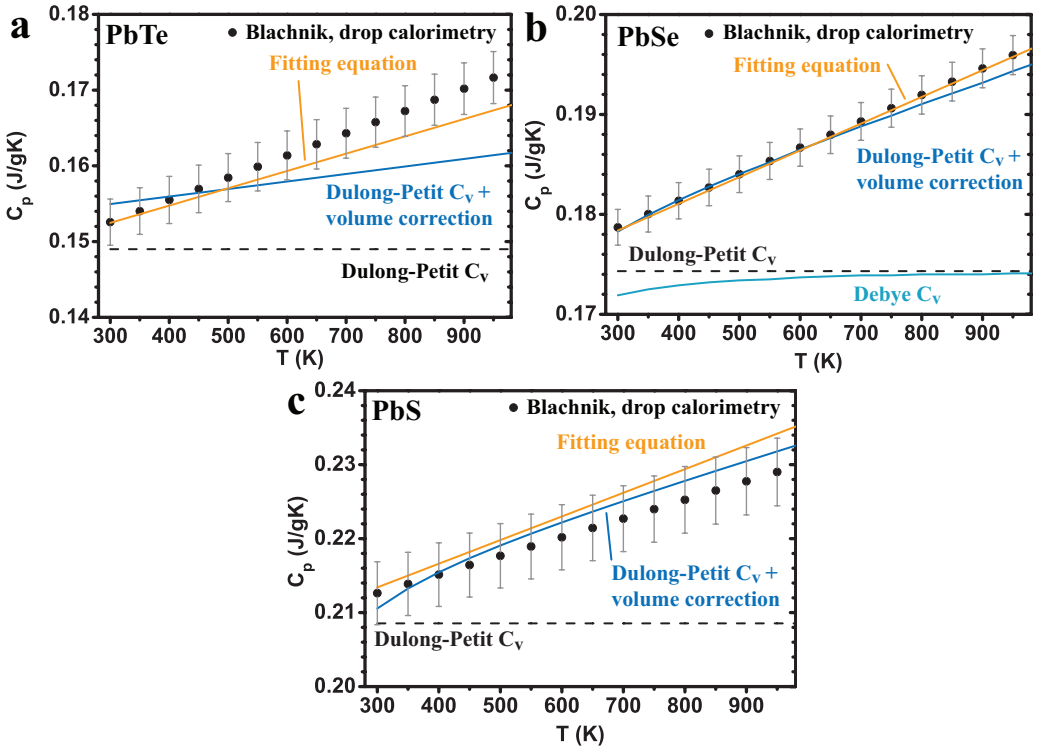

Figure 2.4. A comparison of Cp used in this thesis with results from drop calorimetry measurement as well as theoretical calculation and Dulong-Petit C_v, for a) PbTe, b) PbSe and c) PbS. Error bars represent 1%, 2%, and 2% uncertainty in each plot.

Density values are from measured geometry and weight of each sample. This is much simpler than the Achimedes method, but actually gives very close results. The Achimedes method on the other hand, needs to be carried out very carefully making sure no water (or other liquid) is absorbed by the sample (expecially when density is low, a standard treatment is to weigh the sample than coat the surface with a thin layer of wax to close open pores), or no bubbles forming on surface of sample when it is immersed in the liquid, otherwise the result can be rather inaccurate. The 300 K density is used for κ calculation regardless of temperature. A more accurate value can be obtained considering thermal expansion so:

$$d = \frac{d_{300K}}{1+3a(T-300)} \qquad \text{Equation 2.5}$$

For Pb chalcogenides, $\alpha \approx 2 \times 10^{-5}\ K^{-1}$, so at 900 K the density is roughly 4% less which means the thermal conductivity calculated using a constant density will be overestimated by 4%.

It has been noticed that samples with low density tends to have low thermal conductivities. The values are often lower than expected from the effective median theory. One possible reason is that the pores are not spherical or have broad size distribution. However, this could also be an indication that the laser flash method underestimates κ when sample has low density. I tend to not trust results from samples with < 90% relative density.

Besides the laser flash method, many researchers also measure κ using the direct steady state method. One advantage of this is it doesn't require knowledge on heat capacity, and the result doesn't need further interpretation from models. In this method a constant power is generated by a heater that is in good thermal contact with the sample, the other end of sample is connected to a heat sink and two thermal couples are placed along the direction of heat transfer with known distance. The thermal conductivity is readily obtained from Fourier's equation $Q = \kappa \Delta T/\Delta x$. At high temperature, significant amount of heat is lost through radiation to the environment and this need to be minimized or calibrated. Ioffe Institute has been using steady-state method since 1960s. Their setup[27] uses a radiation shield thermally anchored to both the heater and heat sink to establish a temperature gradient similar to the gradient in the sample. The space between sample and heat shield is filled with thermally insulating powder to further reduce the radiation loss, whereas heat loss due to conduction through the powder was calibrated. Comparing the most recent Ioffe Institute steady-state setup with the laser flash method, the results are fairly consistent up to 700 K for n-type PbSe, suggesting the steady-state method as implemented by the Ioffe Institute could be as accurate. But for a lot of their older publications, the κ tends to be overestimated at least at high temperature compared with results from laser flash method on very similar samples.

Other methods to determine thermal conductivity include the Harman method and the 3ω method, which is mostly used for thin films. These techniques are subject to more complicated model interpretation or calibration and are less accurate for materials with low thermal conductivity.

It is common in the thermoelectric community to claim each measurement has 5% uncertainty. Unfortunately, there hasn't been a "standard method" for most property measurements described above thus there is no way to decide the "real value" for a sample. The 5% claim is at best the statistical uncertainty reflecting the quality of data rather than the difference from the "real value". In fact, difference around 15% is often seen among results from different groups. Even for the simplest dimension measurement on the same sample can easily yield different result by improper use of calibers or just by using different electronic calibers that are common nowadays in labs.

Chapter 3

N-type PbSe Doped on Anion Site

3.1 Introduction

N-type PbSe is a very "simple" semiconductor. The band structure of PbSe has been well determined. The characters of conduction band important to transport properties were reported. Substitutional donors are plenty and most of them are not air sensitive. Surprisingly, the thermoelectric performance of n-type PbSe had not been well characterized. In this study we show that by simply optimizing the carrier density PbSe could exhibit high *zT*, which is comparable with any "*zT* improvement" ever been reported for n-type PbSe based compound. Transport properties from high quality samples follow the theoretical predictions as if in a textbook: the non-parabolic Kane band dispersion relation with proper scattering mechanism assumption explains the Seebeck coefficient and mobility in samples with any carrier density at any temperature between 300 and 850 K. The *zT* was historically underestimated due to inaccurate thermal conductivity measurements. In fact, the good $zT > 1$ is granted by the high quality factor, i.e., the inherent merit of the conduction band.

3.2 Sample Synthesis and Properties

This section and Section 3.3, 3.5 contains adapted reproduction of contents from *Proc. Natl. Acad. Sci. U.S.A.* **109** (2012) 9705.

N-type transport in PbSe can be achieved by adding extra Pb, but for a sufficiently high carrier density extrinsic donors are used. In this study the donor is Br (in form of $PbBr_2$ beads, 99.999% ultra dry, Alfa Aesar). Br is chosen in this study because it is closest in atomic size and electronic structure to Se and thus is expected to have minimal effect on the carrier mobility. It is later realized that Br is not evidently better than other halogen dopants Cl and I. A slight excess of Pb ($Pb_{1.002}Se$ instead of PbSe) is used to minimize compensating metal vacancy that leads to p-type conduction as

well as improving the mechanical strength. Since the amount of $PbBr_2$ is usually very small, all the lightly doped samples are made by mixing an undoped ingot ($Pb_{1.002}Se$) and a heavily doped ingot ($Pb_{1.002}Se_{0.9982}Br_{0.0018}$) with calculated weight ratio assuming the same molar mass. The synthesis involves melting at 1400 K for 12 hours followed by water quench, annealing at 950 K for 72 hours, and hot pressing with 40 MPa pressure under 1 atm Ar at 873 K for 20 minutes, followed by another 60 minutes anneal at 873 K without pressure. Obtained samples are very dense > 98% of theoretical density 8.27 g/cm^{-3}. Table 3.1 lists all samples with labeling, nominal composition, and properties at 300 K.

Table 3.1. A list of Br doped PbSe samples and some transport properties at 300 K.

Label	Composition	Transport Properties		
		n_H(10^{19}cm^{-3})	S (μV/K)	μ_H (cm^2/Vs)
	$Pb_{1.004}Se_1$	0.16	-224.7	-1182
	$Pb_{1.01}Se_1$	0.40	-160.0	-1317
	$Pb_{1.002}Se_{0.9999}Br_{0.0001}$	0.23	-191.7	-1403
	$Pb_{1.002}Se_{0.9998}Br_{0.0002}$	0.53	-126.2	-1328
7E18	$Pb_{1.002}Se_{0.9996}Br_{0.0004}$	0.72	-114.2	-1215
1E19	$Pb_{1.002}Se_{0.9995}Br_{0.0005}$	0.95	-99.7	-1171
	$Pb_{1.002}Se_{0.9994}Br_{0.0006}$	1.7	-80.4	-1032
2E19	$Pb_{1.002}Se_{0.9988}Br_{0.0012}$	1.8	-76.0	-1012
	$Pb_{1.002}Se_{0.9984}Br_{0.0016}$	3.0	-52.1	-828
	$Pb_{1.002}Se_{0.9982}Br_{0.0018}$	3.1	-50.5	-799
3E19	$Pb_{1.002}Se_{0.9980}Br_{0.0020}$	3.3	-50.0	-777
4E19	$Pb_{1.002}Se_{0.9976}Br_{0.0024}$	3.8	-46.5	-719
5E19	$Pb_{1.002}Se_{0.997}Br_{0.003}$	4.5	-42.8	-645
6E19	$Pb_{1.002}Se_{0.996}Br_{0.004}$	5.8	-38.3	-573

As shown in Figure 3.1, Br exhibits 100% doping efficiency up to 0.4%, which is the highest doping level used in this study. The measured values of Hall carrier density n_H is in good agreement with expected value assuming each Br atom contribute 1 free electron.

Both the Seebeck coefficient and resistivity increase with increasing temperature for the majority of the samples in this study as shown in Figure 3.2 a) and b), respectively. These trends are consistent with degenerate semiconducting behavior. The total thermal conductivity (Figure 3.2 c) decreases with temperature, reducing to 1.0 - 1.4 W/mK at 850 K, depending on the doping level.

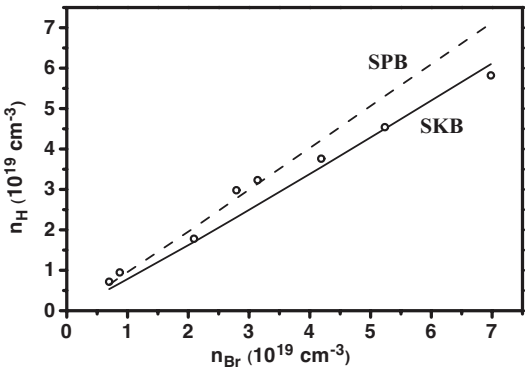

Figure 3.1. Measured Hall carrier density as a function of Br concentration. Lines are expected values with different band model.

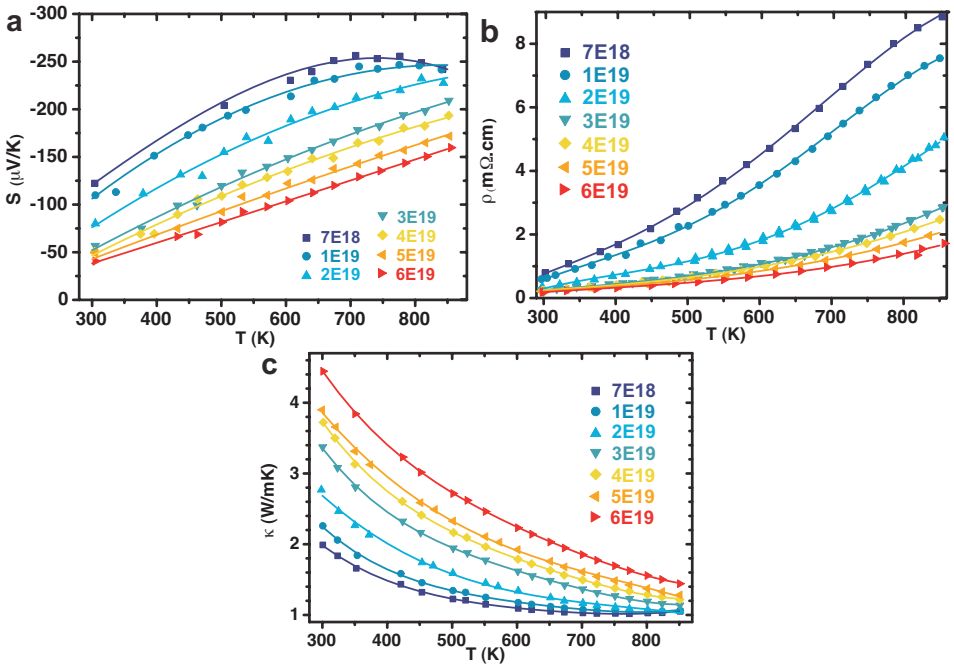

Figure 3.2. Transport properties of Br doped PbSe as function of temperature. a) Seebeck coefficient, b) resistivity and c) thermal conductivity. Lines are polynomial fit (2nd order for Seebeck and 3rd order for others) of experimental results, which are used to calculated *zT*. Same for lines in all plots of properties in this thesis unless stated otherwise.

The lattice thermal conductivity, κ_L, is calculated by subtracting the electronic contribution ($\kappa_e = LT/\rho$) from the measured total thermal conductivity, where Lorenz number L is calculated using the non-parabolic single Kane band (SKB) model with acoustic phonon scattering assumption. The averaged value at high temperature provides a reasonable estimation which indicates ~ 0.75 W/mK around 800 K. This result is comparable with that for p-type[74] PbSe (~0.6 W/mK) as well as PbTe

(~0.8 W/mK for both p-type and n-type). However, near room temperature with even the best estimate of L value from theory, the κ_L were found abnormally low for all doped samples: meaning they are significantly lower than the κ_L from undoped samples (1.7 W/mK) at these temperatures. Figure 3.3 shows the result for a few moderately doped samples as an example. It further seems that the discrepancy increases with doping level. This apparent trend is still unexplained: it is not likely due to inaccurate scattering mechanism assumption as suggested by close matches of other measured transport properties with theory prediction, on the other hand all measurements are checked to be accurate.

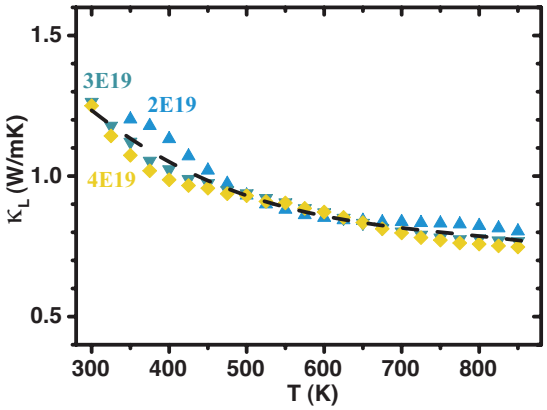

Figure 3.3. Lattice thermal conductivity of a few moderately doped $PbSe_{1-x}Br_x$ samples as function of temperature. Dashed line shows the average value.

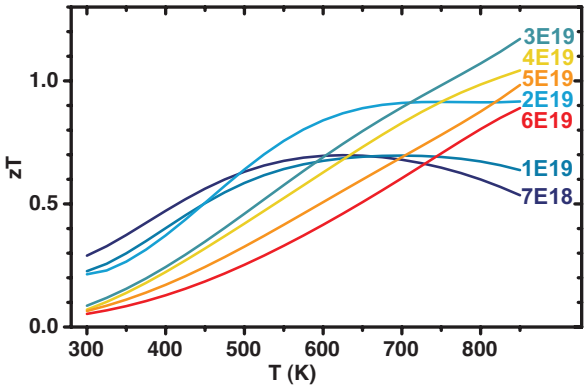

Figure 3.4. zT as function of temperature for Br doped PbSe.

The zT values as a function of temperature are shown in Figure 3.4. The optimal doping level is found to be around 3×10^{19} cm^{-3} achieving zT as high as 1.2 at 850K.

PbSe has isotropic structure and transport properties, thus not surprisingly although transport properties are measured along different directions in this study, under current hot press procedure no anisotropy is seen in any property.

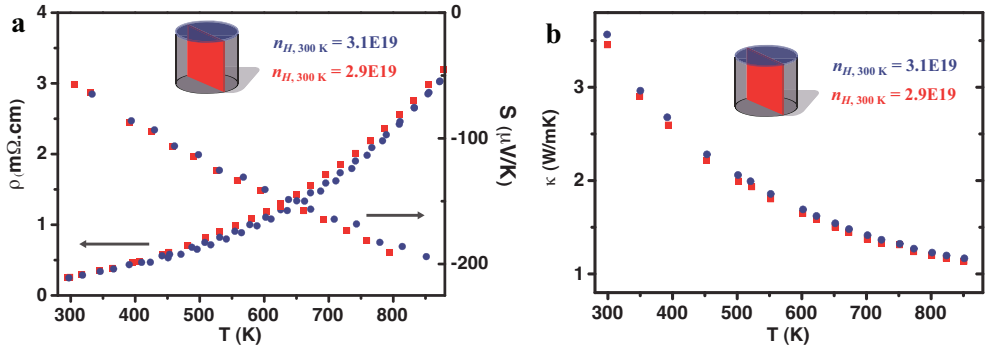

Figure 3.5. Resistivity and Seebeck coefficient a) and thermal conductivity b) of two slices cut from a single cylinder showing the isotropy of properties.

The very similar carrier density and transport properties shown in Figure 3.5 indicate good homogeneity of the hot pressed samples. We further tried to demonstrate the homogeneity using a scanning Seebeck coefficient probe at 300 K on a $Pb_{1.002}Se_{0.9982}Br_{0.0018}$ sample. The scanned area is 6 × 6 mm with 0.2 mm interval. The averaged value is −72 μV/K with a standard deviation of 3.7 μV/K. The current scanning Seebeck setup[75] is most suitable for detecting large contrast in Seebeck coefficient caused by phase segregation that is on the order of 10 μm scale or larger. It could also use a sleeve or a chamber to prevent temperature fluctuation caused by open-air condition, which is a major origin of the standard deviation (the contrast pattern) seen in Figure 3.6.

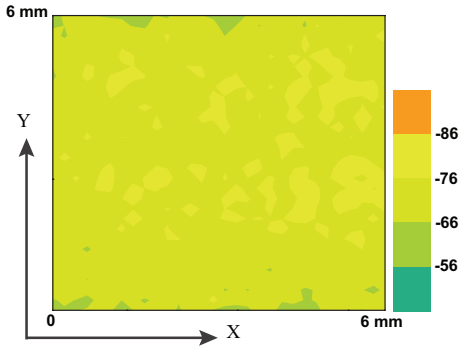

Figure 3.6. Seebeck coefficient scanning on an area of 6×6mm of a 0.18%Br-PbSe (3E19) sample.

To show the reproducibility and repeatability of this *zT*, four samples were individually made with the room temperature Hall carrier density 2.9×10^{19} to 3.4×10^{19} cm^{-3}. The measurements show very similar values in each of the properties, which overall give *zT* between 1.0 and 1.2 at 850 K, as shown in Figure 3.7.

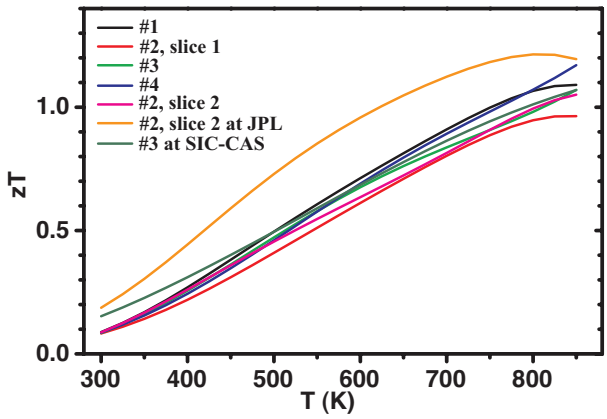

Figure 3.7. Temperature dependent *zT* of 4 samples (5 measurements) with optimum carrier density.

Samples were also sent to Shanghai Institute of Ceramics, Chinese Academy of Science (SIC-CAS) and NASA Jet Propulsion Laboratory (JPL) for crosschecking. Results obtained from these institutes are further compared with recent reports of thermoelectric properties of n-type PbSe in Figure 3.8. The legends in a) and b) represent: sample D by Androulakis[76] (Northwestern high doping), sample C by Androulakis[76] (Northwestern low doping), sample 1 by Alekseeva[77] (Ioffe Institute low doping), and two slices of "$Br_{0.0018}$" samples from this study (Caltech high doping 3.1E19 and 2.9E19). The legends in c) represent: sample 1 by Alekseeva[77] (Ioffe Institute, n), sample 7 by Alekseeva[77] (Ioffe Institute, p), sample C by Androulakis[76] (Northwestern, n, low doping), sample D by Androulakis[76] (Northwestern, n, high doping, solid triangles), sample "PbSe-In 3E19 electron/cm^3 " by Androulakis[78] (Northwestern, n, high doping, open triangles filled with dots), sample "x = 0.01" by Wang[79] (Wuhan Univ. Tech., p, low doping), sample "Cl-PbSe" by Zhang[80] (Boston College, n), sample "2E19" from this study (Caltech, n, low doping), sample "3E19" by Wang[74] (Caltech, p, low doping), sample "3E19" from this study (Caltech, n, high doping), sample "1E20" by Wang[74] (Caltech, p, high doping).

The most noticeable difference is in thermal conductivity where the results from steady-state measurement reported by Alekseeva[77] in 1996 are abnormally higher than all other more recent

results from laser flash method (all from LFA 457). The overestimated thermal conductivity is responsible for the historically under-represented *zT* in n-type PbSe (and a important factor for p-type Pb chalcogenides as well).

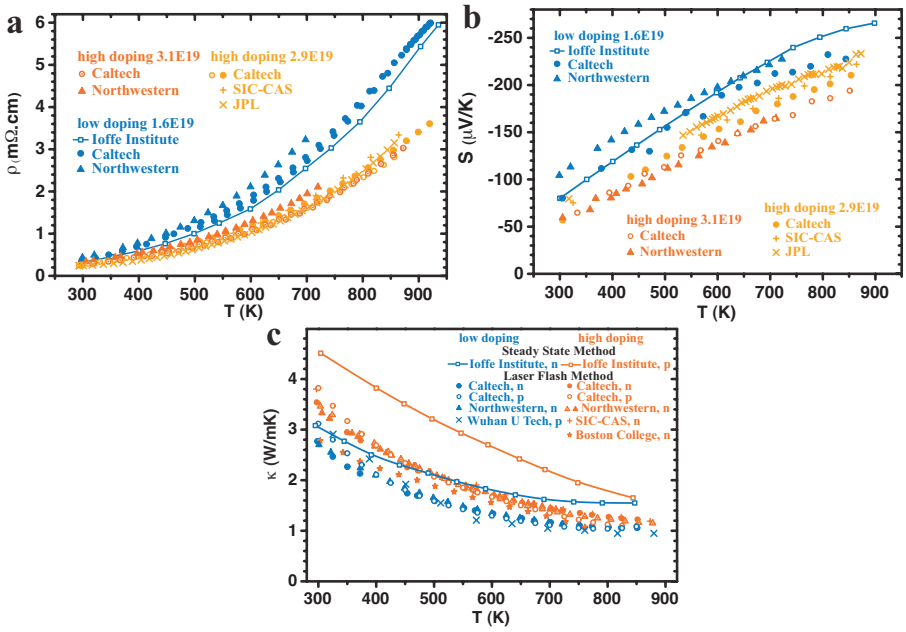

Figure 3.8. A comparison of a) resistivity, b) Seebeck coefficient, and c) thermal conductivity of a few n-type PbSe samples with similar carrier densities, results tested at Caltech, SIC-CAS and JPL (for a) and b)), as well as results from literature. Lines are guides to the eye.

This is not to say the steady-state based measurement can't give accurate results, but rather an implication of its high demand for good practice and poor stability to operator errors. In 2012 we received a set of n type PbSe bulks from the Ioffe Institute of Technical Physics and results provided by the Ioffe Institute are compared with that from Caltech (Figure 3.9). The Ioffe setup measures all three properties on a same sample (and along the same direction) at the same time. For these samples the steady-state thermal conductivity measurement results are very close to the results obtained by laser flash method at Caltech. We do see considerable difference between two sets of data presumably from the same sample, and the difference in Seebeck coefficient result is sometimes on the order of 20%, suggesting again its poor stability under operator error.

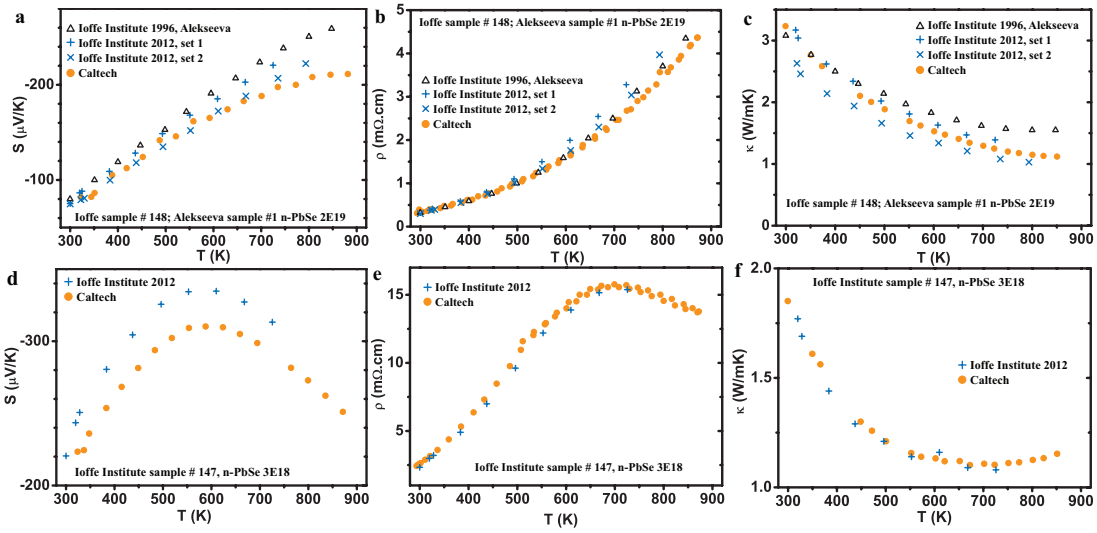

Figure 3.9. Comparison of measurements at Ioffe Institute and at Caltech on two n-type PbSe samples with Hall carrier density a)-c) 2×10^{19} cm^{-3}, d)-f) 3×10^{18} cm^{-3}. The Ioffe Institute used bar-shaped samples about 5×5×10 mm while Caltech used sheet samples ~1.2 mm thick that were cut from the same bar samples.

3.3 Transport Properties Modeling

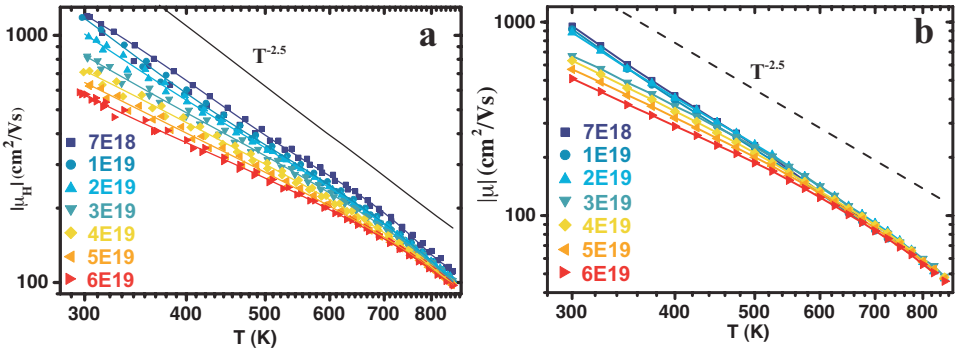

Figure 3.10. Hall mobility a) and drift mobility b) as function of temperature for Br doped PbSe. Drift mobilities are calculated from the polynomial fitted Hall mobility values. Black lines are guide to the eye of temperature dependence $T^{-2.5}$.

Figure 3.10 shows the temperature dependence of mobilities ($\mu = \mu_H/A$, A is the Hall factor) of Br doped PbSe samples. Due to the temperature dependence of effective mass $m^* \sim T^{0.4}$ in lead chalcogenides[12] the mobility governed by acoustic phonon scattering ($\mu \sim \tau/m^* \sim T^{-3/2}/m^{*5/2}$) has the temperature dependence of $\mu \sim T^{-5/2}$. Such a trend can be seen in Figure 3.10, thus enabling us to

assume the acoustic phonon scattering is predominant, as is believed so for heavily doped thermoelectric lead chalcogenides above room temperature.

The transport properties in n-type PbSe can be well modeled with a non-parabolic, single Kane band model with acoustic phonon scattering assumption. Figure 3.11 shows the 300 K Seebeck and Hall mobility as functions of Hall carrier density of n-type PbSe. The solid curves are calculated values from the model. Detailed equations involved will be explained later in Section 3.4. The density of states effective mass, $m^* = N_V^{2/3} m_b^*$, can be readily determined from the carrier density dependence of Seebeck coefficient (called the Pisarenko relation) and is found to be within the range 0.24 – 0.29 m_e. The average longitudinal elastic constant[81] C_l is 91GPa for PbSe, and the conduction band minimum is at L point with degeneracy of 4, thus by fitting the carrier density dependence of Hall mobility the only unknown parameter, the deformation potential coefficient Ξ, can be determined. Depending on the m^* value used, Ξ could vary from 22 eV to 29 eV (for each determined m^* value, the Ξ can be determined with less than ±1 eV uncertainty). The discrepancy seen at low n_H regime is due to the polar scattering, which was later taken into account and lead to a very close match with experimental result.

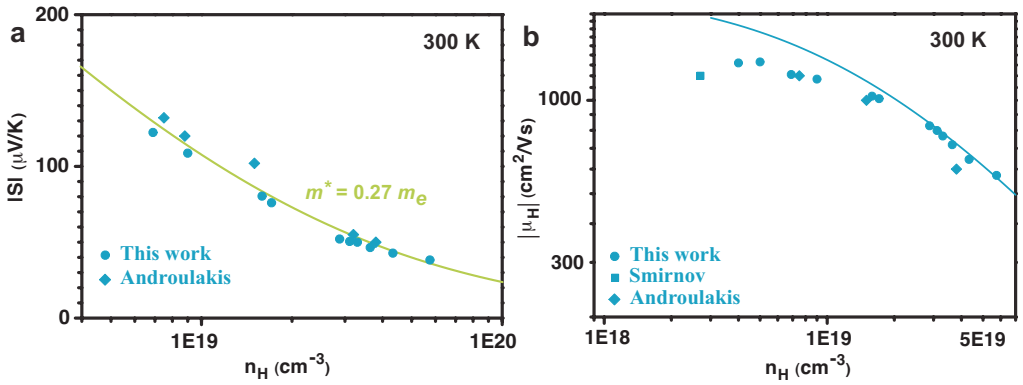

Figure 3.11. Carrier density dependence of 1) Seebeck coefficient and 2) Hall mobility of n-type PbSe at 300 K. Lines are calculated results. Parameters determined as $m^* = 0.27\ m_e$, Ξ = 25 eV.

The band gap of PbSe increases with temperature, from historical study the rate is about 0.4 meV/K. As a property of Kane bands, the band edge effective mass changes proportionally with E_g (more accurately the separation of conduction and valence bands at L point). With such information it is possible to analyze the transport properties at different temperatures. The result is shown in Figure 3.12 below:

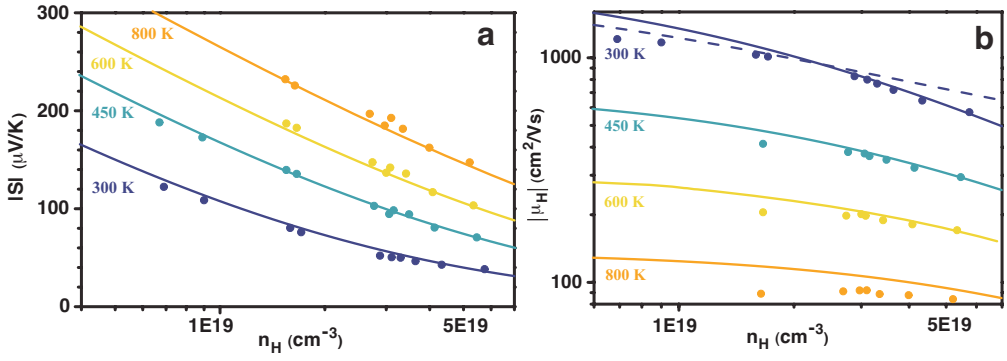

Figure 3.12. Carrier density dependence of a) Seebeck coefficient and b) Hall mobility of Br doped PbSe at different temperatures. Solid curves are modeling results (dashed curve represents the SPB result).

For the Seebeck Pisarenko relations SKB calculation assuming effective mass m^* = 0.27 m_e at 300 K and increases with temperature with their derivative $d\ln m^*/d\ln T$ = 0.5 explains the experimental result very well (see also Figure 3.15). The value 0.27 was chosen also because when extrapolating this dependence down to cryogenic temperatures it yields m^* = 0.13 m_e for 77 K, which is in good agreement with the value determined by longitudinal Nernst-Ettingshausen effect[46] (0.12 m_e). For Hall mobilities the deformation potential coefficient Ξ is fixed at 25 eV, leading to good agreement between experiment and theory up to 650 K. The single parabolic band (SPB) model (dashed curve), on the other hand, failed to predict the fast drop of μ_H at higher doping level, which is direct evidence that the conduction band is non-parabolic, Kane-type. For temperatures above 650 K the calculated values are significantly and systematically higher than the experiments. Even with bipolar conduction taken into account Ξ still needs to increase by 8% to explain the experimental result. This could be a result of softening of the compound at high temperatures, which means the elastic modulus C_l should slowly decrease with temperature, but in the current model was simply held constant.

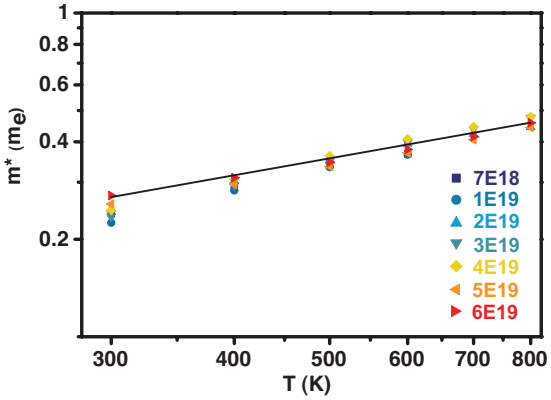

Figure 3.13. The density of states effective mass of each sample as a function of temperature. The solid curve represents $d\ln m^*/d\ln T = 0.5$ with $m^* = 0.27\ m_e$ at 300 K.

3.4 Thermoelectric Quality Factor *B*

This section contains adapted reproduction of contents from Chapter 1, "*Thermoelectric Nanomaterials"*, Springer Series in Materials Science Vol. 182, 2013, p 3-32, Copyright © Springer 2013.

Discussing the material quality factor *B* helps to answer the question why n-type PbSe is such a good thermoelectric material. The answer will eventually be: its conduction band has a very desirable combination of characteristics, which is a large quality factor *B*.

For semiconductors the transport properties that determine figure of merit zT, namely the Seebeck coefficient S, the electric conductivity σ and the electronic component of thermal conductivity κ_e for a given material are each functions of carrier density (or more fundamentally, chemical potential u). This means the full potential of a material as thermoelectrics or, the highest zT, will only be exploited when the carrier concentration is optimized. The tuning of carrier density is a very important goal for research on many compounds to improve zT.

Indeed, the merit of a semiconducting compound as a thermoelectric material can be evaluated without exploring the entire carrier density range, but through several fundamental parameters. Through history of thermoelectrics the combination of such parameters has been pointed out in similar forms by different researchers. It has first been discussed[82] in 1959 by Chasmar and Strattton and referred to as the "material factor" β where:

$$\beta = (k_B / e)^2 T\sigma_c / \kappa_L \propto m^{*3/2}\mu_c T / \kappa_L \qquad \text{Equation 3.1}$$

It was rewritten by[83] Goldsmid and Nolas et. al. as (using SI units):

$$\beta = 5.745\times10^{-6}\left(m^*/m_e\right)^{*3/2}\mu_c / \kappa_L T^{5/2} \qquad \text{Equation 3.2}$$

The same quantity has been called[84] the "*B* factor" by Mahan. *zT* of a material, when the carrier density has been optimized, will be determined by this factor, as shown in Figure 3.14. Additionally, since the electronic properties and lattice thermal conductivity are often considered independently tunable, the electronic part of β or *B* is also stressed for example by Slack when discussing[17] the criteria for good thermoelectric materials as the weighed mobility *U*:

$$U = \mu_0 m^{*3/2} \qquad \text{Equation 3.3}$$

In each the above expressions, m^* is the effective mass (in m_e) μ_c is the mobility value at nondegenerate, classical limit and μ_0 is the mobility value found in the purest samples, i.e., when the material is defect free and the carrier density is low.

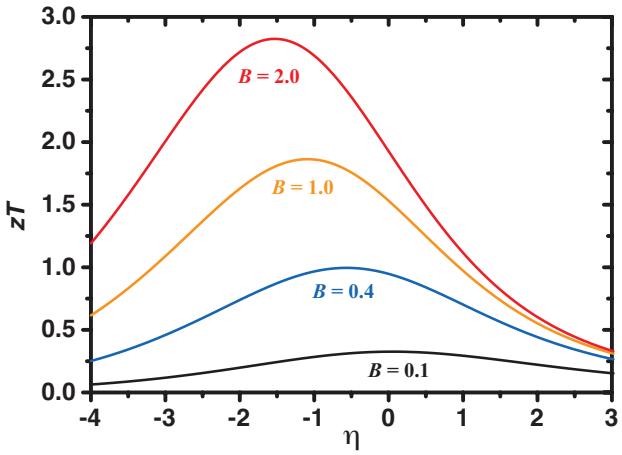

Figure 3.14. calculated *zT* as a function of reduced chemical potential η (u/k_BT) for different quality factor *B* in parabolic bands.

The use of two different types of mobilities in the above equations is understandable. μ_c is used because it is the quantity that related to the transport equations and finally linked to *zT*. μ_0 on the other hand, is a quantity directly measureable, given the compound can be made intrinsic. μ_0 are available for a lot of well-known semiconductors so researches would be able to easily evaluate their potential as thermoelectrics.

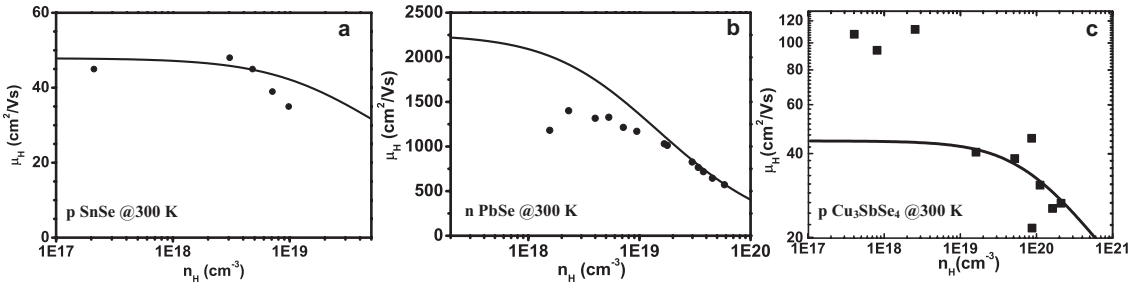

Figure 3.15. Hall mobility versus Hall carrier density for a)p type SnSe, b) n type PbSe and c) p type Cu_3SbSe_4. Mobility from intrinsic samples μ_0 is not always the same as the mobility at nondegenerate limit μ_c that used in modeling of doped samples.

For some compound, μ_0 and μ_c happen to have the same value. However, there is subtle but important difference between μ_0 and μ_c, for many compound this makes these two values quite different. Shown in Figure 3.15 are the mobility (Hall mobility) of three different polycrystalline compound p-type SnSe, n-type PbSe and p-type Cu_3SbSe_4 as functions of carrier density (Hall carrier density) at 300 K, together with mobilities from models. These models explained transport properties of doped samples well and characterized highest zT in each system quite accurately. For SnSe μ_0 and μ_c are found very similar because the acoustic phonon scattering of carriers remains the major mechanism for intrinsic samples. For PbSe, the mobility from intrinsic samples μ_0 is much less than the calculated mobility for nondegenerate samples μ_c assuming acoustic phonon scattering is still the dominant mechanism, because other scattering mechanism contribute significantly at this region. For Cu_3SbSe_4 on the other hand, the mobilities in undoped, intrinsic samples μ_c is found almost twice as high as μ_0 from the model that describes doped samples well, because of difference in scattering mechanisms and fine valence band configuration near the edge. Notice that only by using μ_c could one get reasonable estimate of zT achievable for each compound. In order to best evaluate B (or β), μ_c should be used. This value should be extrapolated to the nondegenerate limit from mobilities of doped samples, with carrier density close to that usually seen in thermoelectrics (10^{19} to 10^{20} cm^{-3}).

The weighed mobility is a characteristic of a compound instead of a specific sample. In some studies the authors report "weighed mobility" for each sample that were studied. This is inappropriate and U values obtained in such a way can't be used to compare the merit of such compound as thermoelectrics with others.

There are a few advantages to rewrite the above expressions for B (or β) by replacing μ_c with other fundamental material parameters. One is the aforementioned subtlety in mobility choices. The other one is about the confusion due to the appearance of β being a product of μ_0 and $m^{*3/2}$, which could lead to the wrong impression that larger effective mass m^* is beneficial for thermoelectrics. For most scattering mechanisms μ_0 is also a function of m^*. Especially when acoustic phonon scattering is dominant, μ_0 will decrease with $m^{*5/2}$, which clearly indicates that for similar compounds, a smaller m^* actually will lead to a larger U (and β or B)[85].

If we rewrite B (or β) under the acoustic phonon scattering assumption, which we call the quality factor since B is the combination of material properties of a semiconductor that directly relates to the maximum material performance, zT, when the carrier concentration is optimized. For materials with conduction from a single spherical Fermi surface:

$$\beta = (\frac{k_B}{e})^2 \frac{2e(k_B T)^{3/2}}{(2\pi)^{3/2}\hbar^3} \frac{\mu_0 m^{*3/2}}{\kappa_L} T = \frac{2k_B^2\hbar}{3\pi} \frac{C_{11}}{m^* \Xi^2 \kappa_L} T \qquad \text{Equation 3.4}$$

Here C_{11} is the longitudinal elastic constant $C_{11} = v_l^2 d$, v_l being the longitudinal sound of speed and d the density, and Ξ is the deformation potential. A small effective mass m^*, small deformation potential Ξ, together with small lattice thermal conductivity κ_L are favorable for larger quality factor B and large maximum zT.

For a general case with degenerate, non-spherical Fermi surfaces, the B factor is written as:

$$B = \frac{2k_B^2\hbar}{3\pi} \frac{C_l N_V}{m_I^* \Xi^2 \kappa_L} T \qquad \text{Equation 3.5}$$

Where N_v is the valley degeneracy and m_I^* is the inertial effective mass defined later in Equation 3.15. Compounds with larger valley degeneracy N_v and small inertial effective mass m_I^* are favorable for high zT.

The best thermoelectric compounds used at high temperatures have B of around 1, whereas for room temperature or cryogenic applications the best materials only have B below half of this value. Figure 3.16 shows the quality factor of B estimated for a few compounds at their operating temperature. The parameters used are given in Table 3.2. Notice that these values are at best rough estimates (except for the Pb chalcogenides): many of these compounds are not composed of a single electronic band. The parameters could still represent (some of) the physical reality in the cases where the multiple bands are from symmetry related degeneracy so that each carrier pocket is

equivalent. This includes the compound of n-type Pb chalcogenides, Si, SnTe, SnSe, Mg_2Si Bi_2Te_3, Bi_2Se_3 and ZrNiSn. In more general cases a single band picture will break down so that the parameters listed are at best an enveloped average attributing all apparent transport phenomenon to a hypothetical "single band" or "multiple equivalent bands with same *Nv*", this includes p-type PbTe and PbSe (*B* for the L band shown), $Si_{0.7}Ge_{0.3}$, $Mg_2Si_{0.6}Sn_{0.4}$, $Bi_{1-x}Sb_x$, $CoSb_3$, La_3Te_4, and Cu_3SbSe_4. Moreover, for some compounds ZrNiSn or solid solutions such as $Si_{0.7}Ge_{0.3}$, $Mg_2Si_{0.6}Sn_{0.4}$ and $Bi_{1-x}Sb_x$ the acoustic phonon scattering is not guaranteed to be the only important mechanism in charge transport. Nonetheless, after putting the *B* values for these systems together it is seen that they agree with the best *zT* reported for each system experimentally reasonably well.

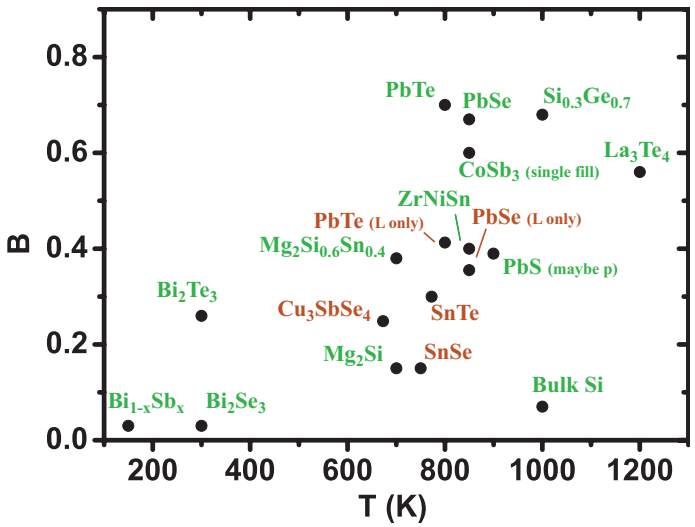

Figure 3.16. Quality factor *B* for a few compounds at their application temperatures. Green indicates n-type and red p-type.

Table 3.2. A list of compounds with their material parameters and B under acoustic phonon scattering assumption.

	PbTe	PbTe	PbSe	PbSe	PbS	$Si_{0.7}Ge_{0.3}$	Bulk Si
type	n	P(L)	n	P(L)	n	n	n
$T_{operate}$	800	800	850	850	900	1000	1000
$\mu_0 m^{*3/2}$							
N_v	4	4	4	4	4	6	6
C_l(GPa)	71	71	91	91	111	150	180
m_I^*	0.15	0.17	0.17	0.17	0.25	0.27	0.26
Ξ	23	28	27	38	28	15	15
κ_L	0.75	0.75	0.65	0.65	0.95	4	45
B	0.7	0.4	0.67	0.33	0.39	0.68	0.07

continued

	Bulk Ge	Mg_2Si	$Mg_2Si_{0.6}Sn_{0.4}$	SnTe	SnSe	Cu_3SbSe_4	Bi_2Te_3
type	n	n	n	p(L)	n	p	n (//c)
$T_{operate}$	1000	700	700	773	750	673	400
$\mu_0 m^{*3/2}$							
N_v	4	3	6	4	2	3	6
C_l	160	120	100	58	58	80	71
m_I^*	0.12	0.5	0.8	0.09	0.47	0.7	0.1
Ξ	20	15	13	28	21	14	24
κ_L	18	3	1.5	1.5	0.5	1	1.5
B	0.14	0.15	0.38	0.3	0.15	0.22	0.26

continued

	$Bi_{1-x}Sb_x$	$CoSb_3$	La_3Te_4	Bi_2Se_3	ZrNiSn
type	n	n	n	n	n
$T_{operate}$	150	850	1200	300	850
$\mu_0 m^{*3/2}$	400		10		150
N_v		3		1	
C_l		100			180
m_I^*		1.6		0.15	
Ξ		10			
κ_L	9	0.5	0.5	1.3	4.5
B	0.03	0.6	0.56	0.03	0.4

Just as the risk it bears when one compares the merit of two different things (or persons) with a simple index, comparing two compounds for thermoelectric performance is not always as simple as comparing their quality factors. First, it is always important to bear in mind the uncertainty, both in zT determination and the parameters used to calculate B, especially when these results are from different groups. Second, B governs the maximum zT rather than the averaged zT over a wide temperature range, and for real application it is the average zT that is of more importance. Unfortunately, some features that make B large is not necessarily in favor of large averaged zT. For example the chemical potential in a system with very light effective mass changes a lot with slight variation of carrier density thus could be sensitive to temperature activated defects, so it is difficult

to keep it close to the optimum position for a wide temperature range. Third, the influence from minority carriers is not taken into account, which could be important for systems with small to moderate band gaps.

One last limitation in comparing B of different compounds is that, the same B factor could map to different maximum zT values in different band models. More specifically as the non-parabolicity increases the maximum zT from the same B factor decreases. This means given the same material parameters a system with parabolic band is always better than a non-parabolic Kane band. Figure 3.17 shows the zT for different reduced chemical potential η under the same B factor of 0.7, but different band non-parabolicity factor $\alpha = k_B T/E_g$ (number next to curves). For direct reference the α factor in PbSe at 900 K is about 0.15. Figure 3.18 shows the maximized zT and the corresponding optimum η as function of quality factor B for systems with different degree of nonparabolicity.

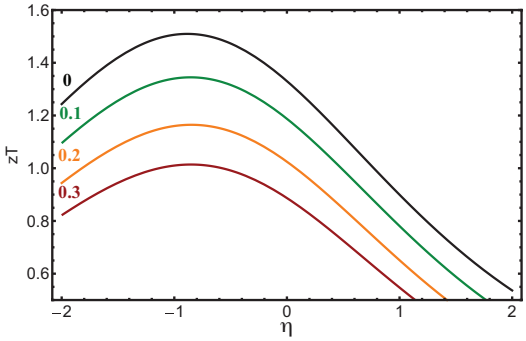

Figure 3.17. zT as functions of reduced chemical potential η for same quality factor $B = 0.7$ but bands with different degree of non-parabolicity.

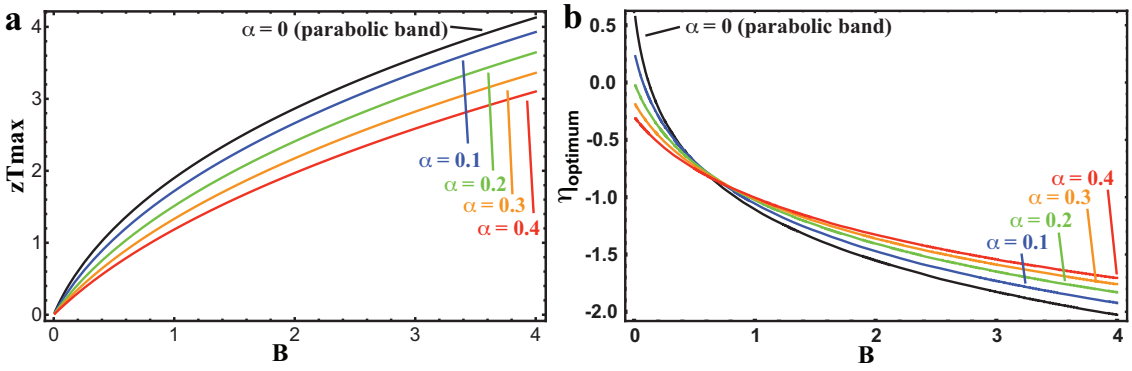

Figure 3.18. a) Maximized zT, and b) corresponding optimum η as function of B for bands with different nonparabolicity factor α.

On the other hand, for the same system the parameters determined while using a parabolic band model will be different from those determined using a non-parabolic band model, meaning the B factor will be different for the same compound. This is actually a convenient fact so that the B - zT correlation could be a one-to-one correlation and it is possible to map B for all compounds into a same metric. Nonetheless, in Table 3.2 and Figure 3.16 the reported values were used regardless of band model used to determine them (Kane model is used for all Pb chalcogenides, SnTe and possibly Bi_2Te_3).

3.5 Band Models and Transport Properties Equations for Single Band

The dispersion relation dE/dk of electronic bands is important for many transport parameters. Although in an exact band structure diagrams a band could literally have any "shape" or E-k correlation. It is a very good approximation that near the extreme of each band, such correlation can be described using a parabola, i.e., $E= \hbar^2k^2/2m^*$. This is the well-known parabolic band assumption, which is a very good first step while working on a new compound (and in many cases are adequate).

Since it has been covered by many book chapters (see, for example Chapter 11 in *Thermoelectrics and Its Energy Harvesting*, CRC press 2012), I will simply list all the transport equations under single parabolic band (SPB) model and acoustic phonon scattering assumption here. These are most often used and are relevant to our further discussion about non-parabolic bands. In Appendix A I will provide a detailed derivation of the expression of transport parameters under SPB model, including carrier density, mobility, Seebeck coefficient and Lorenz number.

The transport properties can be expressed as functions of η under SPB model with acoustic phonon assumption.

(chemical) carrier density:

$$n = \frac{(2m_d^* k_B T)^{3/2}}{2\pi^2\hbar^3} F_{1/2}(\eta) \qquad \text{Equation 3.6}$$

Seebeck coefficient:

$$S = \frac{k_B}{e}\left[\frac{2F_1(\eta)}{F_0(\eta)} - \eta\right] \qquad \text{Equation 3.7}$$

Hall factor ($n_H = n/A$, $\mu_H = \mu A$):

$$A = \frac{3K(K+2)}{(2K+1)^2}\frac{3}{4}\frac{F_{1/2}(\eta)F_{-1/2}(\eta)}{F_0(\eta)^2},\ K = m_{\|}^*/m_{\perp}^* \qquad \text{Equation 3.8}$$

Drift mobility:

$$\mu = \mu_0 \frac{\sqrt{\pi}}{2}\frac{F_0(\eta)}{F_{1/2}(\eta)} = \frac{2^{1/2}\pi\hbar^4 e C_l N_V^{5/3}}{3m_d^{*5/2}(k_B T)^{3/2}\Xi^2}\frac{F_0(\eta)}{F_{1/2}(\eta)} \qquad \text{Equation 3.9}$$

Lorenz number:

$$L = \frac{\kappa}{\sigma T} = \left(\frac{k_B}{e}\right)^2\left[3\frac{F_2(\eta)}{F_0(\eta)} - 4\frac{F_1(\eta)^2}{F_0(\eta)^2}\right] \qquad \text{Equation 3.10}$$

The Fermi integral in these equations are given by:

$$F_x(\eta) = \int_0^\infty \frac{\varepsilon^x}{1+\exp(\varepsilon-\eta)}d\varepsilon \qquad \text{Equation 3.11}$$

With all the transport parameters expressed the total zT is just a function of chemical potential and material quality factor B:

$$zT = [\frac{2F_1(\eta)}{F_0(\eta)} - \eta]^2 / \{[\frac{3F_2(\eta)}{F_0(\eta)} - (\frac{4F_1(\eta)}{F_0(\eta)})^2] + B^{-1}(2F_0(\eta))^{-1}\} \qquad \text{Equation 3.12}$$

So far the constant energy contours of the relevant band are assumed spherical. In many semiconductors the extremes of bands are off the center of Brillouin Zone and the band structures in these cases are referred to as being composed of degenerate valleys, the number of which is called valley degeneracy N_v. Now the (density of state) effective mass of a single valley m_b^* becomes different from the total density of state (DOS) effective mass m_d^* in Equation 3.6 above such that:

$$m_d^* = N_V^{2/3} m_b^* \qquad \text{Equation 3.13}$$

In most multi-valley structures the constant energy contours of each valley are likely not spherical. In such cases two effective masses along two principle directions are used. In semiconductors like silicon, germanium, and lead chalcogenides they are defined as transverse and longitudinal components. The DOS effective mass of a single valley is thus averaged as:

$$m_b^* = (m_{\perp}^{*2} m_{\|}^*)^{1/3} \qquad \text{Equation 3.14}$$

Meanwhile, a different average is defined and called inertial effective mass (also referred to as conductivity effective mass or susceptibility effective mass) by Herring and Goldsmid:

$$m_l^* = 3\left(\frac{2}{m_\perp^*} + \frac{1}{m_\parallel^*}\right)^{-1}$$ Equation 3.15

An interesting result about the shape of these energy contours of bands is that if a spherical surface is distorted and elongated in one direction while keeping the density of state effective mass the same, the direction with smaller effective mass would contribute to conduction more than the directions with heavier masses. The conduction effective mass m_l^* is thus different even though m_d^* is the same. When the (drift) mobility is plotted against carrier density for different K, higher mobilities are found when K differs from 1 (Figure 3.19), which leads to increased power factor and zT since m_d^* and hence S is unchanged. The X valleys in Si and L valleys in Ge have very elongated Fermi surfaces, which is helpful for their high mobilities. The electron pockets in PbTe are more anisotropic than in PbSe while the m_d^* are very close to each other, this helps n type PbTe to achieve a higher mobility and zT compared to PbSe.

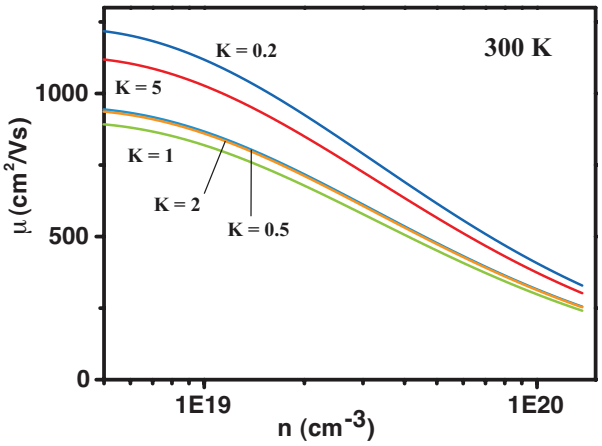

Figure 3.19. Drift mobility as function of carrier density assuming the same m_b^* but different shape of Fermi surface (K). All other parameters used in calculation are taken from n type PbSe.

Other than the band anisotropy, an energy contour could alter from the simplest spherical case by losing its parabolicity. In systems with narrow direct band gaps, the neighboring conduction band and valence band have strong interaction that makes the dispersion relation complicated and the bands non-parabolic. Kane described a band model for InSb that accounted for interactions[86] between all six orbits that are close to the primary band gap. Ravich simplified this model for Pb chalcogenides, considering the most important interaction between two orbits (L_6^+ and L_6^-) and came to the simple expression of dispersion relation:

$$E(1+E/E_g)=\frac{\hbar^2k^2}{2m^*}=\frac{\hbar^2k_\perp^2}{2m_\perp^*}+\frac{\hbar^2k_\parallel^2}{2m_\parallel^*} \qquad \text{Equation 3.16}$$

the ratio E/E_g, measures the high order correction to the parabolic dispersion relation, and since the reduced carrier energy $z = E/k_BT$ (or reduced chemical potential) is more often used in these transport equations, the factor $\alpha = k_BT/E_g$ is used and called the non-parabolicity factor so that $E/E_g = \alpha z$. The parabolic band can be seen as the extreme case when $E_g = \infty$ and $\alpha = 0$.

An important result from the interaction ($k \cdot p$ perturbation theory) is that the effective mass of carriers in a Kane band depends on both the band gap and its energy:

$$m_{\perp,\parallel}^*=\frac{\hbar^2E_g}{\left|\frac{\hbar}{m_e}\left\langle\varphi_{conduct}^*\left|p_{\perp,\parallel}\right|\varphi_{valence}\right\rangle\right|}(1+\frac{2E}{E_g})=m_0^*(1+\frac{2E}{E_g}),\ p_{\perp,\parallel}=-i\hbar\nabla\cdot\overrightarrow{e_{\perp,\parallel}} \qquad \text{Equation 3.17}$$

m_0^*, the band effective mass when $E = 0$, i.e., for carriers at the edge of the band, is proportional to the band gap in a Kane band.

A schematic Kane band E-k diagram is shown in Figure 3.20. As E_g decreases the non-parabolicity increases and the band becomes more linear. When the band gap vanishes the two bands now form a Dirac cone, which is an important concept in topological insulators[87-89] related to band inversion and surface states.

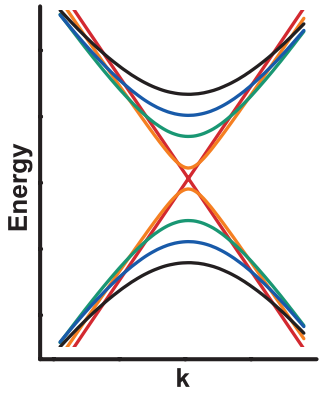

Figure 3.20. Schematic band diagram of Kane band systems with different band gap.

Following the argument in the previous section on B and effective mass. It seems shrinking the band gap of a Kane band system, despite of the simultaneous increase of non-parabolicity factor α,

could potentially lead to an increase of zT, given no bipolar effect is initiated due to the small band gap. This could be a strategy to further improve zT in n-type Pb chalcogenides.

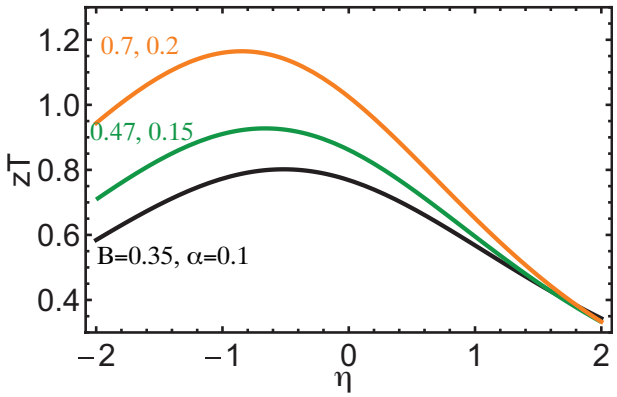

Figure 3.21. Decreasing the band gap of a Kane band system could potentially increase the maximum zT due to decreased band effective mass.

The transport equations for a Kane band system can be readily derived from those for a parabolic band by using own expression in the density of states:

$$g(E)=\frac{dn}{dE}=\frac{8\pi k^2 dk}{8\pi^3 dE}=\frac{k^2}{\pi^2}/\frac{dE}{dk}$$

$$=\frac{k^2}{\pi^2}/[\frac{\hbar^2 k}{m^*}(1+2\varepsilon a)^{-1}]=\frac{m^*}{\pi^2\hbar^2}k(1+2\varepsilon a) \qquad \text{Equation 3.18}$$

$$=\frac{m^*}{\pi^2\hbar^2}\sqrt{\frac{2m^*E(1+\varepsilon a)}{\hbar^2}}(1+2\varepsilon a)=\frac{2^{1/2}m^{*3/2}(k_BT)^{1/2}}{\pi^2\hbar^3}\varepsilon^{1/2}(1+\varepsilon a)^{1/2}(1+2\varepsilon a)$$

instead of that for parabolic bands:

$$g(\varepsilon)=\frac{m^*}{\pi^2\hbar^2}k=\frac{m^*}{\pi^2\hbar^2}\sqrt{\frac{2m^*E}{\hbar^2}}=\frac{1}{2\pi^2}\left(\frac{2m^*}{\hbar^2}\right)^{3/2}\sqrt{E}=\frac{2^{1/2}m^{*3/2}(k_BT)^{1/2}}{\pi^2\hbar^3}\varepsilon^{1/2} \qquad \text{Equation 3.19}$$

The transport equations under acoustic phonon scattering assumption can be expressed as:

(chemical) carrier density:

$$n=\frac{(2m_d^*k_BT)^{3/2}}{3\pi^2\hbar^3}{}^0L_0^{3/2} \qquad \text{Equation 3.20}$$

Seebeck coefficient:

$$S=\frac{k_B}{e}[\frac{{}^1L_{-2}^1}{{}^0L_{-2}^1}-\eta] \qquad \text{Equation 3.21}$$

Hall factor:

$$A = \frac{3K(K+2)}{(2K+1)^2}\frac{{}^0L_{-4}^{1/2}\,{}^0L_0^{3/2}}{({}^0L_{-2}^1)^2} \qquad \text{Equation 3.22}$$

Drift mobility:

$$\mu = \frac{2\pi\hbar^4 eC_l}{m_\chi^*(2m_b^* k_B T)^{3/2}\Xi^2}\frac{3\,{}^0L_{-2}^1}{{}^0L_0^{3/2}} \qquad \text{Equation 3.23}$$

Lorenz number:

$$L = (\frac{k_B}{e})^2[\frac{{}^2L_{-2}^1}{{}^0L_{-2}^1} - (\frac{{}^1L_{-2}^1}{{}^0L_{-2}^1})^2] \qquad \text{Equation 3.24}$$

The generalized Fermi integrals in above expressions is given by:

$${}^nL_l^m(\eta,\alpha) = \int_0^\infty (-\frac{\partial f}{\partial \varepsilon})\varepsilon^n(\varepsilon+\varepsilon^2\alpha)^m(1+2\varepsilon\alpha)^l d\varepsilon \qquad \text{Equation 3.25}$$

Ravich in 1970s proposed[81, 90] for Pb chalcogenides an energy dependent interaction matrix element that brings a correction term in the relaxation time τ_{ac}. Such correction made better matches with experimental results. When taking the energy dependent interaction matrix element into account, the generalized Fermi integrals in the above Equation 3.20 through Equation 3.25 need to be replaced by the integral:

$${}^nF_l^m(\eta,\alpha) = \int_0^\infty (-\frac{\partial f}{\partial \varepsilon})\varepsilon^n(\varepsilon+\varepsilon^2\alpha)^m[(1+2\varepsilon\alpha)^2+2]^{l/2} d\varepsilon \qquad \text{Equation 3.26}$$

The zT of a system with Kane band under acoustic phonon scattering assumption can be written as a function of chemical potential and the quality factor B:

$$zT = [\frac{{}^1F_{-2}^1}{{}^0F_{-2}^1} - \xi]^2 / \{[\frac{{}^2F_{-2}^1}{{}^0F_{-2}^1} - (\frac{{}^1F_{-2}^1}{{}^0F_{-2}^1})^2] + B^{-1}({}^3{}^0F_{-2}^1)^{-1}\} \qquad \text{Equation 3.27}$$

There are uncommon cases where the acoustic phonon scattering assumption is not good enough and other scattering mechanisms need to be taken into account, so that the relaxation time τ_{total} instead of being τ_{ac}, would be an summation of those from each mechanism using Matthiessen's rule:

$$\tau_{total} = 1/\sum_i \frac{1}{\tau_i} \qquad \text{Equation 3.28}$$

The transport equations in this case will be discussed in Chapter 6.

3.6 Acoustic Phonon Scattering and Deformation Potential

This section and Section 3.7 contains adapted reproduction of contents from Chapter 1, "*Thermoelectric Nanomaterials"*, Springer Series in Materials Science Vol. 182, 2013, p 3-32, Copyright © Springer 2013. For the derivation of interaction matrix for acoustic phonon scattering, I acknowledge the great help from presentation slides by Prof. Vasileska and Prof. Ferry at Arizona State University on "acoustic phonon scattering" that is accessible online.

Almost all electric properties of a thermoelectrics are related to the scattering mechanisms of the carriers, or the relaxation time of carriers. The relaxation times under different scattering mechanisms have different dependence on temperature, effective mass of carriers as well as carrier energy (as shown in Figure 3.22), which lead to very different dependence of transport properties on chemical potential or, carrier density. As an example, Figure 3.23 and Figure 3.24 demonstrate how such dependence of Seebeck coefficient, mobility and Lorenz number are affected by different scattering mechanisms as well as band non-parabolicity.

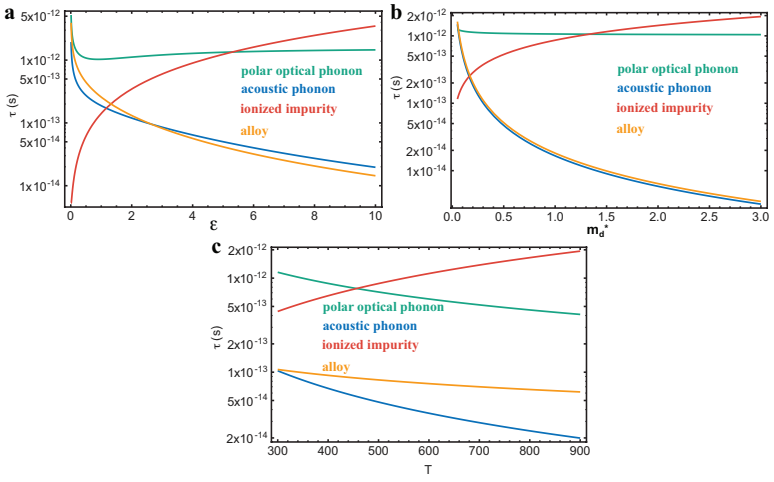

Figure 3.22. Relaxation time τ of charge carriers under different scattering mechanisms as function of a) carrier energy, with chemical potential set equal to ε, b) density of state effective mass, with $\varepsilon = \eta = 2$, and c) temperature, with $\varepsilon = \eta = 2.4$. All other parameters are from PbSe.

Fortunately in most cases, one does not need to embraces this complicity, but instead could simply assume the acoustic phonons scattering is the dominant one and omit the other scattering mechanisms. This assumption has been working well on many systems that many researchers just take for granted that acoustic phonon scattering assumption is valid for the material they are

working on. In this section, rather than directly accepting this assumption we will discuss more detail about carrier scattering mechanisms and demonstrate why the acoustic phonon scattering is often a good assumption. It also indirectly suggests when should we take into account other scattering mechanisms.

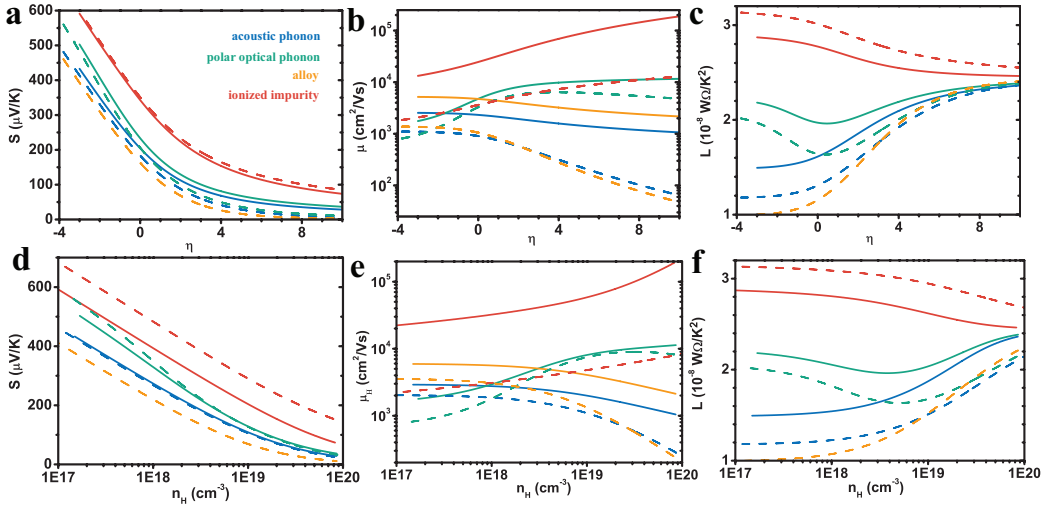

Figure 3.23. Transport parameters as functions of a)-c) reduced chemical potential and d)-f) Hall carrier density for different carrier scattering mechanisms, solid curves are for parabolic band and dashed are for Kane band with $\alpha = 0.2$. When the solid orange curve for alloy scattering is not seen, it overlaps with that for acoustic phonon scattering.

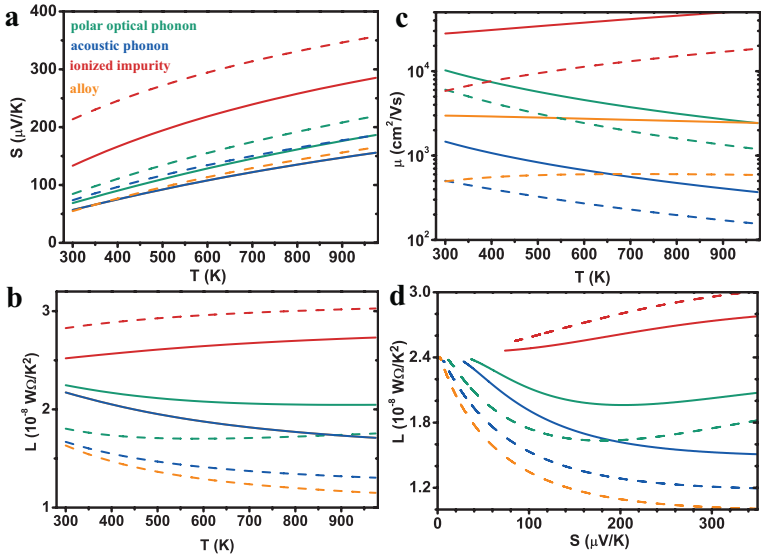

Figure 3.24. a) Seebeck coefficient, b) Lorenz number, c) mobility as functions of temperature assuming constant carrier density 3×10^{19} cm^{-3}, curves are for the same meaning as in previous Figure. d) Lorenz number as a function of Seebeck coefficient.

From a simple Drude model, the carriers are scattered by different scattering centers in a semiconductor under electric field so that they will not be accelerated forever and their velocity not get to infinity. From a quantum mechanics point of view, all scattering processes are transitions of the electrons from its initial state |i> into a new state |f> under certain "force" or, Hamiltonian, which is regarded a perturbation to the original system with its Hamiltonian *H*. The fundamental rule that governs the transition rate of any kind of scattering process is the Fermi's golden rule, which states that the transition rate is given by the squared magnitude of the interaction matrix element (a probability) multiplied by the density of states of the final state:

$$\Gamma_{if} = \frac{2\pi}{\hbar}\left|\langle f \mid H' \mid i\rangle\right|^2 \rho_f \qquad \text{Equation 3.29}$$

The relaxation time for such transition is the summation (usually by integration) of transition rate for all possible final states:

$$\tau(k) = \tau(\varepsilon) = \frac{1}{\Gamma_k} = \frac{1}{\frac{2\pi}{\hbar}\int_{k'}\left|\langle k' \mid H' \mid k\rangle\right|^2 dk' \rho_{k'}} \qquad \text{Equation 3.30}$$

*T*o get τ one needs to know basically two pieces of information: the interaction matrix or, the interaction Hamiltonian *H'* and the dispersion relation or, band model that gives the density of states.

There are two types of scattering processes, one being the elastic process and the other inelastic process. The energy of carriers is conserved in the first process while not in the second (momentum and energy are conserved for the system for both). Elastic processes include most scattering by a point scatter center, such as neutral/ionized impurity and alloy disorder as well as the scattering by low energy acoustic phonons. Relaxation time can be readily defined for these processes. Inelastic processes mainly involves scattering by high-energy optical phonons (optical phonon deformation potential, optical phonon polar, and intervalley). The concept of relaxation time for these processes becomes complicated (because the energy and momentum relaxation are different). Approximated τ are nonetheless defined for these mechanisms under certain conditions.

Although fundamentally the charge carriers are scattered due to the electrostatic interaction with the scattering centers in almost all scattering events, the scattering mechanisms can be sorted into two types as well based on the type of interaction. Scattering by ionized impurities, the polar scattering from optical phonons, and the piezoelectric scattering from acoustic phonons are columbic

interactions where charge carriers are scattered because the existence of a net charge or oscillating dipole along their conduction path. These mechanisms based on columbic force are significantly affected by the screening effect in heavily doped semiconductors. The relaxation time increases with the increase of carrier energy because the net charges are further screened as the carrier density increases. Scattering by alloy disorder, deformation potential from the acoustic phonon or optical phonon, as well as the inter-valley scattering are potential based interaction where charge carriers are scattered because the pseudo-potential of the lattice was disturbed locally by the scattering center. There is no screening effect in potential based mechanisms and the scattering of high-energy carriers is stronger because the density of states of the final state is higher.

For bulk semiconductors the most important scattering mechanisms that could affect their transport properties are those from the interaction with phonons. As an acoustic phonon wave propagates through a crystal it causes compression and dilation of the local lattice which introduces a perturbation of the potential energy of bands and hence the scattering of carriers. Such a process is called the deformation potential scattering from acoustic phonons, or more commonly, acoustic phonon scattering in short (Figure 3.25). The concept of "deformation potential" was first used by[91] Bardeen and Shockley and can be regarded as a measure of the strength of carrier-phonon interaction and is therefore sometimes[21, 92] referred to as the electron-phonon coupling constant.

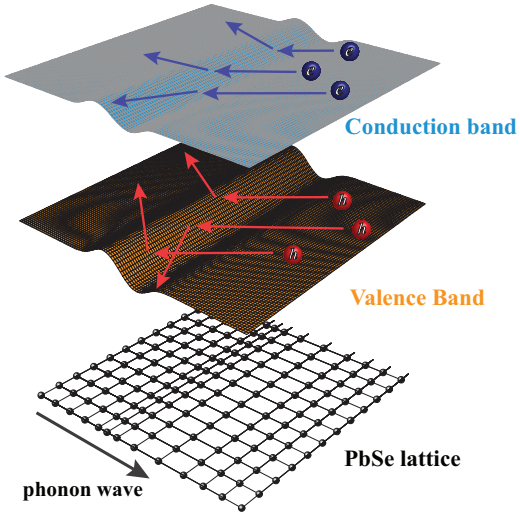

Figure 3.25. Schematic carrier-phonon interaction via deformation potential scattering. Lattice was deformed by phonon waves, which produce the potential energy fluctuation in each band, resulting in scattering of carriers.

The Hamiltonian of a system with both phonons and electrons is given by:

$$H = H_p + H_e + H_{e-p} = \sum_r \frac{P_r^2}{2m_r} + V(r) + \sum_n \frac{P_n^2}{2m_n} + U(k_n, r) + \sum_{i<j} \frac{e^2}{|k_i - k_j|} + H_{e-p} \quad \text{Equation 3.31}$$

The electron states are eigenfunctions that satisfy:

$$H_e \varphi_{n,k} = E_n \varphi_{n,k} \quad \text{Equation 3.32}$$

and the phonon states are those satisfy:

$$H_p \phi = E\phi \quad , \quad \phi = |n_{q1} n_{q2} n_{q3} \ldots\rangle = |n_{q1}\rangle |n_{q2}\rangle |n_{q3}\rangle \ldots \quad \text{Equation 3.33}$$

$|n_{qi}\rangle$ are phonon eigenstates when the Hamiltonian of the quantum oscillator is described with the annihilation and creation operators α and α*:

$$H_p = \frac{1}{2} \sum_q \hbar v_q (a^* a + a a^*) \quad \text{Equation 3.34}$$

so that n_{qi} are integers representing the number of phonons in this particular mode.

The interaction Hamiltonian $H_{e\text{-}p}$ satisfy:

$$H_{e-p} \phi(r) \varphi_{n,k} = -\sum_r \frac{\hbar^2}{m_r} \frac{\partial \phi(r)}{\partial r} \frac{\partial \varphi_{n,k}}{\partial r} \quad \text{Equation 3.35}$$

The deformation potential theorem[93] says that the interaction Hamiltonian, can be approximated by a product:

$$H_{e-p} = \Xi \frac{\partial}{\partial r} u_n(r) \quad \text{Equation 3.36}$$

The first half is the deformation potential meaning the change of potential energy per unit of lattice volume change, which is an operator to the electron states; the second half is the volume change of a unit cell, which is an operator on the phonon states. *u(r)* is the displacement operator of the lattice:

$$u_n(r) = \sum_q \left(\frac{\hbar}{2NMw_{q,n}} \right)^{1/2} \overrightarrow{e_{q,n}} (a_{q,n} e^{iqr} + a_{q,n}^* e^{-iqr}) \quad \text{Equation 3.37}$$

which is based on the displacement in a quantum oscillator:

$$x = \left(\frac{\hbar}{2mw} \right)^{1/2} (a + a^*) \quad \text{Equation 3.38}$$

ω is the frequency, are the step up and step down operators, $\overrightarrow{e_{q,n}}$ is the polarization vector. Notice:

$$\frac{\partial}{\partial r}u_n(r) = i\sum_q \left(\frac{\hbar}{2NMw_{q,n}}\right)^{1/2} q\cdot\overrightarrow{e_{q,n}}(a_{q,n}e^{iqr} - a_{q,n}^{*}e^{-iqr}) \qquad \text{Equation 3.39}$$

The dot product of $q\cdot\overrightarrow{e_{q,n}}$ actually suggests this operator, and hence electron-phonon interaction Hamiltonian will vanish for transverse phonon modes since their wave vectors are normal to the polarization.

The electron-phonon interaction matrix element can be expressed as:

$$M_{kk'} = \left\langle \phi\varphi_{n,k'} \middle| H_{e-p} \middle| \varphi_{n,k}\phi \right\rangle = \left\langle e^{-ik'r_e} \middle| \Xi\left(\frac{\hbar}{2NMw_{q,n}}\right)^{1/2} q\left\langle n_q' \middle| ae^{iqr} - a^{*}e^{-iqr} \middle| n_q \right\rangle \middle| e^{ikr_e} \right\rangle$$

$$= \left\langle e^{-ik'r_e} \middle| \Xi\left(\frac{\hbar}{2NMw_{q,n}}\right)^{1/2} q(\sqrt{n_q}e^{iqr}\delta(n_q', n_q - 1) - \sqrt{n_q + 1}e^{-iqr}\delta(n_q', n_q + 1)) \middle| e^{ikr_e} \right\rangle$$

$$= \left\langle e^{-ik'(r+r')} \middle| e^{\pm iqr}\left(\frac{\hbar}{2NMw_{q,n}}\right)^{1/2} \begin{bmatrix} \sqrt{n_q} \\ -\sqrt{n_q + 1} \end{bmatrix} q\Xi \middle| e^{ik(r+r')} \right\rangle \qquad \text{Equation 3.40}$$

Here the coordinate of each electron r_e is separated into $r_e = r + r'$, the first term being the coordinate of the unit cell and the second the relative coordinate within that cell. Using the property of Bloch waves:

$$\varphi_k(r + r') = e^{ikr}\varphi_k(r') \qquad \text{Equation 3.41}$$

we get:

$$M_{kk'} = \sum_q e^{i(k-k'\pm q)r} \left\langle e^{-ik'r'} \middle| \left(\frac{\hbar}{2NM\omega_{q,n}}\right)^{1/2} \begin{bmatrix} \sqrt{n_q} \\ -\sqrt{n_q + 1} \end{bmatrix} q\Xi \middle| e^{ikr'} \right\rangle \qquad \text{Equation 3.42}$$

$M_{kk'}$ should be the same regardless of which unit cell is considered, this is realized only when $k\text{-}k'\pm q = 0$, so the summation of first term should yield 1. Further by assuming the temperature being high enough so that $n_q \approx n_q + 1$, then regardless of phonon absorption or emission we get:

$$M_{kk'} = \left(\frac{\hbar}{2NM\omega_{q,n}}\right)^{1/2} \sqrt{n_q}\left\langle e^{-ik'r'}\left|q\Xi\right|e^{ikr'}\right\rangle = \left(\frac{\hbar}{2NM\omega_{q,n}}\right)^{1/2} \sqrt{n_q}\left\langle \varphi_{k'}\left|q\Xi\right|\varphi_k\right\rangle \qquad \text{Equation 3.43}$$

Among transitions between all initial and final states φ_k and $\varphi_{k'}$ only those satisfy energy conservation are possible to happen. This simply suggests that the electron states denoted by k and k' are actually from the same eigenstate, which means:

$$\left\langle \varphi_{k'}\left|q\Xi\right|\varphi_k\right\rangle = q\Xi \qquad \text{Equation 3.44}$$

For the final simplification, assuming at high temperature so that the phonon distribution function is classic:

$$n_q = \frac{1}{e^{\hbar\omega/k_BT}-1} \approx \frac{k_BT}{\hbar\omega} \qquad \text{Equation 3.45}$$

For longitudinal acoustic phonons with low wave length, $\omega = V_l q$. the total transition rate is given by (under parabolic band assumption):

$$\Gamma_k = \frac{2\pi}{\hbar}\int_V M_{kk'}^2 g(\varepsilon_k) = \frac{2\pi}{\hbar}\Xi^2 \frac{(2m^*)^{3/2}(k_BT)^{1/2}}{2\pi^2\hbar^3}\varepsilon^{1/2}\int_V \frac{\hbar}{2NM\omega}\frac{k_BT}{\hbar\omega}q^2\,dq$$

$$= \frac{(2m^*)^{3/2}\Xi^2(k_BT)^{1/2}}{\pi\hbar^4}\varepsilon^{1/2}\frac{k_BT}{2NM}\int_V \frac{1}{\omega^2}q^2\,dq$$

$$= \frac{2^{1/2}\Xi^2(m^*k_BT)^{3/2}V}{\pi\hbar^4 NMv_l^2}\varepsilon^{1/2}$$

$$= \frac{2^{1/2}\Xi^2(m^*k_BT)^{3/2}}{\pi\hbar^4\rho v_l^2}\varepsilon^{1/2} \qquad \text{Equation 3.46}$$

Thus the relaxation time governed by acoustic phonon scattering is:

$$\tau_{ac}(\varepsilon) = \frac{1}{\Gamma_k} = \frac{\pi\hbar^4\rho v_l^2}{2^{1/2}\Xi^2(m^*k_BT)^{3/2}}\varepsilon^{-1/2} \qquad \text{Equation 3.47}$$

For the non-parabolic Kane band case, by using proper dispersion relation, one could write:

$$\tau_{ac}(\varepsilon) = \frac{\pi\hbar^4 C_l}{2^{1/2}m_b^{*3/2}(k_BT)^{3/2}\Xi^2}\varepsilon^{-1/2}(1+\varepsilon\alpha)^{-1/2}(1+2\varepsilon\alpha)^{-1} \qquad \text{Equation 3.48}$$

In multi-valley semiconductors, the longitudinal elastic constant C_{11} is replaced by the average longitudinal elastic constant[94] C_l:

$$C_l = \frac{3}{5}C_{11} + \frac{2}{5}C_{12} + \frac{4}{5}C_{44}$$ Equation 3.49

The single effective mass is replaced by an inertial effective mass m_I^* and a DOS effective mass of a single valley m_b^*. Ξ (called here the deformation potential coefficient) is a combination of two deformation potential components Ξ_d, Ξ_u defined by energy shifts caused by different strain elements (for details about the definition see ref. 12, 94-96). For small gap systems, a nonparabolic Kane band model is usually more accurate than the single parabolic band model. In lead chalcogenides the Kane model has even been developed to take into account the energy dependence of interaction matrix. Thus Equation 3.48 above are replaced by:

$$\tau_{ac}(\varepsilon) = \frac{\pi\hbar^4 C_l N_V}{2^{1/2} m_d^{*3/2} (k_B T)^{3/2} \Xi^2} (\varepsilon + \varepsilon^2\alpha)^{-1/2} (1 + 2\varepsilon\alpha)^{-1} [1 - \frac{8\alpha(\varepsilon + \varepsilon^2\alpha)}{3(1 + 2\varepsilon\alpha)^2}]^{-1}$$ Equation 3.50

In PbTe and PbSe, the conduction band and the valence band at the L point have almost identical effective mass, but the conduction band is found to have a smaller deformation potential coefficient Ξ than the (light) valence band. Smaller Ξ gives these n type lead chalcogenides similarly high zT as the p type doped materials, where the presence of a highly degenerate secondary valence band plays an essential role for their good thermoelectric properties.

Despite its importance to thermoelectrics, little is known or studied by researchers in this field. Data are only available for a few thermoelectric semiconductors that have broader interests for other fields also. Evaluating the deformation potential for each band of a compound is also very difficult and large discrepancy exists in the experimental result for Ξ_d and Ξ_u, which add another factor to the difficulty of comparing Ξ from mobility data with those from other measurements.

In principle Ξ can be obtained by calculation, as explained by Bir and Pikus. The deformation potential component Ξ_u can also be obtained from the piezoresistence tensors[95] of intrinsic samples. Consistency is poor among reports from different groups. For n type Ge and Si, Ξ_u is found[94, 95, 97] to be between16 to 19 eV, and 7 to 10 eV, respectively. For PbTe this number is[12, 96] between 2 to 4 eV for the conduction band and 4 to 8 eV for the valence band. Based on the available literature, there is no reliable experimental result on Ξ_d. For lead chalcogenides there is even discrepancy on whether the value is larger (from mobility data) or smaller (from calculation) than the magnitude of Ξ_u.

The deformation potential under hydrostatic pressure ($3\Xi_d + \Xi_u$), especially the difference between the conduction and valence band, is more commonly estimated. This is usually called the optical isotropic deformation potential $D_{iso} = (3\Xi_d + \Xi_u)_c - (3\Xi_d + \Xi_u)_v$.

Bardeen and Shockley suggested[91] several methods to determine D_{iso} of Si and Ge based on the change of band gap with temperature or pressure. Ferreira compared[96] D_{iso} of PbTe estimated from the temperature and pressure dependence of the band gap with that determined from APW calculation. D_{iso} varies only between 10 and 15 eV among these methods. Zasavitskii obtained[98] a similar result of 10 eV from magneto-optical absorption data. In his work D_{iso} for PbSe was also determined to be 14 eV, while Wu's optical spectroscopy result[99] on quantum well structure of PbSe was 17 eV (more comparison is given by Zasavitskii in his paper). But still, these numbers are quite different from the results we get from the mobility of n type and p type PbSe (~10 eV) and PbTe (~5 eV).

Besides the difficulty in measurements, another factor contributing to the poor consistency between deformation potential values from mobility data and other methods lies in the basic assumption that acoustic phonon scattering is the only (predominant) carrier scattering mechanism. We will show later when discussing other phonon scattering mechanisms, how this assumption adjust itself under the presence of other phonon scattering mechanisms.

It is more convenient to give the conclusion of this discussion first, that is: the best way to determine the deformation potential coefficient Ξ in the expression of quality factor is by fitting the mobility data from several samples with n_H close to the optimum range. In this way, the result is actually a combined effective value taking into account the most studied deformation potential scattering from acoustic phonons (correspondingly Ξ_{ac}), the deformation potential scattering from optical phonons whose magnitude is characterized by Ξ_{op}, the short-range potential scattering from the dopant impurities (discussed in Chapter 5), and additionally the inter-valley scattering for complex band structures when allowed.

In the table below we list the Ξ data estimated from mobility for a few systems that are, or can be, approximated as, single band systems with relevant data available. Due to the lack of systematic study some of the values are rough estimations at best, and caution is needed when using these results.

Table 3.3. Deformation potential coefficient, together with other material parameters for some compound semiconductors at 300 K.

	$\mu_0 m_d^{*3/2}$ (cm^2/Vs)	Ξ (eV)	m_d* (m_e)	m_l* (m_e)	N_v	$C_l \times 10^{-10}$ (Pa)	ΔX	Coordination number
PbSe(n)	160	25	0.27	0.1	4	9.1	0.22	6
PbSe(p)	110	35	0.27	0.1	4			
PbTe(n)	200	22	0.26	0.1	4	7.1	0.23	6
PbTe(p)	100	25	0.26	0.1	4			
PbS(n)	160	27	0.41	0.16	4	11.1	0.25	6
Diamond (n)	5370	9	1.84	0.46	6	115.7		4
Si(n)	1700	8	1.1	0.27	6	18		4
Ge(n)	1900	10	0.55	0.12	4	16		4
Bi_2Te_3 (n)	400	24	0.9 (0.35//a)		6	7.1	0.08	6
Bi_2Te_3 (p)	600	24	0.8 (0.35//a)		6			
CoSb3(n)		10	3.3	0.52	3	10	0.17	
$CoSb_3$ (p)	75	33	0.07	0.07	1	10	0.17	
$Bi_{0.9}Sb_{0.1}$ (n)	400	18	0.17		3	6.3	0.03	6
La_3Te_4 (n)	5	29	0.62	0.39	2	5	1	6 (8)
Bi_2Se_3 (n)	42	20	0.15 (//a)		1		0.53	6
InSb(n)	95	33	0.011		1	8.2	0.27	4
InP (n)	114	21	0.077		1	12	0.41	4
GaSb(n)	50	>30	0.04		1	10.4	0.24	4
GaAs(n)	160	25	0.067		1	14.1	0.37	4
GaN(n)	50	25	0.2		1	36.3	1.23	4
ZnSe(n)	38	18	0.16		1	10.7	0.9	4
CdTe(n)	30	25	0.09		1	7	0.41	4

Is the deformation potential coefficient Ξ, phenomenologically related to any other material parameters? The present data are too scattered to show a reliable trend. But it seems systems with light effective masses tend to have larger Ξ, while systems with heavy effective masses often find Ξ small (Figure 3.26). But more often the band structures of these materials are either not well known, or are more complicated than a single parabolic band used for analysis, raising the question of how accurate the reported Ξ are, especially when they are calculated by different groups.

Figure 3.26 b suggests that $1/\Xi^2$ for many semiconductors are roughly in the same range, but what makes good thermoelectrics stand out is the large N_v whereas compounds with N_v = 1 are often found at the bottom of the weighed mobility (which is related to B) plot.

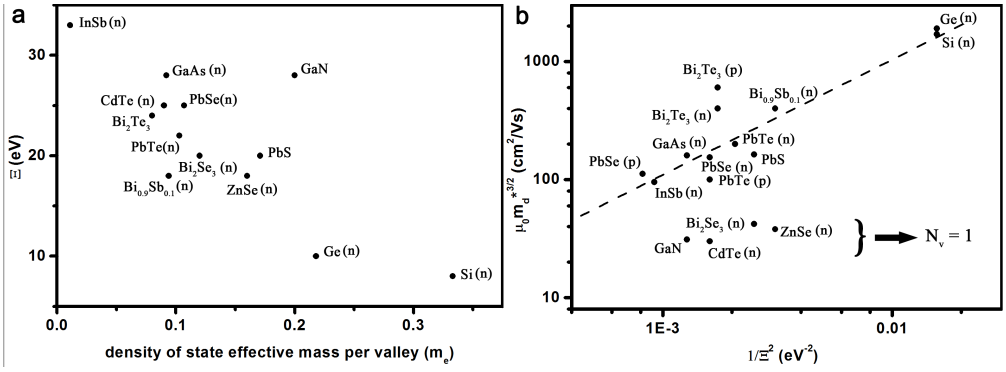

Figure 3.26. Deformation potential Ξ plotted against a) DOS effective mass per valley, and b) weighed mobility for some compound.

3.7 Other Carrier Scattering Mechanisms

3.7.1 Ionized Impurity Scattering

Ionized impurity scattering is important[100] in understanding the mobility of doped silicon. The Debye temperature of silicon is 645 K and the temperature of interest for most silicon based semiconductor devices is around room temperature, meaning the scattering from phonons is still relatively weak. The doping level of silicon rarely exceeds 10^{14} cm^{-3} thus the screening is also weak, both making the scattering from ionized impurities important.

The interaction Hamiltonian for ionized impurity scattering it purely columbic:

$$H'_{ii} = \frac{Ze^2}{4\pi\varepsilon_0 r} e^{-qr} \qquad \text{Equation 3.51}$$

With Z the effective charge, ε_0 the static dielectric constant, and q the screening parameter. The interaction matrix element for electron with wave vector k into that with k' is given by:

$$\langle k' | H'_{ii} | k \rangle = \int \varphi^*_{k'} H'_{ii} \varphi_k \, dr = \int e^{i(k-k')r} \frac{Ze^2}{4\pi\varepsilon_0 r} e^{-qr} \, dr = \frac{Ze^2}{\varepsilon_0} \frac{1}{|k-k'|^2 + q^2} \qquad \text{Equation 3.52}$$

The ionized impurity scattering is of elastic nature so $|k-k'|^2=2k^2(1-\cos\theta)$, θ being the scattering angle. The corresponding transition rate is the square of the matrix element, and the total transition rate can be obtained by integrating over all possible k' states:

$$\Gamma_k = \frac{2\pi}{\hbar} g(\varepsilon) \int_{k'} \left| \langle k' | H'_{ii} | k \rangle \right|^2 dk' = \frac{2m^* Z^2 e^4 k}{\pi \varepsilon_0^2 \hbar^3} \int_0^1 \left(\frac{1}{2k^2(1-x)+q^2} \right)^2 (1-x)\,dx$$

$$= \frac{2m^* Z^2 e^4 k}{\pi \varepsilon_0^2 \hbar^3} \frac{1}{4k^4} \left(\ln(1+b) - \frac{b}{1+b} \right) = \frac{Z^2 e^4 \varepsilon^{-3/2}}{4\sqrt{2}\pi \varepsilon_0^2 m^{*1/2} (k_B T)^{3/2}} \left(\ln(1+b) - \frac{b}{1+b} \right) \qquad \text{Equation 3.53}$$

ε is the reduced energy of carriers and b is given by:

$$b = \frac{2k^2}{q^2} = \frac{4\varepsilon_0 m^* (k_B T)^2 \varepsilon}{n e^2 \hbar^2} \frac{F_{1/2}(\eta)}{F_{-1/2}(\eta)} = \frac{2^{3/2} \pi^2 \varepsilon_0 \hbar (k_B T)^{1/2}}{m^{*1/2} e^2} \frac{\varepsilon}{F_{-1/2}(\eta)} \qquad \text{Equation 3.54}$$

When there are N impurities in a unit volume, the relaxation time can be written as (slightly different expressions are also seen[12, 93]):

$$\tau_{ii}(\varepsilon) = \frac{4\sqrt{2}\pi \varepsilon_0^2 m^{*1/2} (k_B T)^{3/2}}{N_{ii} Z^2 e^4} \varepsilon^{3/2} \left(\ln(1+b) - \frac{b}{1+b} \right)^{-1} \qquad \text{Equation 3.55}$$

According toEquation 3.55 the relaxation time for ionized impurity scattering increases with both temperature and carrier density.

In Kane band model, replacing the proper dispersion relation we can easily get the relaxation time:

$$\tau_{ii}(\varepsilon) = \frac{4\sqrt{2}\pi \varepsilon_0^2 m^{*1/2} (k_B T)^{3/2}}{N_{ii} Z^2 e^4} \varepsilon^{3/2} (1+\varepsilon\alpha)^{3/2} (1+2\varepsilon\alpha)^{-1} \left(\ln(1+b) - \frac{b}{1+b} \right)^{-1} \qquad \text{Equation 3.56}$$

Note for Equation 3.55 and Equation 3.56, since physicists are not very strict about pre-factors and there maybe over counting during different derivations, other similar expressions of relaxation time with different pre-factors are seen, see for example in ref.101.

All quantities in the expression of $\tau_{ii}(\varepsilon)$ are independently measurable, so its magnitude can be pretty much expected for different compounds. In Pb chalcogenides, due to their large static dielectric constants $\tau_{ii}(\varepsilon)$ is usually found on the order of 10^{-12} S at 300 K, one or two orders of magnitude longer than that from acoustic phonon scattering. For common semiconductors with ε_0 around 10 to 20, $\tau_{ii}(\varepsilon)$ could be quite comparable with those from other scattering mechanisms.

3.7.2 Neutral Impurity Scattering

Another scattering mechanism due to impurities is called neutral impurities scattering, which means the scattering at low temperatures by impurities that are not ionized yet. A simple picture of the scattering center is an extra electron (or hole) bound to the vicinity of an impurity that is immersed in a sea of uniformly distributed carriers. This picture leads to the common treatment of a neutral impurity as if it were a hydrogen atom in a medium with carrier effective mass m^* and dielectric constant ε_0. Erginsoy gave[102] the relaxation time for neutral impurity scattering in 1950 as:

$$\tau_{ni} = \frac{m^{*2} e^2}{20\hbar\varepsilon_0 N_{ni}} \qquad \text{Equation 3.57}$$

According to Erginsoy, scattering by neutral impurity is independent of either temperature or carrier energy. So τ_{ni} should be larger than the effective τ of conducting carriers unless at very low temperatures, otherwise the mobility will saturate as the temperature decreases which is not seen in most real semiconductors. However, using typical material parameters $m^* = 1\ m_e$, $\varepsilon_0 = 20\ \varepsilon_{vacuum}$ and $N_{ni} = 10^{18}\ cm^{-3}$, τ_{ni} is found to be around 5×10^{-12} s. This value is actually comparable with a typical relaxation time of carriers seen in semiconductors at room temperature (and is shorter if at low temperatures). The argument is that despite of this, since the transport parameters depend on the integration of τ over energy, and since τ_{ni} is simply energy independent its final contribution is largely weakened when weighed and integrated by energy. Similar argument could also apply to the ionized impurity scattering case where $\tau_{ii}(\varepsilon)$ has a positive dependence on energy.

In other studies, it has been suggested[103] that the pre-factor of 20 in Equation 3.57 is probably an overestimate. Indeed according to McGill, the relaxation time given by Equation 3.57 could be underestimated by a factor of 20 in certain cases.

There has been no evidence showing the neutral impurity scattering is of any importance for thermoelectrics used either above room temperature or below it.

3.7.3 Deformation Potential Scattering from Optical Phonons

Besides the most stressed and studied acoustic phonon scattering, in systems with more than one atom per unit cell there are also optical phonons. For complex structures, where many good thermoelectric materials are found, optical phonon branches are prevalent. Optical phonons interact

with charge carriers in two ways: one is the deformation potential scattering from optical phonons that is analogous to that of acoustic phonons, the other is the polar scattering seen in polar semiconductors which is from the electrostatic force due to the opposite phase of oscillation between the neighboring differently charged lattice ions. Such scattering mechanism is believed important[104] in III-V and II-VI semiconductors.

The derivation of the interaction matrix element and thus transition rate for the deformation potential scattering from optical phonons is largely similar[105] to that for acoustic phonons, a few important differences are:

First, instead of have the deformation potential theorem in the form of Equation 3.36, the interaction Hamiltonian could be written as:

$$H_{e-op} = \Xi_{op}\left(\frac{\pi}{a}\right)\vec{g}u_n(r) \qquad \text{Equation 3.58}$$

g being a reciprocal lattice vector. Applying the displacement operator u_n(r) in Equation 3.37 we get instead of Equation 3.39 for acoustic phonon scattering case, the following equation:

$$H_{e-op} = \frac{\pi}{a}\Xi_{op}\left(\frac{\hbar}{2NMw_{q,n}}\right)^{1/2}\sum_q \vec{g}\cdot\overrightarrow{e_{q,n}}(a_{q,n}e^{iqr} - a^*_{q,n}e^{-iqr}) \qquad \text{Equation 3.59}$$

Without the dot product p•e as in Equation 3.39, it means the interaction with optical phonons is present for both the longitudinal and transverse mode. The dot product of g•e will simply yield[93] unity.

Follow exactly the same derivation for $M_{kk'}$, assuming high temperature $k_BT >> \hbar\omega$, we come to:

$$\Gamma_k = \frac{2\pi}{\hbar}\int_V M^2_{kk'}g(\varepsilon_k) = \frac{2\pi}{\hbar}\Xi^2_{op}\frac{(2m^*)^{3/2}(k_BT)^{1/2}}{2\pi^2\hbar^3}\varepsilon^{1/2}\int_V \frac{\hbar}{2NM\omega}\frac{k_BT}{\hbar\omega}dq$$

$$= \frac{(2m^*)^{3/2}\Xi^2(k_BT)^{1/2}}{\pi\hbar^4}\varepsilon^{1/2}\frac{k_BTV}{2NM\omega^2} \qquad \text{Equation 3.60}$$

Instead of having the acoustic phonon dispersion $\omega = v_l^2 q$, the optical phonon dispersion is neglected at q = 0 so $\omega = \omega_0$, this gives us:

$$\tau_{odp}(\varepsilon) = \frac{1}{\Gamma_k} = \frac{\hbar^4\rho a^2\omega_0^2}{2^{1/2}\pi\Xi^2_{op}(m^*k_BT)^{3/2}}\varepsilon^{-1/2} = \frac{\hbar^2\rho a^2(k_B\Theta)^2}{2^{1/2}\pi\Xi^2_{op}(m^*k_BT)^{3/2}}\varepsilon^{-1/2} \qquad \text{Equation 3.61}$$

at high temperatures.

In Kane band model with energy dependent interaction matrix[105, 106]:

$$\tau_{odp}(\varepsilon) = \frac{2\hbar^2 a^2 \rho (k_B\Theta)^2}{\pi (2m_b^* k_B T)^{3/2} \Xi_{op}^2} (\varepsilon + \alpha\varepsilon^2)^{-1/2} (1+2\alpha\varepsilon)^{-1} [1 - \frac{8\alpha(\varepsilon+\alpha\varepsilon^2)}{3(1+2\alpha\varepsilon)^2}]^{-1} \quad \text{Equation 3.62}$$

Equation 3.62 can be transformed into a form analogous to that for τ_{ac} with the same level of detail only by replacing Ξ with $\Xi_{op}\left(\frac{\pi\hbar}{\alpha k_B\Theta}\right)\left(\frac{C_l}{\rho}\right)^{1/2}$, See Equation 3.64.

At low temperatures, instead of simplification made on phonon population during the derivation of $M_{kk'}$, one comes to a general form given by Seeger[95] (similarly by Askerov[105]) for momentum relaxation time τ_{odp} for a single parabolic, isotropic band:

$$\tau_{odp}(\varepsilon) = \frac{2^{1/2}\pi\rho\hbar^2 k_B\Theta}{m^{*3/2}(k_B T)^{1/2}\Xi_{op}^2} [\exp(\Theta/T)-1][(\varepsilon+\Theta/T)^{1/2} + \exp(\Theta/T)\,\mathrm{Re}\{(\varepsilon-\Theta/T)^{1/2}\}]^{-1} \quad \text{Equation 3.63}$$

where ρ, Θ, and Ξ_{op} are the density, optical phonon Debye temperature and deformation potential for optical phonon scattering (Seeger's format does not contain π/α, thus the unit for Ξ_{op} in his equation is eV/cm), respectively. The terms $(\varepsilon + \Theta/T)^{1/2}$ and $(\varepsilon - \Theta/T)^{1/2}$ represent the absorption and emission of a optical phonon, respectively, and the real part of the latter one is taken since emitting a phonon with energy higher than the electron is prohibited.

There are few reports on the value of deformation potential for optical phonons. For n type Ge Jacoboni[107] suggested this value to be 5.5×10^8 eV/cm, which is equivalent to 3.3 eV when rewriting Equation (19) in an analogous form of Equation (16), comparing with 16 to 19 eV for Ξ_{ac} from acoustic phonon scattering in this material. Deformation potential scattering from optical phonons is negligible in n type Si[108]. For III-V compounds Takeda[109] gives Ξ_{op} around 1.4×10^{10} eV/cm for GaAs and InP, which is considerably larger than the value in n type Ge.

Wiley[110, 111] and Costato[112] have formulated Ξ_{op} in terms of material parameters and compared the calculated results with p-type IV or III-V semiconductors. However, in these materials the conduction behavior has multiple-band character, making the reported results phenomenological instead of reflecting the nature of electron-phonon interaction in a given band.

Using an effective deformation potential coefficient Ξ_{eff} in Equation 3.47, the influence of deformation potential from optical phonons will be also included (Equation 3.64):

$$\tau_{eff}^{-1} = \tau_{ac,0}^{-1}\tau^{-1}(\varepsilon) + \tau_{odp,0}^{-1}\tau^{-1}(\varepsilon)$$
$$= \frac{2^{1/2}(m_b^* k_B T)^{3/2}\Xi_{ac}^2}{\pi\hbar^4 C_l}\tau^{-1}(\varepsilon) + \frac{2^{1/2}\pi(m_b^* k_B T)^{3/2}\Xi_{op}^2}{\alpha^2\hbar^2\rho(k_B\Theta)^2}\tau^{-1}(\varepsilon)$$
$$= \frac{2^{1/2}(m_b^* k_B T)^{3/2}\Xi_{ac}^2}{\pi\hbar^4 C_l}\left[\Xi_{ac}^2 + \Xi_{op}^2\left(\frac{\pi^2\hbar^2 C_l}{\alpha\rho(k_B\Theta)^2}\right)\right]\tau^{-1}(\varepsilon) \qquad \text{Equation 3.64}$$
$$= \frac{2^{1/2}(m_b^* k_B T)^{3/2}}{\pi\hbar^4 C_l}\Xi_{eff}^2(\varepsilon+\alpha\varepsilon^2)^{1/2}(1+2\alpha\varepsilon)^1[1-\frac{8\alpha(\varepsilon+\alpha\varepsilon^2)}{3(1+2\alpha\varepsilon)^2}],\ \Xi_{eff}^2 = \Xi_{ac}^2 + \Xi_{op}^2(\frac{\pi^2\hbar^2 C_l}{a\rho(k_B\Theta)^2})$$

3.7.4 Inter-valley/Inter-band Scattering

Depending on the position in *k* space of the initial and final states the scattering of carriers between them could have different nature. When two bands are located at the same *k* point, such as is the case in Mg_2X (X: Si, Ge, Sn), the scattering requires little change in electron wave vector, and thus, is of similar nature as intra-band scattering by acoustic phonons. Such inter-band scattering is accounted for in the framework of isotropic, parabolic band by Fedorov et al.[113, 114] in a form analogous to intra-band scattering:

$$\tau_{ac,1} = \frac{\pi\hbar^4 C_{11}}{2^{1/2}m_1^{*3/2}(k_B T)^{3/2}\Xi_1^2}\varepsilon^{-1/2} \text{ when } \varepsilon < \Delta E$$
$$[(\frac{\pi\hbar^4 C_{11}}{2^{1/2}m_1^{*3/2}(k_B T)^{3/2}\Xi_1^2}\varepsilon^{-1/2})^{-1} + (\frac{\pi\hbar^4 C_{11}}{2^{1/2}m_2^{*3/2}(k_B T)^{3/2}D^2}(\varepsilon-\Delta E)^{-1/2})^{-1}]^{-1} \text{ when } \varepsilon > \Delta E \qquad \text{Equation 3.65}$$

$$\tau_{ac,2} = [(\frac{\pi\hbar^4 C_{11}}{2^{1/2}m_2^{*3/2}(k_B T)^{3/2}\Xi_2^2}(\varepsilon-\Delta E)^{-1/2})^{-1} + (\frac{\pi\hbar^4 C_{11}}{2^{1/2}m_1^{*3/2}(k_B T)^{3/2}D^2}\varepsilon^{-1/2})^{-1}]^{-1} \text{ when } \varepsilon > \Delta E \qquad \text{Equation 3.66}$$

$\tau_{ac,1}$ and $\tau_{ac,2}$ represents the relaxation time of carriers in the primary valley "1" and secondary valley "2", separated by a reduced energy of $\Delta\varepsilon$ (relative to the edge of the primary band), each is characterized by an effective mass of m_1^* and m_2^* and an intra-band acoustic phonon scattering deformation potential of Ξ_1 and Ξ_2. The inter-band acoustic phonon scattering deformation potential *D* is the same regardless of the initial/final valley, has the same unit as Ξ.

The second term in Equation 3.65 and Equation 3.66 has the same temperature and energy dependence as Equation 3.47. As long as the inter-band deformation potential *D* is small compared

to Ξ (for example < 30% when $\Delta\varepsilon = 2$), they can be very well approximated using Equation 3.47 with a slightly different Ξ value (Figure 3.27). With smaller $\Delta\varepsilon$ this will be true for even larger D. But still, it is difficult to estimate D for a compound without studying the transport properties closely, thus it might be questionable that such an assumption is generally valid. Fedorov estimated this inter-band scattering in $Mg_2Si_{1-x}Sn_x$ alloys and found that up to 400 K the rate of inter-band scattering is on the order of 10^{-3} of that of intra-band scattering, indicating the above assumption should hold for most cases. Fedorov's reasoning is somehow flawed in that it first assumed no inter-band scattering and then attribute the unmatched part between modeling and experiment to inter-band scattering. So instead of proving the inter-band scattering is weak, Fedorov's argument actually proved with a real case that systems with intra- and inter-band scattering can be approximated with model that takes into account only the first process, given Ξ allowed to adjust to fit experimental data.

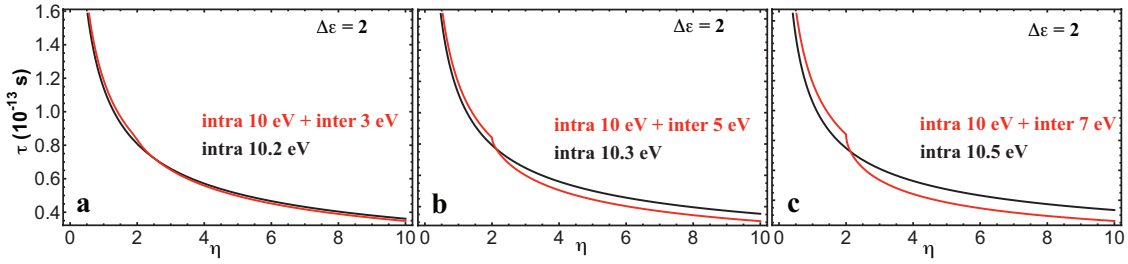

Figure 3.27. The relaxation time of the primary band in a two-band system ($\Delta\varepsilon = 2$), modeled with and without inter-band scattering. Parameter used are: $m^* = 0.5\ m_e$, $C_l = 91$ GPa.

Another case is for the scattering of carriers between equivalent valleys when the band extreme is not located at the center of first Brillion zone. In this case a large change of the carrier's k vector is needed and the scattering process thus resembles that of the optical phonon scattering and is inelastic in nature[53, 108]. Herring studied[115] the transport properties of semiconductors with multi-valley structure and his result has been adopted by most of relevant discussions on this topic. Herring wrote the total relaxation time τ (under isotropic, parabolic band assumption) as:

$$\tau(E) = \left\{ \omega_1 \left(\frac{E}{\hbar\omega}\right)^{1/2} \left(\frac{k_B T}{\hbar\omega}\right) + \omega_2 \left[\frac{\left(\frac{E}{\hbar\omega}+1\right)^{1/2}}{\exp\left(\frac{\hbar\omega}{k_B T}\right)-1} + \mathrm{Re}\left(\frac{\left(\frac{E}{\hbar\omega}-1\right)^{1/2}}{1-\exp\left(-\frac{\hbar\omega}{k_B T}\right)} \right) \right] \right\}^{-1} \qquad \text{Equation 3.67}$$

The first term represents the intra-valley scattering process. The second term further contains two parts that represents the inter-valley phonon absorption and emission, respectively. $\hbar\omega$ is the energy

of phonons that participate the inter-valley scattering (hereinafter called inter-valley phonons). The momentum conservation requires these phonons to have large and (mostly) fixed wave vectors, which means the most contribution comes from high energy optical phonons that can be approximated with a constant energy $\hbar\omega$. Correspondingly there is a characteristic temperature $\Theta_{int} = \hbar\omega/k_B$ which is lower than the optical phonon temperature (or Debye temperature). The factors w_1 and w_2 contains all the parameters that are not explicitly dependent on temperature or carrier energy, and the ratio w_2/w_1 is used to characterize the relative intensity of inter-valley scattering to that of the intra-valley process.

Rewriting Equation 3.67 one get:

$$\tau(\varepsilon) = \left\{ \frac{\omega_1}{(k_B\Theta_{int})^{3/2}} \varepsilon^{1/2}(k_BT)^{3/2} + \omega_2(k_BT)^{1/2}\left[\exp\left(\frac{\Theta_{int}}{T}\right)-1\right]^{-1}\left[(\varepsilon+\Theta_{int}/T)^{1/2} + \exp\left(\frac{\Theta_{int}}{T}\right)\mathrm{Re}((\varepsilon-\Theta_{int}/T)^{1/2})\right]\right\} \qquad \text{Equation 3.68}$$

In this form the second term can be easily recognized as an analog of Equation 3.63 for the deformation potential scattering from optical phonons. The first part shows the same energy and temperature dependence as Equation 3.47 for intra-band deformation potential scattering from acoustic phonons.

With the discussion above and within the context of high temperature ($T > \Theta$) and heavily doped thermoelectrics, the influence of inter-valley scattering, same as the deformation potential scattering from optical phonons, will be included in Equation 3.47 by using an effective deformation potential coefficient Ξ_{eff} (similar to the derivation of Equation 3.64). It can be further anticipated that when the intra-band deformation potential scattering from acoustic phonons is larger than the other two mechanisms, this Ξ_{eff} shouldn't change much from Ξ_{ac} for the intra-band acoustic phonon scattering.

The magnitude of inter-valley transition can be probed by acoustic-electrical (piezoresistence) measurements[95], but convincing studies with comparison to the intra-valley process are very rare. Prediction of w_2/w_1 is otherwise difficult. Nevertheless some important facts regarding the inter-valley process can be drawn from two relatively simple estimates: 1) whether the transition is allowed or forbidden, and 2) the characteristic temperature of the inter-valley phonons, which is comparable to the longitudinal optical phonon temperature or Debye temperature.

According to Fermi's golden rule, when the wave function of the initial and final electron state of a given transition are both odd (or even) functions the interaction matrix vanish and such a transition is forbidden. As an example, the primary conduction/valence band extreme of lead chalcogenides at

the L point is described[116] by the odd/even wave function of L_6^-/L_6^+ so that the inter-valley transition between equivalent L valleys is forbidden (however such restriction is relieved[53] when the nonparabolicity is taken into account and the corresponding states become a mixture of $L_6^-$and L_6^+).

In a general context, a similar story is found in n-type germanium where the transition between conduction band minimums at the L point is found[94, 117-119] to be negligible.

The case of n-type silicon is rather complicated. One widely used result[95, 100, 120, 121] is that inter-valley scattering is important and $w_2/w_1 = 2$. The direct support of such a claim is from the observed[108, 117, 120, 122, 123] (drift) mobility $\mu \sim T^{-2.5}$ in high purity n type Si while the acoustic phonon scattering should only give a $T^{-1.5}$ dependence. Based on Herring's theory, such a difference could be explained by considering inter-valley process with $w_2/w_1 = 2$. However, the original measurements done by Long, Morin, and Ludwig, where this $T^{-2.5}$ relation is observed, were on very lightly doped (with dopant on order of 10^{13} cm^{-3}) Si within the temperature range 30 K to 400 K. Without ruling out the possibility of influence from minority carriers (near room temperature) and the partial ionization of dopants (at low temperature) it may be risky to use the observed temperature dependence as evidence of inter-valley scattering. Additionally, Long and Aubrey concluded that the f type inter-valley scattering rate is two times that of the intra-valley scattering, which forms the main contribution for inter-valley scattering. These authors however also admitted that the characteristic temperature of inter-valley phonons for this f type scattering is around 700 K, yet it is unexplained why the temperature dependence of mobility would change significantly even below room temperature when most of inter-valley phonon states are not populated. On the other hand, the mobilities found in Si with carrier density equal[124] to or above[125] 10^{17} cm^{-3} at room temperature and above actually have the $T^{-1.5}$ ($T^{-1.3}$) dependence, which is just as expected from intra-valley deformation potential scattering processes.

Several more recent studies[107, 126-129] have calculated the inter-valley deformation potential of n type Si and the results vary from 2 to 7 × 10^8 eV/cm. If the pre-factors in Equation 3.63 are rewritten into the same form as in Equation 3.47 (See Equation 3.64) so that the values can be directly compared with Ξ_{ac}, these results will be equivalent to 1.3 to 4.6 eV, whereas the intra-valley acoustic phonon deformation potential is suggested[94, 107, 125, 130, 131] to be 7 to 9 eV (correspondingly the ratio w_2/w_1 would be between 0.1 to 0.7, instead of 2). Such result indicates the inter-valley scattering is important, but not dominant. In fact, assuming the "actual" inter-valley deformation potential is 6 × 10^8 eV/cm and the intra-valley acoustic phonon deformation potential is 8 eV, then for degenerate

samples the total relaxation time will still be well described using Equation 3.47 with an effective deformation potential $\Xi_{eff} = 9$ eV.

In the more specific case of thermoelectric SiGe alloys, extensive modeling work[125, 130-132] has been able to excellently explain the observed transport properties of heavily doped SiGe alloys, without taking into account inter-valley scattering, and the deformation potentials Ξ used in these modeling are in good agreement with measured values. This is another indication that the scattering from inter-valley and optical process is not comparable with the intra-valley acoustic process. Through first principle calculation, Murphy-Armando predicted[133] that for SiGe alloys with Si content up to 50% the former two processes combined only contribute to 1% of the total mobility at 300 K.

3.7.5 Polar Scattering from Optical Phonons

This is more relevant to the content of Chapter 6 and thus will be discussed in detail in Section 6.4.

3.7.6 Alloy Scattering

This will be discussed in Chapter 7, Section 7.4.

Chapter 4

P-type PbSe with Na doping

4.1 Introduction

The valence bands of PbSe include a primary band at L point and a secondary band along the Σ line. Different from common semiconductors like silicon, the band gap of Pb chalcogenides increases with temperature when the primary bands at L (L band) separate from each other. This brings the secondary band (Σ band) close to the edge of the L band. The rate of band gap increasing with temperature was historically determined to be 4 meV per K for PbTe, PbSe and PbS from optical absorption measurements. It has been known that the two valences bands tend to converge at high temperature. This feature makes the p-type PbSe a very promising compound even more interesting than the n-type so that this was the first study carried out for this thesis research. The highest *zT* found was 1.2 and published on Advanced Materials 2011. It was later realized that the resistivity measurement in this study was misrepresented because the thermal couple has measured the temperature of a wrong spot with a higher temperature than the sample. So the *zT* of 1.2, although reproduced by other researchers, is most likely overestimated and the *zT* of p-type PbSe is actually lower (0.9 at 850 K) than the n-type. Transport analysis using a multi-band model revealed the parameters for the L valence band: m_d^* = 0.27 m_e and Ξ = 35 eV. Σ band parameter is difficult to determine accurately and we provide a possible combination of m_d^* = 4.2 and Ξ = 28 eV. The quality factor of each band is also evaluated. The value of p-type PbSe lies in the knowledge we learn from understanding its transport behavior, and applying it to eventually achieve a *zT* that is remarkably higher.

4.2 Sample Synthesis and Transport Properties

PbSe is p-type when there is extra Te in the lattice. Adding acceptors such as Na or Ag could make it heavily doped. Na is a very effective dopant that is relatively convenient to use and most importantly, is capable of bringing the carrier density high enough so the chemical potential reaches the optimum value. The carrier density seems to continue increase up to 2% of Na addition, but a recent study by our collaborators has shown that the solubility of Na in PbTe does not exceed 1.2% and in PbSe is probably lower or similar. Supersaturated Na raises serious concern about long-term stability of heavily doped p-type Pb chalcogenides. Na doping is also sensitive on synthesis as described in Chapter 2, even the final disk samples could change in properties like resistivity and mobility significantly during tests under dynamic vacuum. The p-type samples are also weaker in mechanical strength compared with the n-type ones. Despite all of these, Na doping allows us to probe the interesting science in heavily doped p-type PbSe.

The synthesis involves melting at 1400 K for 6 hours. This was done in a “Carbolite” box furnace. It was found convenient to prepare a large ingot of stoichiometric PbSe first and then mixing it with proper amount of Na and Te in order to get high quality samples. It is also convenient to prepare a large ingot of heavily doped PbSe with for example 2% Na and then make samples with designed carrier density by mixing it with stoichiometric PbSe according to certain weight ratio. Other parts of the synthesis are routinely performed as described in Chapter 2. Obtained disk samples are dense (>98% theoretical density) and mechanically strong enough to perform all necessary measurements. Table 4.1 lists the nominal composition of samples and their room temperature properties.

The doping efficiency of Na is close to 100 % (Figure 4.1), at higher Na content > 1% the density of carriers are fewer than calculated using concentration of Na atom assuming each of them donate one free hole, possibly due to loss of Na to the reaction with quartz during synthesis.

Most doped samples show typical degenerate behavior in resistivity, mobility and Seebeck coefficient. The lightly doped samples show clear onset of bipolar excitation. Figure 4.2 shows the transport properties of Na doped PbSe as functions of temperature. The resistivity decreases with increasing carrier density at high temperature, whereas near room temperature it is found increased again for the two most heavily doped samples. This could be associated with the less-than-100% doping efficiency found in these samples, which caused impurities on grain boundaries.

Table 4.1. A list of Na doped PbSe samples and some transport properties at 300 K.

Label	Composition	Transport Properties		
		$n_H(10^{19}cm^{-3})$	S (μV/K)	μ_H (cm^2/Vs)
1E18	PbSe	0.12	281	803
6E18	$Pb_{1.002}Se_1$	0.06	306	947
	$Na_{0.001}Pb_{0.999}Se$		140	
1E19	$Na_{0.0025}Pb_{0.9975}Se$	1.4	81.7	517
3E19	$Na_{0.0035}Pb_{0.9965}Se$	3.3	57.6	322
6E19	$Na_{0.005}Pb_{0.995}Se$	6.5	43.4	255
9E19	$Na_{0.007}Pb_{0.993}Se$	9.1	35.4	209
1.2E2	$Na_{0.015}Pb_{0.985}Se$	11.6	22.7	163
1.5E2	$Na_{0.0125}Pb_{0.9875}Se$	14.6	17.3	142
1.7E2	$Na_{0.0125}Pb_{0.9875}Se$	16,7	20	115
2.5E2	$Na_{0.025}Pb_{0.975}Se$	25.6	20.8	71

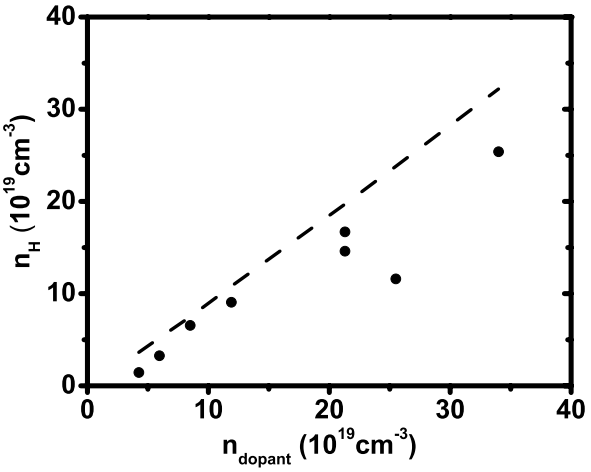

Figure 4.1. Hole concentration versus dopant concentration for Na doped PbSe, dashed line calculated using single Kane band model.

The Seebeck coefficients show typical behavior of degenerate semiconductors and increase with temperature for all doped samples, in agreement with data reported[77] by Alekseeva et al. A rough estimate[134] of band gap E_g was obtained using $E_g = 2eT_{max}S_{max}$ for lightly doped samples that showed a maximum in Seebeck coefficient, where S_{max} and T_{max} represents the maximum of Seebeck coefficient and the temperature at which this value is achieved. Such rough estimate is actually subject to a few factors such as the doping level, and the ratio of the conductivity of majority and minority carriers. Nonetheless, for p-type PbSe this yielded band gaps of 0.33 eV at 630 K (from

6E18), 0.37 eV at 740 K (1E19) and > 0.43 eV at 850 K (3E19), qualitatively consistent with the optical measurement result.

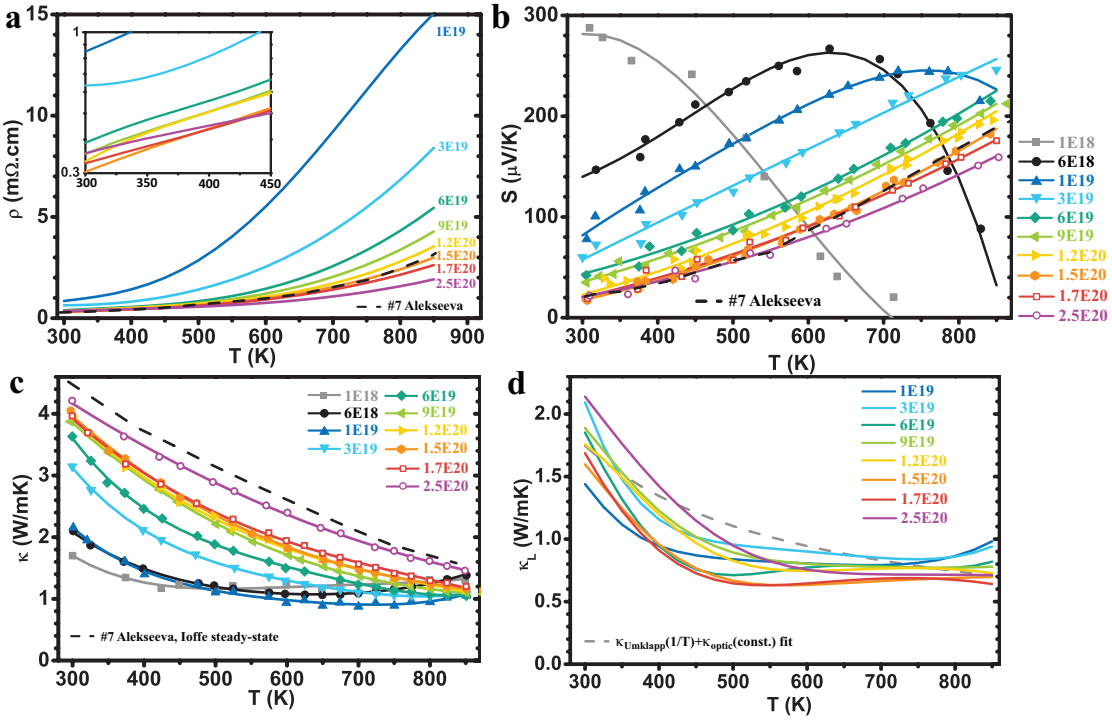

Figure 4.2. Transport properties a) resistivity, b) Seebeck coefficient, c) thermal conductivity, and d) calculated lattice thermal conductivity of Na doped PbSe as function of temperature.

In some compounds the band gap can be also estimated with the resistivity data from an intrinsic sample based on relation between lnρ and 1/T. In Figure 4.3 this is also plotted for the undoped sample "1E18", the linear part of the plot was fitted with activation energy of 0.17 eV. For intrinsic semiconductors take the acoustic phonon scattering assumption with some simplification, one gets the expression for conductivity:

$$\sigma = \sigma_e + \sigma_h = e\left(n_e\mu_e + n_h\mu_h\right)$$

$$\propto \left((m_e^* k_B T)^{3/2} \exp\left(\frac{E_f - E_C}{k_B T}\right)\left(\frac{1}{m_e^{*5/2}(k_B T)^{3/2}}\right) + (m_h^* k_B T)^{3/2} \exp\left(\frac{E_V - E_f}{k_B T}\right)\left(\frac{1}{m_h^{*5/2}(k_B T)^{3/2}}\right)\right)$$

$$\approx \left(\frac{1}{m_e^*} + \frac{1}{m_h^*}\right)\exp\left(\frac{E_g}{2k_B T}\right)$$

$$\approx \left(\frac{1}{m_e^*}+\frac{1}{m_h^*}\right)\exp\left(\frac{dE_g/dT}{2k_B}\right)\exp\left(\frac{E_{g,0}}{2k_BT}\right) \qquad \text{Equation 4.1}$$

Thus the slope of lnρ-1/T can be used to tell the temperature independent part of E_g. In the case of PbSe, the mobilities of electrons and holes are known to be different and the effective mass being function of temperature too. Nonetheless the activation energy calculated from matches very well with the temperature independent band gap energy of PbSe, which is about 0.17 eV.

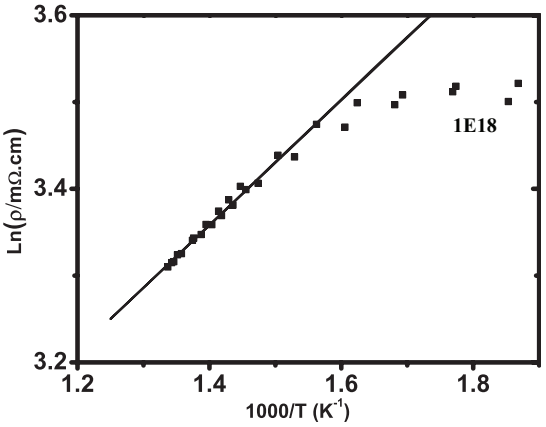

Figure 4.3. Logarithm of resistivity of undoped sample 1E18 versus reciprocal temperature 1000/T, yielding an activation energy 0.17 eV.

Thermal conductivity increases with carrier density at a given temperature and decreases with temperature for each sample, except for the most lightly doped ones where clear bipolar thermal conductivity is seen. Historical result reported by Alekseeva on Na doped PbSe used thermal conductivity measured by steady-state method. The sample (#7) is very similar in resistivity and Seebeck coefficient to the 1.5E20 sample (and the nominal composition is close too). However it is clear that the thermal conductivity of Alekseeva's sample is significantly higher than sample "1.5E20", even at room temperature. We believe the difference seen here is primarily due to operator error when conducting the measurements, whereas the setup they used should be able to give accurate results, as discussed in Chapter 2.

Figure 4.2 d shows the lattice thermal conductivity as function of temperature for all samples. The Lorenz number used to calculate the electronic contribution is from a single Kane band model. Theoretically a more precise multi-band model is required to better account for the electronic contribution, however a simple single Kane band model is still used because a more precise model

substantially increases complicity of calculation while the improved accuracy in result is overshadowed by experimental error. Calculated κ_L varies considerably among different samples. At room temperature the value of κ_L varies from 1.5 W/mK to 2.2 W/mK. The discrepancy should come from the value of L, and more fundamentally, from the simple carrier scattering assumption. This suggests a huge uncertainty if the κ_L is determined from only one doped sample, which is often seen in literatures. The thermal conductivity measured on undoped, high resistive PbSe is 1.7±0.1 W/mK, assuming an Umklapp process T^{-1} dependence, combined with a "background" contribution from optical phonons which is a temperature independent constant[135], the thermal conductivity of PbSe is modeled as the grey dashed curve. At 850 K, κ_L for heavily doped samples (>3E19) are found (0.6 – 0.8 W/mK) very close to the modeled result of 0.7 W/mK.

Figure 4.4 shows the Hall mobility and Hall carrier density as function of all samples. A minimum in n_H (a maximum in A) is seen in the temperature dependent Hall carrier density for each sample. This is an indicator of the onset of two types of carriers contributing to the transport, which in case of heavily doped PbSe means those from the L valence band and Σ valence band. The temperature with minimum n_H correspond to[136] the temperature where the contribution from each type of carrier to conductivity is equal.

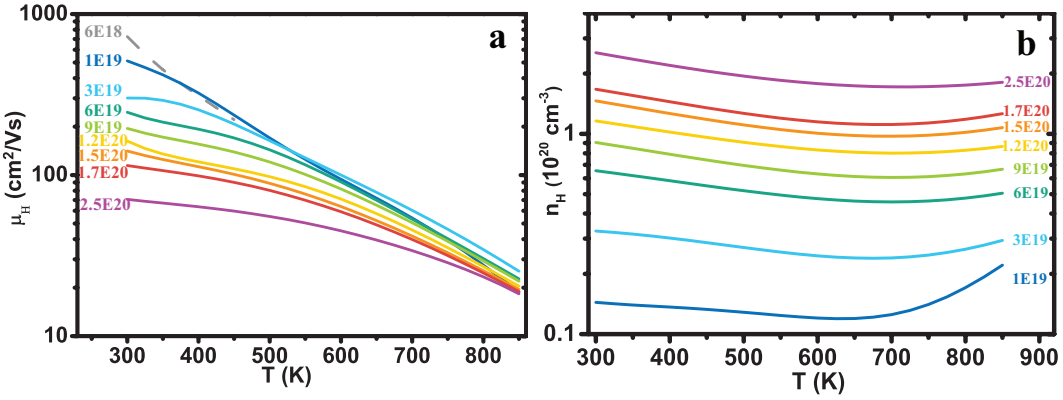

Figure 4.4. a) Hall mobility and b) Hall carrier density as function of temperature for p type PbSe.

The figure of merit zT of p-type PbSe is shown in Figure 4.7. The highest zT reaches 0.9 at 850 K, even with the additional contribution from the Σ band, the zT of p-type PbSe is not as good as the n-type.

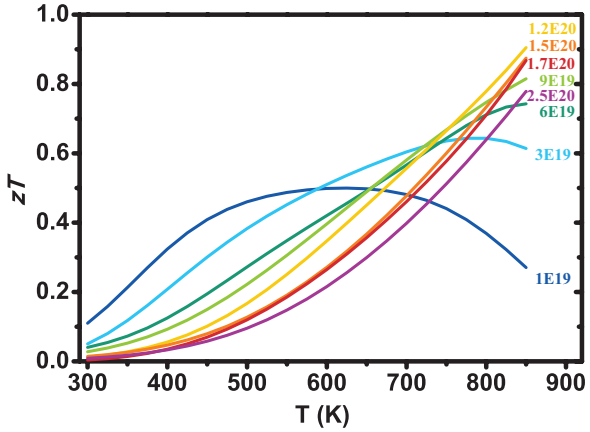

Figure 4.5. *zT* as function of temperature for p-type PbSe.

4.3 Transport Property Modeling

The accurate modeling of the transport properties of p-type PbSe takes into account the contribution from the L valence band, the Σ valence band, as well as the L conduction band. The characteristics of the L conduction band are well determined from the study of n-type samples in Chapter 3. That of the L valence band can be obtained by modeling the transport properties of the lightly doped p-type samples at room temperature with a single Kane band model, when the contribution from Σ band is negligible. Then finally the parameters of the Σ valence band are adjusted to provide the best fit for the transport properties of all p-type samples at all temperatures.

For the scattering mechanisms the modeling takes into account both acoustic phonon scattering and the polar scattering from optical phonons, since the latter is important to explain the transport properties of lightly doped samples near room temperature. Details for the modeling is discussed in Chapter 6.

Figure 4.6 compares the Pisarenko relation and the mobility as function of carrier density of p-type and n-type PbSe at 300 K, literature data[47, 76, 79, 137-141] are also included. Only lightly doped p-type samples are included to prevent the influence from the Σ valence band. The p-type and n-type samples share the same Pisarenko relation, indicating the same density-of-states effective mass m_d^* = 0.27 m_e, and since they have the same degeneracy it is fair to assume the inertial effective mass m_I^* = 0.1 m_e is also the same.

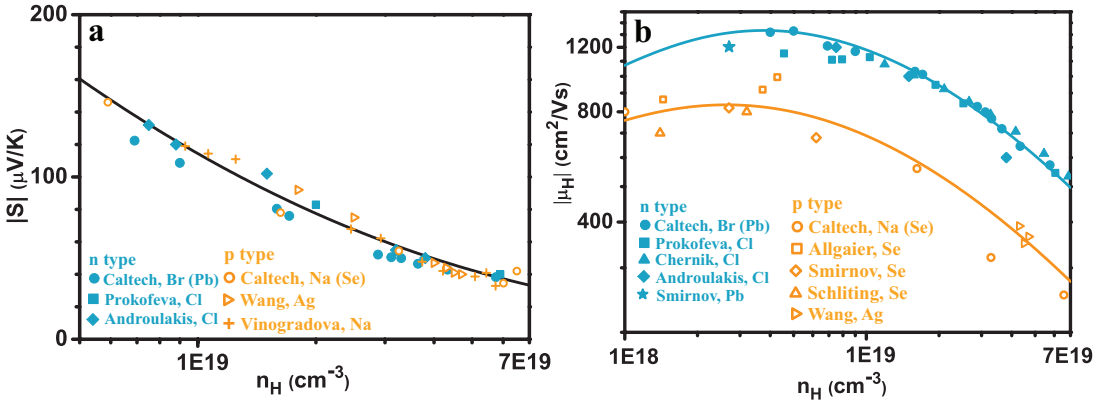

Figure 4.6. a) Seebeck coefficient and b) Hall mobility as function of Hall carrier density for both p-type and n-type PbSe at 300 K. Data from literature are also included.

On the other side it is seen that the mobility of n-type and p-type samples are very different, with the p-types much lower in mobility than the n-types. The same effective masses for both, the elastic constant C_l are further found independent of the type of doping by measuring the speed of sound, which turned out to be identical ($v_l \approx 3200$ m/s, $v_t \approx 1700$ m/s). Thus the difference in mobility indicates a difference in the deformation potential coefficient Ξ, which for the L conduction band was found 25 eV, and for the L valence band it is determined to be 35 eV.

It is necessary to note that the effective mass determination from Seebeck coefficient is subject to a fair amount of uncertainty due to factors such as uncertainty in Seebeck measurement and Hall measurement, as well as the scattering mechanism(s) used. By comparing data from Caltech as well as most of published data on PbSe, as shown in Figure 4.6 a), the majority of results has suggested a same effective mass for the L conduction band and valence band. Bear in mind a possible small difference beyond the resolution of this method, the difference in mobility seen in Figure 4.6 b) could be possibly in part due to such difference as well. However, the difference seen is about a factor of 2 for the acoustic phonon scattering dominated regime, which would require a 30% difference in effective mass to explain and would be certainly detectable in the Pisarenko relation. Thus, it is possible that the conclusion about identical effective masses for the L conduction band and valence band is inaccurate, and the difference in Ξ is not as significant, but the general finding of Ξ being larger in the L valence band than that in the L conduction band should be solid.

So far, it is also known that the bands at L are non-parabolic Kane bands, and the effective mass for the conduction band increases with temperature with $d\ln m^*/d\ln T = 0.5$, this should be the same for

the L valence band. On the temperature dependence of band gap, our most recent study[142] (Figure 4.7) has provided the most accurate estimate of:

$$E_g(eV) = E_{g,0} + 3\times10^{-4}T \qquad \text{Equation 4.2}$$

The zero temperature band gap $E_{g,0}$ is 0.17 eV taken from low temperature measurement results. The Σ valence band is assumed to be parabolic, with effective mass independent of temperature and is isotropic for each valley.

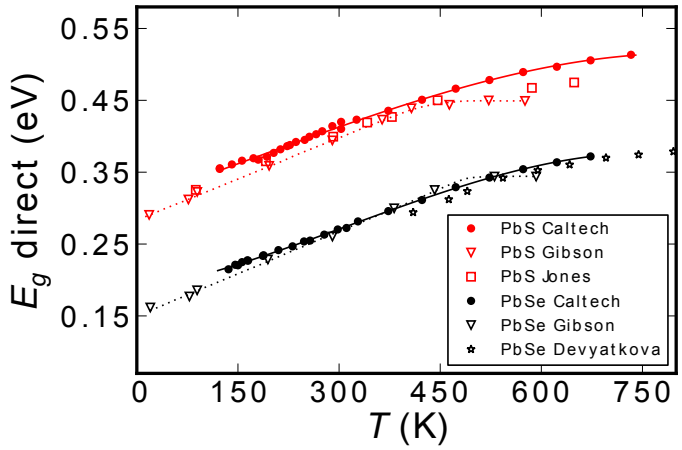

Figure 4.7. Temperature dependent band gap of PbSe and PbS measured at Caltech and re-interpreted from literature. Image taken from Appl. Phys. Lett 103, 262109, 2013.

The expression of transport parameters in a multi-band system given by Putley[143] are used here:

$$n = \sum_{i=Lc,Lv,\Sigma v} n_i \qquad \text{Equation 4.3}$$

$$\sigma = \sum_{i=Lc,Lv,\Sigma v} \sigma_i \qquad \text{Equation 4.4}$$

$$R_H = \sum_{i=Lc,Lv,\Sigma v} R_{H,i}\sigma_i^2 \Big/ \left(\sum_{i=Lc,Lv,\Sigma v} \sigma_i\right) = \sum_{i=Lc,Lv,\Sigma v} eA_i n_i \mu_i^2 \Big/ \left(\sum_{i=Lc,Lv,\Sigma v} n_i\mu_i\right) \qquad \text{Equation 4.5}$$

$$n_H = 1/eR_H \qquad \text{Equation 4.6}$$

$$\mu_H = \sigma / en_H = \sigma R_H = \sum_{i=Lc,Lv,\Sigma v} e^2 A_i n_i \mu_i^2 \qquad \text{Equation 4.7}$$

$$S = \sum_{i=Lc,Lv,\Sigma v} S_i\sigma_i \Big/ \sum_{i=Lc,Lv,\Sigma v} \sigma_i \qquad \text{Equation 4.8}$$

$$\kappa = \kappa_L + \sum_{i=Lc,Lv,\Sigma v} L_i \sigma_i T + T\left[\sum_{i=Lc,Lv,\Sigma v} S_i^2 \sigma_i - \left(\sum_{i=Lc,Lv,\Sigma v} S_i \sigma_i\right)^2 \Big/ \sum_{i=Lc,Lv,\Sigma v} \sigma_i\right] \quad \text{Equation 4.9}$$

The results are shown in Figure 4.8. With the contribution from Σ valence band taken into account, the transport properties of p-type PbSe can be well modeled throughout the temperature range 300 – 800 K. The deformation potential coefficient of L valence band is set at 35 eV while to model the 800 K result it is allowed to increase by 10 %, just as for the L conduction band. Interestingly it doesn't require additional adjustment, which one would expect if the inter-valley scattering gets intensified at higher temperatures. The parameters determined for the Σ valence band are: the effective mass for each valley $m_b^* = m_l^* = 0.8\ m_e$; the deformation potential 28 eV; and its maximum is separated from that of L valence band by:

$$\Delta E = 0.32 - 2.2 \times 10^{-4} T \quad \text{Equation 4.10}$$

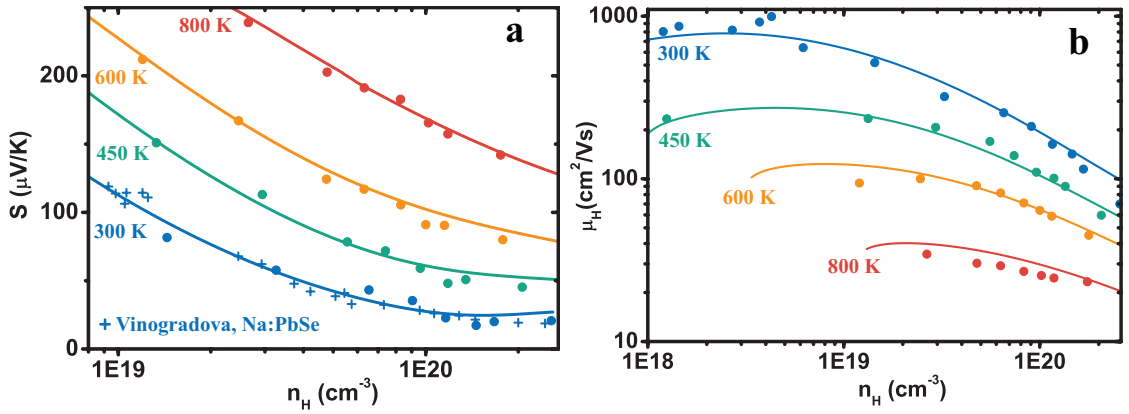

Figure 4.8. a) Seebeck coefficient and b) Hall mobility as function of Hall carrier density for p-type PbSe at different temperatures. Solid curves calculated with multi-band model. Literature data included (not marked) in 300 K mobility.

To some extent, getting information about the Σ band from modeling is not convincing because the result is subject to the formulism of the modeling and its input. The bad news is that there hasn't been a way to directly observe the Σ band. For example for the energy gap measurement, the primary direct transitions happen at much larger probabilities since they do not require phonon participation. They would dominate the absorption spectra making the L–Σ indirect transitions hard to detect. It is even more difficult to get information about effective masses and deformation potential experimentally. To some theorists such a two-band picture is even wrong because the two local maximum are actually from the same eigenstate thus should be regarded as a single band with complex energy contours[144].

Nonetheless, such a simple model has been proven to explain the experiments at different temperatures very well and successfully guided experiments to improve the performance of PbSe.

The advantage of having the Σ band is directly shown in the Seebeck coefficient. Figure 4.9 compares the modeling result on Seebeck coefficient and mobility with and without contribution from Σ band. At 300 K, the influence from the Σ band is evident from modeling, but is arguably observable due to the uncertainty of Seebeck measurements. As temperature increases to 450 K, the difference becomes noticeable and the experiment results clearly suggested the importance of the Σ band. At higher temperatures the Seebeck coefficient is enhanced even at low carrier densities and at 800 K the enhancement is over 30%. On the other hand, the Hall mobility doesn't change much by the presence of the Σ band, especially below 600 K where almost no difference is seen. The total Hall mobility is proportional to the sum of conductivity from each band weighed by mobility. Thus at lower temperatures due to large band offset $\sigma_L >> \sigma_\Sigma$, in addition $\mu_{c,L} >> \mu_{c,\Sigma}$ because of the big difference in effective mass, as a result the overall Hall mobility is dominated by the L band.

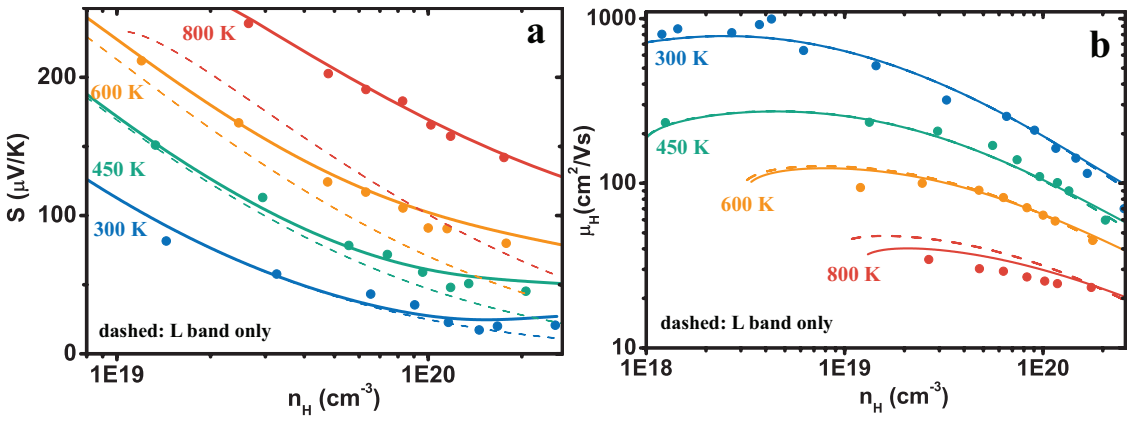

Figure 4.9. a) Seebeck coefficient and b) Hall mobility as function of Hall carrier density modeled with and without the contribution from the Σ band.

Even though the transport properties are well explained by the current model and combination of parameters, it is also important to investigate how much the overall properties would change if the parameters for the Σ band were chosen differently. This result is shown in Figure 4.10. Error bars represent 5% uncertainty in property measurements. The result indicates: changing m_b^*, Ξ, ΔE_{0K} for sigma band by ±25%, 15%, and 13% leads to no difference in the mobility modeling, whereas the difference seen in Pisarenko relations indicates that all combinations

of $\{m_b^*, \Xi, \Delta E_{0K}\}$ within the range of {0.7±0.2 m_e, 30±4 eV, 0.34±0.02 eV} would give reasonably good fit to the experiment result. This is the suggested range for parameters of the Σ band.

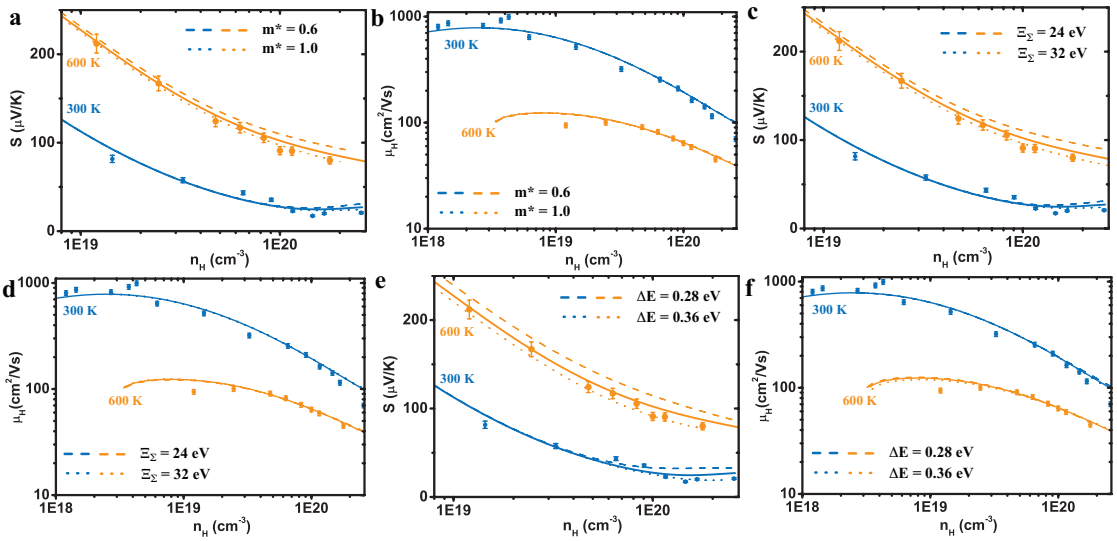

Figure 4.10. Influence of different parameters for the Σ band on overall transport properties at 300 K and 600 K.

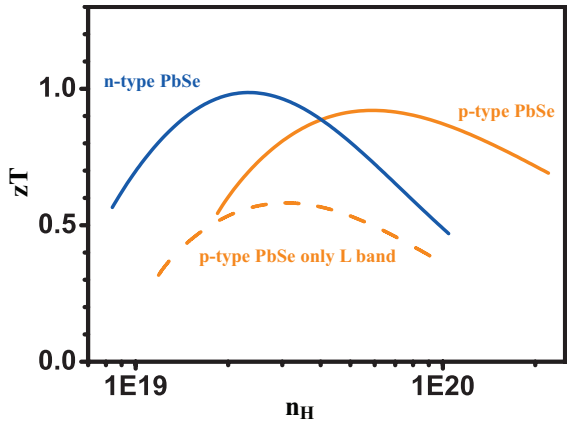

Figure 4.11. zT calculated from 3-band model for n-type and p-type PbSe at 850 K as function of Hall carrier density.

Figure 4.11 plots the zT of both n-type and p-type PbSe calculated at 850 K, based on the 3-band model calculation. It generally predicted the same maximum zT for both types with experimentally suggested ones, although for some unknown reason the Hall carrier densities corresponding to the maximum zT are lower than the optimum carrier density determined experimentally, for both n-type

and p-type. It also shows the zT calculated for the L valence band only, assuming there is no Σ band. Due to its larger deformation potential coefficient, the maximum *zT* if there is no Σ band would be much smaller around 0.6.

4.4 Thermoelectric Merit of Two-band Systems

The analysis of *zT* in term of *B* factor in a two-band system is originally described by my colleague Zachary Gibbs.

It is clear that the quality factor *B* of the band determines the maximum *zT* in a single band system. It is now a very interesting question to ask, for systems with a secondary band for majority carriers, which are the most favorable properties for the secondary band to give the highest *zT*. In fact, going over the expression of *zT* for a two band system and expressing each transport property with the expressions given by Equation 3.20 through Equation 3.26 for Kane bands (the parabolic band is a special case when $\alpha = 0$), it is easily seen that the overall *zT* is only a function of B_1, which is the quality factor of the primary band, B_2 the quality factor of the secondary band, and Δ their band edge offset:

$$zT = \frac{S^2\sigma}{\kappa}T$$

$$= \frac{\frac{(S_1\sigma_1 + S_2\sigma_2)^2}{\sigma_1 + \sigma_2}T}{\left[\kappa_L/T + (L_1 + S_1^2)\sigma_1 + (L_2 + S_2^2)\sigma_2 - \frac{(S_1\sigma_1 + S_2\sigma_2)^2}{\sigma_1 + \sigma_2}\right]T} \qquad \text{Equation 4.11}$$

Rewrite the transport parameters in term of *B* and energy integrals:

$$\sigma = 3\left(\frac{e}{k_B}\right)^2 B\kappa_L/T\,{}^0F_{-2}^1 \qquad \text{Equation 4.12}$$

$$S\sigma = 3\left(\frac{e}{k_B}\right)B\kappa_L/T\left({}^1F_{-2}^1 - \eta\,{}^0F_{-2}^1\right) \qquad \text{Equation 4.13}$$

$$\left(L + S^2\right)\sigma = \left(\frac{{}^2F_{-2}^1}{{}^0F_{-2}^1} - 2\eta\frac{{}^1F_{-2}^1}{{}^0F_{-2}^1} + \eta^2\right)3B\kappa_L/T\,{}^0F_{-2}^1 = 3B\kappa_L/T\left({}^2F_{-2}^1 - 2\eta\,{}^1F_{-2}^1 + \eta^2\,{}^0F_{-2}^1\right) \qquad \text{Equation 4.14}$$

$$\frac{(S_1\sigma_1+S_2\sigma_2)^2}{\sigma_1+\sigma_2}=\frac{9\left(\frac{e}{k_B}\right)^2\left(\kappa_L/T\right)^2\left[B_1\left({}^1F_{-2}^1-\eta\,{}^0F_{-2}^1\right)+B_2\left({}^1F_{-2}^2-(\eta-\Delta)\,{}^0F_{-2}^2\right)\right]^2}{3\left(\frac{e}{k_B}\right)^2\left(\kappa_L/T\right)\left(B_1\,{}^0F_{-2}^1+B_2\,{}^0F_{-2}^2\right)}$$

$$=\frac{3\kappa_L/T\,B_1\left[\left({}^1F_{-2}^1-\eta\,{}^0F_{-2}^1\right)+\frac{B_2}{B_1}\left({}^1F_{-2}^2-(\eta-\Delta)\,{}^0F_{-2}^2\right)\right]^2}{\left({}^0F_{-2}^1+\frac{B_2}{B_1}\,{}^0F_{-2}^2\right)}=A \qquad \text{Equation 4.15}$$

$$\left(L_1+S_1^2\right)\sigma_1+\left(L_2+S_2^2\right)\sigma_2=3B_1\,\kappa_L/T\left[\left({}^2F_{-2}^1-2\eta\,{}^1F_{-2}^1+\eta^2\,{}^0F_{-2}^1\right)+\frac{B_2}{B_1}\left({}^2F_{-2}^2-2(\eta-\Delta)\,{}^1F_{-2}^2+(\eta-\Delta)^2\,{}^0F_{-2}^2\right)\right]=C \qquad \text{Equation 4.16}$$

The energy integrals are defined as:

$${}^nF_l^m={}^nF_l^m(\eta),\ {}^nF_l^m={}^nF_l^m(\eta-\Delta) \qquad \text{Equation 4.17}$$

Thus zT is expressed as:

$$zT(B_1,\frac{B_2}{B_1},\Delta,\eta)=\frac{A}{C-A+\kappa_L/T}=\frac{A^*}{C^*-A^*+1} \qquad \text{Equation 4.18}$$

Where

$$A^*=A\Big/\left(\kappa_L/T\right),\quad C^*=C\Big/\left(\kappa_L/T\right) \qquad \text{Equation 4.19}$$

It is now easy to visualize the relation between zT and different combination of B_1, B_2/B_1, Δ and η. For simplicity, we will assume both bands are parabolic so $\alpha_1 = \alpha_2 = 0$. Two examples are given in Figure 4.12 and Figure 4.13. Assuming the quality factor of the first band is 0.35, which is about the value for the L valence band in PbSe, and 0.7, which is about that for the L conduction band in PbSe. The value of B_1 and B_2 are allowed to change only in a reasonable range based on known quality factors for real compounds. Specifically, for the first band, 0.35 correspond to a mediocre thermoelectric compound that most researches start with, while 0.7 is close to the value for a state-of-the-art thermoelectric material. For the second band, 0.17 is about the minimum quality factor for it to be of any value to contribute for zT, whereas 1.4 is almost impossibly high based on the knowledge on various compounds.

There are several interesting implications from these two figures:

1. Once the quality factor of the first band is fixed, how much improvement of zT the system could achieve with the second band is determined by its quality factor, instead of any individual parameter. More generally it also matters how much the non-parabolicity is for the second band.

2. The quality factor of the first band determines the basis of the zT of the system. The second band adds its contribution depending on the offset between them, when they are aligned ($\Delta = 0$), the zT reaches its maximum, which is about the sum of zT expected for each band using their own B factor.

3. Depending on their ratio the second band only starts to benefit zT when it is closer than 2 to 4 $k_B T$ from the first band edge, Being on the large side when the ratio of B_2/B_1 is large, and around 3 $k_B T$ when the ratio is about 1.

4. There is always a single maximum zT as function of η, given realistic combinations of quality factors, the optimum chemical potential is always close to the edge of the first band, regardless of the quality factor of the second band. There is a shoulder in zT for some B_2/B_1 ratios as the chemical potential moves away from the edge of the first band towards the second band. As seen in Figure 4.12 when B_1 is 0.35, even when B_2 is ten times as good the maximum zT when two bands are not aligned is still found around the edge of the first band. One should try to move the second band closer towards the first band while maintaining the chemical potential near the band edge for better zT.

5. As an extreme exception, when B_1 is very small while B_2 is large, then the maximum zT is found when η moves towards the second band (Figure 4.14). More generally, the optimum η to get maximum zT is always found below or close to the edge of the first band unless the first band has a very small quality factor B_1 close to zero, while the second band is many times as good. For $B_1 \geq 0.3$ the optimum η is always around the edge of first band, regardless of the quality of the second band (Figure 4.15).

6. The optimum chemical potential slightly shifts toward the second band as it comes close to around 1 $k_B T$. This shift is less than half a $k_B T$, even when the second band has a B factor twice as high. As the second band comes even closer η begin to shift back to the band gap again.

7. This relation is between zT and chemical potential η. When the more directly observable n_H is considered, one need to increase n_H in order to keep η constant when there is a second band being brought closer.

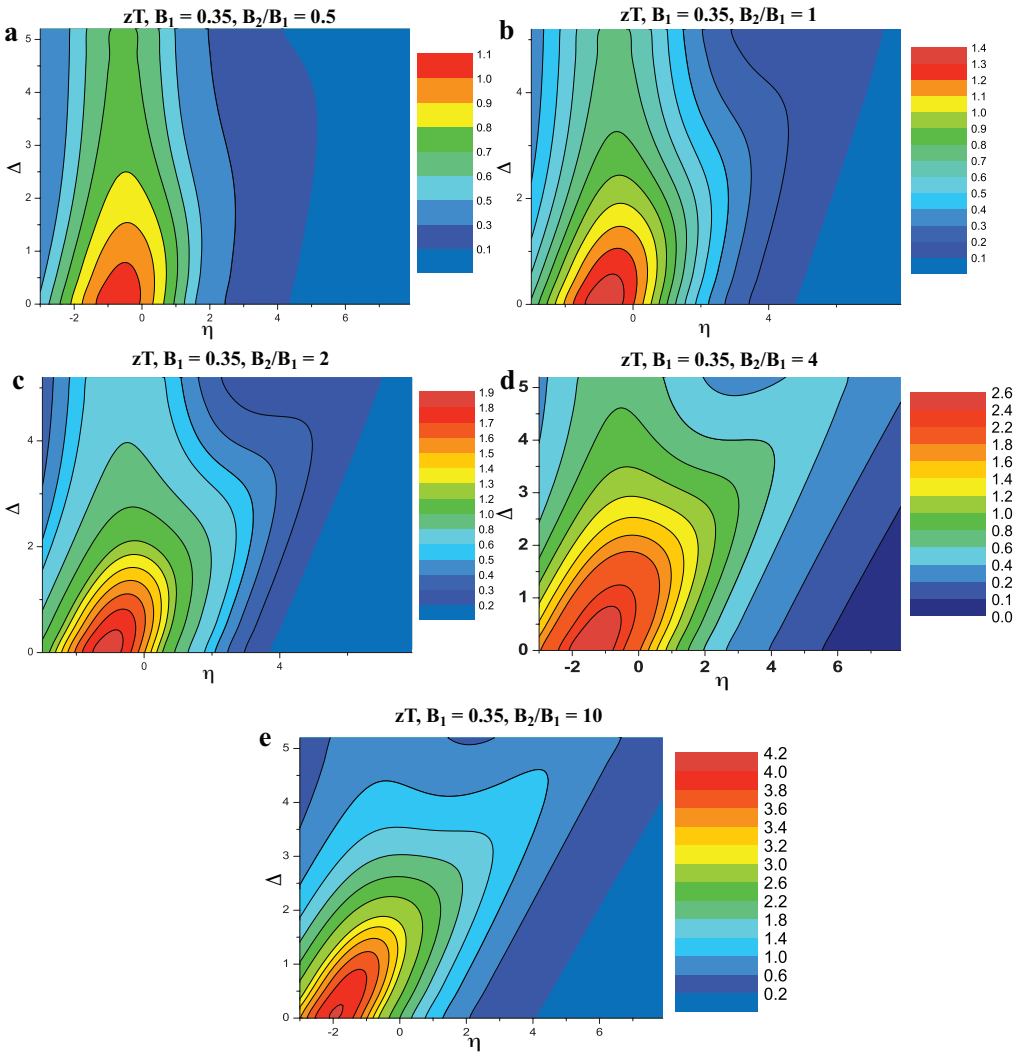

Figure 4.12. *zT* of a two-band system for different combination of parameters for the second band and chemical potential. Quality factor for the first band is 0.35. A secondary band with quality factor greater than 1, as suggested in d) and e) is not very likely in reality.

By calculating the maximum *zT* for a few B_1 values as function of the ratio B_2/B_1 and energy offset Δ, one can estimate the effective quality factor B_{eff} for two-band systems that is equivalent to a single band system respect to maximum *zT*. The ratio of B_{eff}/B_1 is plotted in Figure 4.16. Generally when the two bands are aligned ($\Delta = 0$), B_{eff} is roughly the sum of B_1 and B_2 (the maximum *zT* is lower than the sum of two systems with each band along). For small offsets $\Delta < 0.5$, the two bands can be approximately considered as aligned. With larger Δ, B_{eff} will be smaller than the sum of B_1 and B_2. Also as the quality factor of the first band B_1 increases, it requires the second band to have higher B_2 or to be closer to the first band to result in a B_{eff} greater than B_1 ($f > 1$).

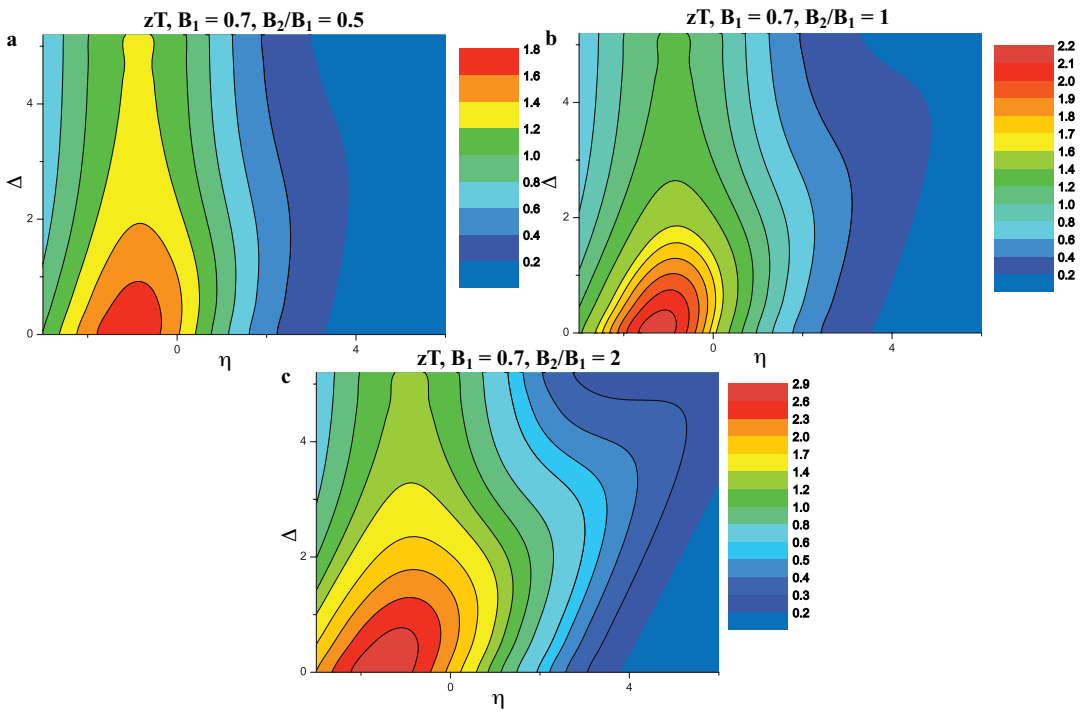

Figure 4.13. *zT* of a two-band system for different combination of parameters for the second band and chemical potential. Quality factor for the first band is 0.7.

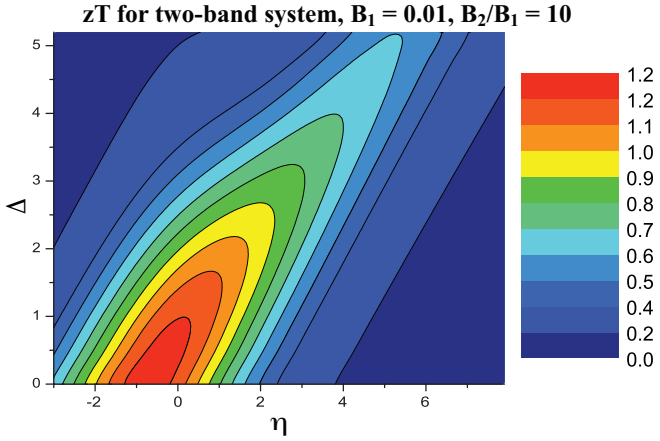

Figure 4.14. *zT* of a two-band system for different combination of parameters for the second band and chemical potential. When the first band has very low quality factor $B_1 = 0.05$ while $B_2 = 0.5$, the chemical potential need to be moved to the edge of the second band for best *zT*.

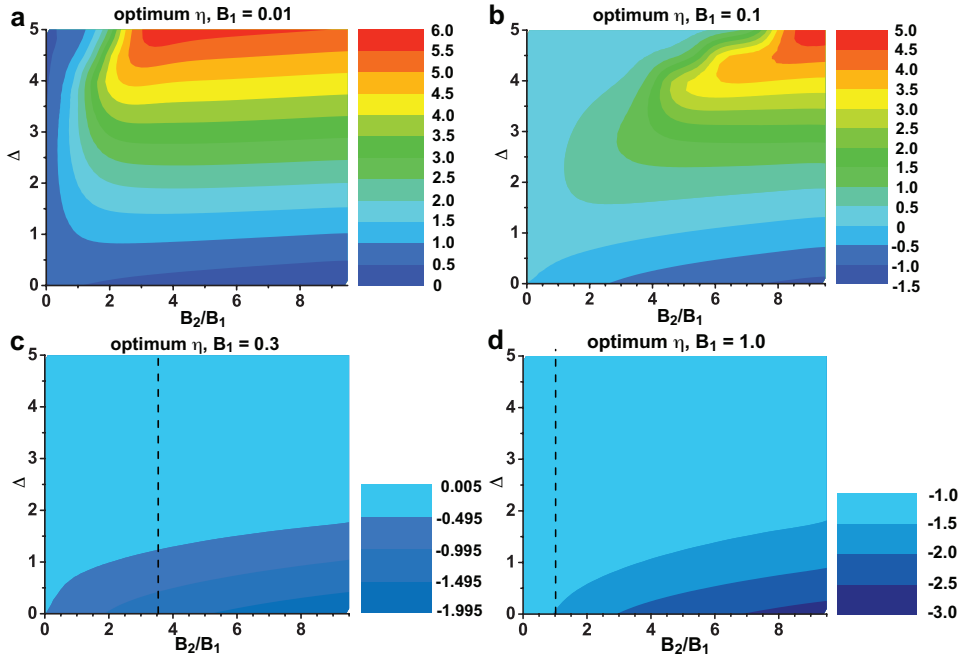

Figure 4.15. The optimum reduced chemical potential η in two-band systems with different energy offset Δ ($=\Delta E/k_BT$) between two bands and the ratio of their quality factor B_2/B_1, for different B_1 values of a) 0.01, b) 0.1, c) 0.3, and d) 1. Dashed lines in c) and d) are rough limits of the ratio B_2/B_1 in each case, the region to their right is not likely achievable in real systems.

In the end, let's come back to the case of p-type PbSe. Using the parameters determined from this study, the quality factor for L valence band is calculated to be 0.32 at 850 K. Compared with the known quality factors of different compounds, this is not quite promising for thermoelectrics. Notice the quality factor for its counterpart the L conduction band, was found about twice as high at 0.67. The reason for such difference is the difference in the deformation potential coefficient or, the strength of electron-phonon interaction. The p-type PbSe would be only ordinary in performance at best if there were not the Σ valence band. For the Σ band we could also give an estimate of its quality factor, which is 0.37. This means the Σ band is better than the L valence band in thermoelectric performance, even though it is not superior (also keep in mind it is parabolic with $\alpha = 0$ while the L band is non-parabolic with $\alpha = 0.17$). But as we learned from the relation between zT and quality factors in a two-band system, the two ordinary band when working together could add up to a remarkable zT. In binary PbSe, the two bands are on the right track when they move close to each other at high temperature: the Σ band is 1.8 k_BT away from the L band edge at 850 K. With this configuration the maximum zT is expected to be 1.0 at 850 K, which is very close to the more careful calculation shown in Figure 4.11, as well as experimental results. But obviously there is extra room for zT if one could make the two bands come even closer at this temperature. We later

demonstrate the implement of this in Chapter 8. But before that we shall draw a blueprint of zT to look for assuming this could be done. The result indicates a maximum zT of 1.5 when the two bands are aligned (Figure 4.17), a 50% increase of zT.

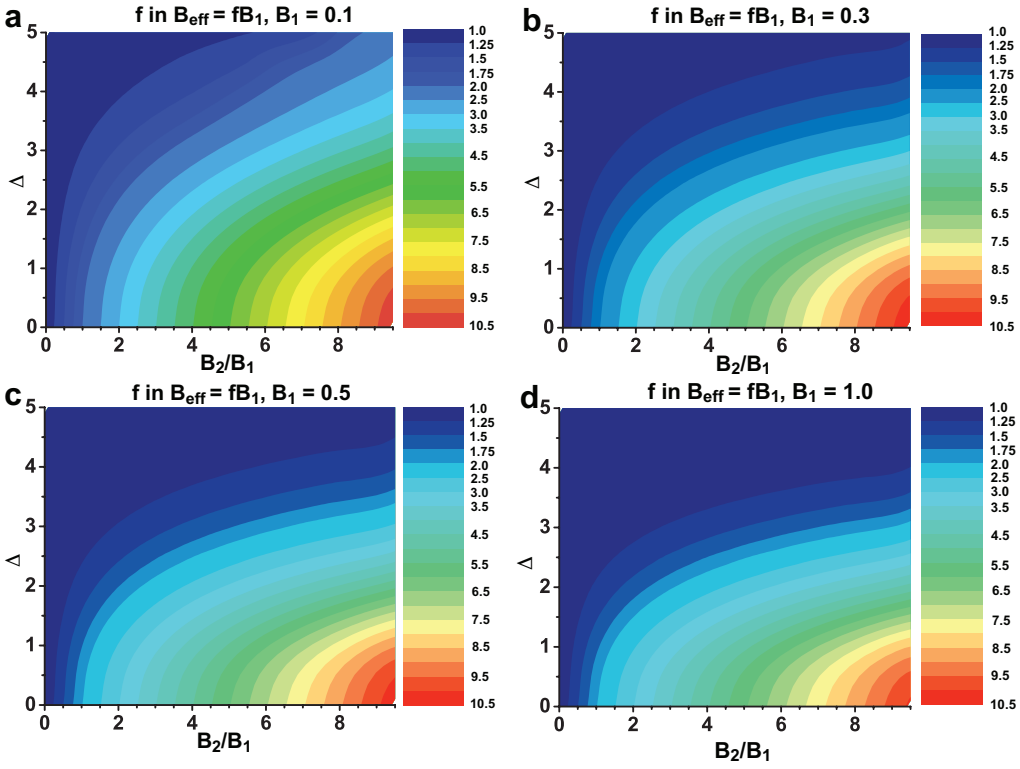

Figure 4.16. The ratio f between effective quality factor B_{eff} and B_1 as function of B_2/B_1 and Δ for systems with different B_1 a) 0.1, b) 0.3, c) 0.5 and d) 1.

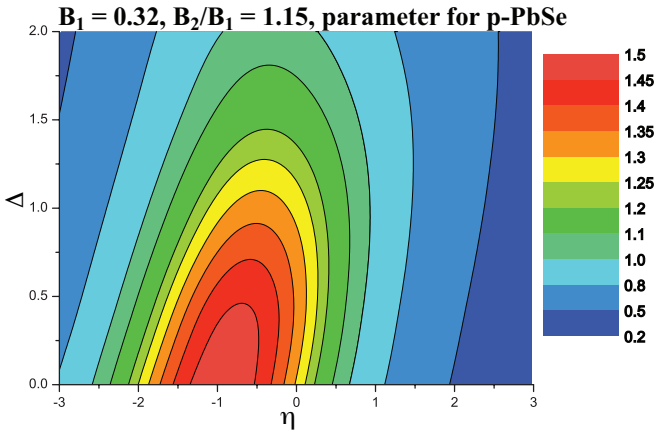

Figure 4.17. zT map of p-type PbSe assuming the energy level of second band can be adjusted freely.

Chapter 5

N-type PbSe Doped on Cation Site

5.1 Introduction

The study on cation site doped n-type PbSe started when with the attempt to dope PbSe with In in order to probe the resonant impurity effect historically reported in this system[140], as a meaning to improve *zT* of the n-type PbSe. The resonant feature were not observed and In behaves just as a regular dopant, only with a lower mobility compared with the Br doped samples. After seeing exactly the same trend in a series of Bi doped PbSe, There seems to be a universal difference between cation site dopants and anion site dopants. This encouraged us to expand the study to other cation site donors like Bi, and La. Besides, a comprehensive literature survey is also carried out to compare with results from this study. Also the study included lots of literature survey on similar compound PbTe, as well as the most typical compound semiconductors of III-V and II-VI compounds. In the end, we studied the thermoelectric performance of a few cation site doped PbSe, but most interestingly we see a difference in mobility which could be the first direct demonstration of a less-known aspect of influence from impurity on transport, called the short-range potential scattering.

5.2 Sample Synthesis and Transport Properties

Doping of PbSe n-type on the cation site turned out to be not trivial. None of the dopants studied could provide an easy and repeatable control of n_H as in the case of Br doped PbSe. In fact, multiple batches of samples were made, all with great care and the Pb:Se ratio was slightly adjusted for different batches from exact stoichiometry 1 to slight cation rich 1.002 in order to suppress the formation of cation vacancies that are acceptors for PbSe.

Figure 5.1 shows the effectiveness of different dopants by comparing the concentration of substitutional dopant (nominal composition $Pb_{1.002}Se_{1-x}Br_x$, $Pb_{1.002-x}In_xSe$, $Pb_{1-x}Bi_xSe$, $Pb_{1-x}La_xSe$)

with the carrier density from Hall measurement at 300 K. For both Br and In 1:1 correspondence is roughly observed up to 0.4 % ($Pb_{1.002}Se_{0.996}Br_{0.004}$ or $Pb_{0.998}In_{0.004}Se$), producing n_H = 6 × 10^{19} cm^{-3} at 300 K. For Br this is the highest content studied and fully activation had been observed up to n_H of 3 × 10^{20} cm^{-3}. For In at higher concentrations the measured n_H starts to deviate from the projection. A similar saturation of carrier density was explained by Fermi level pining due to the resonant nature of In levels in PbSe. But this is not supported by all recent studies[78, 145] on In doping of PbSe. In many compound semiconductors doping limits are found[146, 147] due to the automatic formation of compensating defects with the change of chemical potential regardless of dopant species, it is not the case for In doped PbSe as much higher n_H has been reported for Br doped samples. Thus results here could actually indicate a solubility limit of In in PbSe around 0.4% at room temperature.

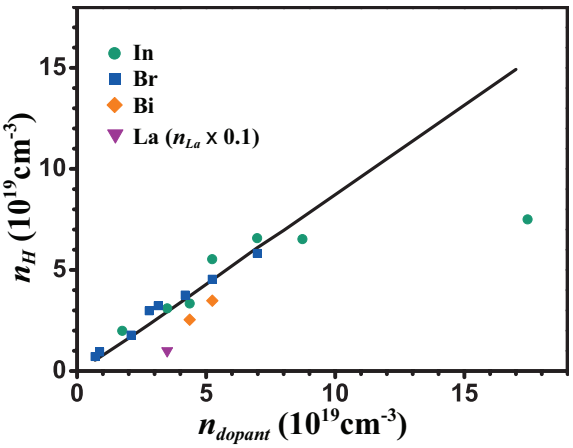

Figure 5.1. Doping efficiency of different dopants in n-type PbSe.

When bismuth is used as dopant it is not fully ionized. Whether the carrier density is close to the theoretical value depends on subtle synthesis condition changes, indicating rather complicated defect chemistry related to Bi doping. Nearly full activation of Bi was found only in some samples.

Many published work on In or Bi doped[148] PbSe and PbTe showed very low carrier density and poor doping efficiency, the discrepancy can be partly understood considering a general dilemma pointed out by Zunger[149] for all cation site doping of n-type semiconductors: effective cation site doping requires cation-rich host compound to suppress the formation of defects (either cation vacancy or anion interstitial) that compensates free electrons; at the same time the host need to be kept cation-poor to ensure good solubility of donors.

La was found mostly inactive in PbSe, being contrary to the case[85] of PbTe where La produced free electrons as much as 1 × 10^{20} cm^{-3}. All PbSe samples made with < 0.5 % La substitution has remained intrinsic with n_H below 5 × 10^{18} cm^{-3}. Only the sample with 2 % La was found extrinsic with n_H = 1 × 10^{19} cm^{-3} at 300 K (about 3 % doping efficiency). Historical studies[150, 151] on rare-earth doped PbSe have also found low doping efficiency for other lanthanides (Gd, Ho, Dy, Yb).

Figure 5.2 shows the measured transport properties of In doped PbSe. Each property changes gradually with the increase of carrier density, following typical degenerate semiconductor behavior except for the 7E19 sample with 1% In, which has higher resistivity and consequently lower thermal conductivity compared with the other heavily doped sample 6E19.

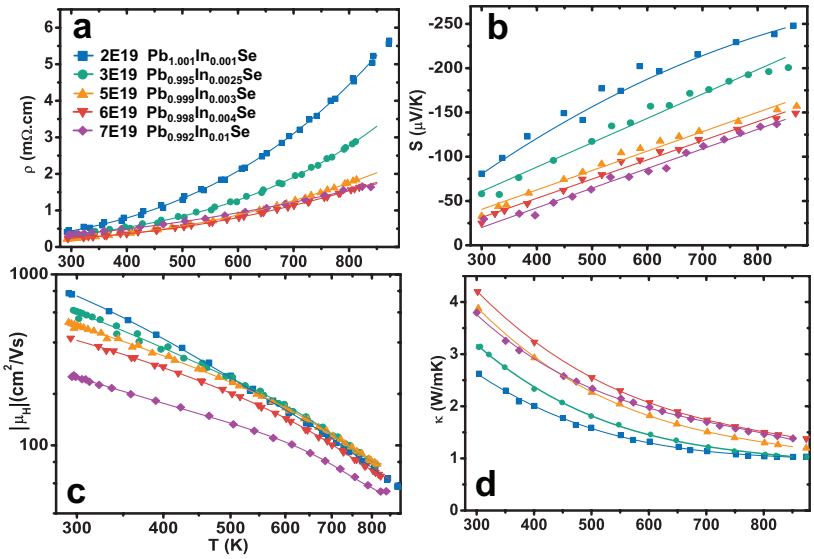

Figure 5.2. Temperature dependent transport properties of In doped PbSe a) resistivity, b) Seebeck coefficient, c) Hall mobility and d) thermal conductivity.

The Hall carrier density is almost independent of temperature for samples with low carrier density, as seen in Figure 5.3. A gradual and slight decrease in n_H is due to the decrease of degeneracy as a result of increasing T, which is commonly seen in heavily doped semiconductors. The uprising of n_H at high temperatures for the two most heavily doped samples is very interesting as such a change in trend is not expected for a single band system like n-type PbSe. In fact this feature was not observed on Br doped PbSe samples. Consider the In doping efficiency is slightly less than 100% for these two samples, this uprising of carrier density could be the result of a temperature dependent solubility of In.

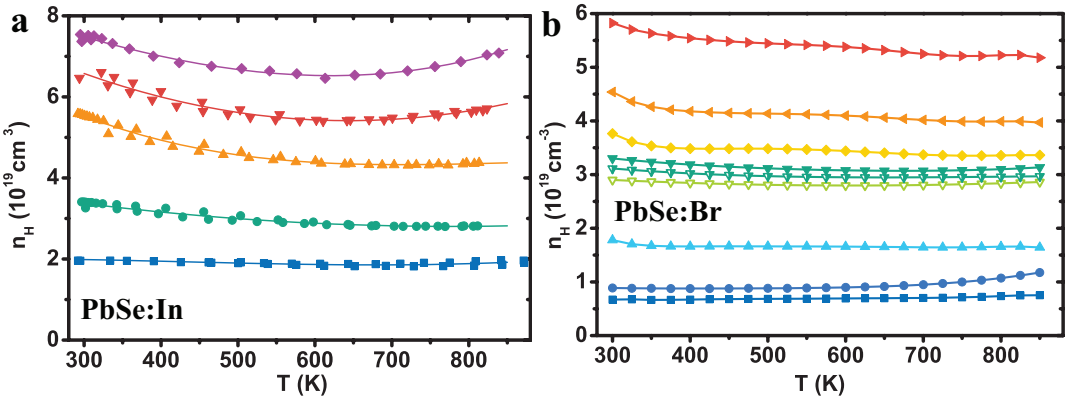

Figure 5.3. Hall carrier density as function of temperature for a) In doped and b) Br doped PbSe.

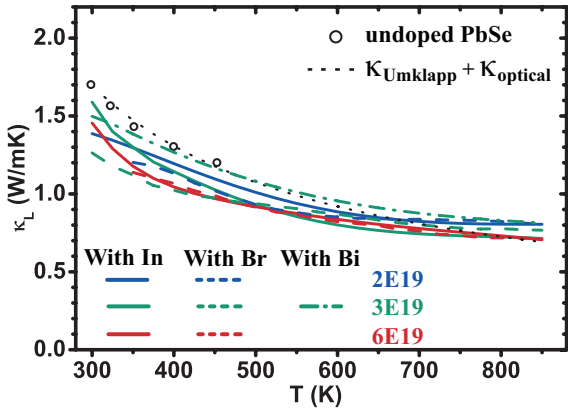

Figure 5.4. Lattice thermal conductivity as function of temperature for n-typed PbSe doped with different impurities, together with result from undoped PbSe.

Figure 5.4 shows the lattice thermal conductivity of In doped PbSe together with analogs using Br or Bi as dopant. Lorenz number calculated from a single Kane band model and combined carrier scattering mechanisms of deformation potential phonon scattering and polar scattering from optical phonons were used. As expected no difference can be concluded as the atomic substitution is dilute. Figure 5.4 also shows the directly measured thermal conductivity of undoped, highly resistive PbSe and a formulated relation (dash line) using 1/T dependence from Umklapp process plus residue constant contribution from optical phonons, which matches well with experimental data from undoped PbSe near room temperature and doped PbSe at high temperatures. All the κ_L calculated from doped samples near room temperature tend to be smaller than the undoped sample. The difference is far beyond the reduction that could have been caused by point defect scattering. Lower κ_L found in doped samples can be partially explained by carrier-phonon scattering, whereas it is still

unclear where is the major source of error seen in κ_L from doped samples. Significant error are often seen in reported κ_L when they are taken from doped samples, especially one doped sample.

The maximum zT of 1.1 at 850 K is achieved when the carrier density is around 3×10^{19} cm^{-3} (Figure 5.5). This result shows In doped PbSe is almost as good as the Br doped ones. For the latter, zT from 5 different samples all with the optimized n_H varied from 1.0 to 1.2. Still, by comparing the mobility as function of carrier density at 850 K for two groups of samples, the Br doped PbSe have slightly higher mobilities, thus, the zT in Br doped PbSe is expected to be slightly higher than in In doped ones.

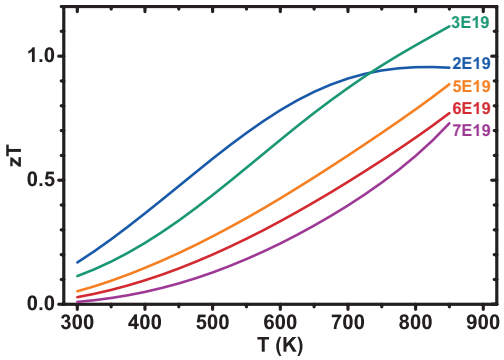

Figure 5.5. zT as function of temperature for In doped PbSe with different carrier density.

Bi doped PbSe is very similar to the In doped samples, with transport properties and zT shown in Figure 5.6.

The transport properties (Figure 5.7) of sample $La_{0.02}Pb_{0.98}Se$ are very different from regular n-type PbSe. There seems to be either an increase of solubility of La with temperature, or a temperature activated ionization of La, such that the Hall carrier density increases linearly with temperature from 1×10^{19} cm^{-3} at room temperature to 3×10^{19} cm^{-3} at 850 K. However, due to its much lower mobility than the other n-type PbSe the zT is found about 0.4 for this sample even though the carrier density is optimized.

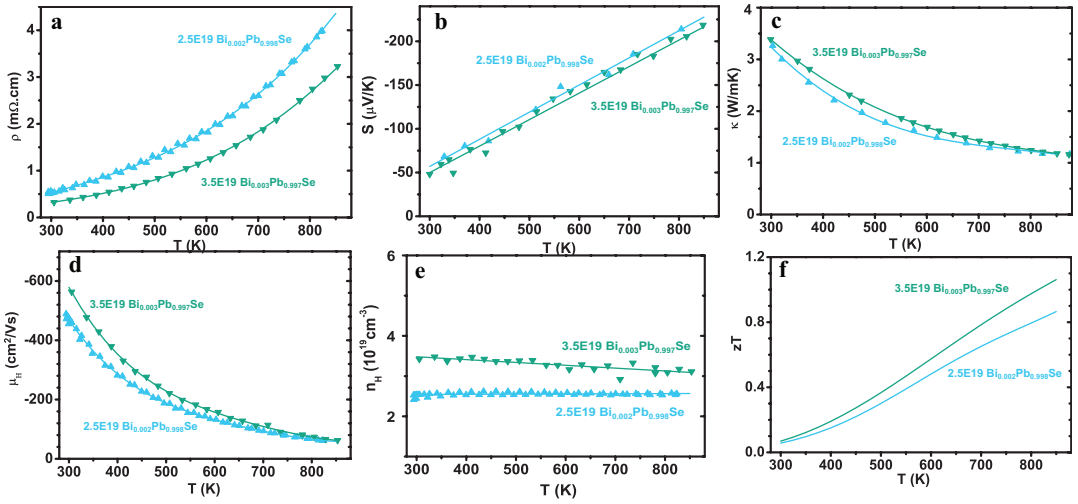

Figure 5.6. Transport properties as function of temperature for Bi doped PbSe a) resistivity, b) seebeck coefficient, c) thermal conductivity, d) Hall mobility, e) Hall carrier density and f) zT.

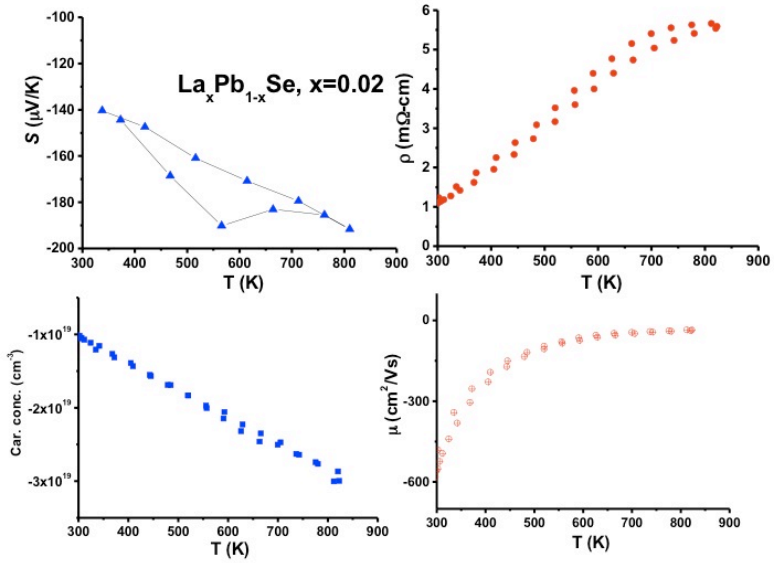

Figure 5.7. Transport properties of $La_{0.02}Pb_{0.98}Se$ as function of temperature.

Figure 5.8 summarizes the *zT* of n-type PbSe doped with different dopants, together with all recent report of *zT* on n-type PbSe.

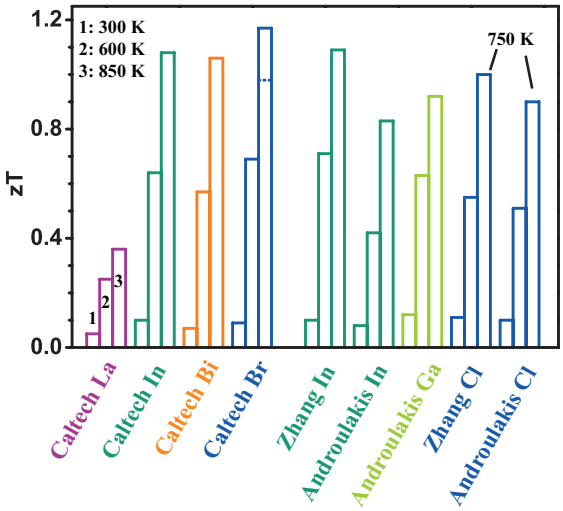

Figure 5.8. Comparison of zT of n-type PbSe with different dopants at 300, 600 and 850 K, including literature results.

5.3 Short-range Potential Scattering from Impurities

Are dopants created equal? Do they make any difference in carrier transport other than tuning the chemical potential (by changing carrier density)? This would be a very interesting question to ask and would mean there is usually a best dopant to chose, not from the processing perspective, but from solid-state theory.

Of course one might immediately answer the second question mentioning right from discussion in Chapter 3, that dopants induce additional carrier scattering through either the ionized impurity scattering or neutral impurity scattering. Neither of these mechanisms distinguish the species of the dopant, that is, all impurities are treated the same as long as they are of the same valence.

It is much less known or realized, that aside of their long-range coulomb potential that give rise to the ionized impurity scattering, the dopants also induce short-range potential, as their occupancy on the lattice sites disturbed the original lattice potential. This is called, by Askerov for example[105], the short-range potential scattering from impurities. It has a much better known analog in the case where the impurity is isovalent with the atom it replaced, called the alloy scattering, which we will discuss in detail in the next chapter. As for the dopant impurity case, to the best of my knowledge, it is never demonstrated and rarely considered for semiconductors. Nonetheless, the existence of such

scattering in theory indicates that different dopants could potentially lead to observable difference in mobility.

If this effect does exist, it should be first seen in compound semiconductors (with cation and anion sites that are not equivalent). Ioffe has a very intuitive argument[12] on the similar alloy scattering in a compound semiconductor, which says the impurity disturbs more the band that formed by orbits of the atoms it substituted. Experimentally, this has already been observed in $PbTe_{1-x}Se_x$ solid solutions.

The III-V and II-VI compounds are very well studied semiconductors, but surprisingly we have been unable to find convincing experimental results that either approve or disapprove the predicted difference in mobility. For example, n-type GaAs can be doped on cation site by Si[152, 153], Sn[154] or on anion site by Te[155], vacancies or O (unintentional doping[156]), these different dopants have lead to no distinguishable difference mobility as a function of carrier density up to mid 10^{18} cm^{-3}. GaAs can be doped p-type more heavily, in this case using Zn[155] or Be[157] (both substitute the cation) result in same mobilities even for n close to 10^{20} cm^{-3}. GaN can be doped n-type with Si[158], Ge[159] on cation site or O on anion site (unintentional doping[159]). The carrier density dependence of mobilities in this case is again found the same for these dopants for n not exceeding 10^{19} cm^{-3}. A hint of difference in mobility in samples with dopants on different sites can be found only in p-type GaAs: when it is doped with Ge the mobilities are found[160, 161] lower than those doped with Sn, Zn or Be on the cation site, when n_H is above 10^{19} cm^{-3} (Figure 5.13).

Among the II-VI compounds, ZnSe and CdS can be doped heavily n-type up to $n_H \sim 5 \times 10^{19}$ cm^{-3}. The dopants used to reach it are halogens[162] for ZnSe and In[163] for CdS. Although In or Al[164] should be as effective in ZnSe and the halogens in CdS as well, we couldn't find any mobility result for n_H above 10^{19} cm^{-3} using these dopants.

The III-V and II-VI compounds are of interest in optoelectronics and solar cells, where the studied doping range rarely exceed 10^{18} cm^{-3}, the impurity is thus very dilute < 0.01 %. These compounds are wide band-gap semiconductors, which in many cases are almost impossible to dope beyond 10^{18} cm^{-3}. In few exemptions mentioned above, the choice of dopants is limited. The mobilities in these cases are always small (at $n_H = 1 \times 10^{19}$ cm^{-3}, μ_H is about 100 cm^2/Vs for p-GaAs, 200 cm^2/Vs for n-ZnSe and 60 cm^2/Vs for n-CdS), meaning the difference can be easily overshadowed by measurement error or scattering of results. Lastly, the majority of research is on thin films, where

the mobility can be greatly affected by the quality of the film. These all account for the reason why the influence on carrier transport from short-range potential of impurities has not been observed.

IV-VI Pb chalcogenides provides a perfect opportunity to compare the mobility from different dopants. Because at least for n-type PbTe and PbSe, heavily doping to the order of high 10^{19} cm^{-3} has been achieved by both anion site doping with halogen or cation site doping with group III or V elements. Besides, the scattering mechanism in Pb chalcogenides are very simple: it is dominated by deformation potential scattering from phonons plus some correction at low doping levels due to polar scattering from optical phonons, both can be easily modeled with known parameters. The mobility is quite high (at $n_H = 1 \times 10^{19}$ cm^{-3}, μ_H is above 1000 cm^2/Vs for both n-PbTe and n-PbSe) compared with other compound semiconductors with similar doping level, meaning the influence from additional scattering mechanism has a better chance to be seen. The extrinsic factors such as grain size and grain boundaries have negligible influence on mobility and high quality polycrystalline samples usually have same mobility compared with single crystals or high quality thin films, given the same carrier density, making the comparison less affected by quality of samples.

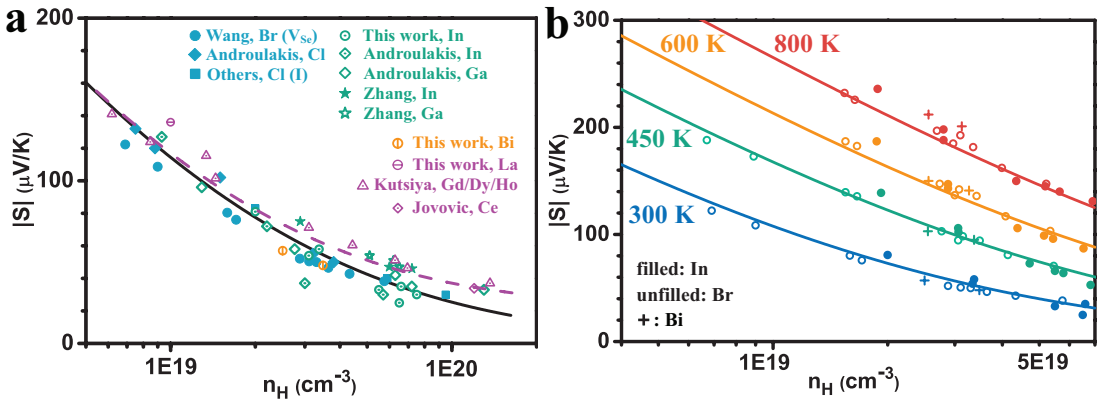

Figure 5.9. Pisarenko relation at a) 300 K and b) different temperatures for PbSe doped with different impurities.

Figure 5.9 shows the Pisarenko relation for n-type PbSe doped with different impurities. Bear in mind the uncertainty in Seebeck measurement it can be concluded for different cation or anion dopants, the Pisarenko relation is identical, meaning the doping has no influence on the band effective mass. The rare earth elements are an exemption: the band effective mass gradually increases with doping. This has been seen and discussed in La doped PbTe. If we are allowed to

model this effect assuming m_d^* increases linearly with carrier density (i.e., density of lanthanide atoms) as 0.1 m_e per 1E20 cm^{-3}, we could provide a reasonable explanation of observed Seebeck coefficient using a single Kane band model with combined scattering mechanism assumption (the purple dashed line). The cation dopants showed no irregularity in Pisarenko relation, which would be expected for impurities with resonant levels.

Figure 5.9 shows the Pisarenko relations at different temperatures. Again no difference is seen between In (and Bi) doped and Br doped samples at all temperatures. Historically In was found to be a resonant dopant in PbSe: a drop of Seebeck coefficient due to resonant scattering in In doped PbSe was found at 85 K when n_H is above 5×10^{19} cm^{-3}. Pisarenko relation from our study in contrary suggests only regular doping behavior at 300 K and above. Other recent studies by Androulakis et al. and Evola et al. have also suggested the same conclusion. Assuming all observations are accurate and repeatable, the absence of resonant behavior above 300 K could have two origins: the In resonant level might have shifted to higher energy with increased temperature; or the resonant nature of In level is weak so that it is mostly overwhelmed by acoustic phonon scattering at or above room temperature.

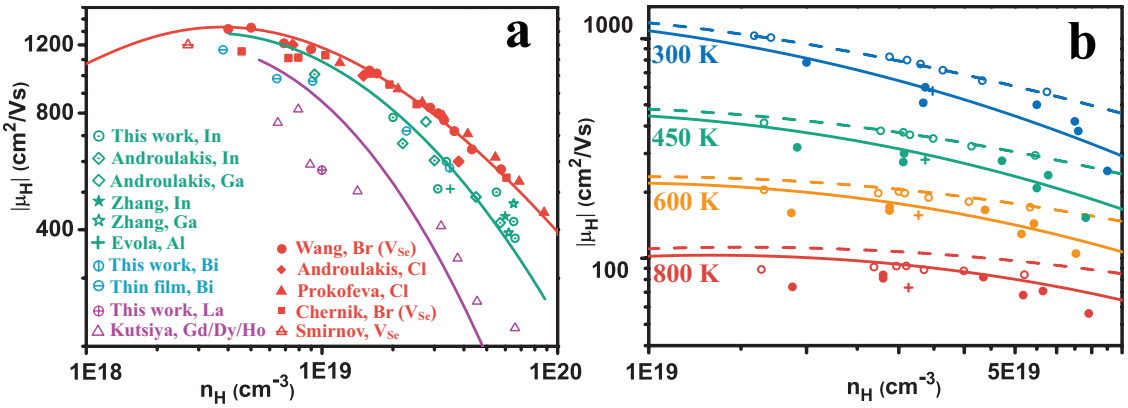

Figure 5.10. Carrier density dependence of mobility for n-type PbSe doped on the anion site and cation site at a) 300 K, and b) different tempertaures.

In Figure 5.10 a) the mobilities of cation and anion doped n-type PbSe at 300 K are compared. Highest mobilities are found in halogen-doped n-type PbSe. Interestingly Cl and Br lead to the same mobility despite their different atomic size. Similarly between the cation dopants In and Bi no appreciable difference is seen. Up to the carrier density range studied here, different dopants on the same lattice site produces similar mobilities if they are fully ionized. Cation site doping in general

produces lower mobility in n-type PbSe especially when the doping level is above 1×10^{19} cm^{-3}. Same trend is also reflected in most reported results. We notice Prokofeva's result is the only exception[140], which showed high mobilities for In doped PbSe, being identical to halogen doped samples, when n_H is below 4×10^{19} cm^{-3}. None of our In doped samples could achieve such high mobilities, same is true for independent study by Androulakis[78] or Evola[145] on In doped PbSe.

From our study the difference in mobility between Br and In doped PbSe retains at smaller n_H down to 1×10^{19} cm^{-3}. Meanwhile, the difference between Br and In does not diminish as temperature increases (Figure 5.10 b). The speed of sound for In and Br doped PbSe at 300 K are measured and found the same, indicating the elastic properties of PbSe is not affected by small amount of dopants. Since the effective mass in both cases is also the same, the difference in mobility seen here could be the result of additional scattering mechanism. Based on the nature of these samples, this mechanism is most likely the short-range potential scattering from impurities that was described theoretically, but not yet found experimentally.

Due to their great similarity, we use the relaxation time from alloy scattering at the dilute limit, and using a Kane band dispersion relation:

$$\tau_{sp} = \frac{8\hbar^4}{3\sqrt{2}\pi\Omega C_{imp} U_{imp}^2 m_d^{*3/2} (k_B T)^{1/2}} \varepsilon^{-1/2} (1+\varepsilon\alpha)^{-1/2} (1+2\varepsilon\alpha)^{-1} \qquad \text{Equation 5.1}$$

We notice Askerov has used[105] a very similar expression with the only difference in the pre-factor (π in his expression versus $8/(3\pi)$ in Equation 5.1), which is commonly seen in relaxation time expression derived by different researchers.

Incorporating the short-range potential scattering with the deformation potential phonon scattering and polar scattering that are already known to exist in n-type PbSe, we are able to account for the lower mobilities in In and Bi doped samples using 5 eV for the only adjustable parameter the short-range potential of impurity U_{imp}. The model further explains mobilities at different temperatures between 300 and 800 K. To understand the mobilities of lanthanide doped PbSe, the model needs to also take into account the change of effective mass with dopant concentration, and the short-range potential is also found larger at 10 eV in the lanthanide case.

In principle, the short-range potential scattering should exist for all dopants, but in the case of anion site doping, it has been shown that the deformation potential scattering plus polar scattering have

been satisfactorily explained mobility measured in Br doped PbSe at any temperatures between 300 and 800 K. The reason is because these two mechanisms have almost the same carrier energy and effective mass dependence, and the temperature dependence is also similar. Since both the deformation potential coefficient Ξ and the short-range potential U_{imp} are determined by fitting experimental mobilities, they can't be both accurately determined at the same time. There is not enough resolution even using mobilities at different temperatures. The current study suggested the presence of the short-range potential scattering by revealing a difference in magnitude of it between cation site dopant and anion site dopant. Another implication from the result is that the difference in for different atom species that substituting the same lattice site is small, whereas the U_{imp} from two elements that substitute different sites are much larger. This is consistent with Ioffes simple picture and explains the same mobilities found between Br and Cl, or Bi and In doped samples.

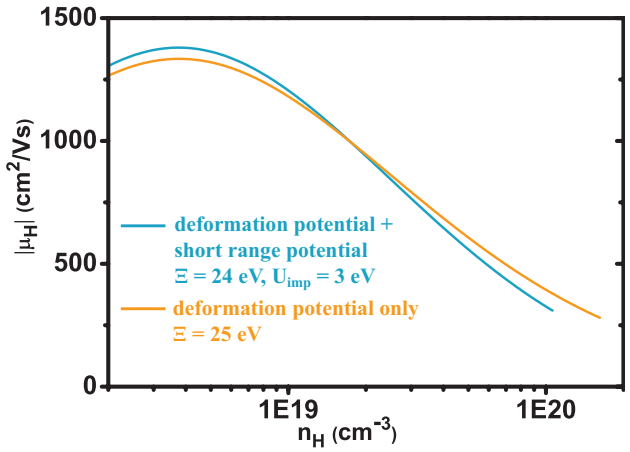

Figure 5.11. modeling of the mobility with deformation potential scattering only, and deformation potential plus short-range potential from impurities. The results are hard to distinguish with experimental results.

This indicates for semiconductors with only one atomic site, or can only be doped efficiently on one atomic site, the influence from short-range potential scattering from impurities would hardly manifest because there will always be deformation potential phonon scattering. Most of its influence would be enveloped into an "effective" deformation potential scattering process (Figure 5.11). Also, for low doping levels below 1×10^{19} cm^{-3}, the impurities are so dilute making the short-range potential scattering negligibly weak. These two factors explain why generally the difference between dopants are not observed or considered for IV, III-V or II-VI semiconductors. As thermoelectrics usually have carrier density above or one order of magnitudes higher than 10^{19} cm^{-3},

and many thermoelectrics can be easily doped, the potential difference caused by the choice of dopants should be considered.

In the other Pb chalcogenide PbTe, a similar difference in mobility is also seen when different dopants[165-171] are used (Figure 5.12). Most of cation site dopant has lead to lower mobilities compared with the anion site doping with I.

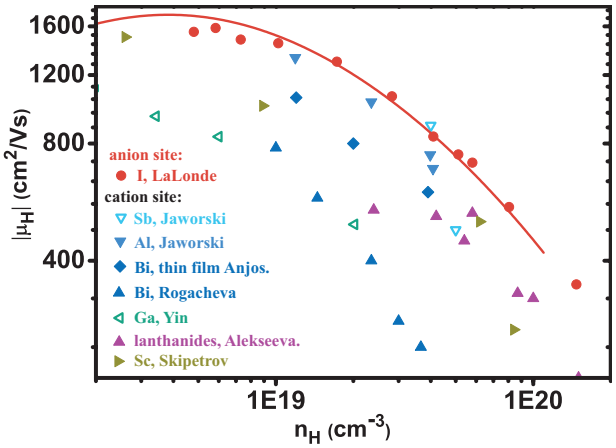

Figure 5.12. Mobility of n-type PbTe as function of carrier density at 300 K. Anion site doping leads to higher mobility compared with cation site doping. Solid curve calculated with deformation potential and polar scattering without considering the short-range potential scattering.

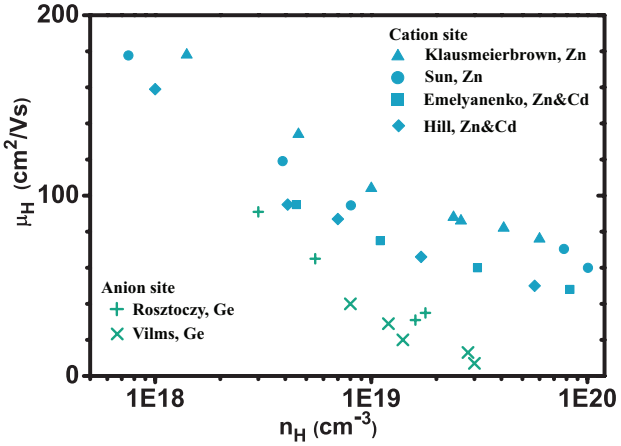

Figure 5.13. Mobility of p-type GaAs as function of carrier density at 300 K. Doping on cation site leads to higher mobility.

Chapter 6

N-type PbS doped with Cl

6.1 Introduction

All rock-salt Pb chalcogenides have the same energy band configuration and are good thermoelectrics. PbS is actually one of the first studied material candidates during the early exploration of thermoelectric effects. PbS has more ionic bonding, and is composed of lighter element of S compared with PbTe or PbSe, thus one would rationally expect the *zT* of PbS to be lower than PbTe or PbSe. The advantage is that it is earth abundant and relatively inexpensive (it even exists in mineral form). From a researcher's aspect, it is a good platform to test the transport models formulated from the study of PbSe and find the difference due to different chemistry of elements. In this study we managed to make polycrystalline PbS with the best quality (with highest mobility). We found n-type PbS inherently has a good *zT* of 0.7 at 850 K. The deformation potential scattering is not the only important mechanism in this material and the polar scattering from optical phonons play an important role at low doping levels. This is successfully accounted for using the formula given by Ravich. The methodology of combining different scattering mechanisms when deriving transport parameters was later applied to PbSe and PbTe to better explain the mobilities found in those materials.

Our interest on PbS is partly inspired by the recent growth in interest of commercial energy harvesting devices and the concern about the scarcity and cost of Te. More importantly, we believe if we establish a better understanding of the material in its binary form, we might be able to make it better and comparable with binary PbSe or even PbTe, with the knowledge and experience on band structure engineering we have accumulated from study of those. The fact it has been studied the least and lowest in *zT* instead make it more suitable as our platform. Unexpectedly, the progress on PbS from other group[172-174] was so quick the room in our opinion for *zT* improvement was filled very quickly around the same time this study was carried out, for both p-type and n-type.

6.2 Sample Synthesis and Transport Properties

The synthesis doesn't differ by much from previous discussed studies on PbSe, except the sulfur was dehydrated before using because almost all commercial sulfur contains crystallized water so their appearance is like salt grains instead of powder. The dehydration was done by first grinding up the small "crystals" and then heat them up at 80 °C in a hot water bath under dynamic vacuum for two or more weeks, until they look powdery. The elements were reacted at 1273 K, which is below the melting temperature of PbS (about 1390 K). The materials inside ampoules were not liquid-like, but after a long time exposure at that temperature (5 days) ingots were obtained as if completely melted, probably due to vapor transfer at high temperature. The samples were single phase and dopant distribution is homogeneous (Figure 6.1). Carrier density control is satisfactory, except for a few exemptions.

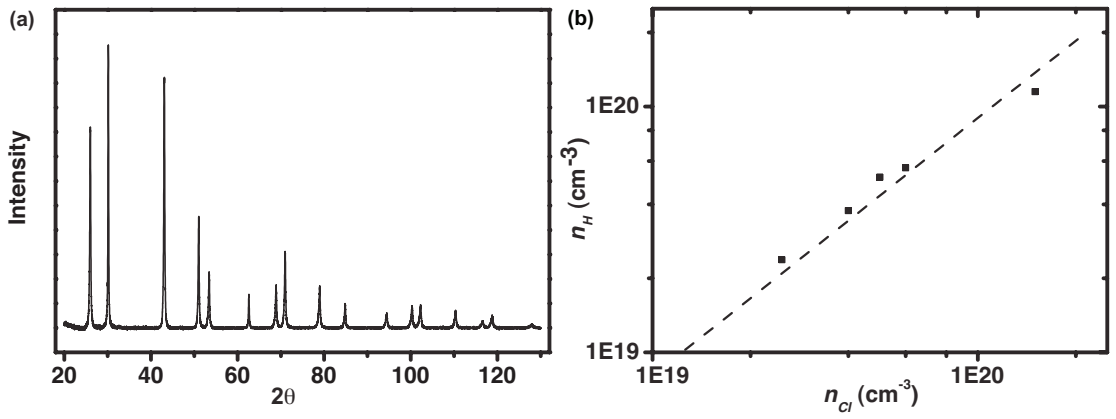

Figure 6.1. a) X-ray diffraction pattern of undoped PbS. b) Hall carrier density as a function of nominal Cl concentration. Dashed line calculated with single Kane band (SKB) model.

All doped samples show degenerate behavior (Figure 6.2). The resistivity increasing with temperature and Seebeck coefficient linearly increase with temperature as well. The Hall carrier density for each sample is shown in Figure 6.2 c and is roughly independent of temperature except for the undoped sample where an increase above 600 K indicates the excitation of minority carriers (holes). PbS has a band gap of 0.41 eV at 300 K, which increases with temperature the same way as

found for the other two lead chalcogenides. Thus, even for the most lightly doped sample with $n_{H,300K} = 2.4 \times 10^{19}$ cm^{-3} no sign of bipolar effect (where minority carriers start to play noticeable role in conduction) was seen up to 850 K. The Hall mobility ($\mu_H = R_H/r$) decrease with temperature monotonously and smoothly, a dashed line was drawn representing the $T^{-2.5}$ dependence, which is typical for Pb chalcogenides with deformation potential phonon scattering the dominant scattering mechanism, but is actually only true for nondegenerate samples (when there is no bipolar influence), the temperature dependence gets weaker as the increase of degeneracy, i.e., the carrier density and for highly degenerate samples a T^{-2} dependence is more likely the case.

Table 6.1. A list of Cl doped PbS samples and some room temperature properties

Label	Composition	Transport Properties			Remark
		$n_H(10^{19}cm^{-3})$	S (μV/K)	μ_H (cm^2/Vs)	
2E18	PbS	0.2	-265	-514	
	PbS		-280		
	$PbS_{1.001}$	0.08	-290	-378	
2E19	$PbS_{0.9987}Cl_{0.0013}$	2.4	-96	-469	React mixed undoped and 1E20 5:1 weight, ingot obtained, ampoule
4E19	$PbS_{0.9978}Cl_{0.0022}$	3.8	-76	-426	Later tested to 950K, Seebeck increase too small, zT not improved, severe evaporation seen.
5E19	$PbS_{0.9973}Cl_{0.0027}$	5.2	-53	-376	Later tested to 950 K,
6E19	$PbS_{0.9968}Cl_{0.0032}$	5.6	-56	-379	
	$PbS_{0.9963}Cl_{0.0037}$	12		-200	
	$PbS_{0.9957}Cl_{0.0043}$	9.9	-46	-185	
1E20	$PbS_{0.992}Cl_{0.008}$	11.5	-40	-210	

PbS, when made stoichiometric, exhibits n-type doping behavior, whereas for PbSe, the compound is still p-type even with 0.1% extra Pb added in the nominal formula. Adding an extra 0.1% of sulfur (in attempt to achieve low p-type doping) reduced the free carrier concentration, but did not change the doping type.

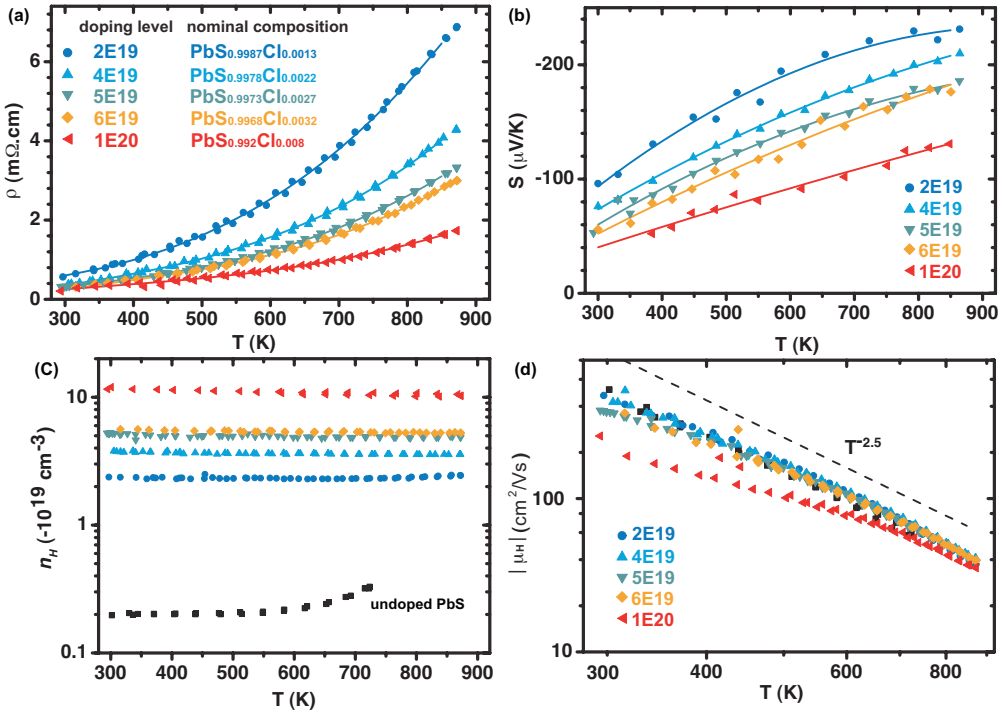

Figure 6.2. Transport properties of Cl doped PbS as function of temperature: a) resistivity, b) Seebeck coefficient, c) Hall carrier density, d) Hall mobility.

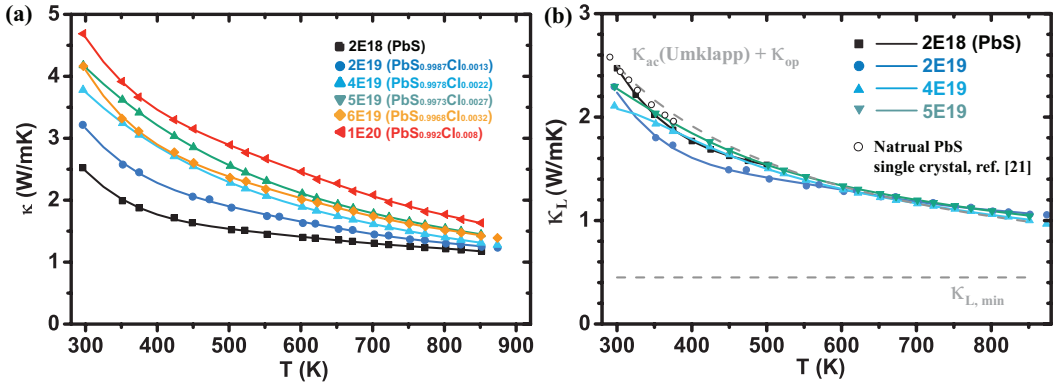

Figure 6.3. The temperature dependence of thermal conductivity a) and lattice thermal conductivity b) for Cl doped PbS.

The thermal conductivity decreases with temperature, even for the undoped sample no obvious bipolar contribution can be seen (Figure 6.3). The lattice thermal conductivity of PbS at room temperature, as revealed by the measured total thermal conductivity in undoped samples (where the resistivity is high and hence the electronic contribution is negligible) is 2.5 W/mK, which is

consistent with previous results[17, 21]. All samples were annealed in this work with grain size large enough for the grain boundary phonon scattering to be neglected. The lattice thermal conductivities are found to be the same as that of single crystalline PbS in its natural mineral form[12]. The observed temperature dependence of κ_L can be understood as the sum of contributions from the Umklapp scattering of acoustic phonons with T^{-1} dependence and the glass like thermal conductivity of the optical phonons (about 0.17 W/mK, largely temperature independent). Up to 850 K κ_L is well above the minimum thermal conductivity predicted with the Cahill model. At 850 K, all the calculated κ_L converge to the value of ~1 W/mK, in comparison to ~0.7 W/mK found in PbSe and PbTe at this temperature.

The calculated zT reaches the maximum of 0.7 at 850 K, for both 4E19 and 6E19 samples. Normally zT of a semiconductor peaks only at a single chemical potential value, thus the apparent optimum carrier density of both 4E19 and 6E19 is for sure not true. The real situation could be: first, the zT of 4E19 was overestimated so 6E19 is the optimum carrier density with maximum zT 0.7; or second, 4E19 was the optimum whereas zT of 6E19 was overestimated; or the last, both zT were accurate but that of the 5E19 was underestimated so the optimum carrier density should actually be 5E19 with maximum zT above 0.7. Fortunately with precise transport modeling we are able to tell, based on the parameters of the compound, that the last case is most likely the real situation.

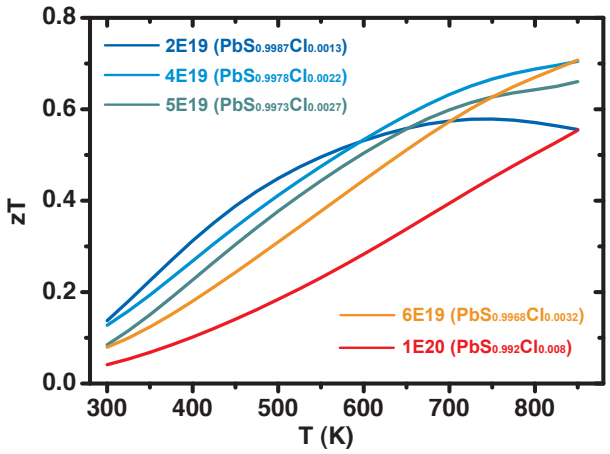

Figure 6.4. zT of Cl doped PbS as functions of temperature.

6.3 Transport Property Modeling with Multiply Scattering Mechanisms

This section contains the adopted reproduction of contents from *Adv. Energy Mater.* 3, 488 (2013), Copyrights © Wiley-VCH 2013, and Chapter 1, "*Thermoelectric Nanomaterials"*, Springer Series in Materials Science Vol. 182, 2013, p 3-32, Copyright © Springer 2013.

Same as the other Pb chalcogenides, a non-parabolic, single Kane band model is needed to better understand the transport properties of n-type PbS. In addition, the simple acoustic phonon scattering assumption needs to be changed. It was first noticed the mobility of undoped PbS are lower than some of the doped samples. The necessity of taking into account additional scattering mechanisms in modeling is realized, and it turns out not only in PbS, but in PbSe and PbTe as well by incorporating the polar scattering mechanism into the expression of relaxation time, the calculated results explained the mobility in low doped Pb chalcogenides surprisingly well.

At high temperatures the relaxation time of polar scattering from optical phonons can be written as[175]:

$$\tau_{po} = \frac{4\pi\hbar^2\varepsilon^{1/2}}{2^{1/2}(k_BT)^{1/2}e^2m_b^{*1/2}(\varepsilon_\infty^{-1}-\varepsilon_0^{-1})}(1+2\varepsilon\alpha)^{-1}(1+\varepsilon\alpha)^{1/2}\{[1-\delta\ln(1+\frac{1}{\delta})]-\frac{2\alpha\varepsilon(1+\varepsilon\alpha)}{(1+2\varepsilon\alpha)^2}[1-2\delta+2\delta^2\ln(1+\frac{1}{\delta})]\}^{-1} \quad \text{Equation 6.1}$$

and δ is a function of carrier energy:

$$\delta(\varepsilon) = \frac{e^2m_d^{*1/2}N_V^{2/3}}{2^{1/2}\varepsilon(k_BT)^{1/2}\pi\hbar\varepsilon_\infty}(1+\varepsilon\alpha)^{-1}{}^0F_1^{1/2} \quad \text{Equation 6.2}$$

With the generalized Fermi integrals given by Equation 3.25, the ε_0 and ε_∞ are the static and high frequency dielectric constants with unit F/m, rather than the unit-less relative values they could refer to.

Adding this to the deformation potential scattering using Matthiessen's rule:

$$\tau_{total}^{-1} = \tau_{ac}^{-1} + \tau_{po}^{-1} \quad \text{Equation 6.3}$$

With multiple scattering mechanisms the transport properties are expressed as functions of the total relaxation time:

Chemical carrier density: $n = \frac{(2m_d^*k_BT)^{3/2}}{3\pi^2\hbar^3}\int_0^\infty(-\frac{\partial f}{\partial\varepsilon})\varepsilon^{3/2}(1+\varepsilon\alpha)^{3/2}\,d\varepsilon$ Equation 6.4

Drift mobility: $\mu = \frac{e}{m_I^*} \frac{\int_0^\infty (-\frac{\partial f}{\partial \varepsilon}) \tau_{total}(\varepsilon)(\varepsilon + \alpha\varepsilon^2)^{3/2}(1+2\alpha\varepsilon)^{-1} d\varepsilon}{\int_0^\infty (-\frac{\partial f}{\partial \varepsilon})(\varepsilon + \alpha\varepsilon^2)^{3/2} d\varepsilon}$ Equation 6.5

Seebeck coefficient: $S = \frac{k_B}{e}(\frac{\int_0^\infty (-\frac{\partial f}{\partial \varepsilon}) \tau_{total}(\varepsilon)\varepsilon^{5/2}(1+\varepsilon\alpha)^{3/2}(1+2\varepsilon\alpha)^{-1} d\varepsilon}{\int_0^\infty (-\frac{\partial f}{\partial \varepsilon}) \tau_{total}(\varepsilon)\varepsilon^{3/2}(1+\varepsilon\alpha)^{3/2}(1+2\varepsilon\alpha)^{-1} d\varepsilon} - \eta)$ Equation 6.6

Hall factor: $A = \frac{3K(K+2)}{(2K+1)^2} \frac{\int_0^\infty (-\frac{\partial f}{\partial \varepsilon}) \tau_{total}(\varepsilon)^2 \varepsilon^{3/2}(1+\varepsilon\alpha)^{3/2}(1+2\varepsilon\alpha)^{-2} d\varepsilon \int_0^\infty (-\frac{\partial f}{\partial \varepsilon}) \varepsilon^{3/2}(1+\varepsilon\alpha)^{3/2} d\varepsilon}{(\int_0^\infty (-\frac{\partial f}{\partial \varepsilon}) \tau_{total}(\varepsilon)\varepsilon^{3/2}(1+\varepsilon\alpha)^{3/2}(1+2\varepsilon\alpha)^{-1} d\varepsilon)^2}$ Equation 6.7

Lorenz number:

$$L = (\frac{k_B}{e})^2 [\frac{\int_0^\infty (-\frac{\partial f}{\partial \varepsilon}) \tau_{total}(\varepsilon)\varepsilon^{7/2}(1+\varepsilon\alpha)^{3/2}(1+2\varepsilon\alpha)^{-1} d\varepsilon}{\int_0^\infty (-\frac{\partial f}{\partial \varepsilon}) \tau_{total}(\varepsilon)\varepsilon^{3/2}(1+\varepsilon\alpha)^{3/2}(1+2\varepsilon\alpha)^{-1} d\varepsilon} - (\frac{\int_0^\infty (-\frac{\partial f}{\partial \varepsilon}) \tau_{total}(\varepsilon)\varepsilon^{5/2}(1+\varepsilon\alpha)^{3/2}(1+2\varepsilon\alpha)^{-1} d\varepsilon}{\int_0^\infty (-\frac{\partial f}{\partial \varepsilon}) \tau_{total}(\varepsilon)\varepsilon^{3/2}(1+\varepsilon\alpha)^{3/2}(1+2\varepsilon\alpha)^{-1} d\varepsilon})^2]$$ Equation 6.8

The same methodology works for more general cases when other scattering mechanism such as the alloy scattering needs to be taken into account.

Figure 6.5 shows the 300 K carrier density dependence of Seebeck and Hall mobility, including literature data reported for PbS. The effective mass m_d^* = 0.39 m_e was determined by fitting the experimental Seebeck data. This value is comparable with the 0.4 m_e suggested in literature[176] using the single parabolic band model. The gray lines are calculated result assuming the same effective mass, but only deformation potential (acoustic) phonon scattering or only polar scattering. At n_H above 4 × 10^{18} cm^{-3}, assuming only acoustic phonon scattering would lead to the same S as when both scattering mechanisms are considered (the blue curve).

The mobility was well explained using the combined relaxation time, which predicted a maximum in mobility of 600 cm^2/Vs in μ_H when n_H is around 7 × 10^{18} cm^{-3}, whereas lower mobilities were observed in samples with both higher and lower carrier densities. maximum Hall mobility of 600 cm^2/Vs indicated by current model is consistent with the values reported by Petritz[177] (single crystal), Allgaier[137] (single crystal) and Johnsen[176] (polycrystalline), no grain size effect on mobility was observed. Zemel's report[178] of 700 cm^2/Vs on the other hand, was found in as-grown synthetic films subject to degradation upon time. Hence the current reported values are believed to reflect the best mobility achievable in high quality materials.

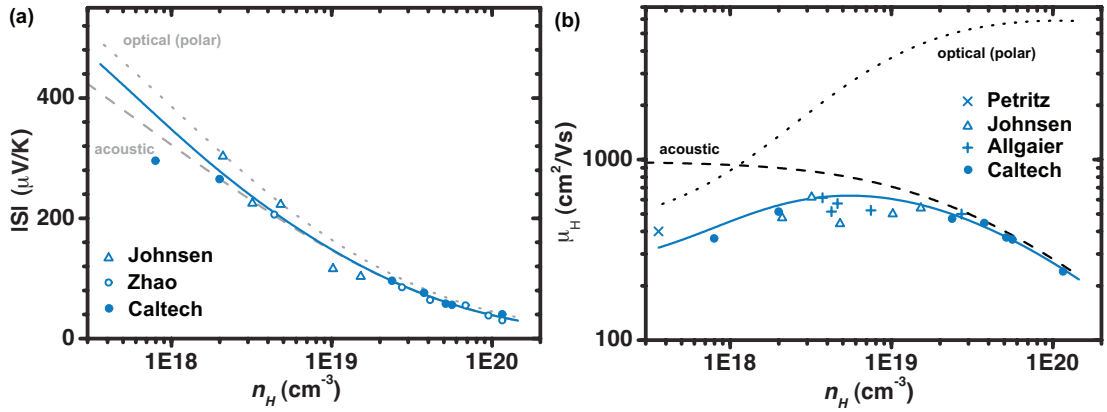

Figure 6.5. Seebeck coefficient a) and Hall mobility b) as function of Hall carrier density at 300 K for n type PbS.

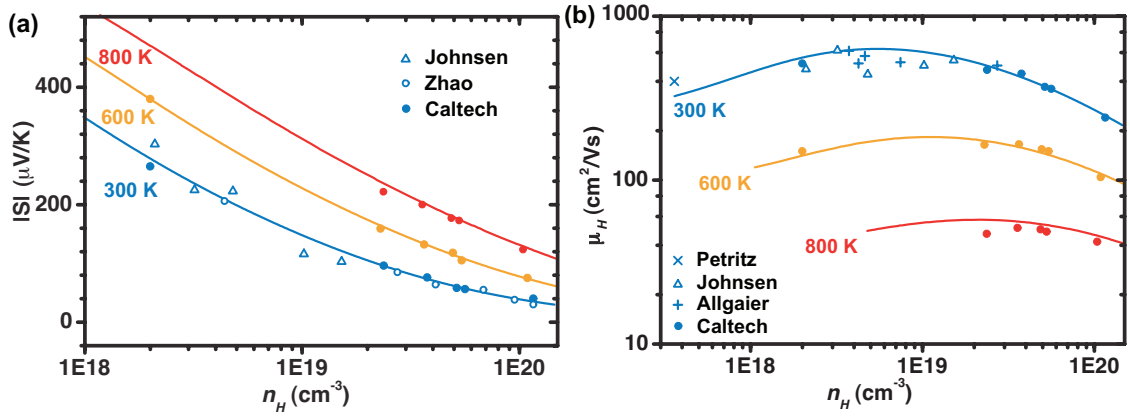

Figure 6.6. Seebeck coefficient a) and Hall mobility b) at different temperatures as function of Hall carrier density.

Every parameter in the expression of τ_{po} has been determined by other experiments, and the only adjustable parameter in the model above is the deformation potential coefficient Ξ, which is found to be 27 eV. This value is higher than the 25 eV found for PbSe probably due to increased polarity. It is further seen that up to n_H of 2×10^{19} cm^{-3} the polar scattering is of appreciable influence on mobility. However, the most efficient thermoelectric PbS has carrier density so high that such influence is secondary. As the temperature increases, the polar scattering becomes less and less important, due to its weaker temperature dependence than that of acoustic phonon scattering. Acoustic phonon scattering becomes predominant when the zT is high as found in most efficient thermoelectric materials. This can be also seen in the temperature dependence of Hall mobility

where the $T^{2.5}$ dependence is found largely obeyed, and the exponent of -2.5 is a sign of acoustic phonon scattering in lead chalcogenides due to the combined effect of temperature dependence of relaxation time and that of the effective mass ($m^* \sim T^{0.4}$ so that $\mu \sim \tau/m^* \sim T^{3/2}/m^{*5/2} \sim T^{-3/2}$).

Table 6.2. Physical properties of n-type lead chalcogenides that determine their thermoelectric performances.

parameter	PbTe	PbSe	PbS	note
Quality factor B at 850 K (L conduction band)	0.7	0.67	0.39	Same B leads to different zT with different α
Energy gap at L point E_g(eV) at 300 K	0.31	0.29	0.42	
Temperature dependence of E_g (meV/K) at L point	0.3	0.3	0.3	
Temperature Σ and L converge (K)	700	1100	1100	
Band non-parabolic parameter α at 850K	0.15	0.16	0.12	
Total density of state effective mass m_d^*, for n type at 300 K (m_e)	0.25	0.27	0.39	
r, $m_d^* \sim T^r$ (L band) at T < 800 K	0.5	0.5	0.4	
Inertial effective mass m_I^*, for n type at 300 K (m_e)	0.09	0.11	0.15	
Effective deformation potential coefficient Ξ, 300 K (eV)	23	25	27	
Lattice parameter c (Å)	6.46	6.13	5.94	
Molar mass	334.8	286.2	239.3	
Density (g/cm^3)	8.16	8.27	7.58	
Grüneisen constant	1.45	1.65	2	
Longitudinal speed of sound V_l (m/s)	2900	3220	3460	measured on polycrystalline disks
Transvers speed of sound V_t (m/s)	1600	1760	1910	
Average speed of sound V_{ave} (m/s)	1780	1960	2110	
Debye temperature θ_D(K)				
from measured speed of sound	163	191	210	
from specific heat measurement	125	160	220	
from longitudinal optical phonon frequency	160	190	300	
κ_L, 300 K (W/mK)	2	1.6	2.5	undoped samples
κ_L,850 K (W/mK)	0.7	0.7	1	moderate doped samples
$\kappa_{L,\,min}$ at high temperature (W/mK)	0.32	0.40	0.45	Cahill model
Vapor pressure, 850 K (10^{-3} atm)	3.3	2.3	0.17	

Moreover, when the same temperature dependence on band gap and effective mass found in PbSe are assumed for PbS. The model explained experimental Seebeck coefficient as well as mobility very well between 300 and 800 K, as shown in Figure 6.6.

In Table 6.2 some physical parameters related to the transport properties for all three lead chalcogenides are given. Compared to the other two compounds there are several factors that makes PbS inferior in thermoelectric performance: firstly for the band structure, the (inertial) effective mass in PbS is about 50% larger which would lead to considerably lower mobility. Secondly the lattice thermal conductivity of PbS is higher, at 850 K by 30% compared to the selenide or telluride as a result of the lighter anion and stiffer bonding (higher speed of sound). PbS actually has a large[12] Grüneisen parameter $\gamma = 2$ as compared with 1.45 for PbTe and 1.65 for PbSe, which is one of the largest known in thermoelectrics. However, this is largely compensated by its low average atomic mass and its strong bonding that leads to high speeds of sound. The deformation potential coefficient Ξ at room temperature is larger for PbS compared to PbSe and PbTe, but only by 8% and 17%, respectively. Moreover at high temperatures such differences become even less so that the deformation potential coefficient Ξ does not account for the lower zT in PbS.

One advantage of PbS over the other two lead chalcogenides is its highest melting point and lowest vapor pressure[179, 180] and thus a (possible) higher working temperature. Assuming the single Kane band model used to model transport properties up to 800 K will still be valid beyond it, the predicted zT would reach 1 at 1000K. This is shown in Figure 6.7. Also shown in this plot is that the optimum carrier density at 850 K would be around 4×10^{19} cm^{-3}, bear in mind that the optimized carrier density from modeling is always smaller than the experimentally determined n_H, even with the most precise three-band model (the reason is still not clear). In fact, the optimum n_H for n-type PbSe given by modeling was around 2×10^{19} cm^{-3}, the relative difference in optimum n_H given by the models is roughly the same as experimental result (5×10^{19} cm^{-3} for PbS versus 3×10^{19} cm^{-3} for PbSe), and the ratio is just the same as that of the band effective masses (0.23 m_e versus 0.15 m_e).

Figure 6.8 compares the electrical properties of PbSe and PbS at 800 K. The larger band mass in PbS has lead to higher Seebeck coefficients, but much lower mobility as well. The larger band mass account for one of the major reasons why PbS has lower zT than PbSe (the other being the higher thermal conductivity). Note zT Figure 6.8 c) for PbSe is higher than shown in Figure 4.11 (result from three-band modeling) mainly because the bipolar thermal conductivity is not considered here.

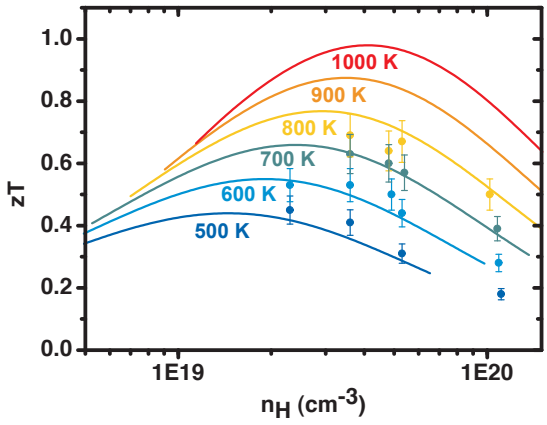

Figure 6.7. *zT* at different temperatures as function of Hall carrier density for n-type PbS. Error bars represent 10% uncertainty.

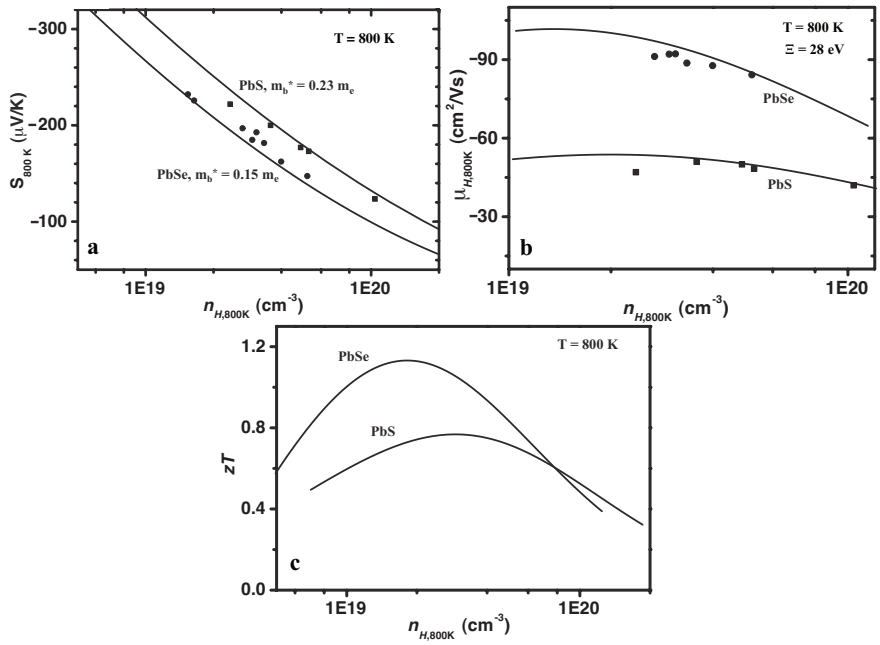

Figure 6.8. A comparison of a) Seebeck coefficient, b) Hall mobility, and c) *zT* of n-type PbSe and n-type PbS at 800 K. all lines calculated using single Kane band model.

6.4 Polar Scattering from Optical Phonon

This section contains the adopted reproduction of contents from Chapter 1, "*Thermoelectric Nanomaterials"*, Springer Series in Materials Science Vol. 182, 2013, p 3-32, Copyright © Springer 2013.

If the lattice contains more than one species of atoms meaning an electronegativity difference between two neighboring atoms, carriers can also be scattered by the changing dipole moment due to optical vibration. The polar scattering differs from the deformation potential scattering form optical phonons in that the interaction is of an electro-static interaction nature rather than a perturbation in lattice potential. There are two important quantities for polar optical scattering. The first is the dimensionless polar coupling constant α_{po}, which governs the magnitude of interaction between carriers and polarization of optical phonons[95, 181]:

$$\alpha_{po} = \frac{e^2}{4\pi\hbar}\left(\frac{m^*}{2\hbar\omega_l}\right)^{1/2}(\varepsilon_\infty^{-1} - \varepsilon_0^{-1}) \qquad \text{Equation 6.9}$$

where ε_0, ε_∞ are the static and high frequency dielectric constant (with unit F/m, not relative values). The second is the optical phonon temperature $k_B\Theta = \hbar\omega_l$ (close to the Debye temperature). Generally materials with large effective mass and low optical phonon Debye temperature Θ are likely to have strong carrier-polarization interaction. Also materials with large ε_0 also tend to have strong interaction. In III-V[109, 182, 183] and II-VI[184, 185] semiconductors, ε_0 is in fact not large but close to ε_∞ so the last term in Equation 6.9 is also large, which makes the polar scattering by optical phonons important, even dominant in certain cases.

For general cases a universal τ can't be defined due to the inelastic nature of the polar scattering, and the transport parameters are calculated using variational method. Detailed calculations have been given by researchers such as Howarth and Sondheimer[104], and Ehrenreich[186]. For most good thermoelectric materials with high temperature application, when $T > \Theta$, a relaxation time can be defined.

Since the rigorous derivation of transition rate following a textbook has not been carried out, it is better here to only list a few key points during the derivation while leaving all details to the reference in Ziman or Askerov. The calculation of interaction Hamiltonian is essentially to determine the electromagnetic field induced by propagation polarization waves that perturbs the electronic states. So the Hamiltonian has the form:

$$H_{po} = e\varphi \qquad \text{Equation 6.10}$$

The field strength is determined from its gradient, which is linked to the polarization vector *P(r)*.

$$4\pi P(r) = \nabla\varphi \qquad \text{Equation 6.11}$$

P(r) is further related to the displacement vector *u(r)*:

$$P(r) = \frac{1}{2}\left[\left(\frac{\hbar\omega}{2\pi V}\right)\left(\frac{1}{\varepsilon_\infty} - \frac{1}{\varepsilon_0}\right)\right]^{1/2} \sum_q \overrightarrow{e_{q,n}}(a_{q,n}e^{iqr} - a_{q,n}^* e^{-iqr}) \qquad \text{Equation 6.12}$$

So the final form for the Hamiltonian is:

$$H_{po} = 2\pi e\left[\left(\frac{\hbar\omega}{2\pi V}\right)\left(\frac{1}{\varepsilon_\infty} - \frac{1}{\varepsilon_0}\right)\right]^{1/2} \sum_q \frac{1}{q}\overrightarrow{e_{q,n}}(a_{q,n}e^{iqr} - a_{q,n}^* e^{-iqr})$$

$$= 2\pi e\left[\left(\frac{\hbar\omega}{2\pi V}\right)\left(\frac{1}{\varepsilon_\infty} - \frac{1}{\varepsilon_0}\right)\right]^{1/2} \frac{1}{q}(a_{q,n}e^{iqr} - a_{q,n}^* e^{-iqr}) \qquad \text{Equation 6.13}$$

The dot product q•e implies the interaction is only between electrons and longitudinal optical branch so the summation of different branch is omitted.

The rest of the derivation is largely similar to that for acoustic phonon deformation potential scattering.

Since thermoelectric materials are usually heavily doped, the screening of polarity vibration by free electrons must also be considered. Ravich's derivation takes into account this together with the band nonparabolicity in lead chalcogenides, which gives Equation 6.1, notice that in this equation all parameters are independent measurable. The static dielectric constant ε_0 of a conductor is probably difficult to measure directly, but can be derived using the ratio of the longitudinal optical phonon frequency over that of the transverse optical phonon at Brillion Zone center $k = 0$, via the Lyddane-Sachs-Teller relation.

Equation 6.1 has been used by other researchers when studying the scattering mechanism in PbTe[106, 187, 188] and Bi_2Te_3.[189] It should also be a reasonable expression for such scattering mechanism in other systems with Kane band behavior, such as $CoSb_3$ at high temperature (Θ for $CoSb_3$ is ~300 K).

Qualitatively from Equation 6.1:

$$\tau_{po} \propto m^{*-1/2} T^{-1/2} \varepsilon^{1/2} \qquad \text{Equation 6.14}$$

Compared to Equation 3.47 for acoustic phonon scattering, relaxation time governed by polar scattering from optical phonons has a weaker dependence on temperature and effective mass. It will increase with carrier energy ε, instead of decrease as for the case of acoustic phonon scattering. This

implies it would be less important for most thermoelectric materials above room temperature. In more general case, the exponent r in $\tau_{po} \sim \varepsilon^r$ is plotted against Θ/T by Ehrenreich, r changes greatly[186] with T and there is a singularity around $T = \Theta/2$.

Table 6.3. The polar coupling constant for a few compound semiconductors

	ε_0	ε_∞	Θ	α_{po}	comment
PbTe	414	33	160	0.29	m^* use 300 K value from Seebeck data
PbSe	204	23	190	0.36	
PbS	169	17	300	0.45	
$CoSb_3$	42 cal[b]	32 cal 25 exp	306	0.07	For p type, m^* use 0.15 m_e
Bi_2Te_3	290 (//c) 75 ($\perp$ c)	85 (//c) 50 ($\perp$ c)	164	0.13 (//c) 0.07 ($\perp$ c)	m^* from Seebeck data from CRC handbook
GaAs	13	11	344	0.08	
InSb	17	16	203	0.01	
ZnO	8	4	660	1.02	
CdTe	10	7	158	0.41	

Lead chalcogenides are unique compounds in term of their extraordinarily large static dielectric constants. For instance for PbTe, ε_0 around 400 has been reported by different groups from different measurement techniques[190, 191]. In contrast, ε_0 for most III-V and II-V compounds are usually[124] from 10 to 20. Considering the low Debye temperatures in lead chalcogenides, large polar coupling constants α_{po} would be expected in these compounds. In the table below α_{po} is compared for a few semiconductors. Lead chalcogenides are seen to have larger α_{po} compared to other typical thermoelectric materials as well as III-V compounds, whereas some II-V compounds show the largest α_{po}, which stems from their small yet different dielectric constants.

From the result shown in Table 6.3 the polar scattering is important around room temperature in lightly doped lead chalcogenides. Its magnitude in other compounds would be less as can be judged from the values of α_{po}. For most heavily doped thermoelectric materials neglecting the contribution of polar scattering from optical phonons should not lead to drastic error in modeling and the acoustic phonon scattering assumption can be considered valid.

Chapter 7

Solid Solutions between Lead Chalcogenides

7.1 Introduction

Alloying, i.e., forming solid solutions is one of the few proven strategies that lead to best *zT*s in materials for high temperature applications. Among them are the well known SiGe and TAGS alloys[192, 193] used in the radioisotope thermoelectric generators (RTGs) powering multiple spacecrafts for decades. Alloying in thermoelectrics provides a wide control of different materials properties, including thermal conductivity[194-196], the band structure[27, 197-200], mechanical properties[201] and even carrier density[92, 202]: all closely related to the thermoelectric performance and *zT*. Alloying has long been considered an effective approach for good thermoelectrics because the lattice thermal conductivities are lower than the constituent compounds due to phonon scattering from disordered lattice. However, this effect could also be compensated by a reduction in carrier mobility due to electron scattering from the same disorder. Pb Chalcogenides provide a perfect platform to study the influence of atomic substitution on transport properties because these compounds are among the best-studied semiconductors so the problem will have a well-defined baseline. Using a specifically designed study of n-type $PbTe_{1-x}Se_x$ solid solution ($0 \leq x \leq 1$) as a function of composition, temperature and doping level, quantitative modeling of transport properties reveals the important parameters characterizing these effects. The same methodology was later applied to $PbSe_{1-x}S_x$ and was found successfully explained experimental results, and disapproved the previously suggested

idea that forming nano-structures is essential to achieve high *zT* in this system. Within the atomic substitutional framework, a general criterion for the improvement of *zT* due to atomic disorder in solid solutions is derived and can be applied to several thermoelectric solid solutions, allowing a convenient prediction of whether better thermoelectric performance could be achieved in a given solid solution. This criterion tells in general whether an improvement of *zT* can be expected if the band parameters of the solid solutions can be approximated by a tie line between their two constituent compounds.

7.2 Sample Synthesis and Transport Properties

The synthesis generally followed normal melting and hot pressing routine. For the $PbTe_{1-x}Se_x$ the synthesis and characterization of samples on the PbTe-rich side were carried out by colleague Aaron LaLonde. Iodine was used as the dopant (in form of PbI_2), whereas those on the PbSe-rich side were doped with Br ($PbBr_2$). The $PbSe_{1-x}S_x$ samples were synthesized by visiting researcher Xianlong Cao and Jianli Wang, samples on PbSe-rich side were doped with Br and the others were doped with Cl ($PbCl_2$).

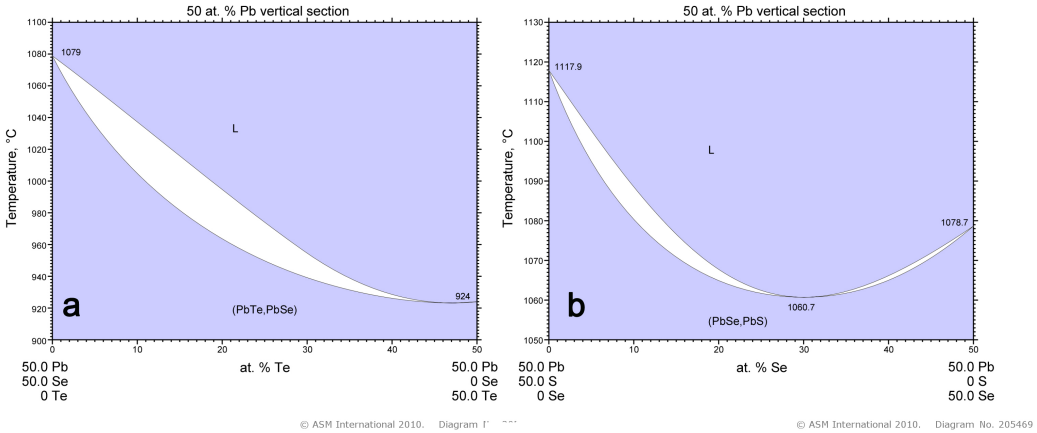

Figure 7.1. Phase diagrams of a) PbTe-PbSe and b) PbSe-PbS systems, complete solid solution is seen in each case. Images taken from ASM alloy phase diagram database.

7.2.1 N-type $PbTe_{1-x}Se_x$

The typical solid solution behavior is suggested by phase diagram (Figure 7.1) and was first checked by XRD on hot pressed samples, lattice parameter changes with composition following the Vegards's law, as seen in Figure 7.2.

Table 7.1. A list of samples of the $PbTe_{1-x}Se_x$ solid solutions and properties at 300 K.

Label	Composition	Transport Properties		
		$n_H(10^{19}cm^{-3})$	S (μV/K)	μ_H (cm^2/Vs)
024-9010	$(PbSe_{0.9}Te_{0.1})_{0.9976}(PbBr)_{0.0024}$	3.76	-51.9	-581
018-9010	$(PbSe_{0.9}Te_{0.1})_{0.9982}(PbBr)_{0.0018}$	2.98	-59.1	-665
012-9010	$(PbSe_{0.9}Te_{0.1})_{0.9988}(PbBr)_{0.0012}$	2.07	-78.3	-750
024-8515	$(PbSe_{0.85}Te_{0.15})_{0.9976}(PbBr)_{0.0024}$	3.77	-49.9	-539
018-8515	$(PbSe_{0.85}Te_{0.15})_{0.9982}(PbBr)_{0.0018}$	2.85	-56.1	-630
012-8515	$(PbSe_{0.85}Te_{0.15})_{0.9988}(PbBr)_{0.0012}$	1.89	-78.1	-767
024-8020	$(PbSe_{0.8}Te_{0.2})_{0.9976}(PbBr)_{0.0024}$	3.86	-45.3	-525
018-8020	$(PbSe_{0.8}Te_{0.2})_{0.9982}(PbBr)_{0.0018}$	2.89	-61.6	-635
012-8020	$(PbSe_{0.8}Te_{0.2})_{0.9988}(PbBr)_{0.0012}$	1.84	-79.5	-738
024-7525	$(PbSe_{0.75}Te_{0.25})_{0.9976}(PbBr)_{0.0024}$	3.86	-47.1	-505
018-7525	$(PbSe_{0.75}Te_{0.25})_{0.9982}(PbBr)_{0.0018}$	2.78	-58.4	-607
012-7525	$(PbSe_{0.75}Te_{0.25})_{0.9988}(PbBr)_{0.0012}$	1.87	-76	-736
024-7030	$(PbSe_{0.7}Te_{0.3})_{0.9976}(PbBr)_{0.0024}$	3.80	-44.4	-465
018-7030	$(PbSe_{0.7}Te_{0.3})_{0.9982}(PbBr)_{0.0018}$	2.65	-58.5	-592
012-7030	$(PbSe_{0.7}Te_{0.3})_{0.9988}(PbBr)_{0.0012}$	1.90	-76.3	-658
028-2575	$(PbSe_{0.25}Te_{0.75})_{0.9972}(PbI)_{0.0028}$	3.84	-41.7	-514
028-2080	$(PbSe_{0.2}Te_{0.8})_{0.9972}(PbI)_{0.0028}$	3.69	-41.3	-527
028-1585	$(PbSe_{0.15}Te_{0.85})_{0.9972}(PbI)_{0.0028}$	3.81	-43.6	-563
028-1090	$(PbSe_{0.1}Te_{0.9})_{0.9972}(PbI)_{0.0028}$	3.67	-46.3	-671
028-0595	$(PbSe_{0.05}Te_{0.95})_{0.9972}(PbI)_{0.0028}$	3.97	-39.4	-678
028-0010	$(PbTe)_{0.9972}(PbI)_{0.0028}$	3.87	-39	-889
0010	PbTe			
0595	$PbSe_{0.05}Te_{0.95}$			
1090	$PbSe_{0.1}Te_{0.9}$			
1585	$PbSe_{0.15}Te_{0.85}$	Only κ_L were measured		
2080	$PbSe_{0.2}Te_{0.8}$			
2575	$PbSe_{0.25}Te_{0.75}$			
7030	$PbSe_{0.7}Te_{0.3}$			
8020	$PbSe_{0.8}Te_{0.2}$			
9010	$PbSe_{0.9}Te_{0.1}$			

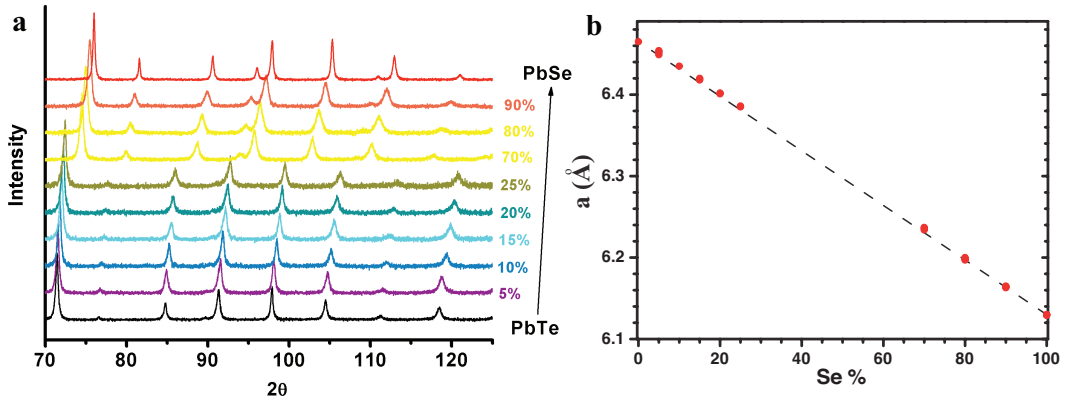

Figure 7.2. a) XRD lattice parameter of $PbTe_{1-x}Se_x$ and b) lattice constant calculated using standard extrapolation method, typical solid solution behavior is seen.

Vegard's law is the signature of solid solutions, which is a quite old concept. The terminology of "solid solution" is actually not very clear. Wikipedia defines a solid solution as a solid that contains one or more solute, while keeping its crystal structure unchanged. This definition does not set requirement for the detailed configuration of solute in the "solvent" lattice, or matrix. Thus, the solute atoms could be either ordered or randomly distributed, or can be either substitutional or interstitial. Generally, if long range ordering exists, the system would be considered a new compound (called ordered alloys) with distinctive diffraction pattern. With this excluded, a "solid solution" could still mean either a random distribution of solute, or random at long scale but ordered in a shorter length scale. The old picture of a (substitutional) solid solution is of completely random distribution of solute atoms. Thermodynamically this should maximize the entropy of system and be the most stable configuration. But it is still possible compositional fluctuation happens at some short scale, or, the solute atoms are correlated when there is more than one type of them, giving rise to nano-structures in the bulk for either case. This is probably true in many solid solution systems as they are examined by advanced TEM technique available these days. Specifically, a lot of PbTe and PbSe based systems have been found[203-207] nanostructured. In this study, we will accept these TEM observations and not to care about the very detailed atomic configurations. We will refer our samples as alloys since it could mean any mixture of two compounds, including nano scale inclusions.

The conduction band of both PbTe and PbSe contains a single minimum at L point of the first Brillouin zone. The dispersion relation near the band edge can be better approximated with the non-

parabolic Kane band model, instead of the parabolic band model. These basic band features should apply for the solid solution between them.

The difference in band structure affects the transport properties, which is understood primarily through the effective mass (when the minority carriers are negligible). The total density-of-state effective mass m_d^* are very similar for the conduction band in PbTe and PbSe (being slightly smaller in PbTe). This quantity for their solid solution is also found nearly independent of composition. To demonstrate this the Seebeck coefficients were plotted against Hall carrier density at different temperatures in Figure 7.3. The solid lines are calculated results using $m_{d\,,300K}^* = 0.27\ m_e$ and $dLnm_d^*/dLnT = 0.48$ under the acoustic phonon scattering dominant assumption and the single Kane band (SKB) model. The open symbols are from PbTe (squares) and PbSe (circles), both showing good agreement with the calculated curves because difference in effective mass of these two compounds is within the uncertainty of measurement. The Seebeck coefficients of solid solutions are also found following the same trend regardless of their composition. In other words m_d^* does not change in n type $PbTe_{1-x}Se_x$ and samples with similar Hall carrier density would have similar Seebeck coefficient values.

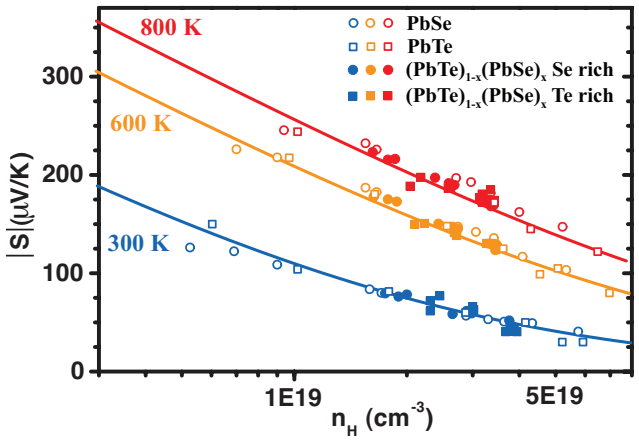

Figure 7.3. Seebeck coefficient versus Hall carrier density of $(PbTe)_{1-x}(PbSe)_x$ solid solutions at different temperatures.

Halogens do not change the band structure of lead chalcogenides[208]. The substitution of Br and I for Se and Te adds one electron per atom to the conduction band as long as these electrons are delocalized. Delocalization occurs at sufficiently high dopant concentrations and temperatures measured in this study. This allows the following discussion on the carrier concentration dependence of Seebeck coefficient without involving additional band structure modification due to

I- or Br-doping. Figure 7.4 shows the Hall carrier density and Seebeck coefficient as function of alloy composition. It demonstrates the consistency of S values among samples with different composition but similar doping level. The very small fluctuation in n_H and S within each group, named after their nominal Hall carrier density at 300K, assures that the following discussions are based on results not affected by carrier density (or chemical potential) difference.

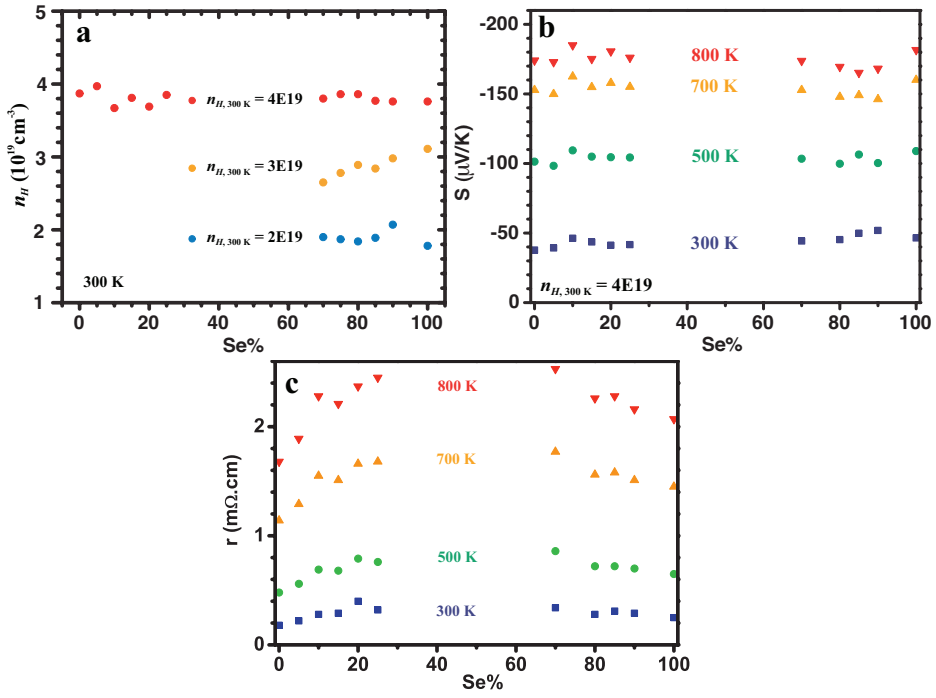

Figure 7.4. a) Hall carrier density at 300 K and b) Seebeck coefficient ($n_{H,\,300K}$ = 4E19) as function of alloy composition.

The band gap of PbTe and PbSe are[116] 0.19 eV and 0.17 eV (0 K), respectively. Temperature dependence of $+3 \times 10^{-4}$ eVK^{-1} was determined for both compounds. According to the two-valence-band model, the band gaps saturate at 0.36 eV for PbTe and 0.47 eV for PbSe when the energy level of L valence band reaches that of the temperature independent Σ band. However, how the band gap changes[209, 210] in $(PbTe)_{1-x}(PbSe)_x$ solid solutions above room temperature has not been studied and it is thus assumed that the band gaps of solid solutions are linear combinations of those of two binary compounds at that temperature. We note that the experimental results on optical band gap measurements is consistent with this assumption within 0.02 eV in undoped samples[210, 211] at both 77 K and 300 K. This is true even for doped samples[207] with influence from free carrier absorption.

In Figure 7.5 the drift mobility ($\mu = \mu_H/A$) of n-type $(PbTe)_{1-x}(PbSe)_x$ is plotted as function of alloy compositions. The mobility drops dramatically as a small amount of different atoms (x ~ 0.05) were introduced and then gradually saturate and reach a region after x > 0.3 where the mobility is relatively insensitive to alloy composition. Two sets of room temperature data are included in Figure 7.5 a). The red dots are from samples with carrier density of about 4×10^{19} cm^{-3}. The black crosses are for undoped samples taken from[212] Efimova and Stil'bans' report. The carrier density of these samples are not reported, the chemical potential is thus estimated according to the reported mobility at both ends PbTe and PbSe, and was decided to be 1.7 (correspond to n_H ~ 1E19).

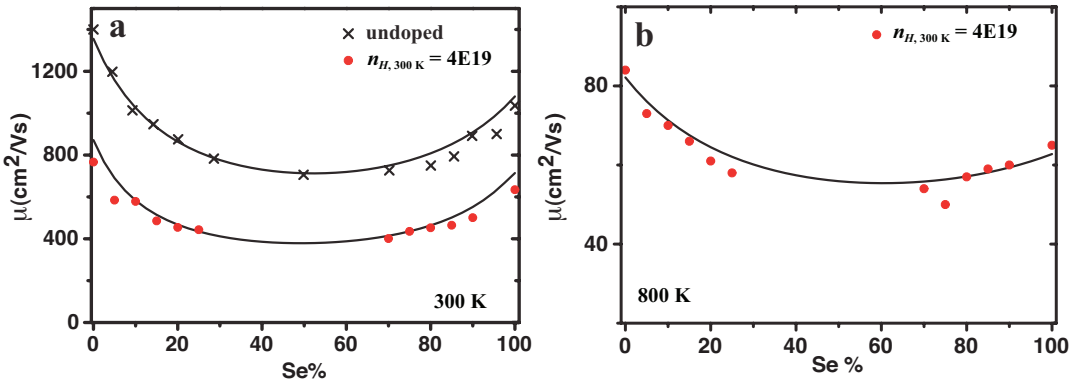

Figure 7.5. The drift mobility at a) 300 K and b) 800 K for $(PbTe)_{1-x}(PbSe)_x$ solid solutions with different doping levels. Solid lines are calculated results.

Solid curves in Figure 7.5 are calculated mobility with single Kane band model taking into account deformation potential phonon scattering, polar scattering from optical phonons, and alloy scattering. All physical parameters in the relaxation time expressions have been determined from previous study, or have been directly measured with independent techniques, except for the alloy scattering potential U, which is used as an adjustable fitting parameter. The solid curves are calculated with U = 1.1 eV, independent of composition or temperature.

The relative reduction of mobility described by μ/μ_{PbX}, where μ_{PbX} is the mobility of corresponding matrix compound with the same carrier density, is plotted in Figure 7.6 at 300 K for samples with different carrier densities. It is found largely the same for different sets of samples with different doping level. This is due to the very close energy dependence between the alloy scattering and the deformation potential scattering.

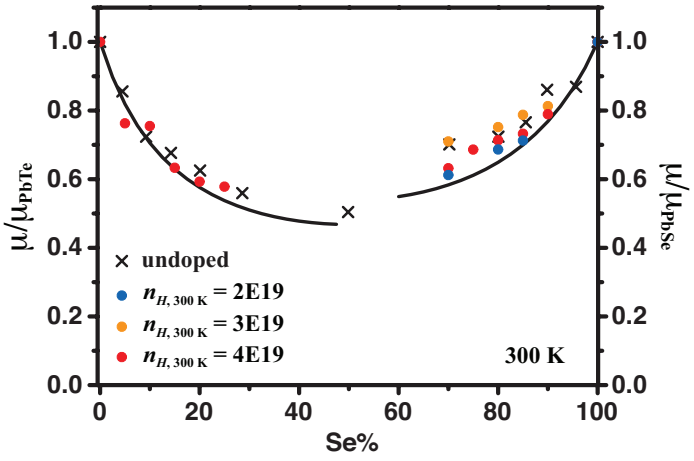

Figure 7.6. Relative mobility reduction in $(PbTe)_{1-x}(PbSe)_x$ at 300 K for samples with different doping level.

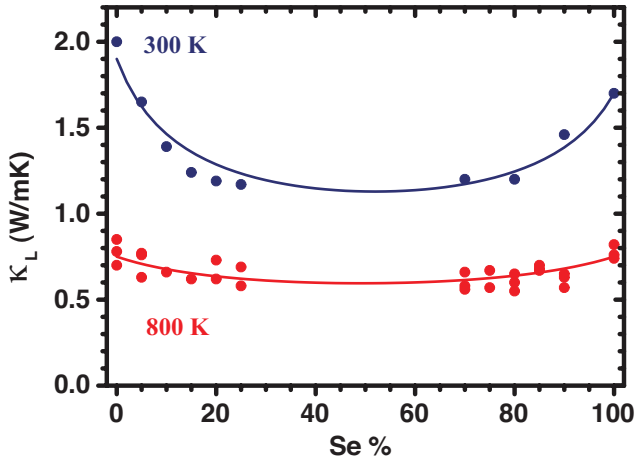

Figure 7.7. Lattice thermal conductivity as function of composition in $PbTe_{1-x}Se_x$.

The other important effect seen in solid solutions is the reduction of lattice thermal conductivity, which most obviously makes solid solutions desirable for thermoelectrics. The experimental result as well as modeled κ_L as function of composition, at both 300 K and high temperature for $PbTe_{1-x}Se_x$ are shown in Figure 7.7. Since the calculation is for the full composition range rather than the dilute limit, the "pure" compounds without alloying are virtual crystals with all properties taken as the linear average of two binary compounds. There are no fitting parameters involved in the calculation of κ_L for the solid solutions. For $PbTe_{1-x}Se_x$ the model as well as experimental result indicates a maximum of 45% reduction (relative to that of pure PbTe) in κ_L at room temperature. We notice that previous study on p-type alloys[7] as well as early Ioffe's result[196] has indicated a

larger reduction (maximum 55%) probably because κ_L were calculated from doped samples for p-type alloys, and casual sample preparation (by simply mixing and pressing PbTe and PbSe powders together) for the early Ioffe result. At 800 K both experiment and the model indicate a much weaker reduction with a maximum of 20%.

In the simplest solid solutions, the net result of alloying on zT relies on two effects with opposite influences: mobility reduction and lattice thermal conductivity reduction. In the case of n type $PbTe_{1-x}Se_x$ these two effects are mostly compensated throughout the composition range. In Figure 7.8 zT at different temperatures (for samples with $n_{H,300K} = 4 \times 10^{19}$ cm^{-3}) are shown as function of alloy composition and no appreciable difference was observed when Se content change from 0% to 100%.

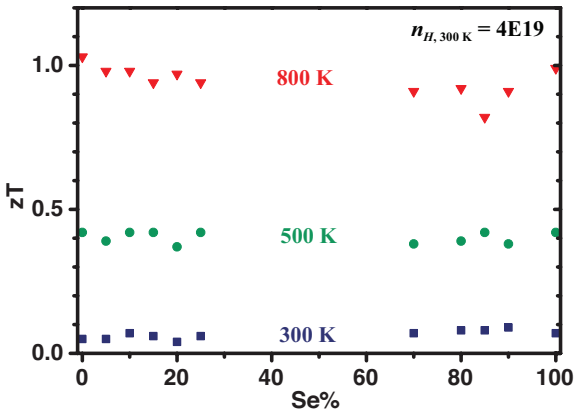

Figure 7.8. zT at different temperatures for $PbTe_{1-x}Se_x$ alloys with different compositions.

With all parameters in the transport model determined, zT can be calculated at a given temperature for samples with any carrier density and alloy composition. Figure 7.9 shows the zT mapping at 800 K. In addition to the good agreement with experimental data (colored dots), the maximum zT (solid cyan line) achievable for each composition is found almost unchanged (around 1.1, see the projection on Se%-zT plane). The optimum Hall carrier density is around 2×10^{19} cm^{-3} (see the projection on n_H-Se% plane). A zT plateau is formed where zT is essentially unaffected by the solid solution composition as long as the optimum carrier density is reached, which is not the case for many other systems. The freedom in composition also means that the lattice parameter can be altered in the range of 6.12 Å to 6.46 Å, which may be advantageous for thin film processing or strain engineering.

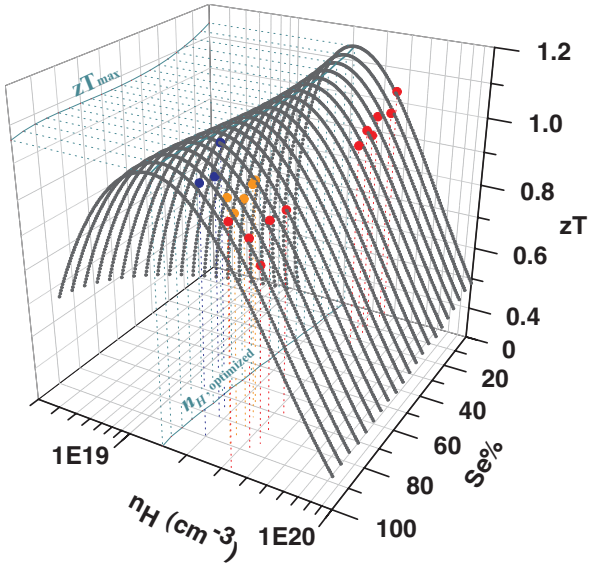

Figure 7.9. Calculated *zT* mapping at 800 K for different alloy composition and Hall carrier density, the maximum *zT* achievable is almost independent of alloy composition. No improvement of *zT* can be achieved by substituting on the anion site.

7.2.2 N-type $PbSe_{1-x}S_x$

The Vegard's law is also observed for $(PbSe)_{1-x}(PbS)_x$ as shown in Figure 7.10.

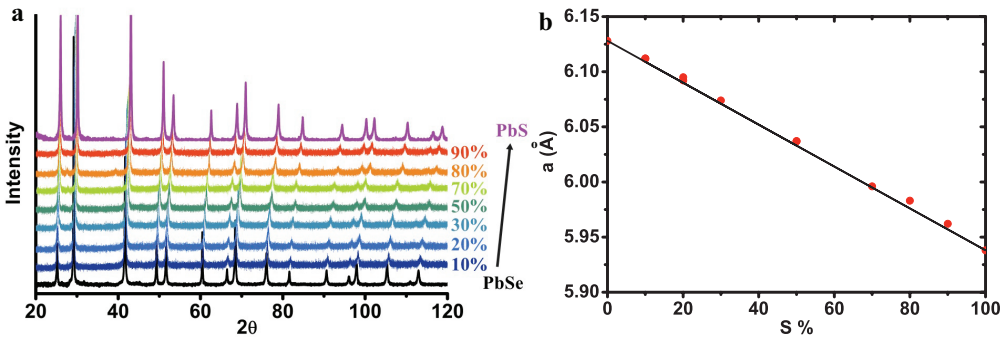

Figure 7.10. a) XRD lattice parameter of $PbSe_{1-x}S_x$ and b) lattice constant calculated using standard extrapolation method.

The hot pressed samples were examined with SEM and no secondary precipitates down to 100 nm could be found, as shown in Figure 7.11 and Figure 7.12.

Table 7.2. A list of samples of $PbSe_{1-x}S_x$ alloys and some properties at 300 K.

Label	Composition	Transport Properties		
		$n_H(10^{19}cm^{-3})$	S (μV/K)	μ_H (cm^2/Vs)
20-90	$(PbSe_{0.9}S_{0.1})_{0.998}(PbBr)_{0.00}$	3.17	-65	-470
20-90-R2	$(PbSe_{0.9}S_{0.1})_{0.998}(PbBr)_{0.00}$	3.54	-60	-425
20-80	$(PbSe_{0.8}S_{0.2})_{0.998}(PbBr)_{0.00}$	2.9	-66	-451
20-80-R1	$(PbSe_{0.8}S_{0.2})_{0.998}(PbBr)_{0.00}$	3.8	-60	-501
20-70	$(PbSe_{0.7}S_{0.3})_{0.998}(PbBr)_{0.00}$	3.39	-54	-418
35-50-t4	$(PbSe_{0.5}S_{0.5})_{0.9965}(PbCl)_{0.0}$	6.19	-40	-291
35-50-b4	$(PbSe_{0.5}S_{0.5})_{0.9965}(PbCl)_{0.0}$	7.34	-39	-242
18-30	$(PbSe_{0.3}S_{0.7})_{0.9982}(PbCl)_{0.0}$	2.62	-83	-415
35-20-t4	$(PbSe_{0.2}S_{0.8})_{0.9965}(PbCl)_{0.0}$	6.2	-42	-281
32-20-43#	$(PbSe_{0.2}S_{0.8})_{0.9968}(PbCl)_{0.0}$	5.4	-71	-202
18-20-28#	$(PbSe_{0.2}S_{0.8})_{0.9982}(PbCl)_{0.0}$	3	-78	-292
42-10-50#	$(PbSe_{0.1}S_{0.9})_{0.9958}(PbCl)_{0.0}$	7.4	-46	-313
32-10-30#	$(PbSe_{0.1}S_{0.9})_{0.9968}(PbCl)_{0.0}$	6.1	-57	-277
18-10-29#	$(PbSe_{0.1}S_{0.9})_{0.9982}(PbCl)_{0.0}$	3.2	-82.5	-208
35-10-6#	$(PbSe_{0.1}S_{0.9})_{0.9965}(PbCl)_{0.0}$	6.7	-52	-325
28-05	$(PbSe_{0.05}S_{0.95})_{0.9972}(PbCl)_0$	4.4	-67	-320
28-10	$(PbSe_{0.1}S_{0.9})_{0.9972}(PbCl)_{0.0}$	4.7	-66	-343
28-20	$(PbSe_{0.2}S_{0.8})_{0.9972}(PbCl)_{0.0}$	4.8	-56	-287
28-30-5#or48#	$(PbSe_{0.3}Te_{0.7})_{0.9972}(PbCl)_{0.}$	5.4	-55	-358
28-50	$(PbSe_{0.5}Te_{0.5})_{0.9972}(PbCl)_{0.}$	4.7	-58	-373
05	$PbSe_{0.05}S_{0.95}$	0.42	-230	-562
10	$PbSe_{0.1}S_{0.9}$	0.27	-255	-494
20	$PbSe_{0.2}S_{0.8}$	0.37	-245	-564
30	$PbSe_{0.7}S_{0.3}$	0.29	-229	-590
50	$PbSe_{0.5}S_{0.5}$	0.36	-207	-687
70	$PbSe_{0.7}S_{0.3}$	0.25	-218	-802
80	$PbSe_{0.8}S_{0.2}$	0.51	-185	-655
90	$PbSe_{0.9}S_{0.1}$	0.3	-203	-964
p-50	$PbSe_{0.5005}S_{0.5005}$	0.24	218	487
p-60	$PbSe_{0.6006}S_{0.4004}$	0.08	310	593
p-70bi	$PbSe_{0.7007}S_{0.3003}$	0.04	190	209
p-80	$PbSe_{0.8008}S_{0.2002}$	0.12	254	780
p-90bi	$PbSe_{0.9009}S_{0.1001}$	0.04	320	333

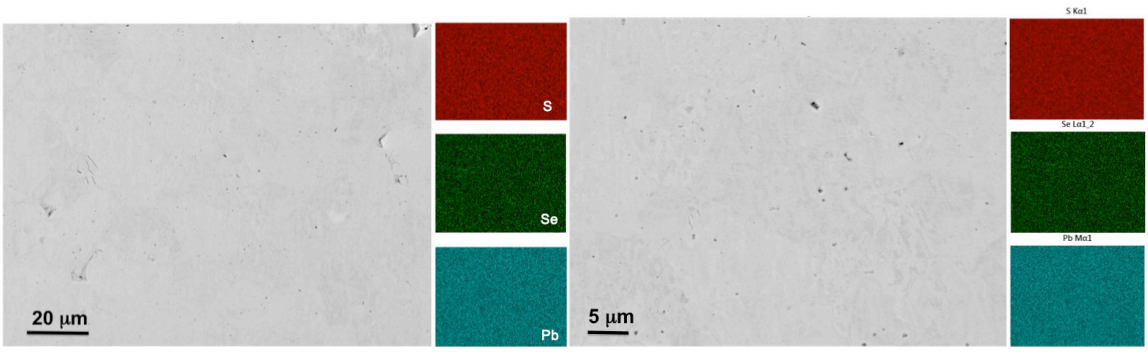

Figure 7.11. Back scattered SEM image on polished surface of $PbSe_{0.3}S_{0.7}$ and the EDS mapping result on two different scales. No microstructural feature other than pores were seen and each element is found evenly distributed.

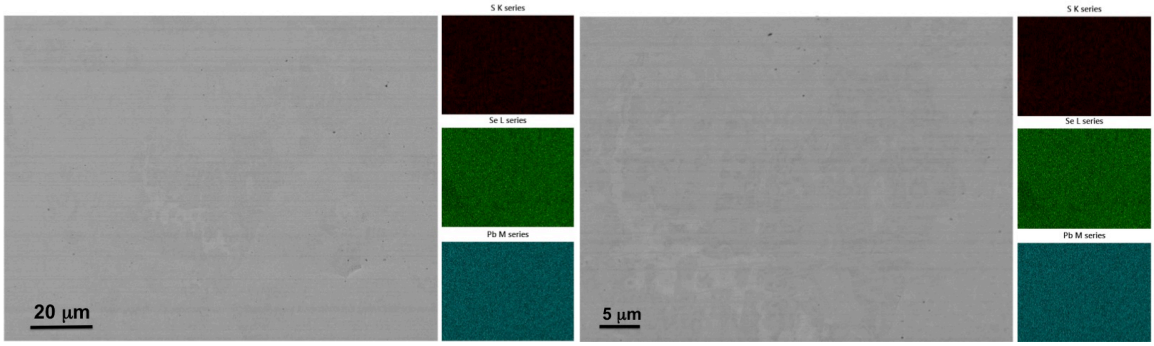

Figure 7.12. Back scattered SEM image on polished surface of $PbSe_{0.7}S_{0.3}$ and the EDS mapping result on two different scales.

Compared with $PbTe_{1-x}Se_x$, the $PbSe_{1-x}S_x$ system has added complexity in that the conduction bands of PbSe and PbS have quite different effective masses, as a result instead of sharing the same Pisarenko relation as for the $PbTe_{1-x}Se_x$ system, samples with different composition are found following different Pisarenko relations. Figure 7.13 a) shows the Pisarenko relation for different alloy compositions. The (density-of-state, DOS) effective masses (m_d^*) are estimated under the assumption of single Kane band (SKB) model with combined carrier scattering of acoustic phonon scattering as well as polar scattering from optical phonons and alloy scattering. The $PbSe_{1-x}S_x$ alloys have different m_d^* values depending on the value of x, which can be explained by the different effective masses of the conduction band for binary PbSe (0.27 m_e) and PbS (0.39 m_e). As shown in Figure 7.13 b), the effective mass increases with increasing S content, roughly following the linear average between two binary compounds (solid line). An abrupt change of DOS effective mass, which is often an indication of band convergence, is not observed. Within experimental uncertainty

the effective mass changes linearly, although there could be slight bowing (nonlinearity) as seen in some III-V semiconductor alloys[213]. For dilute alloys the difference in effective mass is comparable with experimental uncertainty, which is probably why no difference in effective mass was observed in a previous study by Androulakis et al. on the same system.

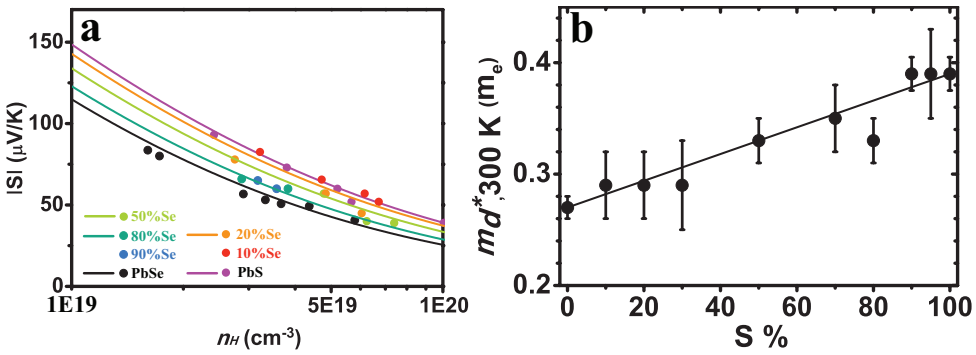

Figure 7.13. a) Pisarenko relations at 300 K for $PbSe_{1-x}S_x$ samples with different composition, b) density of states effective mass calculated by fitting the Pisarenko relation, error bars are based on number of samples the fitting was based on.

The observed mobility reduction for $PbSe_{1-x}S_x$ samples is not symmetric: it decreases quickly as PbS is added to PbSe whereas only a marginal reduction in mobility is seen when PbSe is introduced to PbS, regardless of doping or temperature. Same analysis is also performed to model the mobilities in solid solutions, with the changing effective mass taken into account. The alloy scattering potential U is found to be 1.0 eV, a very similar value as seen in $PbTe_{1-x}Se_x$. With no more adjustable parameters, the modeled mobility is consistent with experimental result on doped samples at both 300 K and 800 K, as well as undoped samples at 300 K. the results[214] reported by Stavitskaya were also included.

The solid lines in Figure 7.14 shows the calculated mobilities assuming constant $\eta = E_F/k_BT$ of -0.3 (for undoped), 3.6 (for doped), and -0.2 (for doped samples at 850 K). The calculation, based on classic concept of solid solutions, matches the observed results reasonably well in all cases. The asymmetrical mobility reduction is also reproduced by the calculation. The alloy scattering potential U is constant throughout the composition range, which means the asymmetry is not due to the different magnitude of scattering from S and Se. Actually, as shown by the Pisarenko relation, m_d^* changes (through change of m_b^*) with alloy composition which is responsible for the asymmetrical mobility reduction.

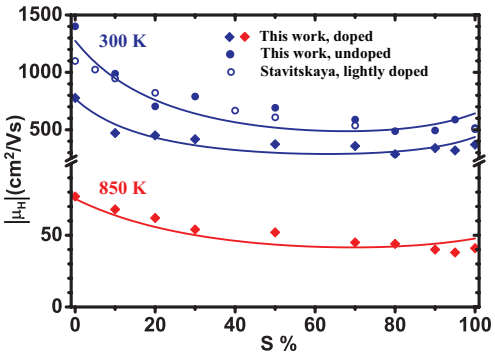

Figure 7.14. Hall mobility of $PbSe_{1-x}S_x$ alloys at 300 K and 800 K.

About the lattice thermal conductivity reduction, the experimental results as well as calculated κ_L according to the point defect scattering thermal conductivity model, at both 300 K and 850 K are shown in Figure 7.15. At 300 K the experimental result from undoped samples perfectly matches with calculated result, κ_L calculated from doped samples are often found larger, due to the uncertainty of κ_e determination. The maximum reduction is achieved with 40 % S substitution. This composition is off the middle of the composition mainly because the κ_L for PbS is significantly higher than that of PbSe. The maximum reduction is found 30% (relative to PbSe, or 48% relative to PbS) at 300 K. Substituting Se with S leads to smaller κ_L reduction compared with Te, due to the smaller size contrast and the lower $\kappa_{L,pure}$. At 850 K, the reduction become very slight and within the uncertainty of κ_L determined from different doped samples. The recently reported[37] κ_L for PbSe with PbS addition ($\leq$ 16%), with nanostructures observed and believed responsible for their thermal conductivity reduction, exhibit the same magnitude of reduction compared with result from this study both at 300 K and 850 K. This suggests the nano-scale compositional fluctuation, produces the same level of κ_L reduction compared with completely random atomic substitution.

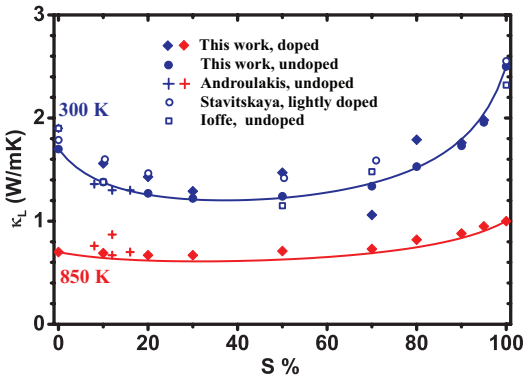

Figure 7.15. Lattice thermal conductivity as function of composition in $PbSe_{1-x}S_x$ alloys.

The zT value of $PbSe_{1-x}S_x$ samples at different temperatures is plotted in Figure 7.16. The carrier densities of samples shown are carefully controlled: $n_{H,300\,K} = 3 \times 10^{19}\,cm^{-3}$ (±10%) for alloys with $x < 0.5$ and $5 \times 10^{19}\,cm^{-3}$ (±10%) for alloys with $x \geq 0.5$. The Seebeck coefficient values at 850 K for these samples are about the same at -190 μV/K (±10%). These will lead to zT values close to the optimized ones at 850 K for all compositions. At 850 K, zT is found to increase when substituting S in PbS with Se, while it is found to decrease when substituting Se in PbSe with S. Neither of these changes, however, is significant especially when compared with the averaged zT from the rule of mixing between PbSe and PbS (the dashed lines).

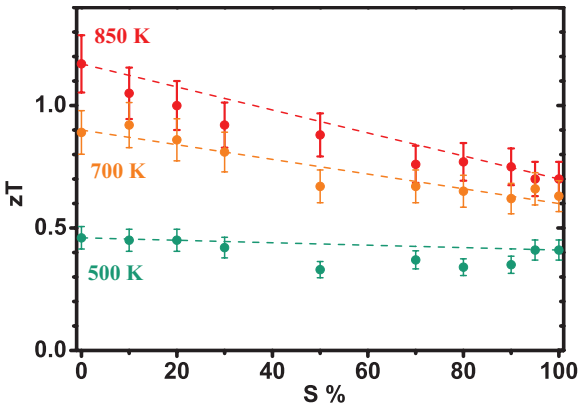

Figure 7.16. Measured zT versus composition at different temperatures for $PbSe_{1-x}S_x$. Error bars represent 10% uncertainty.

7.3 Alloy Scattering of Charge Carriers

Consider a substitutional atom was placed on a lattice site of a crystal, with its own atomic potential being different from that forms the lattice potential. It introduces a perturbation to the electronic Hamiltonian and thus acts as a scattering mechanism. This is called the disorder scattering, or alloy scattering. Such effect was first studied by Nordheim[215] in metal alloys from the 1930s and the associated electron relaxation time τ_{alloy} was shown depending on alloy composition and carrier energy. Brooks later[117] pointed out that τ_{alloy} also has a temperature dependence of $T^{-1/2}$ as oppose to the $T^{-3/2}$ dependence for acoustic phonon scattering. Glicksman et al. studied[216] Si-Ge and III-V alloys and developed the expression for mobility due to alloy scattering. The first explicit expression of relaxation time τ_{alloy} was later developed by Harrison and Hauser[217, 218] for nondegenerate III-V semiconductors.

If we define an average lattice potential in a disordered system by,

$$\overline{U} = xU_A + (1-x)U_B \qquad \text{Equation 7.1}$$

x being the concentration of atom A in the alloy, so for a lattice site occupied by atom A, the local potential fluctuation would be,

$$H_{e-alloy,A} = U_A - \overline{U} = (1-x)\Delta U \qquad \text{Equation 7.2}$$

The scattering rate by A atoms amounting N_A can be readily expressed as,

$$\left|M_{k,A}\right|^2 = n_A \sum_{k'} \left|\left\langle k \left| H_{e-alloy,A} \right| k' \right\rangle\right|^2 = n_A \left[(1-x)\Delta U\right]^2 = x(1-x)^2 \Delta U^2 \qquad \text{Equation 7.3}$$

Similarly the scattering rate by B atoms,

$$\left|M_{k,B}\right|^2 = n_B \sum_{k'} \left|\left\langle k \left| H_{e-alloy,B} \right| k' \right\rangle\right|^2 = n_B \left[x\Delta U\right]^2 = (1-x)x^2 \Delta U^2 \qquad \text{Equation 7.4}$$

So the total relaxation time given by Fermi's golden rule is,

$$\tau_{alloy} = \frac{\hbar}{2\pi\left(\left|M_{k,A}\right|^2 + \left|M_{k,B}\right|^2\right)} g(\varepsilon)^{-1} = \frac{\hbar}{2\pi} \frac{\pi^2\hbar^3}{\Omega 2^{1/2} m^{*3/2} (k_B T)^{1/2} \varepsilon^{1/2}} \frac{1}{x(1-x)\Delta U^2} \qquad \text{Equation 7.5}$$

The volume per atom Ω is introduced so the potential ΔU has the unit of energy (eV.)

Harrison[219] went through a similar derivation of the transition probability and finally gets to a similar expression of the relaxation time that only differs in the pre-factors.

$$\tau_{alloy} = \frac{8\hbar^4}{3\sqrt{2}\pi\Omega C_A (1-C_A) U^2 m_d^{*3/2} (k_B T)^{1/2}} \varepsilon^{-1/2} \qquad \text{Equation 7.6}$$

Harrison's use of Ω came from the interatomic distance of III-V compounds, which he derived this equation for. As the relation between interatomic distance and lattice parameter differ with crystal structure, the pre-factor in Equation 7.6 is expected to be different when applied to other systems. Fortunately, Harrison himself also mentioned[219] the arbitrariness on the choice of this distance so that it is not necessary to think of one specific pre-factor should be the only rigorous result. Difference in pre-factors is quite common in scattering related equations derived by different researchers. In specific for τ_{alloy}, after a short literature survey we found that the pre-factor used by

Makowski and Glicksman[216] is roughly 2 times as large. The one used by Chattopadhyay[220] is 0.5 times as large. Mahrotra used[221] the pre-factor in Equation 7.5, which is very close to Equation 7.6 numerically. The same situation is seen in the expression of thermal conductivity governed by the Umklapp phonon scattering as well. Caution is needed when comparing results from literature.

For non-parabolic Kane bands, Equation 7.6 becomes:

$$\tau_{alloy} = \frac{8\hbar^4}{3\sqrt{2}\pi\Omega C_A(1-C_A)U^2 m_d^{*3/2}(k_B T)^{1/2}}(\varepsilon+\varepsilon^2\alpha)^{-1/2}(1+2\varepsilon\alpha)^{-1} \qquad \text{Equation 7.7}$$

Although it also involves potential fluctuation just as deformation potential phonon scattering, the alloy scattering is limited to short range interaction only and phonon is not involved in this process. With the relaxation time defined for alloy scattering, the mobility of any solid solution composition can be calculated. Beyond the dilute limit, the material properties of the alloys, such as the elastic constants C_l, deformation potential coefficient Ξ, and effective mass, will be different from the constituent compounds. How would these quantities change with solid solution composition is usually not well studied. In the study of Pb chalcogenide solid solutions, we assumed a linear average of each of these properties, and we were able to explain the experimental results very well.

The alloy scattering potential U, according to how these equations are derived, should be the offset of atomic potentials between solvent and solute atoms. How to acquire information about this quantity from well-determined physical parameters is not clear. The value of U should be, according to[117] Brooks, related to the band gap difference between the constituent compounds. This is later suggested[219, 222] to be inaccurate to calculate U whereas the difference of electron affinity might be a possible alternative. Neither of these could however explain the value of U found for n-type PbTe-PbSe or PbSe-PbS: Figure 7.17 compares these two quantities between different Pb chalcogenides. We see for both n-type $(PbTe)_{1-x}(PbSe)_x$ and $(PbSe)_{1-x}(PbS)_x$, the band offset is about 0.1 eV at 0 K. while the alloy scattering potential is found much larger at around 1 eV for both cases.

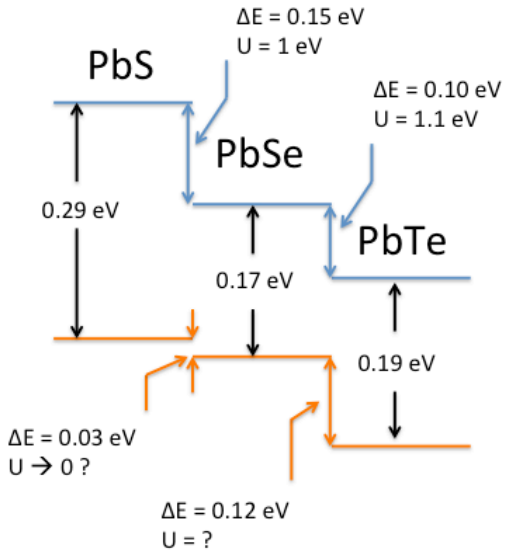

Figure 7.17. Position of conduction and valence band of Pb chalcogenides relative to each other, plotted according to calculated band energy at 0 K reported by Wei and Zunger.

Even though the alloy scattering potential U is not exactly the band offset ΔE, it is still reasonable to expect U being proportional to ΔE. Then immediately from Figure 7.17 arises an interesting question, will the alloy scattering be negligible in p-type $PbSe_{1-x}S_x$, since the valence band offset[223] is only 0.03 eV (at 0 K, at room temperature or above this result may be different)? Trying to probe the answer, we have made undoped $PbSe_{1-x}S_x$ with 0.1% extra anions. It turns out all the samples on PbS-rich side are n-type, while only samples rich in PbSe are found p-type and these are listed in Table 7.2. Considering samples without bipolar conduction, we compared the measured mobility with the calculated mobility of p-type PbSe as well as $(PbSe)_{1-x}(PbS)_x$ omitting alloy scattering (Ξ of p-type PbS was assigned the value 38 eV based on PbSe result), all with the same carrier density. The result is listed in Table 7.3. Limited by the number of samples and the scatter of mobility result, no conclusion could be made yet at this stage. However, none of the measured mobilities from all three samples is significantly smaller than calculated mobility for $PbSe_{1-x}S_x$ without alloy scattering, suggesting a good chance that the alloy scattering is negligibly weak in p-type $PbSe_{1-x}S_x$. We notice that Ioffe has made a very intuitive argument[12] that since the valence band is formed primarily by anion atom orbits, substituting on the anion site will lead to more scattering in p-type solid solutions than n-type ones. Ioffe's intuitive picture seems to be consistent with what had been found in $PbTe_{1-x}Se_x$ (since the band offset in the valence band happen to be larger than in conduction band), but most probably would fail when applied to the $PbSe_{1-x}S_x$ case.

Table 7.3. Mobility for undoped p-type $PbSe_{1-x}S_x$ compared with calculated mobility for p-type PbSe, and $PbSe_{1-x}S_x$ without alloy scattering contribution, assuming the same carrier density.

Sample	n_H (10^{18} cm^{-3})	μ_H (cm^2/Vs)	μ_H PbSe	μ_H $PbSe_{1-x}S_x$
p-50	2.4	487	784	520
p-60	0.8	593	694	467
p-80	1.2	780	739	606

In general, the value of alloy scattering potential U is of key importance to the magnitude of alloy scattering and the mobility reduction in solid solutions. Values of U, however, are reported only for a few systems[220, 221, 224-227]. These are shown in Table 7.4 along with some other physical property differences of the alloy components[228, 229]. The typical magnitude of U is found between 0.6 to 2 eV, which is much smaller than a typical effective deformation potential coefficient Ξ (8 to 35 eV).

Table 7.4. A comparison of alloy scattering potential U in a few solid solutions together with the difference between two constituents in electron affinity ΔX, band gap ΔEg, molar mass ΔM, and lattice parameter $\Delta\alpha$.

Alloy system	ΔX (eV)	ΔE_g (eV)	ΔM	Δα (Å)	U (eV)	note
n-$Al_{1-x}Ga_xN$	3.5	2.69	42.7	0.21	1.5 – 2.0	Δa compare c direction
n-$Al_{1-x}Ga_xAs$	0.43	1.72	42.7	0.01	1.1	
n-$Cd_{1-x}Zn_xTe$	0.8	0.88	88.2	0.37	0.8	
n-$InAs_{1-x}P_x$	0.5	0.99	44	0.19	0.6	
n-$Si_{1-x}Ge_x$	0.05	0.46	44.5	0.23	0.6 - 1.0	
n-$PbSe_{1-x}Te_x$	0.1	0.02	48.6	0.33	1.1	
n-$PbSe_{1-x}S_x$	0.1	0.12	47.0	0.19	1.0	

7.4 Point Defect Scattering of Phonons

The heat transport problem are usually discussed within the diffusive regime where the heat carrying particles, the phonons moves from the hot side of a solid to the cold side, scattering with different scattering centers on their way and lose momentum and energy, which causes thermal giving rise to the definition of thermal conductivity, in a similar way as the electrical conductivity. Thermal conductivity is the sum of contribution from charge carriers and the lattice. The first is related to electrical conductivity via Weidemann-Franz Law. The discussion here will be limited to the lattice thermal conductivity.

Similar as modeling the charge carrier mobility and thus conductivity, the problem of heat conduction is depicted using the concept of phonon scattering and relaxation time approximation. The total thermal conductivity is usually calculated using the Debye-Callaway model[230, 231]:

$$\kappa_L = \frac{k_B^4}{2\pi^2\hbar^3 v} T^3 \int_0^{\Theta/T} \tau_{total} \frac{x^4 e^x}{(e^x - 1)^2} dx \qquad \text{Equation 7.8}$$

Here v is the averaged speed of sound, Θ the Debye temperature, x stands for $\hbar\omega/k_B T$, and τ_{total} is the combined relaxation time of different scattering mechanisms. At high temperatures, the last term in the integrant can be approximated by x^2, as shown in Figure 7.18. In fact, as long as T is above Debye temperature, which for the majority of thermoelectric compounds is below or around 300 K, this approximation will lead to error that does not exceeding 8%.

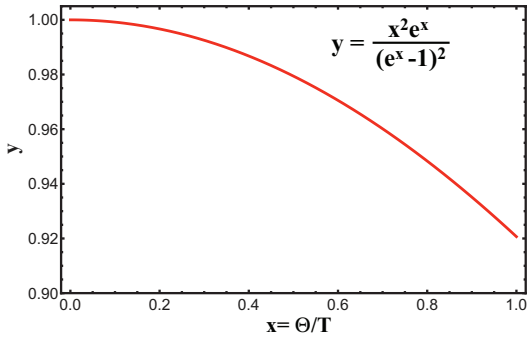

Figure 7.18. The integrant in Debye model can be approximated at high temperature with x^2.

So that Equation 7.8 at high temperatures becomes:

$$\kappa_L = \frac{k_B^4}{2\pi^2\hbar^3 v} T^3 \int_0^{\Theta/T} \tau_{total} x^2 \, dx \qquad \text{Equation 7.9}$$

For bulk materials, there are three different scattering mechanisms that are usually considered: the Umklapp phonon scattering, the point defect scattering, and the boundary scattering.

Umklapp process refers to phonon-phonon collision where the final wave vector q is out of the Brillion zone boundary resulting in an energy loss and thermal resistance. The relaxation time under Umklapp scattering is formulated by Slack[232] as:

$$\tau_U^{-1}(\omega) = \frac{\hbar\gamma^2\omega^2}{Mv^2\Theta} T \exp(-\Theta/3T) = \frac{k_B^2\gamma^2}{\hbar M v^2 \Theta} x^2 T^3 \exp(-\Theta/3T) \qquad \text{Equation 7.10}$$

ω is phonon frequency and γ is the Grüneisen parameter that characterizes the anharmonicity of lattice vibration. The other type of phonon-phonon interaction is the Normal process where the final wave vector q is in the same Brillion zone, Normal process is generally considered having no contribution to thermal resistance because there is no energy loss for the phonons. Some researchers, for example Zaitsev et al. argued[233] that the Normal process has its contribution to thermal resistance by redistributing phonons so that more will participate the Umklapp scattering. The treatment of Normal process, is essentially adding a phenomenological factor to the relaxation time of Umklapp scattering.

The point defect scattering of phonons has a Rayleigh scattering characteristic that scattering rate changes with λ^{-4}, so the short wavelength phonons will get scattering most.

$$\tau_D^{-1}(\omega) = \frac{\Omega\Gamma}{4\pi v^3}\omega^4 = \frac{k_B^4\Omega\Gamma}{4\pi\hbar^4 v^3}x^4T^4 \qquad \text{Equation 7.11}$$

Γ is the point defect scattering parameter.

The boundary scattering is simply a function of the distance between the boundaries, usually grain size.

$$\tau_B^{-1} = \frac{v}{L} \qquad \text{Equation 7.12}$$

Some researchers would also add the transmissivity[234] of phonons into this equation:

$$\tau_B^{-1} = \frac{v}{L}\frac{4(1-t)}{3t} \qquad \text{Equation 7.13}$$

This version does not necessarily lead to more accurate estimate because the transmissivity t is not an easily observable and well-determined parameter, so essentially the second term would become a fitting pre-factor.

In nano-structured systems, researchers also tend to introduce other scattering mechanisms such as scattering from precipitates or dislocations around the precipitates. Theories on such mechanisms are rather complicated and the expressions of relaxation time include one or more parameters that can't be well determined experimentally[235]. Also because the samples are always annealed for a long time and are single phase, these mechanisms are not considered.

Adding all three mechanisms and calculating κ_L using Equation 7.8 has been successfully adopted for studies of other material systems, but for Pb chalcogenide, the results even for pure binary compound at room temperature are found overestimated significantly. The difficulty of accurately calculating κ_L of binary compounds at any given temperature has made us use another treatment[235-237] suggested by Callaway and Klemens for κ_L of solid solutions, which allows us to use experimentally determined κ_L for the binary compounds as an input. The assumption behind his derivation is, in addition to the high temperature approximation, that a combined scattering mechanism with Umklapp-type relaxation time for the unalloyed "pure" compound (this would allow the contribution from Normal process), and the only added scattering mechanism is the point defect scattering in the alloys or, solid solutions. Klemens' formula can be written as:

$$\frac{\kappa_{L,alloy}}{\kappa_{L,pure}} = \frac{arc\tan(u)}{u} \qquad \text{Equation 7.14}$$

where u is given by:

$$u^2 = \frac{\pi\theta_D\Omega}{2\hbar v^2}\kappa_{L,pure}\Gamma \qquad \text{Equation 7.15}$$

For the calculation of scattering parameter Γ there has been some discrepancy. In the early works on the thermal conductivity affected by point defects, researchers primarily studied the influence from the isotopes and their expression of Γ only took into account the mass difference. Many researchers continued to use such expression because the impurity is very close in atomic size to the atom it replaced. Actually, Klemens' full analysis from continuum theorem took into account influences from mass difference, binding force difference and strain field induced by a point defect. The full expression of Γ contains 3 terms:

$$\Gamma = \sum_i \Gamma_i = \sum_i x_i\{(\frac{\Delta M}{M})^2 + 2[(\frac{\Delta K}{K}) - 2Q(\frac{\Delta R}{R})]^2\} \qquad \text{Equation 7.16}$$

M, K and R are the atomic mass, bulk modulus and bonding length of the pure compound and ΔM and ΔK are the difference of each quantity between matrix and introduced compounds. ΔR is the difference of local bonding length caused by a point defect. Q accounts for the accumulative influences on surrounding bonds from the point defect for which Klemens[235] used 4.2 for substitutional impurities and 3.2 for vacancies. Abeles[194] replaced the term $\Delta R/R$ with $\Delta d/R$ where Δd is the difference of bonding length of matrix and alloying atom in their own lattices so that for binary ($A_{1-x}B_x$ type) or pseudo-binary ($(AB)_{1-x}(AC)_x$ type) systems:

$$\Gamma = x(1-x)[(\frac{\Delta M}{M})^2 + \varepsilon(\frac{\Delta a}{a})^2] \qquad \text{Equation 7.17}$$

ΔM and $\Delta\alpha$ are the difference in mass and lattice constants between two constituents, M and α are the molar mass and lattice constant of the alloy. The parameter ε is related to the Grüneisen parameter γ and elastic properties. Abeles wrote ε as[194] (for some reason Abeles used 6.4 instead of 8.4 as would expected from Klemens' value for the factor Q):

$$\varepsilon = \frac{2}{9}[(G + 6.4\gamma)\frac{1+r}{1-r}]^2 \qquad \text{Equation 7.18}$$

G is a ratio between the contrast in bulk modulus ($\Delta K/K$) and that in the bonding length ($\Delta R/R$). The ratio G is relatively constant within similar materials systems. Scientists have been studying the relationship between bulk modulus and the volume of unit cell for a lot of compounds. An example can be seen from Anderson's study[238, 239] on lots of crystals of different types. From the slopes seen in his plot it is found that for covalent IV and III-V structures $G = 4$, for more ionic II-VI and I-VII structures $G = 3$, for complex oxide structures $G = 9$. So for Pb chalcogenides we suggest the use of $G = 3$. r is the Poisson ratio, which can be calculated from the longitudinal and transverse speed of sound via:

$$\frac{v_l}{v_t} = \sqrt{\frac{2(1-r)}{1-2r}} \qquad \text{Equation 7.19}$$

the Poisson ratio r for most semiconducting compounds is found[240] between 0.15 and 0.3 (for most solids it is between 0 to 0.5). With all the parameters in Equation 7.18 determined, the value of ε could be calculated for any binary compounds, given adequate information. ε calculated for PbTe, PbSe and PbS are 100, 110 and 150, respectively. ε for PbTe based systems was previously suggested to be 65 by Alekseeva[241] by fitting experimental results, this value has been used in lots of studies on relevant materials including ours. We now believe the use of 100 instead of 65 is of more physical origin and it does not lead to significant inconsistency between model and experiments. In studies of other compounds in general, ε is mostly taken as an empirically adjustable fitting parameter, which is understandable since the elastic parameters needed to calculate ε for a compound are not all necessarily studied.

When there is more than one type of substitution, how to determine the scattering parameter Γ in the point defect model is of debate. Abeles has suggested to generalize the expression in Equation 7.17 into:

$$\Gamma = \sum_i \Gamma_i = \sum_i x_i \left[\left(\frac{\Delta M_i}{M} \right)^2 + \varepsilon \left(\frac{\Delta \alpha_i}{\alpha} \right)^2 \right] \qquad \text{Equation 7.20}$$

Yang et al.'s treatment[242] is another widely adopted method, which considered different substitutions on each different site all together. Detail about such treatment was described in *Appl Phys Letter 85*, 1140 2004. Expressions from these two treatments are not consistent and the difference (which is not simply proportional) diverges as the number of atoms in a unit cell increases. It is worth noticing that Yang's derivation was based on Slack's expression[243] of Γ but arguably generalized it to cases where both mass and size differences are considered, while Slack's work only considered the mass difference. So without careful derivation, replacing the equation (7) in Yang's paper with

$$\Gamma_s = \frac{\sum_{i=1}^{n} c_i \left(\frac{\bar{r}_i}{\bar{\bar{r}}} \right)^2 f_i^1 f_i^2 \varepsilon_i \left(\frac{r_i^1 - r_i^2}{\bar{r}_i} \right)^2}{\left(\sum_{i-1}^{n} c_i \right)} \qquad \text{Equation 7.21}$$

seems to be more justifiable.

No matter which treatment is used, there hasn't been a systematic study on the thermal conductivity of a multi-substituted solid solution to compare the theory with. The Gurieva et al. suggested[244] that the effect from multiple substitutional atoms are not additive, which is reasonable considering they both primarily affect phonons with the same wavelength range, and Matthiessen's rule works best only when different mechanisms acts on different parts of the phonon spectrum.

$Si_{1-x}Ge_x$ or $Mg_2Si_{1-x}Sn_x$ are examples where the lattice thermal conductivity in solid solutions is greatly reduced (up to 94% reduction in $Si_{1-x}Ge_x$[245] and 75% in $Mg_2Si_{1-x}Sn_x$[233]) and hence a significant improvement in zT has resulted. The reduction in $(PbTe)_{1-x}(PbSe)_x$ was found only about 45%, which is considerably less than such examples because the mean free path is already small due to efficient Umklapp scattering in lead chalcogenides. In Table 7.5 the κ_L reduction is compared among different material systems with the same degree of alloying (30%), together with the magnitude of the contribution from mass ($\Delta M/M$) and strain field ($\Delta\alpha/\alpha$ and ε) contrast. It is seen that the strain field contrast does not change much for different material systems and none of them is large due to the required similarity in lattice constant for the solid solution to form. The PbTe based system has one of the largest ε, which actually leads to the largest total strain contribution among these systems. The mass contrast in $PbTe_{0.7}Se_{0.3}$ on the other hand is small compared to the

other systems. The factor with the highest correlation with the thermal conductivity reduction ($\Delta\kappa_L/\kappa_{L,pure}$) is the magnitude of $\kappa_{L,pure}$.

Table 7.5. Relative lattice thermal conductivity reduction in alloy systems with the same degree of alloying (30%) together with the contribution from mass (ΔM/M) and strain field (Δα/α and ε) contrast. ε stands for values been used as fitting parameter, and ε_{calc} are calculated values. $\kappa_{L,pure}$ for the major constituent compound.

	$\Delta\kappa_L/\kappa_{L,pure}$ (300 K)	ΔM/M	Δα/α	ε	ε_{calc}	$\kappa_{L,pure}$ (300 K)
$PbTe_{0.7}Se_{0.3}$	45%	0.15	0.05	65	100	1.9
$PbSe_{0.7}S_{0.3}$	30%	0.17	0.03		110	1.7
$Si_{0.7}Ge_{0.3}$	94%	1.1	0.04	39	47	150
$Mg_2Si_{0.7}Sn_{0.3}$	75%	0.87	0.06	23	67	7.9
$Ga_{0.7}In_{0.3}As$	86%	0.29	0.07	45	51	45

7.5 Criteria of Beneficial Disorder for Thermoelectrics

The highest zT that can be achieved in a given material system is governed by its quality factor:

$$B = T\frac{2k_B^2\hbar}{3\pi}\frac{C_l N_V}{m_I^* \Xi^2 \kappa_L} \qquad \text{Equation 7.22}$$

High efficiency thermoelectrics are heavily doped so that the deformation potential (acoustic phonon) scattering is predominant ($\tau_{pure} \approx \tau_{ac}$). In alloy systems following the derivation of B one gets:

$$B_{alloy} = T\frac{2k_B^2\hbar}{3\pi}\frac{C_l N_V}{m_I^* \Xi^2 [1 + A(\frac{U}{\Xi})^2]\kappa_{L,alloy}}, \quad A = \frac{3\pi^2 x(1-x)C_l\Omega}{8k_B T} \qquad \text{Equation 7.23}$$

Substituting Equation 7.14 into Equation 7.23:

$$B_{alloy} = T\frac{2k_B^2\hbar}{3\pi}\frac{C_l N_V}{m_I^* \Xi^2 [1 + A(\frac{U}{\Xi})^2]\kappa_{L,pure}\arctan(u)/u} \qquad \text{Equation 7.24}$$

The relative change of quality factor after forming solid solutions can be written as:

$$\frac{\Delta B}{B_{pure}} = \frac{B_{alloy}}{B_{pure}} - 1 = \frac{u/\arctan(u)}{1 + \frac{3\pi^2 x(1-x)C_l\Omega}{8k_B T}(\frac{U}{\Xi})^2} - 1 \qquad \text{Equation 7.25}$$

Where u is defined in Equation 7.14 and Equation 7.15. Equation 7.25 being greater than zero indicates a possible improvement of zT in solid solutions. While it is valid over the entire composition range it is more useful to examine the initial effect of alloying in the dilute limit, as it will more directly indicate whether the alloying is beneficial or detrimental.

In dilute solid solutions $x << 1$ and $u << 1$, the changing rate of $\Delta B/B_{pure}$ can be expressed as:

$$\left.\frac{d}{dx}\frac{\Delta B}{B_{pure}}\right|_{x=0} = \frac{\pi^2\Omega^{1/3}}{k_B T}\{\frac{6^{-1/3}\pi^{1/3}\hbar}{k_B\theta_D}\kappa_{L,pure}T[(\frac{\Delta M}{M})^2+\varepsilon(\frac{\Delta\alpha}{\alpha})^2]-\frac{3C_l\Omega^{2/3}}{8}(\frac{U}{\Xi})^2\} \quad \text{Equation 7.26}$$

The pre-factor $\pi^2\Omega^{1/3}/k_BT$, with its $1/T$ dependence, indicates that the disorder in thermoelectrics become less effective as temperature increases. The main part (inside the braces) contains two terms, which originate from the thermal conductivity reduction and electronic mobility reduction, respectively. The sign of Equation 7.26 determines whether the solid solution is beneficial (have higher thermoelectric quality factor) compared with the pure compound.

We further note that $\kappa_{L,pure}$ is expected to decrease with temperature as T^{-1} for Umklapp scattering dominant systems, and assuming the other parameters are temperature independent, then the second part of Equation 7.26 is temperature independent. Thus this part can all be evaluated from the room temperature materials properties:

$$\left.\frac{d}{dx}\frac{\Delta B}{B_{pure}}\right|_{x=0} = 7.2\times10^3\frac{(\Omega^{1/3}/\text{Å})}{(T/K)}\{\frac{18.5}{(\theta_D/K)}(\kappa_{L,pure,300K}/Wm^{-1}K^{-1})[(\frac{\Delta M}{M})^2+\varepsilon(\frac{\Delta\alpha}{\alpha})^2]-0.038(C_l/GPa)(\Omega^{2/3}/\text{Å}^2)(\frac{U}{\Xi})^2\} \quad \text{Equation 7.27}$$

M and α can be approximated with those for the matrix compound. As the few known values of alloy scattering potential U are around 1 eV, this value should be a reasonable estimate for other systems.

Equation 7.27 provides a criterion determining whether disorder is beneficial for all temperatures from only the values of parameters measured at room temperature. Even though it is derived for dilute solid solutions it is qualitatively applicable as a criterion for the full composition range. Calculations using combinations of realistic material parameters indicate that whenever an appreciable increase of B is achieved for an arbitrary solid solution composition, the rate of $\Delta B/B_{pure}$ in the dilute limit is always large and positive. Thus Equation 7.27 being greater than zero is a prerequisite of possible zT improvement by forming solid solutions. This criterion is applied to different solid solution systems and the results are listed in Table 7.6.

Equation 7.27 can be further simplified as $\kappa_{L,pure,300K}$ is related to C_l and θ_D through the speed of sound:

$$C_l = v_l^2 d \qquad \text{Equation 7.28}$$

$$\theta_D = \frac{\hbar}{k_B}\left(\frac{6\pi^2}{\Omega}\right)^{1/3} v \qquad \text{Equation 7.29}$$

where d is the density, v_l is the longitudinal speed of sound, and v is the average speed of sound v given by:

$$\frac{1}{v^3} = \frac{1}{3v_l^3} + \frac{2}{3v_t^3} \qquad \text{Equation 7.30}$$

Since usually the transverse speed of sound v_t is roughly 60% of the longitudinal speed of sound v_l, the ratio v_l/v can be approximated as 1.5 if the exact values are not known. Now the thermal conductivity can be written as:

$$\kappa_{L,pure} = C\frac{Mv^3}{TV^{2/3}\gamma^2} \qquad \text{Equation 7.31}$$

Using the value of 0.096 for C reduces Equation 7.27 to:

$$\frac{d}{dx}\frac{\Delta B}{B_{pure}}\bigg|_{x=0} = \frac{\pi K\Omega}{4k_B T}\left\{\frac{1}{4\gamma^2}\left[\left(\frac{\Delta M}{M}\right)^2 + \varepsilon\left(\frac{\Delta\alpha}{\alpha}\right)^2\right] - 10.6\left(\frac{U}{\Xi}\right)^2\right\} \qquad \text{Equation 7.32}$$

The factor C of 0.096 was used in Equation 7.31 based on the result of study on $(PbTe)_{1-x}(PbSe)_x$ where the two effects of disorder are found almost fully compensated. The examples in Table III when evaluated with Equation 7.32 indicate the same trends in maximum zT change as observed experimentally.

Besides the temperature T, the effectiveness of disorder for improving thermoelectric performance is affected by several physical properties of the matrix compound. Those with low Grüneisen parameter γ, large deformation potential coefficient Ξ, stiff bonds (large bulk modulus K) and large average volume per atom Ω are more likely to benefit from disorder. Thus for many poor thermoelectric materials that have many of these features, forming a solid solution could potentially enhance their performance greatly. For a given matrix compound, it is best to select a s solid solution component to create as large contrast of mass $\Delta M/M$ and size $\Delta\alpha/\alpha$ as well as a low alloy scattering potential U as possible to achieve the largest improvement of zT by forming solid solution. While these qualitative guidelines are no surprise to the field, Equation 7.32 gives a

quantitative estimate to the improvement in *B* and therefore *zT* for each of these effects that can be used to rationally select from a wide range of materials for study.

Table 7.6. Criteria based on the relative change of quality factor, applied to different solid solutions. Only the part inside the braces of each equation is considered. Result is expressed as the thermal conductivity reduction part minus the mobility reduction part. As a comparison the change of maximum *zT* observed experimentally is also included.

	Equation 7.27 (κ part – μ part)	Equation 7.32 (κ part – μ part)	reported *zT*
PbTe-PbSe (n)	0.063 – 0.064	0.025 – 0.024	not observed
PbSe-PbS (n)	0.016 – 0.053	0.0075 – 0.018	not observed, both this study and literature
PbS-CaS (p)	0.16 – 0.23	0.048 – 0.066	- to 1.1(900K), increase not expected from disorder, U 3 eV, Ξ 38 eV used.
Mg_2Si-Mg_2Sn (n)	0.50 – 0.10	0.21 – 0.029	0.7 to 1.1 (800K)
Si-Ge (n)	9.85 – 0.22	1.79 – 0.047	- to 1.0 (1100K)

As suggested by Table 7.6 this criterion seems to be very successful predicting *zT* enhancement in thermoelectric solid solutions, it is however important to stress that forming a solid solution might also change the band structure (valley degeneracy, effective mass, etc.) as is the case for Si-Ge[197] and Mg_2Si-Mg_2Sn.[29] These effects are not considered by this criterion. In experimentally well-examined systems, analysis as outlined above could lead to indications of whether such changes of band structure are present.

In systems with theoretical insights on how alloying affects the band structure, Equation 7.27 and Equation 7.32 can be used to predict the potential improvement of *zT* after adding these influences accordingly as extra terms on the left hand side. Estimates on how the change of band structure affects each parameter in the quality factor *B* would help estimate the sign and magnitude of these terms. In p-type PbTe-PbSe alloy for example[7], the manipulated band convergence adds a positive term so that a *zT* improvement is achieved.

In a broader context, the thermal conductivity reduction due to alloying (through the point defect scattering of phonons) is most effective in scattering high frequency (small wavelength) phonons. Further reduction could be achieved in solid solutions if low frequency (long wavelength) phonons are also scattered by scatterers that produce efficient boundary scattering, such as grain boundaries[246,247] and larger scale nanostructures.[59] In systems where the electron mean free path is much smaller than this length scale this would result in further zT enhancement.

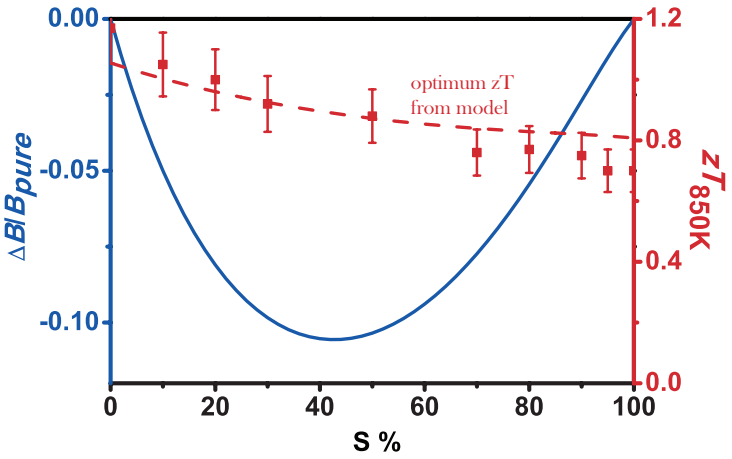

Figure 7.19. Relative change of quality factor with composition (blue line) and change of zT (red dashed line and squares) at 850 K with composition. Dashed line is the calculated maximum zT for each composition.

For the system of $PbSe_{1-x}S_x$, the criteria has yield negative values for the two limiting case of PbSe and PbS with small addition of each other. So a noticeable increase of zT is not expected when solid solution is formed. Figure 7.19 shows the relative change of quality factor in solid solutions as a function of composition, the change in quality factor remains negative throughout entire composition range. The calculated optimized zT based on the described models is shown as dashed line in Figure 7.19, much higher zT over the optimized ones of each binary compound is not likely.

PbS and PbSe have different optimum values of zT, and the alloys between them have different effective masses depending on the composition. Nonetheless, as m_d^* (thus m_I^*) is approximated by a linear extrapolation between the two compounds, so will the quality factor of the virtual system to which the change in alloys is compared. In general cases when a gradual linear extrapolation is obeyed by all material properties (m_I^*, Ξ, C_l, N_v) that depend on composition, the criteria (9) and (10) can still be applied to estimate the change of zT relative to the weighed average of optimum zT of the two compounds.

Chapter 8

P-type $Pb_{1-x}Sr_xSe$ with Band Engineering

8.1 Introduction

Band engineering in semiconductors is important for their application in electronic or optoelectronic devices. For heavily doped thermoelectric semiconductors it is also crucial for the high *zT* found in $PbTe_{1-x}Se_x$,[7] $Pb_{1-x}Mg_xTe$,[248, 249] and $Mg_2Si_{1-x}Sn_x$.[27] For high temperature bulk thermoelectrics most of such engineering is realized by forming solid solutions. In this study we demonstrate successful band tuning of p-type PbSe using $Pb_{1-x}Sr_xSe$ solid solutions. Although similar to its well-studied analog PbTe, PbSe has easily recognizable difference in band structure: the secondary valence band is further away from the primary band maximum. This is an important factor that leading to different transport behavior and lower maximum *zT* in PbSe compared with PbTe. The introduction of Sr makes the contribution from the secondary, multi-valley valence band in carrier transport greater over a broader temperature range thus the good *zT* found in p-type PbSe could be further enhanced. It is well known that forming solid solutions is desirable for thermoelectrics due to their lower thermal conductivities. We demonstrate here that the ability to change not only the band gap, but also the relative positions of different band maxima grants another important benefit for solid solutions as thermoelectrics. Actually, we found in this study that the reduction of lattice thermal conductivity by alloying has been compensated by the counter effect of reduced carrier mobility, as also been found in the n-type solid solutions $PbTe_{1-x}Se_x$ and $PbSe_{1-x}S_x$ where simply forming solid solutions without band engineering effect has failed to improve *zT*. Therefore we conclude that the change in band structure with formation of solid solution accounts for the improvement of *zT* in p-type PbSe from 1.0 to 1.5 at 900 K.

In PbSe as well as PbTe, the secondary valence band maximum (along the Σ line of the Brillouin Zone, called the Σ band) contributes to the carrier transport at high temperature when the energy of the primary valence band (the L band) decreases as the band gap increases with temperature. The best thermoelectric performance is found around temperatures where the two valence bands are converged (within a few k_BT of one another). For PbTe the convergence temperature (T_{cvg}) was historically believed to be around 450 K based on both optical band gap measurements[44, 250] and temperature dependent Hall coefficient data[251, 252]. However, new evidence and data interpretation has indicated that the actual convergence temperature should be higher. In PbSe, the Σ band is further away[253, 254] (~ 0.3 eV at 0 K) from the primary band maximum and the two bands converge at a higher temperature. Early works[47, 253, 255] based on Hall coefficient data has pointed to a T_{cvg} around 750 K. However, result based on optical absorption spectra[142, 256] (for T below 500K) suggests that this value in PbSe should be around 1200 K, which is beyond the highest feasible operating temperature for PbSe. Bringing this temperature down to, for instance, 800 K by tuning up the valence band structure of PbSe would thus potentially improve the thermoelectric performance of p-type PbSe (see Figure 4.17 and relevant discussion in Chapter 4).

There are two strategies to perform such a tuning for PbSe: the first strategy is alloying PbSe with PbTe. Being analogous to the effect seen in PbTe rich $PbTe_{1-x}Se_x$ alloys, the addition of PbTe into PbSe would make the valence bands more PbTe-like therefore lower T_{cvg}. Two drawbacks can be anticipated for this strategy: First, an excessive degree of alloying will be needed due to the small difference in band structures (50% PbTe addition estimated to bring T_{cvg} down to 800 K). Second, the disorder introduced by Te substitution of Se in PbSe is not thermoelectrically beneficial. (We notice a recent publication[257] on K doped $PbSe_{0.85}Te_{0.15}$ where zT 1.7 at 873 K was reported, this value should be overestimated based on zT reported for similar systems by the same group.)

The other strategy is alloying PbSe with alkaline-earth selenides that are of rock-salt structures and wide band gaps. No report on phase diagrams between PbSe and MSe (M = Mg, Ca, Sr, Ba) can be found. It is thus still unknown that if such an alloy is thermodynamically stable, nor the effect of alloying on band structure or transport properties in the bulk form. However, there is knowledge on MBE grown $Pb_{1-x}Sr_xSe$ thin films where the lattice constant changes gradually following the Vegard's law and the band gap tunable in a wide range with different SrSe content[258-260]. Given the rock-salt structure and the lattice parameter[259] of 6.25 Å for SrSe it is highly probable that an appreciable solubility of SrSe in PbSe in the bulk form could be found. On the other hand, recent studies[261] on thermoelectric PbTe with SrTe addition implied that SrTe lead to noticeable thermal

conductivity reduction without significantly impairing the carrier mobility, which means the disorder might be beneficial in $Pb_{1-x}Sr_xSe$ alloys as well.

In this study we synthesized bulk $Pb_{1-x}Sr_xSe$ with different 'x' up to 12%. For each alloy composition p-type dopant Na (K for two samples) is used to tune the carrier density and multiple doping levels are studied. Our result demonstrates that PbSe and SrSe form thermodynamically stable solid solutions in bulk form and the solubility of SrSe in PbSe is no less than 8%. The effect of Sr on band structure is revealed by transport as well as optical absorption edge measurements. The band structure is sensitive to and gradually tunable with small amount of Sr. The band gap is doubled with 12% Sr addition. Appreciable enhancement in thermoelectric performance was achieved and the maximum zT of 1.5 is found at 900 K (1.4 ± 0.1 in multiple samples with different compositions).

8.2 Sample Synthesis and Microstructure

The p-type $Pb_{1-x}Sr_xSe$ system is the most challenging in term of synthesis in this thesis research. Elemental Sr is hard metal stored in mineral oil with surface covered by hard oxide layer, the Sr granules are more like filings compressed together rather than dense pieces, with oxidized interfaces inside any pieces bigger than 2 mm. To get oxide free Sr a Dremel electrical polisher with stainless steel milling bit was used to remove all the oxide on surface, big pieces were cut and pealed along oxidized interfaces until very small dense and oxide-free pieces were obtained. To ensure different samples with same nominal alloy composition have the same actual substituted Sr content, the synthesis started with making undoped $Pb_{1-x}Sr_xSe$ bases. To make the undoped alloys, the sealed material were first heated rapidly to 1400/1440/1480/1520 K for 2%, 4%, 8%, 12% SrSe samples, respectively by induction heating and held there for 15 minutes followed by uncontrolled fast cooling. This is to form complete liquid phase that enables proper initial mixing of Sr in PbSe matrix. Higher temperatures are used as the Sr content increases because the melting point of PbSe and SrSe are 1350 K and 1880 K, respectively. Without proper phase diagram we have to take the most conservative estimate, that the melting point of the alloys will roughly follow the tie line between these two temperature as for an isomorphous system, thus the melting point of the alloys would be higher than 1350 K and increase with Sr content. However, instead of using even higher melting temperature (quartz could bear about 1500 K without significant pressure) and long enough soaking time for complete homogenization the ingots were only kept at liquid state for 15 minutes because at such high temperatures Sr would react with quartz. Instead, the further homogenization

of Sr was done by solid-state reaction in which each ingot was ground into powder under argon and hot pressed at 950 K for 20 minutes. The obtained cylinders were polished then sealed in ampoules for anneal at 1073 K for 21 days then quenched and ground under argon. To make doped samples ~ 3g powder of undoped alloys was loaded into carbon coated ampoules with Na and Se. 0.3% extra Se was used to compensate intrinsic defects and element loss during synthesis. Again the melting points of these samples are high enough that the reaction of Sr and Na with quartz becomes a concern. Hence the ampoules were heated to 1120 K and hold for 4 days. Even a liquid phase will not form high vapor pressure of Na at this temperature would allow fairly even distribution of the dopant. The obtained powders indeed have started to weld together due to vapor phase transfer and grow. These were then consolidated by induction heating hot press, resulting in disk shaped samples with >97 % density for the property tests. Table 8.1 listed all the samples prepared for this study.

As the first step of study on solid solutions, the phase composition and lattice parameter were studied with XRD on hot pressed undoped samples. the solid solution behavior and Vegard's law is observed all through sample with 12% Sr, as shown in Figure 8.1.

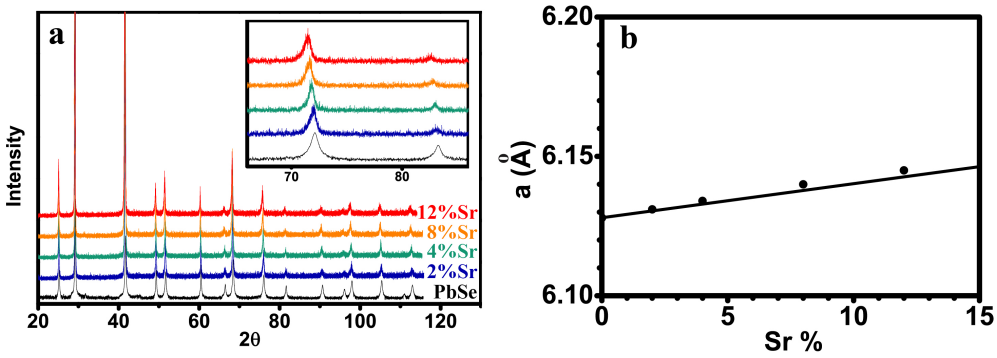

Figure 8.1. a) XRD pattern and b) lattice parameter from standard extrapolation for $Pb_{1-x}Sr_xSe$ system.

The microstructure of undoped samples were further studied with SEM. Figure 8.2 shows the backscattered image of 8%Sr ($Pb_{0.92}Sr_{0.08}Se$) and 12%Sr ($Pb_{0.88}Sr_{0.12}Se$) ingots, while no phase separation or secondary phase precipitates was seen in 8%Sr sample, large Sr-rich inclusions (~10 μm in size) are found in 12% Sr sample with > 10 μm intervals: a length scale well beyond the mean free path of charge carriers or phonons. The inhomogeneity usually suggests a solubility limit, but here is more likely due to insufficient mixing of Sr and slow diffusion across some of the grain boundaries. As can be seen from Figure 8.2 c) the black contrast gradually blends into the matrix

along certain directions of each inclusion, and on other sides of them without such gradient transition, cracks or pores are usually seen, which inhibited diffusion along that direction.

Table 8.1. A list of samples of $Pb_{1-x}Sr_xSe$ solid solution and some room temperature properties.

Label	Composition	Transport Properties		
		$n_H(10^{19}cm^-$	S (μV/K)	μ_H (cm^2/Vs)
0002b2	$Pb_{0.98}Sr_{0.02}$ Se	0.3	200	530
0004base	$Pb_{0.96}Sr_{0.04}$ Se	0.02	438	259
0008b1	$Pb_{0.92}Sr_{0.08}$ Se	0.13	268	383
0012b1	$Pb_{0.88}Sr_{0.12}$ Se	0.15	263	142
0502b5	$Na_{0.005}(Pb_{0.98}Sr_{0.02})_{0.995}Se_{1.003}$	10.6	44	72
1002b5	$Na_{0.01}(Pb_{0.98}Sr_{0.02})_{0.99}Se_{1.003}$	17.9	28	65
1502b5	$Na_{0.015}(Pb_{0.98}Sr_{0.02})_{0.985}Se_{1.003}$	28.9	27	55
2002b5	$Na_{0.02}(Pb_{0.98}Sr_{0.02})_{0.98}Se_{1.003}$	35.2	27	44
2502b5	$Na_{0.025}(Pb_{0.98}Sr_{0.02})_{0.975}Se_{1.003}$	32.2	27	36
K1502b5	$K_{0.015}(Pb_{0.98}Sr_{0.02})_{0.985}Se_{1.003}$	14.4	35	40
0504b6	$Na_{0.005}(Pb_{0.96}Sr_{0.04})_{0.995}Se_{1.003}$	6.0	58	121
1004b6	$Na_{0.01}(Pb_{0.96}Sr_{0.04})_{0.99}Se_{1.003}$	14.0	38	75
1504b6	$Na_{0.015}(Pb_{0.96}Sr_{0.04})_{0.985}Se_{1.003}$	18.4	34	55
2004b6	$Na_{0.02}(Pb_{0.96}Sr_{0.04})_{0.98}Se_{1.003}$	32.0	30	37
0508b6	$Na_{0.005}(Pb_{0.92}Sr_{0.08})_{0.995}Se_{1.003}$	8.2	62	55
1508b6	$Na_{0.015}(Pb_{0.92}Sr_{0.08})_{0.985}Se_{1.003}$	25.0	42	28
2008b6	$Na_{0.02}(Pb_{0.92}Sr_{0.08})_{0.98}Se_{1.003}$	36	36	23
K1508b5	$K_{0.015}(Pb_{0.92}Sr_{0.08})_{0.985}Se_{1.003}$	15.3	45	63
1508b1	$Na_{0.015}(Pb_{0.92}Sr_{0.08})_{0.985}Se$	28.0	-	50
1002b6	$Na_{0.01}(Pb_{0.88}Sr_{0.12})_{0.99}Se_{1.003}$	14.7	74	22
1512b6	$Na_{0.015}(Pb_{0.88}Sr_{0.12})_{0.985}Se_{1.003}$	20.0	60	24
2012b6	$Na_{0.02}(Pb_{0.88}Sr_{0.12})_{0.98}Se_{1.003}$	34.0	52	17

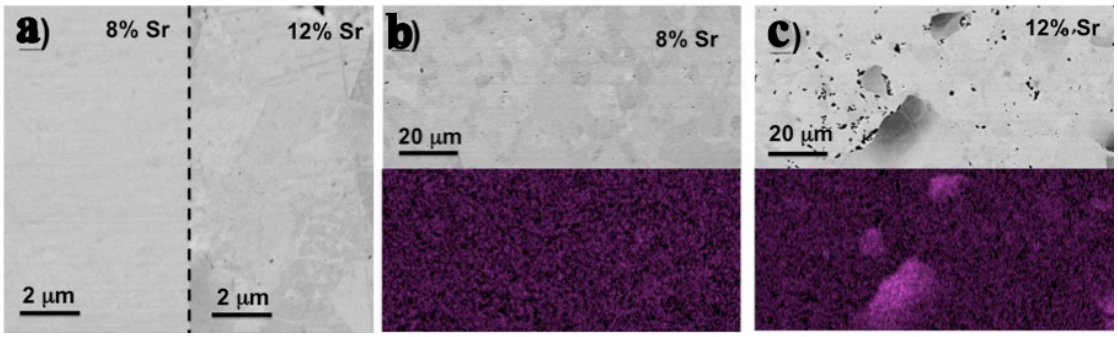

Figure 8.2. SEM backscattered images of $Pb_{0.92}Sr_{0.08}Se$ and $Pb_{0.88}Sr_{0.12}Se$ ingots, with corresponding EDS mapping result in b) and c).

8.3 Changing of Valence Band Structure

In 8.1 we hypothesized that alloying PbSe with SrSe would reduce the energy gap between primary L valence band and Σ valence band. Unfortunately other than calculating the band structure of PbSe with different Sr addition (which may not be considered "direct observation"), there is no direct way to "observe" the change of energy gap between L and Σ valence bands. Historically Veis have used optical transition[253, 256, 262] between two valence bands to derive the position of Σ band edge. This method to us is subject to interpretation and is prone to significant uncertainty. Instead, in this study we demonstrate this change of valence band structure by combining evidence from optical absorption measurements, first principle calculation, and transport property measurements.

The optical band gaps (measured and analyzed by colleague Zachary Gibbs) of undoped $Pb_{1-x}Sr_xSe$ alloys are noticeably larger than that of PbSe (Figure 8.3). Band gaps increase linearly with Sr content through 12% and roughly doubled at this Sr content. For all alloys the absorption spectra actually can be fitted according to either direction transition or indirect transition leading to different band gap values. The apparent fit with an indirect transition was actually observed historically and was seen in the spectrum of binary PbSe as well, probably due to phonon aided transition process rather than a real transition over the band gap, since the band structure of Pb chalcogenides have been very well known as direct both experimentally and theoretically and the values accurately determined. Thus the spectrums are fitted with direct transitions and are attributed to L-L transitions[254] as in pure PbSe.

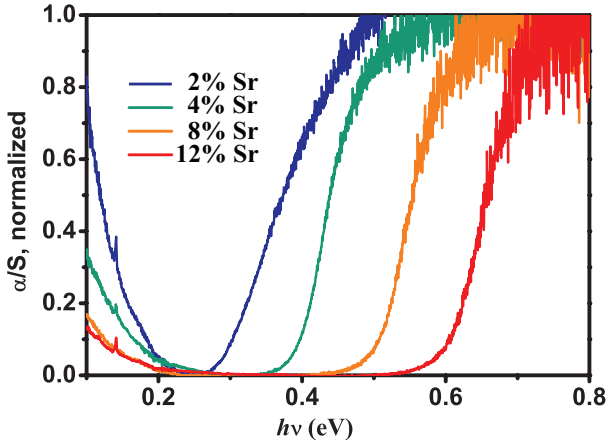

Figure 8.3. Infrared absorption spectrums for undoped $Pb_{1-x}Sr_xSe$, band gaps were obtained by extrapolating the squared absorption coefficient (not shown) versus photon energy $h\nu$.

Optical absorptions in the lead chalcogenides begin with direct transitions across the fundamental gap at the L point. Because these direct transitions do not require phonon participation, they dominate the absorption spectra compared with the L-Σ indirect transitions, which should occur at higher energies. This limits traditional optical absorption to accurately determining the position of Σ band edge.

To obtain such information, we take a look at the Pisarenko relation at 300 K for samples with different Sr content (Figure 8.4), as the change of band structure will consequently affect the transport properties. For PbSe, due to the large offset between two valence-band maxima at room temperature, contribution from the secondary Σ band on transport is negligible and the Pisarenko relation (data in black squares) can be approximated with a single band model (black curve) up to high carrier density of 2×10^{20} cm^{-3} (difference seen from 1×10^{20} in modeling but experimentally undistinguishable). With the addition of Sr, the Seebeck coefficients start to deviate from the curve significantly at high doping levels, with higher values compared to PbSe given the same carrier density. Among the $Pb_{1-x}Sr_xSe$ alloys the Seebeck coefficient also increases as the Sr content increases. If increased Seebeck values were simply due to a larger effective mass, the Seebeck value would be proportionally larger at all n_H, which is not observed in $Pb_{1-x}Sr_xSe$ alloys with low n_H. Alternatively the deviation from a single band model (the black curve) at high n_H indicates the contribution from a second band becomes important as the Fermi level moves into the second valence band, which is also the explanation for the similar Pisarenko behavior in p-type PbTe. The continuous change in the direct L-L band gap due to SrSe alloying can explain the gradual change

of Pisarenko relation. If the energy of the L valence band is reduced as the band gap increases and this reduces the band offset in PbSe between L and Σ valence bands, the secondary Σ band will play a noticeable role in heavily doped, Sr containing PbSe. Assuming half of band gap change results in decreasing separation between L and Σ valence bands, as inspired by observation[260] on thin films at 77 K, the calculated Pisarenko relations for each $Pb_{1-x}Sr_xSe$ alloy composition are shown in Figure 8.4 with colored curves, and are in reasonable agreement with the observed results. The details about the calculation and relevant considerations are length thus will be included in the last section of this chapter.

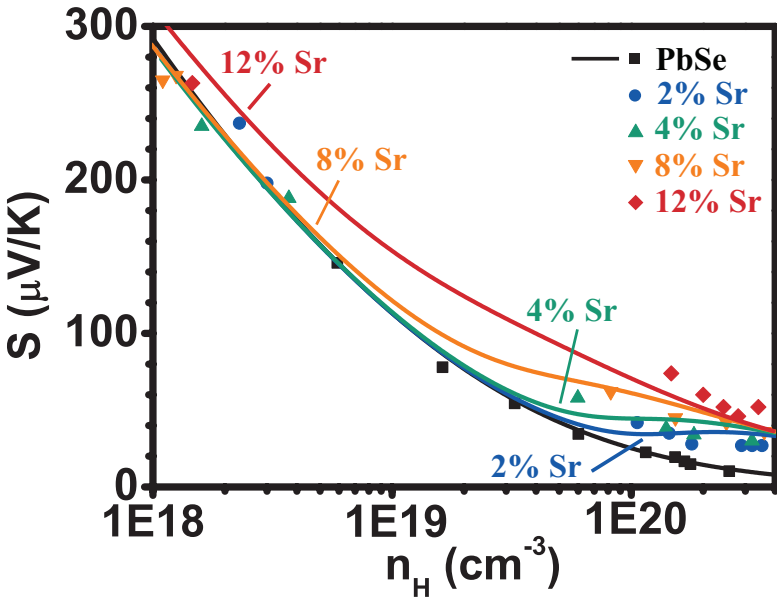

Figure 8.4. Pisarenko relation of p-type PbSe and $Pb_{1-x}Sr_xSe$. Calculated result matches observation reasonably well, suggesting the difference seen in $Pb_{1-x}Sr_xSe$ comes from reduced gap between L and Σ valence bands.

For more independent evidence of how the band structure changes with Sr content, we performed first principle calculation (performed by collaborator Yoshiki Takagiwa) using the Korringa-Kohn-Rostoker Green function formalism under the coherent potential approximation[263-265] (KKR-CPA). For such calculation the experimental room-temperature lattice constants and the von Barth–Hedin formula[266] for the exchange energy were used. For all atoms (Pb, Se, and Sr), the angular momentum cut-off, $l_{max} = 2$, was set and semi-relativistic calculations of core level were employed. A dense mesh of 550 k points in the irreducible wedge of the Brillouin-zone was used. Final converged total energy below 10^{-6} Ry was applied in the self-consistent cycle. The KKR-CPA

method is a powerful tool for visualizing the electronic density of states (DOS) for disordered materials without establishing a supercell and is widely used in studies of thermoelectrics with random substitution[65, 165, 267, 268]. The calculated DOS for each composition (Figure 8.5 a)) shows an abrupt increase around -0.1 eV, this is attributed to the additional states in the Σ band and its position is used to estimate the gap between L and Σ bands. The trend clearly showed the reduction of gap between L and Σ bands. These are in good consistence with the proposed model as well as optical measurements (Figure 8.5 b).

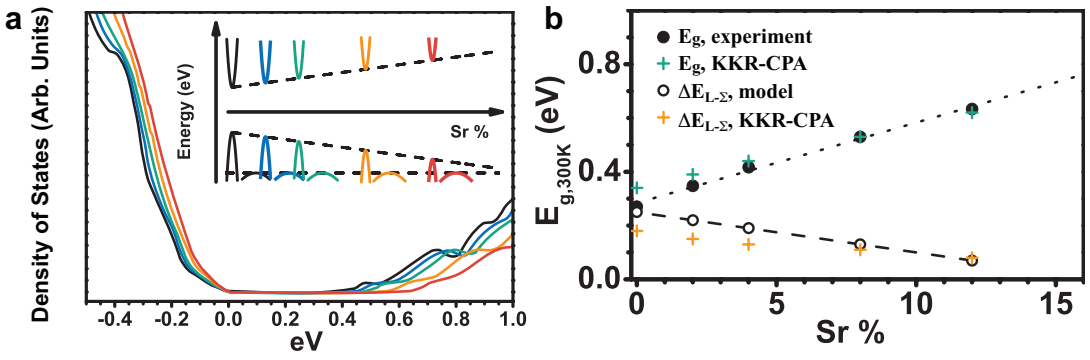

Figure 8.5. a) calculated DOS of $Pb_{1-x}Sr_xSe$, inset shows suggested change of band structure with Sr content, which is used to calculation Pisarenko relation. b) Calculated band gap matches with experimental results, and calculated gap between two valence bands consistent with the model.

Temperature dependent band gap measurement (Figure 8.6) shows that the rate of band gap increase with temperature, dE_g/dT, is also decreased as the increase of Sr, and this rate decreases linearly with Sr content up to 12% at about 0.018 meV K^{-1}/Sr%, so the effect of alloying with Sr on band structure, is not merely moving L and Σ bands closer, but also decreased the rate of how fast the L band position change with temperature. When all these effects are taken into account, we could plot out the reduced energy gap between L and Σ for each alloy composition at different temperatures (Figure 8.7). For 2%, 4%, 8% and 12% Sr, the two bands are effectively converged (gap within $3k_BT$) at 600K, 550K, 400 K and 300K, respectively. Consider that good p-type samples are heavily doped, the Σ would contribute to transport at even lower temperatures for $Pb_{1-x}Sr_xSe$ alloys.

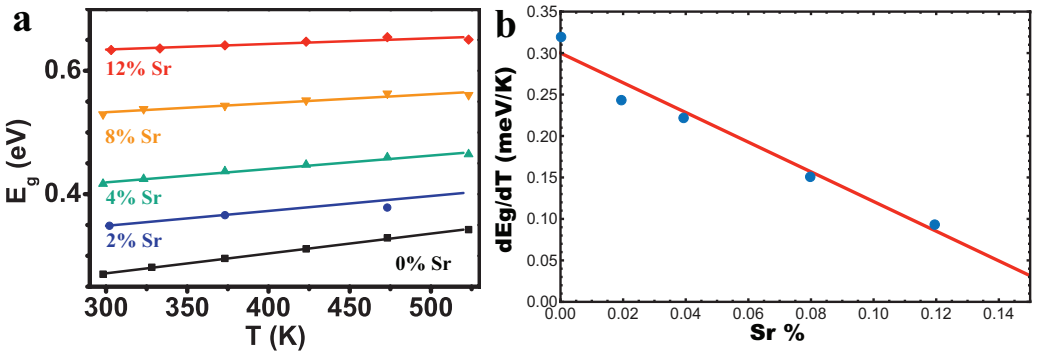

Figure 8.6. a) temperature dependent bang gap of $Pb_{1-x}Sr_xSe$ and b) change in rate dE_g/dT with Sr content.

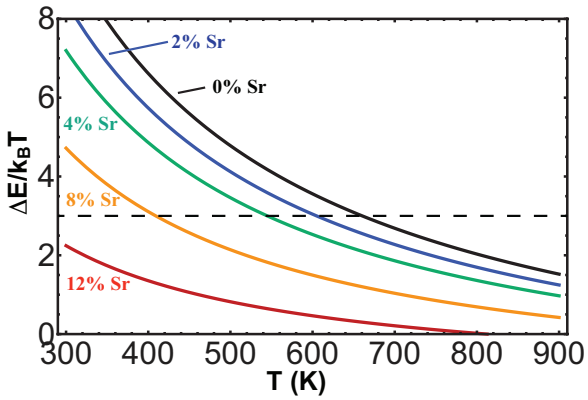

Figure 8.7. Reduced energy gap between two valence bands in $Pb_{1-x}Sr_xSe$ as function of temperature, dashed line denotes $3k_BT$.

8.4 Transport Properties

Figure 8.8 through Figure 8.12 shows the temperature dependence of transport properties and zT for all samples, grouped according to the Sr content. For each group, degenerate semiconductor behavior is seen, and each property changes with doping level in an expected way. To calculate the lattice thermal conductivity, the electronic contribution was subtracted with Lorenz number L calculated from single parabolic band model. The use of single parabolic band model here is because of its simplicity, i.e., being a function of only the Seebeck coefficient. Although a more precise model is available to account for the influence from all three bands and their changes with Sr content, calculating L for each sample at each temperature using this model is very complicated and time consuming. A single parabolic band model on the other hand, would capture qualitative the trend which is enough for an overall visualization.

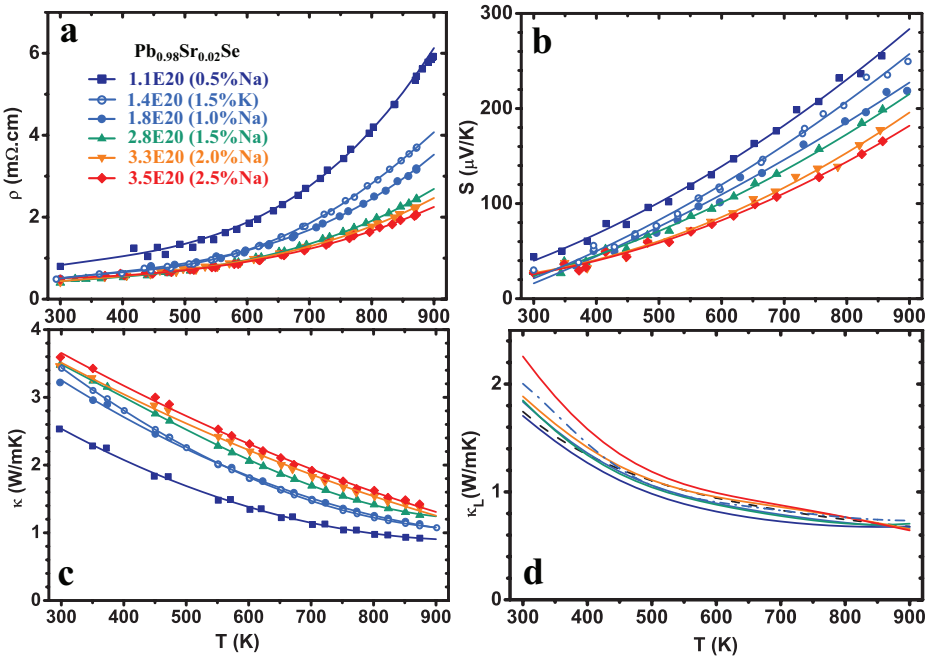

Figure 8.8. Temperature dependence of a) resistivity, b) Seebeck coefficient, c) thermal conductivity and d) lattice thermal conductivity for $Pb_{0.98}Sr_{0.02}Se$ with different doping level.

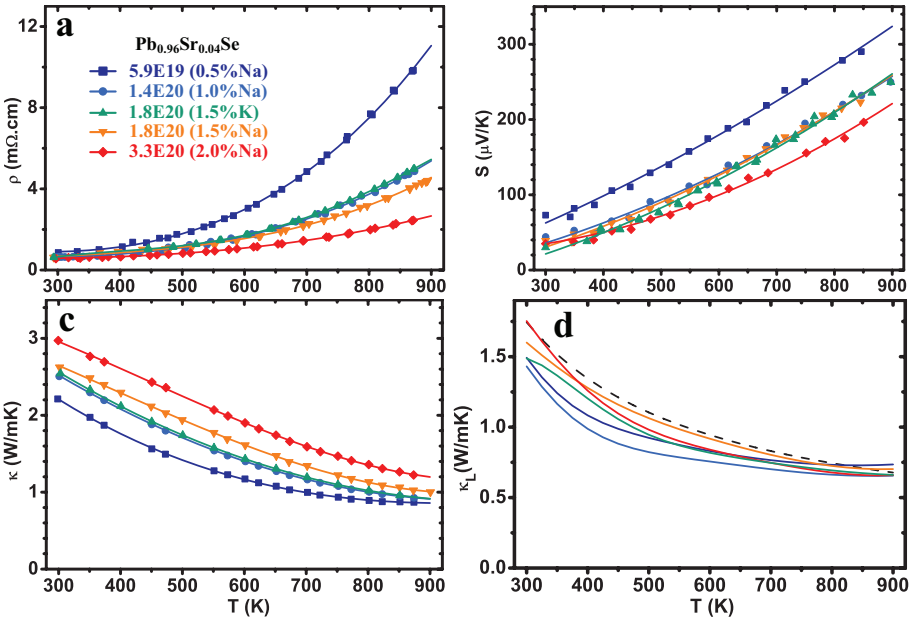

Figure 8.9. Temperature dependence of a) resistivity, b) Seebeck coefficient, c) thermal conductivity and d) lattice thermal conductivity for $Pb_{0.96}Sr_{0.04}Se$ with different doping level.

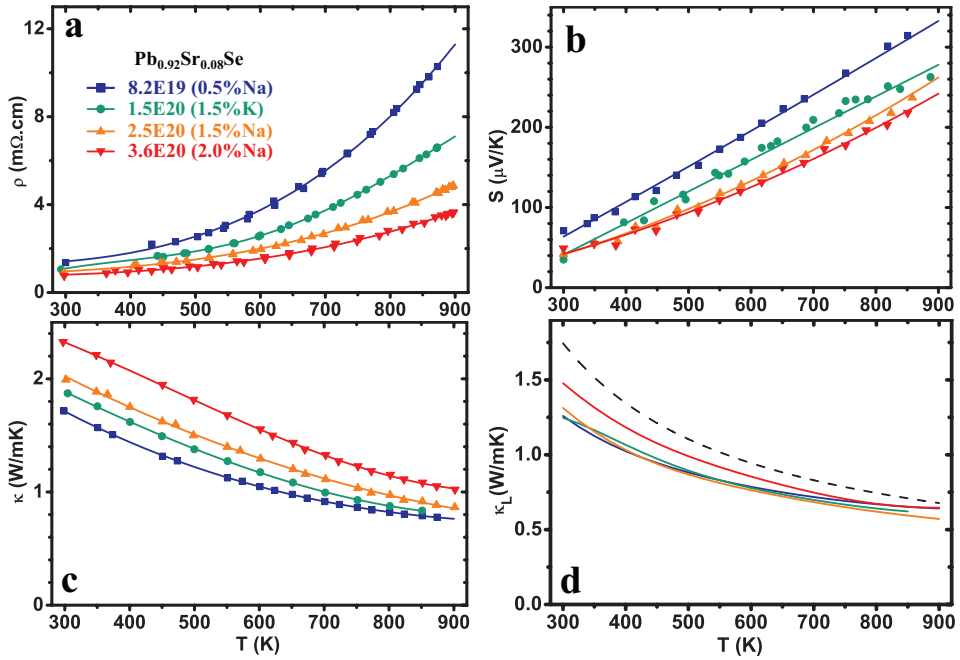

Figure 8.10. Temperature dependence of a) resistivity, b) Seebeck coefficient, c) thermal conductivity and d) lattice thermal conductivity for $Pb_{0.92}Sr_{0.08}Se$ with different doping level.

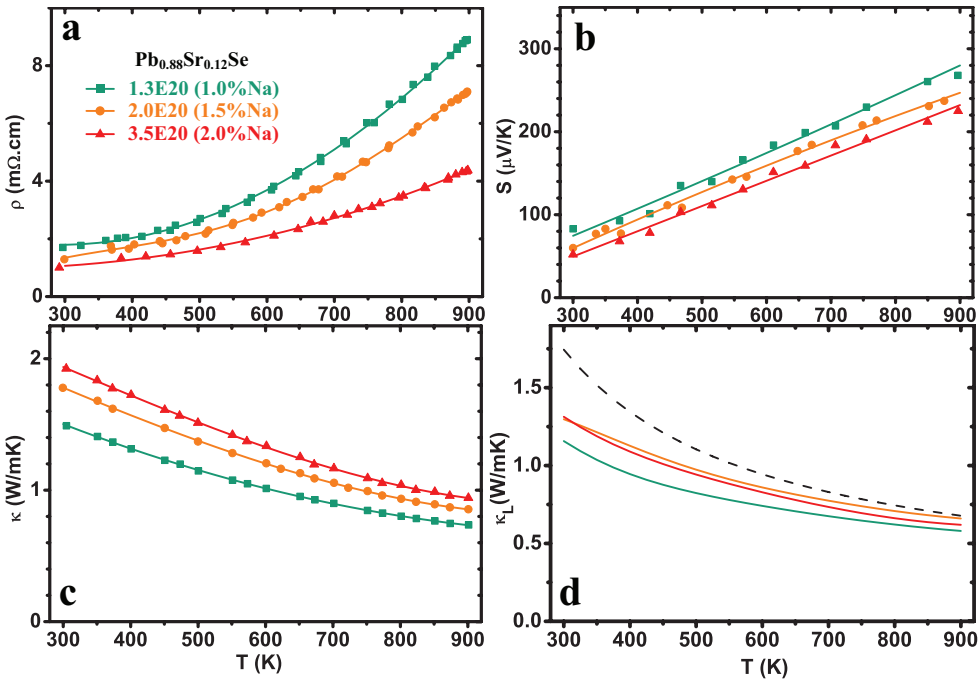

Figure 8.11. Temperature dependence of a) resistivity, b) Seebeck coefficient, c) thermal conductivity and d) lattice thermal conductivity for $Pb_{0.88}Sr_{0.12}Se$ with different doping level.

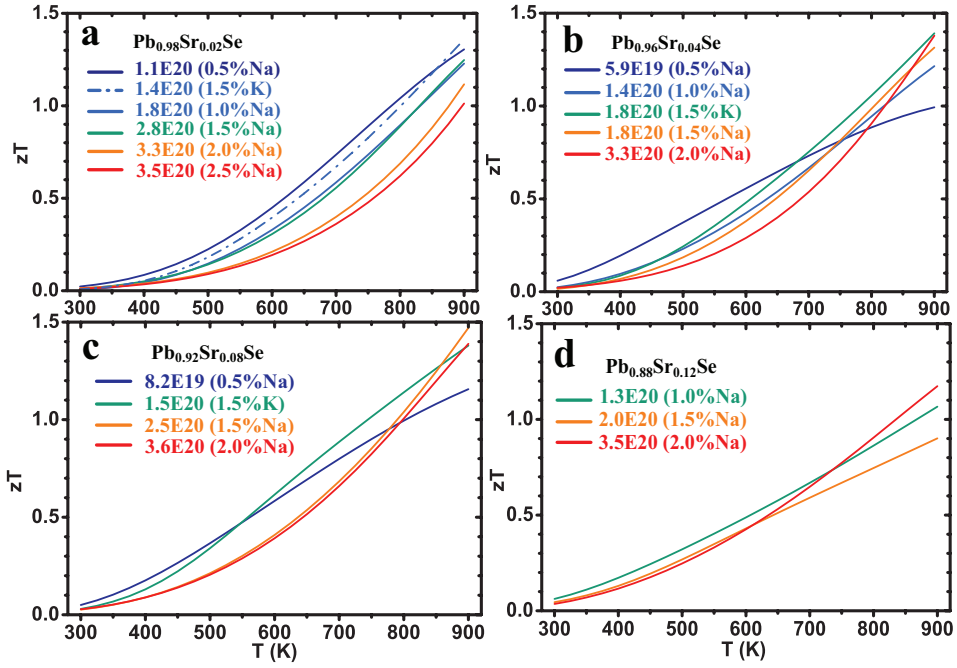

Figure 8.12. Temperature dependence of zT for all $Pb_{1-x}Sr_xSe$ samples

With the comprehensive data shown. We will now demonstrate the effect of Sr on transport properties, and more evidence on reduced gap between two valence bands in a more direct way.

In Figure 8.13 the temperature dependent transport properties of $Pb_{1-x}Sr_xSe$ alloys with different Sr contents are compared. Samples chosen are of similar Hall carrier density at room temperature between 1.3 and 1.8 × 10^{20} cm^{-3}. Na and K do not change the band structure of lead chalcogenides[41] and transport properties of Na and K doped samples are comparable when carrier density is similar, thus all the difference shown in Figure 8.13 is due to different Sr content. The resistivity increases significantly with Sr content, which can be expected from increased alloy scattering of carriers. The increased resistivity also stems from the increased contribution from the Σ band that has a heavier effective mass. Compared with results from this study, PbSe with 0%, 2% and 4% SrSe in Lee's work[269] has very similar resistivities at high temperatures: only subtle difference is seen between PbSe and PbSe with 2% Sr, but the increase of resistivity in PbSe with 4% Sr compared to PbSe is obvious.

As shown in Figure 8.13 b) alloys with higher Sr content have higher Seebeck coefficients. This trend is observed through the entire temperature range up to 8% Sr. The higher S values can be explained by the carrier redistribution between two valence bands, which populates more states in

the high density-of-states Σ band in alloys with more Sr, so for a given carrier density the alloys with higher Sr content have more carriers in the Σ band hence the chemical potential is closer to the band edge. The alloy with 12% Sr shows higher *S* value compared with the 8% Sr alloy mainly around room temperature. This can be understood considering that as the T_{cvg} continues to decrease the Σ band plays primary role in transport at high temperature in both 8% and 12% alloys thus the difference in chemical potential between them is small. The increase of *S* with Sr content was not as recognizable in Lee's work where the difference between samples with 2%Sr and 4% Sr is comparable with measurement uncertainty, even though for each sample the result is generally consistent with this study.

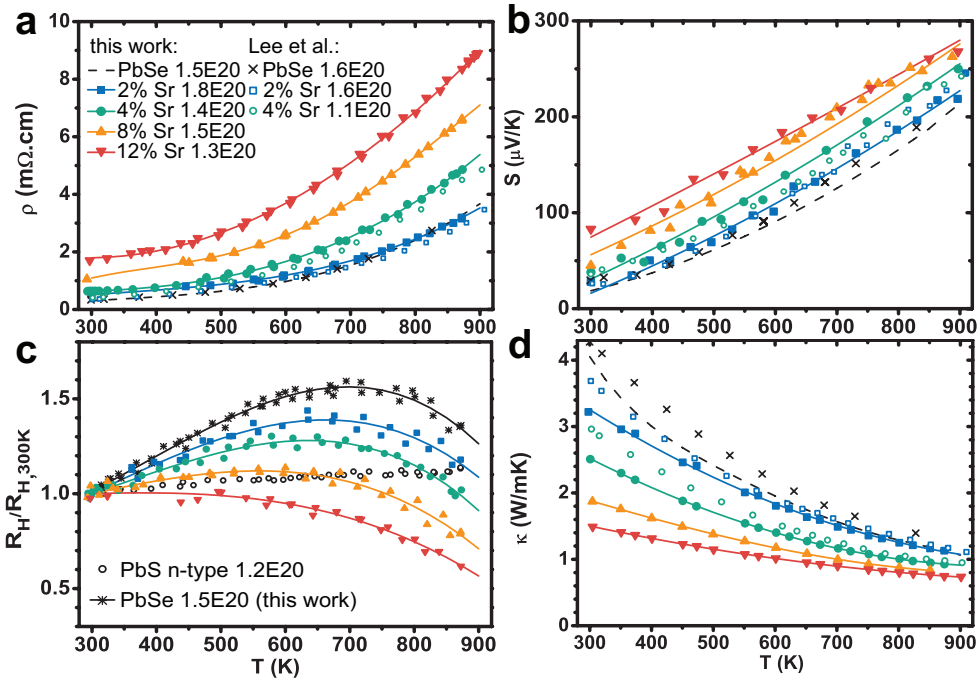

Figure 8.13. Temperature dependence of a) resistivity, b) Seebeck coefficient, c) Hall coefficient and d) thermal conductivity of $Pb_{1-x}Sr_xSe$ alloys. Legends denote Hall carrier density at 300 K.

The temperature dependence of Hall coefficient (R_H) of each sample is compared in Figure 8.13 c. The relative ratios to their room temperature values are presented. In single-band systems the temperature dependence of R_H is weak and monotonic (see R_H for n-type PbS with $n_H = 1.2 \times 10^{20}$ cm^{-3}). Non-monotonic R_H-*T* curves usually indicates two types of carriers (electrons and holes, or electrons/holes with different effective masses) co-existing in transport, and R_H peaks when the contribution from each type of carriers on conduction are equal (T_{cvg} should be higher than the temperature where R_H peaks). Given their similar carrier density the difference in temperature

where R_H peaks among different samples are primarily caused by the difference in the band structure: lower peaking temperature indicates more contribution from the secondary Σ band at a given temperature, which is the outcome of reduced energy offset between L and Σ band.

The thermal conductivities of $Pb_{1-x}Sr_xSe$ alloys are lower than that of PbSe (Figure 8.13 d)). Compared with the values reported[269] by Lee et al., thermal conductivities of $Pb_{1-x}Sr_xSe$ alloys in this work are found lower near room temperature due to larger resistivities. At high temperatures the results for the same alloy composition from both studies are found to be very similar.

Figure 8.14 shows the maximum *zT* of different $Pb_{1-x}Sr_xSe$ alloys compared with that of PbSe. The *zT* for p-type PbSe, has been reevaluated as shown in Chapter 3 and the maximum was found to be 1.0 at 900 K. This value agrees with Lee's recent report. Compared with PbSe, noticeable improvement of *zT* is seen in $Pb_{1-x}Sr_xSe$ alloys for Sr content as low as 2%: both this study and the Lee's report have measured *zT* of 1.3 at 900 K. Result from this study also indicates that *zT* can be further improved as Sr content increases, *zT* of 1.5 is observed at 900 K for properly doped alloy with 8% Sr, further increasing Sr content seems to reduce the maximum *zT*. *zT* of 1.4 ± 0.1 at 900 K was achieved in multiple samples with different Sr content, each requiring different carrier densities. As shown in Figure 8.14 more carriers are required for alloys with higher Sr content, as the density-of-state effective mass increases with increased contribution from Σ band.

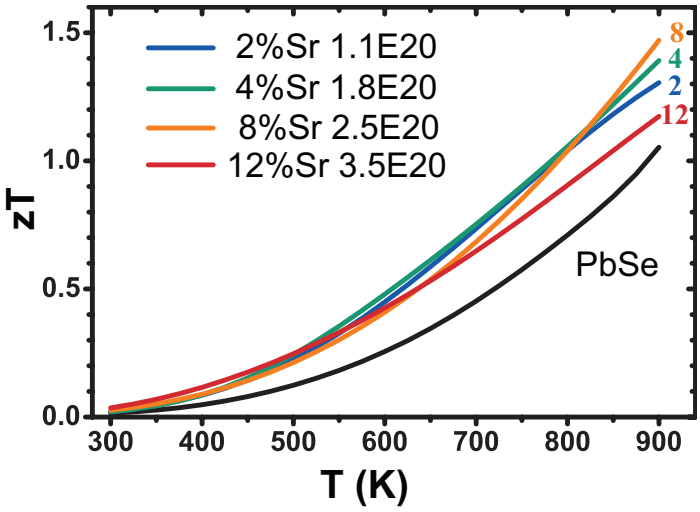

Figure 8.14. Temperature dependence of *zT* from samples with carrier density optimized to achieve maximum zT at 900 K with different Sr content.

Now that we have demonstrated the successful improvement of zT by alloying PbSe with SrSe, it is important to identify the origin of such improvement, since the disorder brought by atomic substitution is also often believed beneficial for thermoelectrics.

In Figure 8.15 a, κ_L of alloys with different Sr content at both 300 K and 850 K are compared. The 300 K data from this work are taken from undoped samples with high electrical resistivity and therefore negligible κ_e. κ_L at 850 K are evaluated with Lorenz number L from single parabolic band model from doped samples. The thermal conductivity reduction in $Pb_{1-x}Sr_xSe$ alloys, which is more effective at room temperature and less so at 850 K, can be well explained by Callaway and Klemens' point defect model discussed in Chapter 7 (the solid curves). For 10% Sr as an example the κ_L reduction is 25% at 300 K, and 15% at 850 K as suggested by both the experiment and model. At high temperature, κ_L from Lee's work is found to follow the same trend. Differences can be seen at room temperature where larger reduction of κ_L with Sr content has been reported. However, such report is of less reliability as they were calculated from doped samples, as seen plenty of times in the previous chapters this potentially leads to significant amount of error in κ_L.

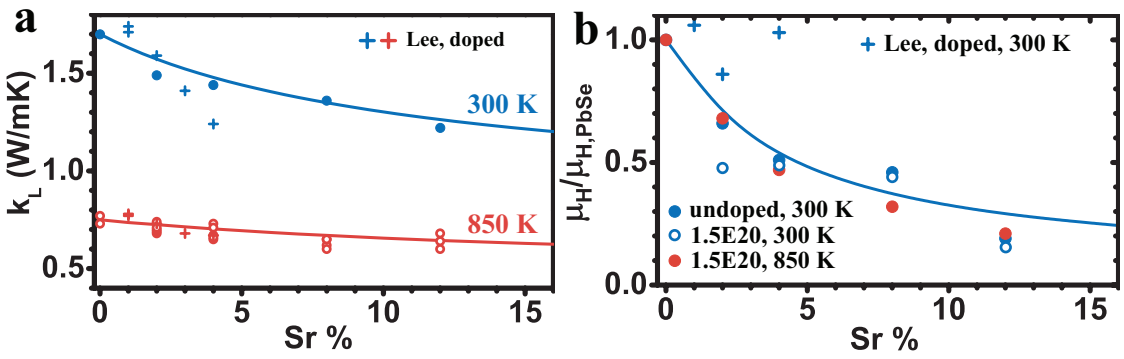

Figure 8.15. The influence of Sr substitution on a) lattice thermal conductivity, and b) Hall mobility due to Pb site disorder.

The Sr addition is also found to reduce the carrier mobility. In undoped samples the mobility reduction is solely related to the alloy scattering because the contribution of the secondary band is minimal and the effective mass of L valence band stays unchanged in Sr alloys as in PbSe. For the mobility reduction in undoped $Pb_{1-x}Sr_xSe$ alloys ($n_{H,300\ K} \leq 3\times10^{18}$ cm^{-3}) at 300 K (expressed as measured Hall mobility relative to Hall mobility of PbSe with same carrier density) shown in Figure 8.15 b), the observed trend can be understood with alloy scattering discussed in Chapter 7. The magnitude of alloy scattering in the L valence band is adjusted to fit the experimental result, the

model involves contribution from all three relevant bands, and takes into account combined scattering mechanisms of deformation potential phonon scattering, polar scattering from optical phonons and alloy scattering. The alloy scattering potential U is estimated to be 3 eV for the L band. This is a fairly large U value compared to those reported for other systems.

Strictly speaking, mobility reduction in heavily doped samples is the result of intertwined influence of alloy scattering and carrier re-distribution associated with change of valence band offset. Nonetheless as shown in Chapter 4 for p-type PbSe the Hall mobility of a two-valence-band system as PbSe is primarily dominated by the L band at most temperatures. So approximately the mobility of doped samples should show similar level of reduction at the same temperature. In Figure 8.15 b) the normalized mobilities for a few doped samples with n_H around 1.5×10^{20} cm^{-3} are also shown. Many of these values seem to be affected by crystal imperfection thus are lower than expected, however, largely the similar trend is still followed. The relative mobilities of these samples at 850 K are also shown and they have indicated roughly the same level of reduction as at 300 K. In this case, as the two valence bands come close at high temperatures and the carrier population increases greatly in the Σ band, the measured Hall mobility could no longer be approximated by that of the L band along. So it is hard to factorize how much of the mobility reduction seen here is due to alloy scattering and how much was due to the Σ band with heavier mass and lower mobility.

The mobility of doped samples ($n_{H,300\,K} > 1\times10^{20}$ cm^{-3}) at 300 K was found in Lee's work not decreased compared to PbSe, being similar to the previously suggested absence of mobility reduction[261] in Sr added PbTe. We suspect the reason is because Sr was not alloyed into the PbSe lattice in Lee's samples. The way Lee's samples were synthesized didn't fully consider high melting temperature of SrSe and reaction of Sr with quartz over long time exposure above 1400 K. The trend in Seebeck coefficient of the 2% and 4% Sr sample is essentially the same as PbSe, which is a strong indication of Sr not alloying in. Lee's work would be on the other hand interesting if it proved that under some specific configuration, such as in nano scale clusters instead of substituting Pb, Sr will perform lattice thermal conductivity reduction without scattering the carriers (there will be no band structure tuning as well) and lead to zT improvement. However, the reported reduction of κ_L at room temperature is not convincing without direct measurement of κ_L from undoped samples and the stability of such configuration is very questionable. Basically it is the same system that has been studied in both works, and there could be only one thermodynamically stable configuration, by comparing the synthesis details we have enough reason to believe samples presented here are closer to thermodynamic equilibrium than those in Lee's work.

With all this said, assuming Lee's κ_L and mobilities are accurate, it could suggest that there could be some intermediate configuration of solute atoms in systems that are supposed to be solid solutions thermodynamically, under which the lattice thermal conductivity could be reduced without affecting carrier mobility. This would be an effect very useful for thermoelectrics around room temperature.

Let's come back to the case of $Pb_{1-x}Sr_xSe$ with random substitution. We compare it with a relevant case, the substitution of Se by Te, which has overall compensated effects for n-type PbSe. For instance, 10% Te substitution resulted in roughly 20% decrease at 300 K in both lattice thermal conductivity and carrier mobility. As for $Pb_{1-x}Sr_xSe$, the κ_L reduction is higher at 25% for 10% Sr substitution, but the mobility suppression is much worse, down to < 50%. The slightly larger κ_L reduction comes from larger mass contrast between Sr and Pb (compared with that between Se and Te). The much larger alloy scattering potential U (U around 1 eV for n-type $PbSe_{1-x}Te_x$) is probably linked to the larger mismatch of valence band energy: the electron affinity of SrSe is[270] 1.8 eV and its band gap (Γ-X) is[271, 272] 3.8 eV, the top of its valence band at Γ point is thus 5.6 eV below the vacuum level. On the other hand the work function of PbSe is[273] 4.6 eV and the band gap 0.3 eV, which means the top of its L valence band is 4.8 eV below the vacuum level: a 0.8 eV difference in band energy between PbSe and SrSe. For comparison, the difference in conduction band energy between PbSe and PbTe is only[223] 0.1 eV. Moreover, if the same argument can be applied to SrTe and PbTe system, the band energy mismatch is also large so the absence of alloy scattering in mobility is not expected theoretically, which is again an indication of Sr not dissolving in PbTe lattice.

The substitution of Pb by Sr in PbSe should be an undesired disorder, this is certain for L band dominated regime. The same conclusion can also be drawn by applying the criteria for beneficial disorder. At high temperatures when the Σ band comes into play, a definite conclusion is hard because almost all parameters for the Σ band are of great uncertainty. It seems to be less detrimental, but still more likely to be unwanted. Nonetheless, zT improvement is still achieved in $Pb_{1-x}Sr_xSe$ alloys because the valence band structures are tuned in favor of thermoelectric properties. Specifically, the gap between the primary L band and secondary Σ band is decreased, so that the highly degenerate Σ band could contribute more to the carrier transport. This effect, in $Pb_{1-x}Sr_xSe$, competes with the undesirable Pb site disorder. The net result is a significant increase of zT over a broad range of Sr content from 2% to 8%. When the Sr content is further increased, the negative effect of Pb site disorder overwhelms resulting in decreased zT.

8.5 Details on Modeling the Band Structure Change

The model used to characterize how band structure and thus transport properties change with Sr content takes into account the primary valence band (the light band, L band), the secondary valence band (the heavy band, Σ band) and the conduction L band. The light band and the conduction band are Kane bands whereas the heavy band is parabolic. The carrier scattering mechanism takes into account the deformation potential scattering (acoustic phonon scattering), the polar scattering from optical phonons and the alloy scattering. The relaxation time of each mechanism is described in previous Chapters 3, 6 and 7. The transport parameters for each single band are calculated using the method described in Chapter 6, and each transport property is calculated using Putley's equations for multiple band systems described in Chapter 4. A lot of parameters, mainly those about the Σ band are hard to determine accurately, and the total number of unknown parameters exceeds the number of known transport properties to solve them with. Nonetheless we managed to determine all the parameters needed based on the best fit of experimental result. The parameters are determined based on the following considerations:

1. The density-of-state effective mass of the light band and the conduction band is taken as 0.27 m_e at 300 K and changes with temperature following $d\ln m^*/d\ln T = 0.5$, the anisotropy factor K is taken as a constant 1.75. The deformation potential for the conduction band and the light band were determined as 25 and 35 eV. These are determined from the study of binary PbSe, and assumed not changed by small amount of Sr addition (up to 12%).

2. For the parameters of the heavy band, based on suggested values from Veis' report[253] and temperature dependent transport properties of p-type PbSe these parameters are determined as: DOS effective mass 4.2 m_e, $K = 1$, and the deformation potential 28 eV. As shown in Chapter 4, the overall fitting does not change sensitively with these parameters, for each parameter there is a range of possible values, so the values used here is a bit arbitrary.

3. The band gap and its temperature dependence as well as the dependence on Sr content can be accurately determined from optical absorption measurements, the 0 K position of Σ and or, the gap between two valence bands ΔE is a parameter in the modeling of p-type PbSe and was chosen as 0.32 eV. We assume half of the band gap change due to Sr results in the decrease of ΔE. While for the temperature dependence of ΔE, based on modeling of p-type PbSe and considering Russian researchers report, we described the position of Σ band as largely constant but moves slightly,

resulting in a rate of decrease in ΔE that is slightly larger than half of the band gap increase. The rate of band gap decreasing with temperature also changes with Sr content as found experimentally, this is also taken into account, and we further assume half of this will affect the change of $d\Delta E/dT$. The summarized E_g and ΔE under different temperature and Sr content ($Pb_{1-x}Sr_xSe$) are:

$$E_g/\text{eV} = 0.27 + (3-17.9x) \times 10^{-4} (T/\text{K}-300) + 3.2x \quad \text{Equation 8.1}$$

$$\Delta E/\text{eV} = 0.25 - (2.2-8.9x) \times 10^{-4} (T/\text{K}-300) - 1.6x \quad \text{Equation 8.2}$$

4. The alloy scattering potential U due to Sr substitution, for the light valence band is determined as 3 eV, which is estimated from measured Hall mobility of undoped $Pb_{1-x}Sr_xSe$ alloys. The same U is taken for the conduction band because no data is available so far to estimate it more accurately, as the result of increased band gap and heavily doped samples, the parameter of conduction band does not affect the final result very significantly. U for the heavy band is assumed to be 1.5 eV. A smaller U for the heavy band is consistent with the assumption that the heavy band position does not explicitly depend on Sr content. The value of 1.5 eV is used to provide the best overall fitting for Pisarenko relations of alloys.

Appendix A

Derivation of Transport Parameters from Boltzmann Transport Equation

Under single parabolic band model we have relatively simple expressions for transport parameters as functions of η, m^*, and τ. Especially when we further simplify the energy dependence of τ under single scattering mechanism (usually acoustic phonon as long as T is not too low), these expressions can be written as:

1. The chemical carrier density

$$n = \frac{4\pi(2m^* k_B T)^{3/2}}{h^3} F_{1/2}(\eta) \tag{A.1}$$

2. The electrical conductivity:

$$\sigma = -\frac{e^2}{3\pi^2 m^*}\left(\frac{2m^*}{\hbar^2}\right)^{3/2}(r+3/2)\tau_0\left(k_B T\right)^{r+3/2} F_{r+1/2}(\eta) \tag{A.2}$$

the drift mobility

$$\mu_d = \frac{\sigma}{ne} = \frac{-\frac{2e}{3m^*}(r+3/2)\tau_0\left(k_B T\right)^r F_{r+1/2}(\eta)}{F_{1/2}(\eta)} \tag{A.3}$$

3. the Seebeck Coefficient, and the approximated equation for two extreme cases:

$$S = \frac{k_B}{e}\left[\eta - \frac{(r+5/2)F_{r+3/2}(\eta)}{(r+3/2)F_{r+1/2}(\eta)}\right] \tag{A.4}$$

$$S = \frac{k_B}{e}\left(A + \ln\frac{2(2\pi m^* k_B T)^{3/2}}{h^3 n}\right) \qquad \text{for nondegenerate}$$

$$= \frac{8\pi^2 k_B{}^2}{3eh^2} m^* T\left(\frac{\pi}{3n}\right)^{2/3} \qquad \text{for degenerate}$$

4. The Lorenz number L in Wiedemann-Franz Law

$$L = \left(\frac{k_B}{e}\right)^2\left[\frac{r+7/2}{r+3/2}\times\frac{F_{r+5/2}(\eta)}{F_{r+1/2}(\eta)} - \left(\frac{r+5/2}{r+3/2}\right)^2 \times \frac{F_{r+3/2}(\eta)^2}{F_{r+1/2}(\eta)^2}\right] \tag{A.5}$$

5. the Mott relation, not quite useful for modeling but is often used to make general argument:

$$S = \frac{\pi^2}{3}\cdot\frac{k_B{}^2 T}{e}\frac{\partial \ln\sigma_E}{\partial E}\bigg|_\eta \tag{A.6}$$

In this Appendix A will derive some of the equations above. My reference include: 1) V. I. Fistul, *Heavily Doped Semiconductors*, Plenum Press, New York, 1969. 2) G. S. Nolas, J. Sharp, and H. J. Goldsmid, *Thermoelectrics Basic Principles and New Materials Developments,* Springer, Berlin, Heidelberg, 2001. 3) A. F. Ioffe, *Physics of Semiconductors,* Academic Press Inc. New York, 1960.

1. for n this is a very straightforward derivation with the concept of density-of-states.

$$\begin{aligned} n &= \int_0^\infty g(E) f_0(E) dE \\ &= \int_0^\infty 4\pi\left(\frac{2m^*}{h^2}\right)^{3/2}\sqrt{E} f_0(E) dE \\ &= \frac{4\pi\left(2m^* k_B T\right)^{3/2}}{h^3}\int_0^\infty \sqrt{\frac{E}{k_B T}}\frac{1}{1+\exp\left(\frac{E-\mu}{k_B T}\right)} d\frac{E}{k_B T} \\ &= \frac{4\pi\left(2m^* k_B T\right)^{3/2}}{h^3} F_{1/2}(\eta) \end{aligned} \tag{A.7}$$

To get the rest of the equations the Boltzmann Equation is needed. The following paragraphs is to help understand this equation in general:

If we describe the transport process using statistic mechanics then all the movement of particles could be expressed by the change of their overall distribution function. So consider electrons moving in external fields, in statistical mechanics the steady state is described by:

$$\left(\frac{\partial f}{\partial t}\right)_{fields} + \left(\frac{\partial f}{\partial t}\right)_{collision} = 0 \tag{A.8}$$

The first term represents the external fields (electric and temperature for example) disturbing the distribution function *f* of electrons, and the second term here represents the effect of collisions (or, scattering) that keeps electrons from infinitely accelerating under external forces, or say, restoring the distribution function.

A simple assumption about the scattering process, the so-called relaxation time approximation is: The rate that scattering restores the distribution function is linearly proportional to the extent of deviation of distribution function from its equilibrium (though we tend to assume the difference between them is small). The rate of restoration is constant for all types of external forces. Accordingly we can write the collision term as:

$$\left(\frac{\partial f}{\partial t}\right)_{collision} = \frac{f - f_0}{\tau_E} \tag{A.9}$$

This is generally the case when dealing with phonon scattering of electrons at high temperature ($T>\Theta$), or scattering by point defects.

For the first term:

$$\begin{aligned}\left(\frac{\partial f}{\partial t}\right)_{fields} &= \frac{\partial f}{\partial \mathbf{x}}\cdot\frac{\partial \mathbf{x}}{\partial t} + \frac{\partial f}{\partial \mathbf{k}}\cdot\frac{\partial \mathbf{k}}{\partial t} \\ &= -\left(\mathbf{v}\nabla f + \frac{1}{\hbar}\frac{\partial \mathbf{p}}{\partial t}\cdot\nabla_k f\right) \\ &= -\left(\mathbf{v}\nabla f + \frac{1}{\hbar}F\cdot\nabla_k f\right)\end{aligned} \tag{A.10}$$

F here represents a generalized form of force. In the case of electric field it is $-eE$, for more complicated cases it is tabulated in *Fistul*:

2. For σ, consider the electrical conduction, when the temperature is uniform (means $\nabla f = 0$).

$$
\begin{aligned}
i &= \int e\mathbf{v}dn \\
&= \frac{2e}{(2\pi)^3}\int \mathbf{v}f(k)d^3k \\
&= \frac{2e\hbar}{(2\pi)^3 m^*}\int \mathbf{k}f(\mathrm{k})d^3k \\
&= \frac{2e\hbar}{(2\pi)^3 m^*}\int \mathbf{k}\tau\frac{f-f_0}{\tau}d^3k
\end{aligned}
\tag{A.11}
$$

Here we used the fact that no electric current at equilibrium, *i.e.,*

$$
i_0 = \int e\mathbf{v}\,dn = \frac{2e}{(2\pi)^3}\int \mathbf{v}f_0(k)d^3k = 0
\tag{A.12}
$$

Use:

$$
\frac{f-f_0}{\tau} = -\left(\frac{\partial f}{\partial t}\right)_{collision} = \left(\frac{\partial f}{\partial t}\right)_{field} = \frac{eE}{\hbar}\nabla_k f = -\frac{eE}{\hbar}\frac{\partial f}{\partial k} = \frac{eE}{\hbar}\frac{\partial f_0}{\partial k}
\tag{A.13}
$$

we have

$$
\begin{aligned}
i &= \frac{2eh}{(2\pi)^4 m^*}\int \mathbf{k}\tau\frac{f-f_0}{\tau}d^3k \\
&= \frac{2e^2E}{(2\pi)^3 m^*}\int \mathbf{k}\tau\frac{\partial f_0}{\partial k}d^3k \\
&= \frac{2e^2E}{(2\pi)^3 m^*}\int k^3\tau\frac{\partial f_0}{\partial k}\sin\theta d\theta d\phi dk \\
&= \frac{2e^2E}{(2\pi)^3 m^*}\int \mathbf{k}k^2\tau\frac{\partial f_0}{\partial k}\sin\theta d\theta d\phi dk \\
&= \frac{e^2E}{\pi^2 m^*}\int \mathbf{k}k^2\tau\frac{\partial f_0}{\partial k}dk \\
&= \frac{e^2E}{\pi^2 m^*}\int (k_1 i + k_2 j + k_3 k)\cdot k^2 i\tau\frac{\partial f_0}{\partial k}dk,\ k_1,k_2,k_3 \text{ indistinguishable, deg}\textit{eneracy} \text{ gives factor 3} \\
&= \frac{e^2E}{3\pi^2 m^*}\int k^3\tau\frac{\partial f_0}{\partial k}dk
\end{aligned}
\tag{A.14}
$$

Substitute *k* with energy E, and use the definition of electrical conductivity $\sigma = i/E$

$$\sigma = \frac{i}{E} = \frac{e^2}{3\pi^2 m^*}\int_0^\infty \left(\frac{2m^*}{\hbar^2}\right)^{3/2} E^{3/2}\tau_E \frac{\partial f_0}{\partial E} dE$$
$$= -\frac{e^2}{3\pi^2 m^*}\left(\frac{2m^*}{\hbar^2}\right)^{3/2}\int_0^\infty f_0 \frac{\partial (E^{3/2}\tau_E)}{\partial E} dE$$
$$= -\frac{e^2}{3\pi^2 m^*}\left(\frac{2m^*}{\hbar^2}\right)^{3/2}\left(r+3/2\right)\tau_0\left(k_B T\right)^{r+3/2} F_{r+1/2}(\eta) \tag{A.15}$$

Thus we have the expression for electrical conductivity with the assumption that there is only one predominant scattering mechanism. The drift mobility comes out immediately. Unfortunately, the derivation of r_H has not been done. Fistul's book has detailed explanation for interested readers.

3. For Seebeck coefficient S, we start with the Boltzmann equation. As discussed above, the field term can be written as:

$$\left(\frac{\partial f}{\partial t}\right)_{fields} = \frac{\partial f}{\partial \mathbf{x}}\cdot\frac{\partial \mathbf{x}}{\partial t} + \frac{\partial f}{\partial \mathbf{k}}\cdot\frac{\partial \mathbf{k}}{\partial t} \tag{A.16}$$

Now some tricks are needed to rewrite this equation in a form that leads us to the familiar expression. The idea is to substitute all forms of partial derivatives of f with one single form, the partial derivative of f respect to energy. Also, f is arbitrarily exchangeable with f_0 the equilibrium distribution of electrons (Fermi-Drac distribution) in the following derivation, since the system is not far away from equilibrium.

The details are listed below:

For the first term,

$$\frac{\partial f}{\partial x}\cdot\frac{\partial x}{\partial t} = \frac{\partial f}{\partial E}\cdot\frac{\partial E}{\partial T}\cdot\frac{\partial T}{\partial x}\cdot\frac{\partial x}{\partial t} = \frac{\partial f}{\partial E}\cdot\frac{\partial E}{\partial T}\cdot\frac{\partial T}{\partial x}\cdot v \tag{A.17}$$

$$\frac{\partial E}{\partial T} = \frac{\partial f}{\partial T}\Big/\frac{\partial f}{\partial E} \approx \frac{\partial f_0}{\partial T}\Big/\frac{\partial f_0}{\partial E} \tag{A.18}$$

$$\frac{\partial f_0}{\partial T} = \frac{\partial\left(\frac{1}{e^{\frac{E-\mu}{k_B T}}+1}\right)}{\partial T} = -\frac{\frac{E-\mu}{k_B T}\cdot -\frac{E-\mu}{k_B T^2}}{\left(e^{\frac{E-\mu}{k_B T}}+1\right)^2} \tag{A.19}$$

$$\frac{\partial f_0}{\partial E} = \frac{\partial\left(\frac{1}{e^{\frac{E-\mu}{k_B T}}+1}\right)}{\partial E} = -\frac{\frac{E-\mu}{k_B T}\cdot\frac{1}{k_B T}}{\left(e^{\frac{E-\mu}{k_B T}}+1\right)^2} \tag{A.20}$$

$$\frac{\partial E}{\partial T} = -\frac{E-\mu}{T} \tag{A.21}$$

$$\frac{\partial f}{\partial x}\cdot\frac{\partial x}{\partial t} = v\cdot\frac{\partial f_0}{\partial E}\cdot -\frac{E-\mu}{T}\cdot\nabla T \tag{A.22}$$

Now consider the second term:

$$\frac{\partial f}{\partial k}\cdot\frac{\partial k}{\partial t} = \frac{\partial f}{\partial E}\cdot\frac{\partial E}{\partial k}\cdot\frac{1}{\hbar}\frac{\partial p}{\partial t}$$
$$\frac{\partial E}{\partial k} = \frac{\hbar^2 k}{m^*}, \frac{\partial p}{\partial t} = -\frac{\partial \mu}{\partial x} \tag{A.23}$$

The last equation is true because both sides represent the force.

$$\frac{\partial f}{\partial k}\cdot\frac{\partial k}{\partial t} = \frac{\partial f_0}{\partial E}\cdot v\cdot\left(-\frac{\partial \mu}{\partial x}\right) \tag{A.24}$$

Finally we rewrite these two terms and get the form we need to deduce our equations:

$$\frac{f-f_0}{\tau_E} = v\cdot\frac{\partial f_0}{\partial E}\left(\frac{\partial \mu}{\partial x}+\frac{E-\mu}{T}\cdot\nabla T\right) \tag{A.25}$$

We express the electric current ‘i’ in the following way:

$$i = ven = \int_0^\infty veg(E)\,fdE \tag{A.26}$$

Analogously consider the ‘heat charge’ carried by a single electron as E-μ instead of e, the heat current w is then expressed as:

$$w = \int_0^\infty v(E-\mu)g(E)\,fdE \tag{A.27}$$

g(E) is the density of states for electrons. Under the parabolic band assumption it is:

$$g(E) = \frac{dn}{dE} = \frac{8\pi k^2 dk}{8\pi^3 dE} = \frac{k^2}{\pi^2}\cdot\frac{m^*}{\hbar^2 k} = \frac{m^*}{\pi^2\hbar^2}\sqrt{\frac{2m^*E}{\hbar^2}} = \frac{1}{2\pi^2}\left(\frac{2m^*}{\hbar^2}\right)^{3/2}\sqrt{E} \tag{A.28}$$

It is obvious that at equilibrium there should be no current, so:

$$i_{equilibrium} = \int_0^\infty veg(E) f_0 dE = 0 \tag{A.29}$$

Combine this term with the general expression of *i*:

$$i = \int_0^\infty veg(E)\left(f - f_0\right)dE = \int_0^\infty v^2 eg(E)\tau_E \frac{\partial f_0}{\partial E}\left(\frac{\partial \mu}{\partial x} + \frac{E-\mu}{T}\cdot \nabla T\right)dE \tag{A.30}$$

When there is only electric field and the temperature is the same everywhere:

$$i = \int_0^\infty v^2 eg(E)\tau_E \frac{\partial f_0}{\partial E}\frac{\partial \mu}{\partial x}dE \tag{A.30}$$

$$\sigma = \frac{i}{E} = \frac{i}{\frac{1}{e}\cdot -\frac{\partial \mu}{\partial x}} = -e^2\int_0^\infty g(E)v^2\tau_E \frac{\partial f_0}{\partial E}dE = -\frac{2e^2}{3m^*}\int_0^\infty g(E)E\tau_E \frac{\partial f_0}{\partial E}dE \tag{A.31}$$

In the last step we used $v^2 = \frac{2E}{3m^*}$, considering v is the drift velocity in one dimension and total kinetic energy is contributed by velocities in all three equivalent dimensions.

To obtain the expression for *S*, we need to consider a special case without electric current (open circuit condition, so that the Seebeck coefficient is an open circuit voltage). So we have

$$\int_0^\infty v^2 g(E)\tau_E \frac{\partial f_0}{\partial E}\frac{\partial \mu}{\partial x}dE + \int_0^\infty v^2 g(E)\tau_E \frac{\partial f_0}{\partial E}\frac{E-\mu}{T}\cdot \nabla T dE \overset{i=0}{=} 0 \tag{A.32}$$

Remember the interpretation of Seebeck coefficient as the entropy carried per unit charge of carriers. Or just simply imagine *S* as the electric field (E=F/e) generated per unit temperature difference. This leads us to the expression:

$$\begin{aligned} S &= \frac{\partial \mu}{\partial x}/e\frac{\partial T}{\partial x} \\ &= -\frac{1}{eT}\left[\int_0^\infty v^2 g(E)\tau_E \frac{\partial f_0}{\partial E}(E-\mu)dE \Big/ \int_0^\infty v^2 g(E)\tau_E \frac{\partial f_0}{\partial E}dE\right] \\ &= \frac{1}{eT}\left[\mu - \int_0^\infty g(E)\frac{2E}{m^*}\tau_E \frac{\partial f_0}{\partial E}EdE \Big/ \int_0^\infty g(E)\frac{2E}{m^*}\tau_E \frac{\partial f_0}{\partial E}dE\right] \end{aligned} \tag{A.33}$$

Now define:

$$
\begin{aligned}
K_s &= \int_0^\infty g(E)E^{s+1}\frac{\partial f_0}{\partial E}\tau_E dE \\
&= \int_0^\infty \frac{1}{2\pi^2}\left(\frac{2m^*}{\hbar^2}\right)^{3/2} E^{s+r+3/2}\frac{\partial f_0}{\partial E}\tau_0 dE \\
&= \int_0^\infty \frac{1}{2\pi^2}\left(\frac{2m^*}{\hbar^2}\right)^{3/2} (s+r+3/2)E^{s+r+1/2} f_0\tau_0 dE \\
&= \frac{1}{2\pi^2}\left(\frac{2m^*}{\hbar^2}\right)^{3/2} (s+r+3/2)\tau_0\int_0^\infty E^{s+r+1/2} f_0 dE \\
&= \frac{1}{2\pi^2}\left(\frac{2m^*}{\hbar^2}\right)^{3/2} (s+r+3/2)\tau_0(k_B T)^{s+r+3/2} F_{s+r+1/2}(\frac{\mu}{k_B T})
\end{aligned}
\tag{A.34}
$$

So that:

$$
\begin{aligned}
S &= \frac{1}{eT}\left[\mu - K_1/K_0\right] \\
&= \frac{k_B}{e}\left[\eta - \frac{(r+5/2)F_{r+3/2}(\eta)}{(r+3/2)F_{r+1/2}(\eta)}\right]
\end{aligned}
\tag{A.35}
$$

In other forms of this equation, S might be written as:

$$
S = \frac{k_B}{e}[\eta - \frac{r'+2}{r'+1}\times\frac{F_{r'+1}(\eta)}{F_{r'}(\eta)}]
\tag{A.36}
$$

Both are correct because r is defined as $\tau_E = \tau_0 E^r$, whereas r' is defined as $l_E = l_0 E^{r'}$. The relaxation time and mean free path is again related through $l = \tau \cdot v = \tau \cdot \sqrt{2E/3m^*} = A\tau E^{1/2}$, which means $r = r'$-1/2.

4. From now we will derive the expression for the Lorenz number.

The heat current:

$$
\begin{aligned}
w &= -\frac{\mu}{e} i + \int_0^\infty v^2 g(E) \tau_E E \frac{\partial f_0}{\partial E} \left(\frac{d\mu}{dx} + \frac{E-\mu}{T} \cdot \nabla T \right) dE \\
&= \int_0^\infty v^2 g(E) \tau_E E \frac{\partial f_0}{\partial E} \left(\frac{d\mu}{dx} + \frac{E-\mu}{T} \cdot \nabla T \right) dE \\
&= \int_0^\infty v^2 g(E) \tau_E E \frac{\partial f_0}{\partial E} \left(\left(- \frac{\int_0^\infty v^2 g(E) \tau_E \frac{\partial f_0}{\partial E} (E-\mu) \frac{\nabla T}{T} dE}{\int_0^\infty v^2 g(E) \tau_E \frac{\partial f_0}{\partial E} dE} \right) + \frac{E-\mu}{T} \cdot \nabla T \right) dE \\
&= \frac{\nabla T}{T} \left[- \frac{\left(\int_0^\infty v^2 g(E) \tau_E E \frac{\partial f_0}{\partial E} dE \right)^2}{\int_0^\infty v^2 g(E) \tau_E \frac{\partial f_0}{\partial E} dE} + \mu \int_0^\infty v^2 g(E) \tau_E E \frac{\partial f_0}{\partial E} dE + \int_0^\infty v^2 g(E) \tau_E E^2 \frac{\partial f_0}{\partial E} dE - \mu \int_0^\infty v^2 g(E) \tau_E E \frac{\partial f_0}{\partial E} dE \right] \\
&= \frac{\nabla T}{T} \left[- \frac{\left(\int_0^\infty v^2 g(E) \tau_E E \frac{\partial f_0}{\partial E} dE \right)^2}{\int_0^\infty v^2 g(E) \tau_E \frac{\partial f_0}{\partial E} dE} + \int_0^\infty v^2 g(E) \tau_E E^2 \frac{\partial f_0}{\partial E} dE \right]
\end{aligned}
\tag{A.37}
$$

By its definition:

$$
\begin{aligned}
\kappa &= -w / \nabla T \\
&= \frac{1}{T} \left[\frac{\left(\int_0^\infty v^2 g(E) \tau_E E \frac{\partial f_0}{\partial E} dE \right)^2}{\int_0^\infty v^2 g(E) \tau_E \frac{\partial f_0}{\partial E} dE} - \int_0^\infty v^2 g(E) \tau_E E^2 \frac{\partial f_0}{\partial E} dE \right] \\
&= \frac{2}{3 m^* T} \left(\frac{K_1^{\,2}}{K_0} - K_2 \right)
\end{aligned}
\tag{A.38}
$$

Recall the expression for electric conductivity:

$$
\sigma = \frac{i}{E} = \frac{i}{\frac{1}{e} \cdot - \frac{\partial \mu}{\partial x}} = -e^2 \int_0^\infty g(E) v^2 \tau_E \frac{\partial f_0}{\partial E} dE = -\frac{2e^2}{3m^*} \int_0^\infty g(E) E \tau_E \frac{\partial f_0}{\partial E} dE
\tag{A.39}
$$

Thus the Lorenz number can be written as:

$$
L = \frac{\kappa}{\sigma T} = \frac{1}{e^2 T^2} \left(\frac{K_2}{K_0} - \frac{K_1^{\,2}}{K_0^{\,2}} \right) = \left(\frac{k_B}{e} \right)^2 \left[\frac{r + 7/2}{r + 3/2} \times \frac{F_{r+5/2}(\eta)}{F_{r+1/2}(\eta)} - \left(\frac{r + 5/2}{r + 3/2} \right)^2 \times \frac{F_{r+3/2}(\eta)^2}{F_{r+1/2}(\eta)^2} \right]
\tag{A.40}
$$

Due to the same reason this equation is also often seen as:

$$
L = \frac{\kappa}{\sigma T} = \left(\frac{k_B}{e} \right)^2 \left[\frac{r'+3}{r'+1} \times \frac{F_{r'+2}(\eta)}{F_{r'}(\eta)} - \left(\frac{r'+2}{r'+1} \right)^2 \times \frac{F_{r'+1}(\eta)^2}{F_{r'}(\eta)^2} \right]
\tag{A.41}
$$

Now, we try to go from the S equation above to the Mott relation. This derivation may be not rigorous, but I don't have any better route to lead myself to Mott relation in a simple way. (Luckily, in Andrew May's thesis there is a section in appendix on Mott relation. The derivation used there is probably more classic.)

We start from Equation A.35:

where:

$$K_s = \int_0^\infty g(E)E^{s+1}\frac{\partial f_0}{\partial E}\tau_E dE$$

We rewrite *S* as:

$$S = \frac{1}{eT}\left[\mu - K_1/K_0\right] = \frac{k_B}{e}\frac{\int_0^\infty g(E)\tau_E E(\eta - \frac{E}{k_B T})\frac{\partial f}{\partial E}dE}{\int_0^\infty g(E)\tau_E E\frac{\partial f}{\partial E}dE} = \frac{k_B}{e}\frac{\int_0^\infty \sigma_E(\eta - \frac{E}{k_B T})\frac{\partial f}{\partial E}dE}{\int_0^\infty \sigma_E\frac{\partial f}{\partial E}dE} \quad \text{(A.42)}$$

Now before we continue we need to varify that $g(E)\tau_E E$ can be replaced by σ_E, which is defined as $\sigma = \int_0^\infty \sigma_E \frac{\partial f}{\partial E}dE$. Consider:

$$\begin{aligned}\sigma &= \int_0^\infty \frac{n(E)e^2\tau_E}{m^*}dE \\ &= \frac{e^2}{m^*}\int_0^\infty g(E)\tau_E f dE\end{aligned} \quad \text{(A.43)}$$

If we assume parabolic band, acoustic phonon scattering, then $g(E)\tau_E = g_0 E^{1/2}\cdot\tau_0 E^{-1/2} = g_0\tau_0$, thus:

$$\begin{aligned}\sigma &= \frac{e^2}{m^*}\int_0^\infty g(E)\tau_E f dE \\ &= \frac{e^2}{m^*}\int_0^\infty \frac{\partial g(E)\tau_E E}{\partial E}f dE \\ &= -\frac{e^2}{m^*}\int_0^\infty g(E)\tau_E E\frac{\partial f}{\partial E}dE\end{aligned} \quad \text{(A.44)}$$

As a result, we have $\sigma_E = -\frac{e^2}{m^*}g(E)\tau_E E$. This validates the last step in the *S* equation. This part is where I felt the derivation became less rigorous. It seems that, based on the math here, Mott relation is limited to the parabolic band, acoustic phonon scattering case while Mott relation is in fact valid without such limitations. On the other hand, from this derivation σ_E seems be different from the

common differential conductivity usually defined. So while using the common definition of differential conductivity Mott relation can be written as:

$$S = \frac{\pi^2}{3}\cdot\frac{{k_B}^2 T}{e}\frac{\partial \ln \sigma_E}{\partial E}\bigg|_\eta = \frac{\pi^2}{3}\cdot\frac{{k_B}^2 T}{e}\left(\frac{\partial \ln n(E)}{\partial E}+\frac{\partial \ln \tau(E)}{\partial E}+\frac{\partial \ln v^2(E)}{\partial E}\right)\bigg|_\eta \tag{A.44}$$

but if $\sigma_E = \frac{n(E)e^2\tau_E}{m^*}$, we won't have the third term.

Now we apply Taylor expansion to σ_E at the neighborhood of η:

$$\sigma_E = \sigma_E(\eta) + (e-\eta)\frac{\partial \sigma_E}{\partial E}\bigg|_\eta + (e-\eta)^2\frac{\partial^2 \sigma_E}{\partial E^2}\bigg|_\eta + \ldots \tag{A.45}$$

We plug in this result and combine it with the Sommerfeld expansion, which tells us in a integral with such a polynomial only even order terms contribute to the result, and that term can be written as:

$$\int_0^\infty \frac{1}{2n!}(e-\eta)^{2n}\frac{\partial^{2n}\sigma_E}{\partial E^{2n}}\bigg|_\eta \frac{\partial f}{\partial E}dE = C_{2n}(k_B T)^{2n}\frac{\partial^{2n}\sigma_E}{\partial E^{2n}}\bigg|_\eta \tag{A.46}$$

We take the first non-zero term for both the numerator and denominator. For the denominator it simply yields $\sigma_E(\eta)$, while for the numerator the first non-zero term is $(e-\eta)^2\frac{\partial \sigma_E}{\partial E}\Big|_\eta$, which gives us:

$$S = \frac{k_B}{e}\frac{2C_2\cdot\frac{\partial \sigma_E}{\partial E}\Big|_\eta}{\sigma_E(\eta)} = 2C_2\cdot\frac{k_B}{e}\frac{\partial \ln \sigma_E}{\partial E}\bigg|_\eta \tag{A.47}$$

The constant C_2 is a known Sommerfeld expansion coefficient. For the second order term it is $\pi^2/6$. This finally gives us the Mott relation:

$$S = \frac{\pi^2}{3}\cdot\frac{{k_B}^2 T}{e}\frac{\partial \ln \sigma_E}{\partial E}\bigg|_\eta \tag{A.48}$$

As the final part, we will use the general equation for *S* Equation A.4 to derive equations for its non-degenerate $\eta<<0$ and degenerate $\eta>>0$ form. We start from the non-degenerate one:

$$S = \frac{k_B}{e}(A + \ln\frac{2(2\pi m^* k_B T)^{3/2}}{h^3 n}) \tag{A.49}$$

First we have the general form of carrier density Equation A.1, When η<<0 (the non-degenerate region), the Fermi integrals can be approximated as:

$$F_n(\eta) = \exp(\eta)\Gamma(n+1) \tag{A.50}$$

The gamma function has the property:

$$\Gamma(n+1) = n\Gamma(n)$$

$$\text{and } \Gamma(1/2) = \frac{\sqrt{\pi}}{2},\ \Gamma(0) = 1 \tag{A.51}$$

so

$$\begin{aligned} n &= \frac{4\pi(2m^* k_B T)^{3/2}}{h^3} F_{1/2}(\eta) \\ &= \frac{4\pi(2m^* k_B T)^{3/2}}{h^3}\frac{\sqrt{\pi}}{2}\exp(\eta) \\ &= \frac{2(2\pi m^* k_B T)^{3/2}}{h^3}\exp(\eta) \end{aligned} \tag{A.52}$$

thus

$$\eta = -\ln(\frac{2(2\pi m^* k_B T)^{3/2}}{nh^3}) \tag{A.53}$$

for the other term:

$$\frac{(r+5/2)F_{r+3/2}(\eta)}{(r+3/2)F_{r+1/2}(\eta)} \approx \frac{(r+5/2)\exp(\eta)\Gamma(r+3/2+1)}{(r+3/2)\exp(\eta)\Gamma(r+1/2+1)} = \frac{(r+5/2)(r+3/2)\Gamma(r+1/2+1)}{(r+3/2)\Gamma(r+1/2+1)} = (r+5/2)$$

As a result, we have for non-degenerate region:

$$\begin{aligned} S &= \frac{k_B}{e}\left[\eta - \frac{(r+5/2)F_{r+3/2}(\eta)}{(r+3/2)F_{r+1/2}(\eta)}\right] \\ &= -\frac{k_B}{e}(A + \ln(\frac{2(2\pi m^* k_B T)^{3/2}}{nh^3})) \end{aligned}$$

$A = r + 5/2$ or, if use $r' = r + 1/2$ then $A = r' + 2$.

For the degenerate version:

$$S = \frac{8\pi^2 {k_B}^2}{3eh^2} m^* T \left(\frac{\pi}{3n}\right)^{2/3} \tag{A.54}$$

following the same way but keep in mind for η>>0 the Fermi integrals could be simplified as:

$$F_r(\eta) \approx \frac{\eta^{r+1}}{r+1} \tag{A.55}$$

so from Equation A.1:

$$n = \frac{4\pi(2m^* k_B T)^{3/2}}{h^3} F_{1/2}(\eta)$$

we have:

$$\begin{aligned} n &\approx \frac{4\pi(2m^* k_B T)^{3/2}}{h^3} \cdot \frac{\eta^{3/2}}{3/2} \\ \Rightarrow \eta &= \left(\frac{4\pi(2m^* k_B T)^{3/2}}{h^3} \cdot \frac{1}{\frac{3}{2}n} \right)^{-2/3} = \left(\frac{8m^* k_B T}{h^2}\right)^{-1} \left(\frac{\pi}{3n}\right)^{-2/3} \end{aligned} \tag{A.56}$$

for the expression for *S* in order to yield a non-zero equation we need to take into account the second order term in Fermi integral approximation:

$$F_r(\eta) \approx \frac{\eta^{r+1}}{r+1} + \frac{n\pi^2}{6}(\eta)^{n-1} \tag{A.57}$$

thus, for the acoustic phonon dominant regime:

$$\begin{aligned} S &= \frac{k_B}{e}\left[\eta - \frac{2F_1(\eta)}{F_0(\eta)}\right] = -\frac{k_B}{e}\left[\eta - \frac{2(\frac{\eta^2}{2} + \frac{\pi^2}{6})}{\eta}\right] \\ &= -\frac{k_B}{e} \cdot \frac{\pi^2}{3\eta} = \frac{8\pi^2 k_B^2}{3eh^2} m^* T \left(\frac{\pi}{3n}\right)^{2/3} \end{aligned} \tag{A.58}$$

BIBLIOGRAPHY

1. A. F. Ioffe, *Semiconductor thermoelements, and Thermoelectric cooling*, Infosearch, ltd., 1957.
2. H. J. Goldsmid, *Thermoelectric Refrigeration*, Temple Press Books Ltd., London, 1964.
3. C. Wood, *Energy Conv. Manag.*, 1984, **24**, 317-329.
4. D. A. Wright, *Metall. Rev.*, 1970, **15**, 147-160.
5. G. J. Snyder and E. S. Toberer, *Nat. Mater.*, 2008, **7**, 105-114.
6. L. E. Bell, *Science*, 2008, **321**, 1457-1461.
7. Y. Pei, X. Shi, A. LaLonde, H. Wang, L. Chen and G. J. Snyder, *Nature*, 2011, **473**, 66-69.
8. K. Biswas, J. He, I. D. Blum, C. I. Wu, T. P. Hogan, D. N. Seidman, V. P. Dravid and M. G. Kanatzidis, *Nature*, 2012, **489**, 414-418.
9. L. D. Ivanova, L. I. Petrova, Y. V. Granatkina and V. S. Zemskov, *Inorg. Mater.*, 2007, **43**, 933-937.
10. B. Poudel, Q. Hao, Y. Ma, Y. C. Lan, A. Minnich, B. Yu, X. Yan, D. Wang, A. Muto, D. Vashaee, X. Chen, J. Liu, M. Dresselhaus, G. Chen and Z. Ren, *Science*, 2008, **320**, 634-638.
11. W.-S. Liu, Q. Zhang, Y. Lan, S. Chen, X. Yan, Q. Zhang, H. Wang, D. Wang, G. Chen and Z. Ren, *Adv. Energ. Mater.*, 2011, **1**, 577-587.
12. Y. I. Ravich, B. A. Efimova and I. A. Smirnov, *Semiconducting lead chalcogenides*, Plenum Press, New York, 1970.
13. R. W. Fritts, in *Thermoelectric Materials and Devices*, eds. I. B. Cadoff and E. Miller, Reinhold Pub. Corp., New York, Editon edn., 1960, pp. 143-162.
14. J. P. Dismukes, L. Ekstrom, E. F. Steigmeier, I. Kudman and D. S. Beers, *J. Appl. Phys.*, 1964, **35**, 2899-2907.
15. D. M. Rowe and C. M. Bhandari, *Appl. Energ.*, 1980, **6**, 347-351.
16. C. B. Vining, W. Laskow, J. O. Hanson, R. R. Van der Beck and P. D. Gorsuch, *J. Appl. Phys.*, 1991, **69**, 4333-4340.
17. G. A. Slack, in *CRC Handbook of Thermoelectrics*, ed. D. M. Rowe, CRC Press, Boca Raton, Editon edn., 1995, pp. 407-440.
18. G. S. Nolas, D. T. Morelli and T. M. Tritt, *Annu. Rev. Mater. Sci.*, 1999, **29**, 89-116.
19. X. Shi, J. Yang, J. R. Salvador, M. F. Chi, J. Y. Cho, H. Wang, S. Q. Bai, J. H. Yang, W. Q. Zhang and L. D. Chen, *J. Am. Chem. Soc.*, 2011, **133**, 7837-7846.
20. T. Caillat, A. Borshchevsky and J. P. Fleurial, *J. Appl. Phys.*, 1996, **80**, 4442-4449.
21. A. F. May, E. S. Toberer, A. Saramat and G. J. Snyder, *Phys. Rev. B*, 2009, **80**, 125205.
22. A. May, J.-P. Fleurial and G. Snyder, *Phys. Rev. B*, 2008, **78**, 125205.
23. E. S. Toberer, A. F. May and G. J. Snyder, *Chem. Mat.*, 2010, **22**, 624-634.
24. A. Zevalkink, G. S. Pomrehn, S. Johnson, J. Swallow, Z. M. Gibbs and G. J. Snyder, *Chem. Mat.*, 2012, **24**, 2091-2098.
25. V. M. Grabov, O. N. Uryupin and V. A. Komarov, Proceedings ICT 98. XVII International Conference on Thermoelectrics, 1998.
26. A. M. Ibrahim and D. A. Thompson, *Mater. Chem. Phys.*, 1985, **12**, 29-36.
27. V. K. Zaitsev, M. I. Fedorov, E. A. Gurieva, I. S. Eremin, P. P. Konstantinov, A. Y. Samunin and M. V. Vedernikov, *Phys. Rev. B*, 2006, **74**, 045207.
28. W. Liu, X. Tang, H. Li, K. Yin, J. Sharp, X. Zhou and C. Uher, *J. Mater. Chem.*, 2012, **22**, 13653-13661.

29. W. Liu, X. Tan, K. Yin, H. Liu, X. Tang, J. Shi, Q. Zhang and C. Uher, *Phys. Rev. Lett.*, 2012, **108**, 166601.
30. S. K. Bux, M. T. Yeung, E. S. Toberer, G. J. Snyder, R. B. Kaner and J.-P. Fleurial, *J. Mater. Chem.*, 2011, **21**, 12259.
31. H. Hohl, A. P. Ramirez, C. Goldmann, G. Ernst, B. Wolfing and E. Bucher, *J. Phys.: Cond. Mat.*, 1999, **11**, 1697.
32. Q. Shen, L. Chen, T. Goto, T. Hirai, J. Yang, G. P. Meisner and C. Uher, *Appl. Phys. Lett.*, 2001, **79**, 4165-4167.
33. H. Xie, H. Wang, Y. Pei, C. Fu, X. Liu, G. J. Snyder, X. Zhao and T. Zhu, *Adv. Funct. Mater.*, 2013, **23**, 5123-5130.
34. L. D. Zhao, D. Berardan, Y. L. Pei, C. Byl, L. Pinsard-Gaudart and N. Dragoe, *Appl. Phys. Lett.*, 2010, **97**, 092118.
35. J. Li, J. Sui, Y. Pei, C. Barreteau, D. Berardan, N. Dragoe, W. Cai, J. He and L.-D. Zhao, *Energy Environ. Sci.*, 2012, **5**, 8543.
36. J. Sui, J. Li, J. He, Y.-L. Pei, D. Berardan, H. Wu, N. Dragoe, W. Cai and L.-D. Zhao, *Energy Environ. Sci.*, 2013, **6**, 2916.
37. H. L. Liu, X. Shi, F. F. Xu, L. L. Zhang, W. Q. Zhang, L. D. Chen, Q. Li, C. Uher, T. Day and G. J. Snyder, *Nat. Mater.*, 2012, **11**, 422-425.
38. G. J. Snyder, M. Christensen, E. Nishibori, T. Caillat and B. B. Iversen, *Nat. Mater.*, 2004, **3**, 458-463.
39. X. Lu, D. T. Morelli, Y. Xia, F. Zhou, V. Ozolins, H. Chi, X. Zhou and C. Uher, *Adv. Energ. Mater.*, 2013, **3**, 342-348.
40. E. J. Skoug, J. D. Cain and D. T. Morelli, *Appl. Phys. Lett.*, 2011, **98**, 261911.
41. E. K. Iordanishvili, *Thermoelectric Power Supplies*, Defense Technical Information Center, 1969.
42. M. Telkes, *J. Appl. Phys.*, 1947, **18**, 1116-1127.
43. L. S. Stil'bans, DSc Dissertation, A. F. Ioffe Physical-Technical Institute, Leningrad, 1960.
44. A. F. Gibson, *P. Phys. Soc. Lond. B*, 1952, **65**, 378-388.
45. F. E. Faradzhev, V. I. Tagirov, A. S. Mekhtiev, E. A. Akopyan and G. A. Galandarov, *Sov. Phys. Semicond.*, 1982, **16**, 583-584.
46. I. N. Dubrovskaya, B. A. Efimova and E. D. Nensberg, *Sov. Phys. Semicond.*, 1968, **2**, 436-440.
47. I. A. Smirnov, B. Y. Moizhes and E. D. Nensberg, *Sov. Phys-Sol. State*, 1961, **2**, 1793-1804.
48. R. S. Allgaier, *J. Appl. Phys.*, 1966, **37**, 302.
49. S. V. Airapetyants, M. N. Vinogradova, I. N. Dubrovskaya, N. V. Kolomoets and I. M. Rudnik, *Sov. Phys-Sol. State*, 1966, **8**, 1069-1072.
50. M. Lach-hab, M. Keegan, D. A. Papaconstantopoulos and M. J. Mehl, *J. Phys. Chem. Solids*, 2000, **61**, 1639-1645.
51. D. J. Singh, *Funct. Mater. Lett.*, 2010, **3**, 223-226.
52. T. S. Stavitskaya, I. V. Prokofeva, Y. I. Ravich and B. A. Efimova, *Sov. Phys. Semicond.*, 1968, **1**, 952-957.
53. L. Y. Morgovskii and Y. I. Ravich, *Sov. Phys. Semicond.*, 1971, **5**, 860-861.
54. I. N. Dubrovskaya, Y. I. Ravich and O. S. Gryaznov, *Sov. Phys. Semicond.*, 1970, **3**, 1500-1502.
55. E. O. Kane, *J. Phys. Chem. Solids*, 1957, **1**, 249-261.
56. T. C. Harman, P. J. Taylor, M. P. Walsh and B. E. LaForge, *Science*, 2002, **297**, 2229-2232.
57. T. C. Harman, M. P. Walsh, B. E. laforge and G. W. Turner, *J. Electron. Mater.*, 2005, **34**, L19-L22.

58. K. F. Hsu, S. Loo, F. Guo, W. Chen, J. S. Dyck, C. Uher, T. Hogan, E. K. Polychroniadis and M. G. Kanatzidis, *Science*, 2004, **303**, 818-821.
59. M. G. Kanatzidis, *Chem. Mat.*, 2010, **22**, 648-659.
60. J. R. Sootsman, D. Y. Chung and M. G. Kanatzidis, *Angew Chem Int Ed Engl*, 2009, **48**, 8616-8639.
61. L.-D. Zhao, V. P. Dravid and M. G. Kanatzidis, *Energy Environ. Sci.*, 2014, **7**, 251.
62. J. P. Heremans, V. Jovovic, E. S. Toberer, A. Saramat, K. Kurosaki, A. Charoenphakdee, S. Yamanaka and G. J. Snyder, *Science*, 2008, **321**, 554-557.
63. Y. Pei, A. LaLonde, S. Iwanaga and G. J. Snyder, *Energy Environ. Sci.*, 2011, **4**, 2085-2089.
64. V. I. Kaidanov, S. A. Nemov and Y. I. Ravich, *Sov. Phys. Semicond.*, 1992, **26**, 113-125.
65. J. P. Heremans, B. Wiendlocha and A. M. Chamoire, *Energy Environ. Sci.*, 2012, **5**, 5510-5530.
66. Q. Zhang, B. Liao, Y. Lan, K. Lukas, W. Liu, K. Esfarjani, C. Opeil, D. Broido, G. Chen and Z. Ren, *Proc. Natl. Acad. Sci. U. S. A.*, 2013, **110**, 13261-13266.
67. A. D. LaLonde, T. Ikeda and G. J. Snyder, *Rev. Sci. Instrum.*, 2011, **82**, 025104.
68. S. Iwanaga, E. S. Toberer, A. Lalonde and G. J. Snyder, *Rev. Sci. Instrum.*, 2011, **82**, 063905.
69. W. J. Parker, R. J. Jenkins, G. L. Abbott and C. P. Butler, *J. Appl. Phys.*, 1961, **32**, 1679-1684.
70. R. D. Cowan, *J. Appl. Phys.*, 1963, **34**, 926-927.
71. J. A. Cape and G. W. Lehman, *J. Appl. Phys.*, 1963, **34**, 1909-1913.
72. O. Delaire, A. F. May, M. A. McGuire, W. D. Porter, M. S. Lucas, M. B. Stone, D. L. Abernathy, V. A. Ravi, S. A. Firdosy and G. J. Snyder, *Phys. Rev. B*, 2009, **80**, 184302.
73. R. Blachnik and R. Igel, *Z.Naturforsch.(B)*, 1974, **B 29**, 625-629.
74. H. Wang, Y. Pei, A. D. Lalonde and G. J. Snyder, *Adv. Mater.*, 2011, **23**, 1366-1370.
75. S. Iwanaga and G. J. Snyder, *J. Electron. Mater.*, 2012, **41**, 1667-1674.
76. J. Androulakis, D. Y. Chung, X. L. Su, L. Zhang, C. Uher, T. C. Hasapis, E. Hatzikraniotis, K. M. Paraskevopoulos and M. G. Kanatzidis, *Phys. Rev. B*, 2011, **84**, 155207.
77. G. T. Alekseeva, E. A. Gurieva, P. P. Konstantinov, L. V. Prokofeva and M. I. Fedorov, *Semiconductors*, 1996, **30**, 1125-1127.
78. J. Androulakis, Y. Lee, I. Todorov, D. Y. Chung and M. Kanatzidis, *Phys. Rev. B*, 2011, **83**, 195209.
79. S. Wang, G. Zheng, T. Luo, X. She, H. Li and X. Tang, *J. Phys. D: Appl. Phys.*, 2011, **44**, 475304.
80. Q. Zhang, H. Wang, W. Liu, H. Wang, B. Yu, Q. Zhang, Z. Tian, G. Ni, S. Lee, K. Esfarjani, G. Chen and Z. Ren, *Energy Environ. Sci.*, 2012, **5**, 5246-5251.
81. Y. I. Ravich, B. A. Efimova and V. I. Tamarchenko, *Phys. Status Solidi B*, 1971, **43**, 453-469.
82. R. P. Chasmar and R. Stratton, *J. Electron. Contrl.*, 1959, **7**, 52-72.
83. G. S. Nolas, J. Sharp and H. J. Goldsmid, *Thermoelectrics Basic Principles and New Materials Developments*, Springer, Berlin, Heidelberg, 2001.
84. G. D. Mahan, in *Solid State Physics*, Academic Press Inc., San Diego, 1998, vol. 51, pp. 81-157.
85. Y. Pei, A. D. LaLonde, H. Wang and G. J. Snyder, *Energy Environ. Sci.*, 2012, **5**, 7963-7969.
86. J. O. Dimmock and G. B. Wright, *Phys. Rev. A-Gen. Phys.*, 1964, **135**, A821-A830.
87. L. Fu and C. L. Kane, *Phys. Rev. B*, 2007, **76**.

88. P. Dziawa, B. J. Kowalski, K. Dybko, R. Buczko, A. Szczerbakow, M. Szot, E. Lusakowska, T. Balasubramanian, B. M. Wojek, M. H. Berntsen, O. Tjernberg and T. Story, *Nat. Mater.*, 2012, **11**, 1023-1027.
89. S. Y. Xu, C. Liu, N. Alidoust, M. Neupane, D. Qian, I. Belopolski, J. D. Denlinger, Y. J. Wang, H. Lin, L. A. Wray, G. Landolt, B. Slomski, J. H. Dil, A. Marcinkova, E. Morosan, Q. Gibson, R. Sankar, F. C. Chou, R. J. Cava, A. Bansil and M. Z. Hasan, *Nat. Commun.*, 2012, **3**.
90. Y. I. Ravich, B. A. Efimova and V. I. Tamarchenko, *Phys. Status Solidi B-Basic Res.*, 1971, **43**, 11-33.
91. J. Bardeen and W. Shockley, *Phys. Rev.*, 1950, **80**, 72.
92. E. S. Toberer, C. A. Cox, S. R. Brown, T. Ikeda, A. F. May, S. M. Kauzlarich and G. J. Snyder, *Adv. Funct. Mater.*, 2008, **18**, 2795-2800.
93. J. M. Ziman, *Electrons and Phonons: The Theory of Transport Phenomena in Solids*, Clarendon Press, 1996.
94. C. Herring and E. Vogt, *Phys. Rev.*, 1956, **101**, 944.
95. K. Seeger, *Semiconductor Physics An Introduction*, Springer, Berlin, Heidelberg, 2004.
96. L. G. Ferreira, *Phys. Rev.*, 1965, **137**, 1601-1609.
97. M. V. Fischetti and S. E. Laux, *J. Appl. Phys.*, 1996, **80**, 2234-2252.
98. I. I. Zasavitskii, E. Silva, E. Abramof and P. J. McCann, *Phys. Rev. B*, 2004, **70**, 115302.
99. H. Z. Wu, N. Dai and P. J. McCann, *Phys. Rev. B*, 2002, **66**, 045303.
100. C. B. Vining, *J. Appl. Phys.*, 1991, **69**, 331-341.
101. D. Chattopadhyay and H. J. Queisser, *Rev. Mod. Phys.*, 1981, **53**, 745-768.
102. C. Erginsoy, *Phys. Rev.*, 1950, **79**, 1013-1014.
103. T. C. McGill and R. Baron, *Phys. Rev. B*, 1975, **11**, 5208-5210.
104. D. J. Howarth and E. H. Sondheimer, *P. R. Soc. Lond. A Mat.*, 1953, **219**, 53-74.
105. B. M. Askerov, *Electron Transport Phenomena in Semiconductors*, World Scientific Publishing Co. Pte. Ltd., Singapor, New Jersey, London, Hong Kong, 1991.
106. D. I. Bilc, S. D. Mahanti and M. G. Kanatzidis, *Phys. Rev. B*, 2006, **74**, 125202.
107. C. Jacoboni and L. Reggiani, *Rev. Mod. Phys.*, 1983, **55**, 645-705.
108. W. A. Harrison, *Phys. Rev.*, 1956, **104**, 1281.
109. K. Takeda and N. Matsumoto, *J. Phys. C-Solid State Phys.*, 1984, **17**, 5001-5015.
110. J. D. Wiley and Didomeni.M, *Phys. Rev. B*, 1970, **2**, 427-433.
111. J. D. Wiley, *Solid State Commun.*, 1970, **8**, 1865-1868.
112. M. Costato, G. Gagliani, C. Jacoboni and L. Reggiani, *J. Phys. Chem. Solids*, 1974, **35**, 1605-1614.
113. M. I. Fedorov, D. A. Pshenay-Severin, V. K. Zaitsev, S. Sano, M. V. Vedernikov, in *Proceedings ICT03: XXIII International Conference on Thermoelectrics,* New York, 2003, 142-145.
114. D. A. Pshenay-Severin and M. I. Fedorov, *Phys. Solid State*, 2010, **52**, 1342-1347.
115. C. Herring, *Bell Syst. Tech. J.*, 1955, **34**, 237-290.
116. Y. I. Ravich, in *Lead Chalcogenides Physics and Applications*, ed. D. Khokhlov, Taylor & Francis, New York, 2003, vol. 18.
117. H. Brooks, *Theory of the Electrical Properties of Germanium Silicon*, Academic Press Inc., NY, 1955.
118. M. I. Nathan, W. Paul and H. Brooks, *Phys. Rev.*, 1961, **124**, 391-407.
119. W. P. Mason and T. B. Bateman, *Phys. Rev. Lett.*, 1963, **10**, 151-154.
120. D. Long, *Phys. Rev.*, 1960, **120**, 2024-2032.
121. J. E. Aubrey, W. Gubler, T. Henningsen and S. H. Koenig, *Phys. Rev.*, 1963, **130**, 1667-1670.
122. F. J. Morin and J. P. Maita, *Phys. Rev.*, 1954, **96**, 28-35.

123. G. W. Ludwig and R. L. Watters, *Phys. Rev.*, 1956, **101**, 1699-1701.
124. Springer Materials, The Landolt-Bornstein Database.
125. G. A. Slack and M. A. Hussain, *J. Appl. Phys.*, 1991, **70**, 2694-2718.
126. J. G. Nash and J. W. Holmkennedy, *Phys. Rev. B*, 1977, **15**, 3994-4006.
127. P. D. Yoder, V. D. Natoli and R. M. Martin, *J. Appl. Phys.*, 1993, **73**, 4378-4383.
128. S. V. Obukhov and V. G. Tyuterev, *Phys. Solid State*, 2009, **51**, 1110-1113.
129. Z. Wang, S. D. Wang, S. Obukhov, N. Vast, J. Sjakste, V. Tyuterev and N. Mingo, *Phys. Rev. B*, 2011, **83**, 205208.
130. A. J. Minnich, H. Lee, X. W. Wang, G. Joshi, M. S. Dresselhaus, Z. F. Ren, G. Chen and D. Vashaee, *Phys. Rev. B*, 2009, **80**, 155327.
131. C. B. Vining, in *Materials Research Society Symposium Proceedings*, eds. D. D. Allred, C. B. Vining and G. A. Slack, Materials Research Society, Editon edn., 1991, vol. 234.
132. M. N. Tripathi and C. M. Bhandari, *J. Phys.-Condes. Matter*, 2003, **15**, 5359-5370.
133. F. Murphy-Armando and S. Fahy, *Phys. Rev. B*, 2008, **78**, 035202.
134. H. J. Goldsmid and J. W. Sharp, *J. Electron. Mater.*, 1999, **28**, 869-872.
135. E. S. Toberer, A. Zevalkink and G. J. Snyder, *J. Mater. Chem.*, 2011, **21**, 15843-15852.
136. C. Jaworski, M. Nielsen, H. Wang, S. Girard, W. Cai, W. Porter, M. Kanatzidis and J. Heremans, *Phys. Rev. B*, 2013, **87**.
137. R. S. Allgaier and W. W. Scanlon, *Phys. Rev.*, 1958, **111**, 1029-1037.
138. M. N. Vinogradova, I. M. Rudnik, L. M. Sysoeva and N. V. Kolomoets, *Sov. Phys. Semicond.*, 1969, **2**, 892-893.
139. U. Schlichting and K. H. Gobrecht, *J. Phys. Chem. Solids*, 1973, **34**, 753-758.
140. L. V. Prokofeva, E. A. Gurieva, S. M. Zhumaksanov, P. P. Konstantinov, K. R. Mailina, Y. I. Ravich and L. S. Stilbans, *Sov. Phys. Semicond.*, 1987, **21**, 1078-1080.
141. I. A. Chernik, V. I. Kaidanov and E. P. Ishutinov, *Sov. Phys. Semicond.*, 1969, **2**, 825-829.
142. Z. M. Gibbs, H. Kim, H. Wang, R. L. White, F. Drymiotis, M. Kaviany and G. Jeffrey Snyder, *Appl. Phys. Lett.*, 2013, **103**, 262109.
143. E. H. Putley, *Journal of Physics C: Solid State Physics*, 1975, **8**, 1837-1840.
144. D. Parker and D. J. Singh, *Phys. Rev. B*, 2010, **82**, 035204.
145. E. G. Evola, M. D. Nielsen, C. M. Jaworski, H. Jin and J. P. Heremans, *J. Appl. Phys.*, 2014, **115**, 053704.
146. S. B. Zhang, S. H. Wei and A. Zunger, *Phys. Rev. Lett.*, 2000, **84**, 1232-1235.
147. W. Walukiewicz, *Physica B*, 2001, **302**, 123-134.
148. S. A. Nemov and P. A. Osipov, *Semiconductors*, 2001, **35**, 700-702.
149. A. Zunger, *Appl. Phys. Lett.*, 2003, **83**, 57-59.
150. N. M. Kutsiya, Y. P. Lukyanchikov, S. A. Stavrianidis and R. R. Shvangiradze, *Inorg. Mater.*, 1990, **26**, 1959-1961.
151. V. Jovovic, S. J. Thiagarajan, J. West, J. P. Heremans, T. Story, Z. Golacki, W. Paszkowicz and V. Osinniy, *J. Appl. Phys.*, 2007, **102**.
152. S. M. Sze and J. C. Irvin, *Solid-State Electron.*, 1968, **11**, 599-&.
153. A. Jalil, J. Chevallier, R. Azoulay and A. Mircea, *J. Appl. Phys.*, 1986, **59**, 3774-3777.
154. V. A. Kulbachinskii, V. G. Kytin, R. A. Lunin, A. V. Golikov, V. G. Mokerov, A. S. Bugaev, A. P. Senichkin, R. T. F. van Schaijk, A. de Visser and P. M. Koenraad, *Semicond. Sci. Tech.*, 1999, **14**, 1034-1041.
155. S. Z. Sun, E. A. Armour, K. Zheng and C. F. Schaus, *J. Cryst. Growth*, 1991, **113**, 103-112.
156. G. B. Stringfellow, *J. Appl. Phys.*, 1979, **50**, 4178-4183.
157. M. E. Klausmeierbrown, M. R. Melloch and M. S. Lundstrom, *Appl. Phys. Lett.*, 1990, **56**, 160-162.
158. J. K. Sheu and G. C. Chi, *J. Phys.-Condes. Matter*, 2002, **14**, R657-R702.

159. K. H. Ploog and O. Brandt, *J. Vac. Sci. Tech. A*, 1998, **16**, 1609-1614.
160. F. E. Rosztoczy, F. Ermanis, I. Hayashi and B. Schwartz, *J. Appl. Phys.*, 1970, **41**, 264-270.
161. J. Vilms and J. P. Garrett, *Solid-State Electron.*, 1972, **15**, 443-455.
162. N. Shibata, A. Ohki and A. Katsui, *J. Cryst. Growth*, 1988, **93**, 703-707.
163. H. R. Vydyanath and F. A. Kröger, *J. Appl. Phys.*, 1975, **46**, 2670.
164. D. C. Oh, J. H. Chang, T. Takai, J. S. Song, K. Godo, Y. K. Park, K. Shindo and T. Yao, *J. Cryst. Growth*, 2003, **251**, 607-611.
165. C. M. Jaworski, J. Tobola, E. M. Levin, K. Schmidt-Rohr and J. P. Heremans, *Phys. Rev. B*, 2009, **80**, 125208.
166. C. Jaworski and J. Heremans, *Phys. Rev. B*, 2012, **85**.
167. A. M. P. dos Anjos, E. Abramof, P. H. O. Rappl, A. Y. Ueta and H. Closs, *Braz. J. Phys.*, 2004, **34**, 653-655.
168. E. I. Rogacheva, S. G. Lyubchenko, O. S. Vodorezl, A. M. Kuzmenko, M. S. Dresselhaus, in *Proceedings ICT 06: XXV International Conference on Thermoelectrics* 2007, 656-661.
169. L. L. Yin, Y. G. Yan, X. F. Tang, H. J. Liu and Q. J. Zhang, in *Proceedings ICT 07: Twenty-Sixth International Conference on Thermoelectrics* 2008, 71-73.
170. G. T. Alekseeva, M. V. Vedernikov, E. A. Gurieva, P. P. Konstantinov, L. V. Prokof'eva and Y. I. Ravich, *Semiconductors*, 1998, **32**, 716-719.
171. E. P. Skipetrov, L. A. Skipetrova, A. V. Knotko, E. I. Slynko and V. E. Slynko, *J. Appl. Phys.*, 2014, **115**, 133702.
172. L. D. Zhao, J. He, C. I. Wu, T. P. Hogan, X. Zhou, C. Uher, V. P. Dravid and M. G. Kanatzidis, *J. Am. Chem. Soc.*, 2012, **134**, 7902-7912.
173. L. D. Zhao, J. He, S. Hao, C. I. Wu, T. P. Hogan, C. Wolverton, V. P. Dravid and M. G. Kanatzidis, *J. Am. Chem. Soc.*, 2012, **134**, 16327-16336.
174. L. D. Zhao, S. H. Lo, J. He, H. Li, K. Biswas, J. Androulakis, C. I. Wu, T. P. Hogan, D. Y. Chung, V. P. Dravid and M. G. Kanatzidis, *J. Am. Chem. Soc.*, 2011, **133**, 20476-20487.
175. Y. I. Ravich and L. Y. Morgovskii, *Sov. Phys. Semicond.*, 1970, **3**, 1278-1286.
176. S. Johnsen, J. Q. He, J. Androulakis, V. P. Dravid, I. Todorov, D. Y. Chung and M. G. Kanatzidis, *J. Am. Chem. Soc.*, 2011, **133**, 3460-3470.
177. R. L. Petritz and W. W. Scanlon, *Phys. Rev.*, 1955, **97**, 1620-1626.
178. J. N. Zemel, J. D. Jensen and R. B. Schoolar, *Phys. Rev.*, 1965, **140**, A330-A342.
179. W. Palosz, H. A. Alexander and K. Grasza, *J. Cryst. Growth*, 2000, **216**, 283-292.
180. J. Botor, G. Milkowska and J. Konieczny, *Thermochim. Acta*, 1989, **137**, 269-279.
181. R. Dalven, *Phys. Rev. B*, 1971, **3**, 1953-1954.
182. V. W. L. Chin, R. J. Egan and T. L. Tansley, *J. Appl. Phys.*, 1991, **69**, 3571-3577.
183. D. L. Rode, *Phys. Rev. B*, 1970, **2**, 1012-1024.
184. D. L. Rode, *Phys. Rev. B*, 1970, **2**, 4036-4044.
185. A. R. Hutson, *Phys. Rev.*, 1957, **108**, 222-230.
186. H. Ehrenreich, *J. Appl. Phys.*, 1961, **32**, 2155-2166.
187. D. M. Zayachuk, *Semiconductors*, 1997, **31**, 173-176.
188. C. M. Bhandari and D. M. Rowe, *J. Phy. D: Appl. Phys.*, 1985, **18**, 873.
189. B.-L. Huang and M. Kaviany, *Phys. Rev. B*, 2008, **77**, 125209.
190. E. G. Bylander and M. Hass, *Solid State Commun.*, 1966, **4**, 51-53.
191. Y. Kanai and K. Shohno, *Jpn. J. Appl. Phys.*, 1963, **2**, 6-10.
192. E. A. Skrabek and D. S. Trimmer, in *CRC Handbook of Thermoelectrics*, ed. D. M. Rowe, CRC Press, Boca Raton, 1995, pp. 267-275.
193. E. M. Levin, S. L. Bud'ko and K. Schmidt-Rohr, *Adv. Funct. Mater.*, 2012, **22**, 2766-2774.
194. B. Abeles, *Phys. Rev.*, 1963, **131**, 1906-1911.
195. C. M. Bhandari and D. M. Rowe, *J. Phys. D-Appl. Phys.*, 1977, **10**, L59-L61.
196. A. V. Ioffe and A. F. Ioffe, *Sov. Phys-Sol. State*, 1960, **2**, 719-728.

197. P. E. Batson and J. F. Morar, *Appl. Phys. Lett.*, 1991, **59**, 3285-3287.
198. F. Ben Zid, A. Bhouri, H. Mejri, M. Said, N. Bouarissa, J. L. Lazzari, F. A. d'Avitaya and J. Derrien, *Physica B*, 2002, **322**, 225-235.
199. M. S. Park, J.-H. Song, J. E. Medvedeva, M. Kim, I. G. Kim and A. J. Freeman, *Phys. Rev. B*, 2010, **81**, 155211.
200. F. Herman, M. Glicksman and R. H. Parmenter, in *Progress in semiconductors*, eds. A. F. Gibson, R. E. Burgess and P. Aigrain, John Wiley &Sons, Inc., New York, 1957, vol. 2, pp. 3-33.
201. F. Ren, E. D. Case, E. J. Timm and H. J. Schock, *Phil. Mag.*, 2007, **87**, 4907-4934.
202. Y. Gelbstein, Z. Dashevsky and M. P. Dariel, *J. Appl. Phys.*, 2008, **104**, 033702.
203. J. Q. He, J. R. Sootsman, L. Q. Xu, S. N. Girard, J. C. Zheng, M. G. Kanatzidis and V. P. Dravid, *J. Am. Chem. Soc.*, 2011, **133**, 8786-8789.
204. J. Androulakis, I. Todorov, J. He, D. Y. Chung, V. Dravid and M. Kanatzidis, *J. Am. Chem. Soc.*, 2011, **133**, 10920-10927.
205. C. B. Lioutas, N. Frangis, I. Todorov, D. Y. Chung and M. G. Kanatzidis, *Chem. Mat.*, 2010, **22**, 5630-5635.
206. M. K. Han, X. Y. Zhou, C. Uher, S. J. Kim and M. G. Kanatzidis, *Adv. Energ. Mater.*, 2012, **2**, 1218-1225.
207. P. F. P. Poudeu, J. D'Angelo, H. J. Kong, A. Downey, J. L. Short, R. Pcionek, T. P. Hogan, C. Uher and M. G. Kanatzidis, *J. Am. Chem. Soc.*, 2006, **128**, 14347-14355.
208. Y. Takagiwa, Y. Pei, G. Pomrehn and G. J. Snyder, *Appl. Phys. Lett.*, 2012, **101**, 092102.
209. M. V. Valeiko, Zasavitskii, II, V. L. Kuznetsov, A. V. Kurganskii and B. N. Matsonashvili, *Sov. Phys. Semicond.*, 1985, **19**, 388-390.
210. F. E. Faradzhev, *Sov. Phys. Semicond.*, 1984, **18**, 1311-1312.
211. W. W. Scanlon, *J. Phys. Chem. Solids*, 1959, **8**, 423-428.
212. B. A. Efimova, T. S. Stavitskaya, L. S. Stilbans and L. M. Sysoeva, *Sov. Phys-Sol. State*, 1960, **1**, 1217-1223.
213. I. Vurgaftman, J. R. Meyer and L. R. Ram-Mohan, *J. Appl. Phys.*, 2001, **89**, 5815.
214. T. S. Stavitskaya, DSc Dissertation, A. F. Ioffe Physical-Technical Institute, Leningrad, 1968.
215. L. Nordheim, *Ann. Phys-Berlin*, 1931, **9**, 607-640.
216. L. Makowski and M. Glicksman, *J. Phys. Chem. Solids*, 1973, **34**, 487-492.
217. J. W. Harrison and J. R. Hauser, *J. Appl. Phys.*, 1976, **47**, 292-300.
218. J. R. Hauser, M. A. Littlejohn and T. H. Glisson, *Appl. Phys. Lett.*, 1976, **28**, 458-461.
219. J. W. Harrison and J. R. Hauser, *Phys. Rev. B*, 1976, **13**, 5347-5350.
220. D. Chattopadhyay, *Solid State Commun.*, 1994, **91**, 149-151.
221. S. R. Mehrotra, A. Paul and G. Klimeck, *Appl. Phys. Lett.*, 2011, **98**, 173503.
222. M. A. Littlejohn, J. R. Hauser, T. H. Glisson, D. K. Ferry and J. W. Harrison, *Solid-State Electron.*, 1978, **21**, 107-114.
223. S.-H. Wei and A. Zunger, *Phys. Rev. B*, 1997, **55**, 13605-13610.
224. E. Bellotti, F. Bertazzi and M. Goano, *J. Appl. Phys.*, 2007, **101**, 123706.
225. W. L. Li, G. A. Csathy, D. C. Tsui, L. N. Pfeiffer and K. W. West, *Appl. Phys. Lett.*, 2003, **83**, 2832-2834.
226. V. W. L. Chin, *J. Phys. Chem. Solids*, 1991, **52**, 1193-1195.
227. J. J. Tietjen and L. R. Weisberg, *Appl. Phys. Lett.*, 1965, **7**, 261-263.
228. S. Movchan, F. Sizov and V. Tetyorkin, *Semicond. Phys., Quant. Electron. Opto.*, 1999, **2**, 84-87.
229. H. Dumont, J.-E. Bouree, A. Marbeuf and O. Gorochov, *J. Cryst. Growth*, 1993, **130**, 600-610.

230. J. Callaway, *Phys. Rev.*, 1959, **113**, 1046-1051.
231. C. J. Glassbrenner and G. A. Slack, *Phys. Rev.*, 1964, **134**, A1058-A1069.
232. G. A. Slack and S. Galginaitis, *Phys. Rev.*, 1964, **133**, A253-A268.
233. V. K. Zaitsev, E. N. Tkalenko and E. N. Nikitin, *Sov. Phys-Sol. State*, 1969, **11**, 221-224.
234. J. Q. He, S. N. Girard, M. G. Kanatzidis and V. P. Dravid, *Adv. Funct. Mater.*, 2010, **20**, 764-772.
235. P. G. Klemens, *P. Phys. Soc. A*, 1955, **68**, 1113-1128.
236. J. Callaway and H. C. Vonbaeyer, *Phys. Rev.*, 1960, **120**, 1149-1154.
237. P. G. Klemens, *Phys. Rev.*, 1960, **119**, 507-509.
238. O. L. Anderson and J. E. Nafe, *J. Geophys. Res.*, 1965, **70**, 3951-3963.
239. D. L. Anderson and O. L. Anderson, *J. Geophys. Res.*, 1970, **75**, 3494-3500.
240. Electronic Archive on Physical Properties of Semiconductors at Ioffe Physical Technical Institute, available at: http://www.ioffe.ru/SVA/ NSM/Semicond/index.html
241. G. T. Alekseeva, B. A. Efimova, L. M. Ostrovskaya, O. S. Serebryannikova and M. I. Tsypin, *Sov. Phys. Semicond.*, 1971, **4**, 1122-1125.
242. J. Yang, G. P. Meisner and L. Chen, *Appl. Phys. Lett.*, 2004, **85**, 1140-1142.
243. G. A. Slack, *Phys. Rev.*, 1962, **126**, 427-441.
244. E. Gurieva, P. Konstantinov, L. Prokof'eva, Y. Ravich and M. Fedorov, *Semiconductors*, 2003, **37**, 276-282.
245. E. F. Steigmeier and B. Abeles, *Phys. Rev.*, 1964, **136**, A1149-A1155.
246. D. M. Rowe and V. S. Shukla, *J. Appl. Phys.*, 1981, **52**, 7421-7426.
247. D. M. Rowe, V. S. Shukla and N. Savvides, *Nature*, 1981, **290**, 765-766.
248. Y. Z. Pei, A. D. LaLonde, N. A. Heinz, X. Y. Shi, S. Iwanaga, H. Wang, L. D. Chen and G. J. Snyder, *Adv. Mater.*, 2011, **23**, 5674-5678.
249. L. D. Zhao, H. J. Wu, S. Q. Hao, C. I. Wu, X. Y. Zhou, K. Biswas, J. Q. He, T. P. Hogan, C. Uher, C. Wolverton, V. P. Dravid and M. G. Kanatzidis, *Energy Environ. Sci.*, 2013, **6**, 3346.
250. A. N. Veis, *Sov. Phys. Semicond.*, 1982, **16**, 724-725.
251. A. A. Andreev and V. N. Radionov, *Sov. Phys. Semicond.*, 1967, **1**, 145-148.
252. N. V. Kolomoets, M. N. Vinogradova and L. M. Sysoeva, *Sov. Phys. Semicond.*, 1968, **1**, 1020-1024.
253. A. N. Veis, R. F. Kuteinikov, S. A. Kumzerov and Y. I. Ukhanov, *Sov. Phys. Semicond.*, 1976, **10**, 1320-1321.
254. T. R. Globus and A. O. Olesk, *Sov. Phys. Semicond.*, 1985, **19**, 385-388.
255. M. N. Vinogradova, N. V. Kolomoet, I. M. Rudnik and L. M. Sysoeva, *Sov. Phys. Semicond.*, 1969, **3**, 231-232.
256. A. N. Veis, V. I. Kaidanov, R. F. Kuteinikov, S. A. Nemov, S. A. Rudenko and Y. I. Ukhanov, *Sov. Phys. Semicond.*, 1978, **12**, 161-163.
257. Q. Zhang, F. Cao, W. Liu, K. Lukas, B. Yu, S. Chen, C. Opeil, D. Broido, G. Chen and Z. Ren, *J. Am. Chem. Soc.*, 2012, **134**, 10031-10038.
258. W. Z. Shen, H. F. Yang, L. F. Jiang, K. Wang, G. Yu, H. Z. Wu and P. J. McCann, *J. Appl. Phys.*, 2002, **91**, 192-198.
259. A. Lambrecht, N. Herres, B. Spanger, S. Kuhn, H. Bottner, M. Tacke and J. Evers, *J. Cryst. Growth*, 1991, **108**, 301-308.
260. A. Majumdar, H. Z. Xu, F. Zhao, J. C. Keay, L. Jayasinghe, S. Khosravani, X. Lu, V. Kelkar and Z. Shi, *J. Appl. Phys.*, 2004, **95**, 939-942.
261. K. Biswas, J. Q. He, Q. C. Zhang, G. Y. Wang, C. Uher, V. P. Dravid and M. G. Kanatzidis, *Nat. Chem.*, 2011, **3**, 160-166.
262. A. N. Veis and Y. I. Ukhanov, *Sov. Phys. Semicond.*, 1976, **10**, 780-783.
263. H. Akai, *J. Phys. Soc. Jpn.*, 1982, **51**, 468-474.

264. H. Akai, *J. Phys. Cond. Mat.*, 1989, **1**, 8045-8063.
265. M. Schröter, H. Ebert, H. Akai, P. Entel, E. Hoffmann and G. G. Reddy, *Phys. Rev. B*, 1995, **52**, 188-209.
266. U. V. Barth and L. Hedin, *J. Phys. C: Solid State Phys.*, 1972, **5**, 1629.
267. C. M. Jaworski, B. Wiendlocha, V. Jovovic and J. P. Heremans, *Energy Environ. Sci.*, 2011, **4**, 4155-4162.
268. Y. Takagiwa, Y. Pei, G. Pomrehn and G. Jeffrey Snyder, *APL Materials*, 2013, **1**, 011101.
269. Y. Lee, S.-H. Lo, J. Androulakis, C.-I. Wu, L.-D. Zhao, D.-Y. Chung, T. P. Hogan, V. P. Dravid and M. G. Kanatzidis, *J. Am. Chem. Soc.*, 2013, **135**, 5152-5160.
270. K. Y. Tsou and E. B. Hensley, *J. Appl. Phys.*, 1974, **45**, 47-49.
271. I. B. S. Banu, M. Rajagopalan, B. Palanivel, G. Kalpana and P. Shenbagaraman, *J. Low Temp. Phys.*, 1998, **112**, 211-226.
272. D. Rached, M. Rabah, N. Benkhettou, B. Soudini and H. Abid, *Phys. Status Solidi B-Basic Res.*, 2004, **241**, 2529-2537.
273. R. Graham and D. Yu, *Nano Lett.*, 2012, **12**, 4360-4365.